Synergetic effects inside a simplified friction material: study of the role of ingredients

POLITECNICO DI TORINO

PHD IN MATERIALS SCIENCE AND TECHNOLOGY

FINAL DISSERTATION

XXVIII CYCLE

SYNERGETIC EFFECTS INSIDE A SIMPLIFIED FRICTION MATERIAL: STUDY OF THE ROLE OF INGREDIENTS

FLORENCE VIVIER

TUTORS: PROF. MARCO SANGERMANO

PH.D. DIEGO PELLEREJ

DECEMBER 1ST 2016

ACKNOWLEDGEMENTS

First of all, I would like to express my special appreciation and thanks to Dr. Pietro Buonfico, Diego Santamaria and Marco Sangermano to be at the origin of this PhD project and to give me the opportunity to work in ITT. Diego, you have been a tremendous mentor for me, thanks for your encouragement and your trust since the beginning. I can't count all the great moments spent together, thank you for your friendship up till today. A special thanks goes to Diego Pellerej, I don't even know where to start. Your disponibility, your permanent support and patience, your brilliant comments and suggestions saved my PhD work; your good spirit makes people around you in a cheerful ambience, I couldn't think of a better tutor.

Thanks to my ITT colleagues: Vale, I miss you so much (the delizia card is waiting for you), Marco, Robbie and his wonderful laugh, Mily, the sweetest lab girl, Ylenia and her wall of fame (remember: our side is the best side), Valentina, Flavio, Fede my coach (you definitively deserve a special prize for that), Giulia and her contagious good mood and finally Davide and Simone who lighted up these last months. Thanks to all the others I can't list here but contributed to make unique this experience.

Giovanna, Maria Giulia the days spent together in Turin were priceless to me, as professionally than personally. Maria Giulia I have no words to thank you for your last minute help… Prof. Colombo, it has been a real pleasure to work with you, thank you for your always wise advice and your pleasant company. It is an honor for me to have you as jury member today.

Even if time passed, how could I write these acknowledgements without thinking about people who have been present for me since my first italian days. I would like to thank Prof.ssa Bongiovanni for her trust in me years ago, I owe her so much. Thanks to Prof Priola for his support. To my wonderful friends: Annalisa, you know how much your friendship meant to me, I will always be grateful to you for that. Gio and your sense of humour, Ale for our complicity and Ignazio too of course, always present to help but also to have fun: such a perfect friend. I don't forget the ones who arrived after: Erika (don't worry, you will manage to do everything!), Arnaud and Fede. Then last but not least, Sophie and Julia my Italiane nel cuore, since we don't talk in french together everything

will be ok! I wish you, in better, everything you wish. You mean the world for me, there is no day I don't feel lucky to have you: thank you.

Thanks to people I met during my trips in various congresses, who made me enjoy even more my work.

Of course a special thanks to my mum and dad who permit me to study whatever and wherever I wanted, even if it has not always been a piece of cake. Thanks to my Poupette, to show me the way.

Thanks to my little family, to be this little paradise island when I come back home. I dedicate this thesis to both of you.

CONTENTS

INTRODUCTION

I - GENERALITIES

In the last two decades, the formulation and production of friction materials for braking systems in automotive or aircraft industries have undergone major changes. The braking material system in automobile has been considered as one of the key features among the overall performance of the vehicle. The reason of this high interest depends on its crucial roles in various aspects of the total performance such as a stopping distance, pedal feel, induced vibrations and disc wear. Since a single material has never been successful for commercial brake friction materials, important efforts have been addressed to improve the performance of the friction material and numerous multicomponents composites have been tested as friction material from the early stage of vehicle development (1) (2) (3).

In a tribological couple of counterface materials used in friction, one can consider the friction force as the result of the combined effects of the asperities deformation, the adhesion force in the contacts, and the ploughing of the hard asperities, hard particles and wear debris. The relative contribution of all of these forces depends on the surfaces topography, the history of the sliding movement, the materials nature and the environment. The nature of the contact interface between friction material composites and disc surfaces is so particular that it can't be classified neither as a metal-metal nor a metal-elastomer combination. The wear phenomena associated with the friction dynamics reflect mechanisms which are characteristic of both types of interfaces (4) (5).

II - BRAKING PROCESS

The dynamic of stopping for any vehicle is the consequence of the simultaneous action of the friction forces between the two counterparts brake and disc, the resistance to rolling, the resistance to movement caused by the air and the internal resistance of the engine. The frictional force depends on the brakes design, on the force used to actuate the brakes, and on the system used to transmit the friction force. To sum up, the stopping of a vehicle presents complex dynamics that depend on many parameters as the vehicle, the

road, and the driver. It must be easy to stop the vehicle in a quick and reliable way under various conditions. For instance, in a car, when the brake pads are pressed against the disc, the cohesion forces tend to shear the friction material. The main components which constitute the disc brake assembly are the disc, the caliper and the two pads. The caliper is built up with one or more cylinders and with one piston for each. Between a piston and its corresponding cylinder a piston seal is placed; and the pads are located between the piston and the disc. The pads are linked to the caliper by retaining pins, which permit movement of the pads during braking. FIGURE 1 is a schematic illustration of this.

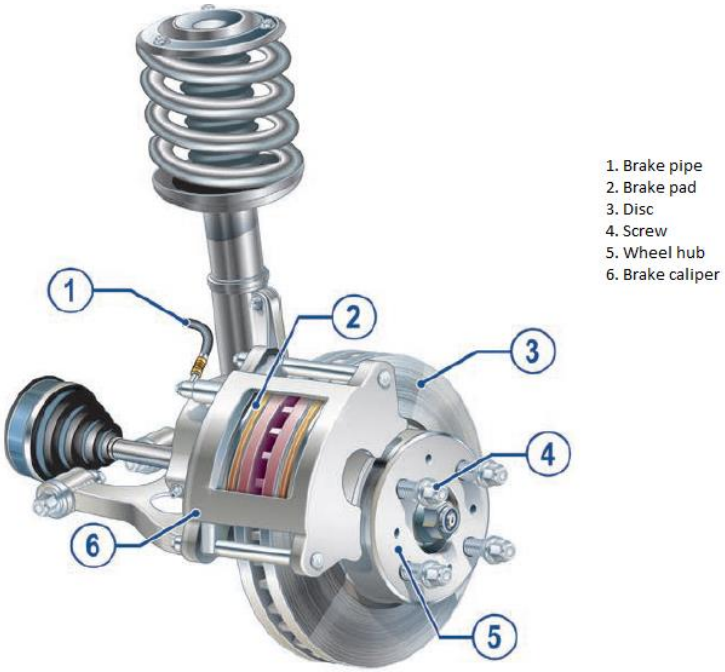

FIGURE 1SCHEMATIC DIAGRAM OF A DISC BRAKE SYSTEM (6)

The working of a disc-brake assembly is relatively simple. A movement on the brake pedal forces a piston to move in the master cylinder: this causes a pressure on the liquid ahead of the piston, forcing the liquid under pressure against the caliper. As a consequence the pistons in the caliper are activated and the pads are forced against the disc. At the end of the braking, after releasing the hydraulic pressure, the caliper pistons come back to their resting position, ready for a new brake application. The brake material is a mixture of components specially designed to obtain the best properties compromise for the braking action, being the mechanism that transforms the applied pressure into mechanical forces that retard the wheel movement until final stopping (7) (8) (9) (10) (11) (12) (13).

III - BRAKE PAD COMPOSITION

Usually, a commercial friction material contains more than 20 components to achieve the desired properties (14) (15) (16) (17); in the literature several hundred ingredients have been reported for being commonly used to tailor the friction composites characteristics. They are classified into four main categories, namely, binder, structural modifiers, friction modifiers and fillers, based on the first function they perform from wear resistance to friction control. The synergy existing between all these ingredients and their influence on properties is so complex that formulation is still referred as an art more than science (14). These materials have to satisfy numerous features such as friction stability, resistance to high temperatures or ecofriendly nature.

Eighty years ago a significant change happened in frictional materials formulation due to the use of asbestos fibres, a natural mineral fibre that acts as an ideal component thanks to its outstanding properties, as high heat resistance (stable until 500°C around), mechanical strength, easy processability and low cost. Thermosetting phenol formaldehyde resins reinforced with this fibre constituted the basis for the development of friction materials in the automotive sector. Asbestos is nowadays considered to be a health hazard, since its occupational exposure can lead to some lung disease (also called asbestosis). As a consequence, the industry has been actively attempting to replace it. Nevertheless, replacing asbestos in frictional materials has proven to be a very harsh task. So far, no other single fibre (from synthetic or natural origin) can by itself replace asbestos, since no other single material exhibits a similar morphology or the same combination of thermal stability, frictional performance and low cost.

As explained by G. Crosa et al (18), to replace the asbestos fibres, manufacturers of friction materials use combinations of different fibres, typically blends of long and short fibres. In fact short fibres are needed to reinforce the areas between and around the long fibres and to confer other important physical, thermal, and frictional properties on the composite material. Some examples are steel, aramid, glass, ceramic, mineral and carbon fibres (19). The binder is the glue that holds all the components together. The binder mostly used in pad material and chosen in the present study is a phenol-formaldehyde thermosetting resin, like the novolac type (7). Friction modifiers are added to tune the mechanical and frictional characteristics of the material. Abrasive like aluminum or chromium oxide are commonly used to increase the friction coefficient. Brass, copper or other types of metal chips can be added to the mixture to improve the dissipation of the

heat generated during braking. Lubricants, such as graphite, are added to reduce the friction coefficient and wear. Moreover, various additives are necessary for optimizing the overall properties, for instance to extend the elastic properties to a range of temperatures far beyond the characteristics of the phenolic resin if used alone. In addition, to reduce costs minerals such as barites, clay or calcium carbonate, are added to the mixture. Thus, in the classic friction materials there are four different categories of ingredients, with occasional overlap of functions.

Then the basic manufacturing process consists of the mixing of these ingredients, followed by their pressing at a temperature range from 130°C to 160°C and at pressures high enough to assure the desired level of packing. Hereafter the frictional material composite is submitted to various treatments as heating, cooling, and finishing operations (drilling, cutting, etc).

IV - BRAKE PAD PROPERTIES

The most important feature of a friction material is for sure a suitable friction coefficient. It has to be as constant as possible in the desired interval of temperatures that ranges from below 0°C in the winter to above 600°C in case of sudden and extreme braking. The friction coefficient has also to be stable regarding different velocities, pressures and environments with typical values in the [0.3-0.5] range. The second fundamental parameter to take in account is the wear of the friction materials and of the metallic counterface since they determine the useful lifetime of the components. The wear value of the pad material is related to the friction coefficient, not only through the basic tribological correlations between friction and wear, but also due to the influence of the wear particles, formed as a consequence of the sliding contact during braking, on the friction coefficient. Among the parameters which contribute to the specific wear of the material, the working temperatures and the surface finish have to be taken in account. Any kind of wear generation is not to avoid, as a moderate amount of wear is absolutely necessary in order to renew the surface, thus averting the risk of carbonization of some elements at high temperature, that results in a change of the tribological characteristics. Many other factors complicate the understanding of the tribological situation and make it difficult to control, and often the observed effects are the opposite to the expected ones. For example, a significant amount of abrasive in the composite can suggest a high friction coefficient, a wear rate decrease of the composite, and a wear increase of the metallic disc. But these are the only expected consequences in the simple and theoretical case,

where the dissipative forces don't generate high temperatures in the contact points. If the temperature increases above a certain value (typically above 300°C for phenolic resin composites, which corresponds to its degradation temperature) this simple picture may be completely changed.

Due to local heating during the contact, the softening of the phenol formaldehyde resin matrix induces changes in the general properties of the surface especially in the loss of cohesion of some components with the matrix. The abrasive particles that quit the composite due to the loss of adhesion, can act as hard third-body abrasive, behaving as protective layer which insures more stability to the friction. The consequences of these mechanisms could be an increase of the wear of the composite and, if the third body is continuously supplied, a friction coefficient increase (4). Due to the formulation complexity of a typical polymer composite used as friction material, the third body formation mechanism, nature and then protective action for the two counterfaces are always different and so the tribological resulting characteristics of the system. It is noteworthy that the wear debris are generated mostly in the initial phase of the friction contact and the participation to the third body can result in further abrasion or in a lubrication that decreases the friction coefficient and wear rate. For these various reasons, friction coefficient and wear can be considered as the resulting performances of all the braking process and the testing conditions: to better understand them, it is necessary to take in account thermal, morphological and physical-mechanical properties of all the friction material components and their eventual mutual interaction. This point is usually left aside, which represents an obvious gap toward the full mechanism comprehension.

AIM OF THE WORK

The work of this PhD thesis is about interaction between components of a friction material.

The selection of the different mixture components and their relative amounts in the formulation, have been largely relied on experience and systematic studies of the friction material for optimum brake pad performance are difficult to found in literature because of the complexity of the system. As reported by C.-F. Tang et al (20), several studies have been performed about a new way to select and evaluate raw materials role in the friction process. Elzey et al. (21) proposed an intelligent selection of materials approach in which micro-mechanics modeling was the method to relate the overall performance to the choice of constituent materials. Multiple regression analysis were used by Kato et al. (22) (23) to analyze the effect of each volume fraction ingredient on final friction performances. Drava et al. (24) applied chemiometric analysis to investigate the effect of process variables on the friction characteristics of the materials and then to perform a screening of the raw materials for optimal formulations. Relational grade analysis was used to rank the contributions of each ingredients and search optimal compositions (25). However, a scientific criterion of selection of ingredients has not yet been established. As the methods mentioned above can only get useful information about the sensitivity of each ingredient on the final and main important friction features (26), the interaction effects among the ingredients on friction performance are difficult to study and to understand in these multiple components composites.

To take in account the components interaction as well as their single contribution, Y. Lu et al (27) worked on novel combinatorial approach, as shown in FIGURE 2. This approach includes mainly the following steps: first, fibres and fillers (all are called “additives”) are screened and the interaction effects between the chosen binder and each additive is studied using the two component systems (A + B systems, where A is an additive and B is a binder). The interaction effects between two additives can be evaluated in turn using the three component systems (A + B + C systems, where A and C are two different additives) (28) (20). The interaction effects among three, four and more additives can be

evaluated using four, five and more component systems. This way, the friction performance of multiple component friction materials can be optimized using the n-component systems.

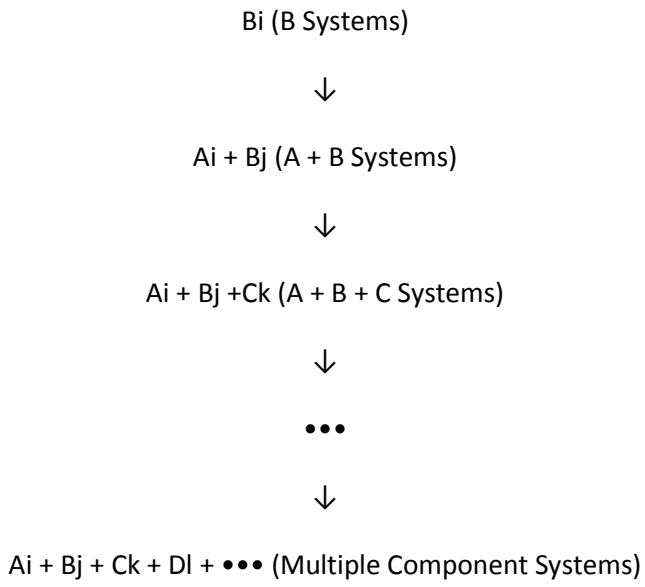

FIGURE 2 COMBINATORIAL APPROACH FOR FRICTION MATERIALS (27)

Unfortunately this approach presents many defects. First it doesn't take in account the specificity of optimal content for each filler: all fillers are dispersed at standard contents (18%vol, 40%vol, 50%vol) whereas some of them are commonly used at even less than 5%vol, as silicon carbide or aluminum oxide. Then, only tribological tests are performed and the friction coefficient and wear rate are the only parameters on which the study is based on; there is no explanation at molecular or physical scale of the obtained results, thus no deep comprehension of the results. Finally, Y. Lu et al present this theoretical approach of a formulation study, but in their articles (20) (27) (25) (28) a maximum of three components are mixed up, far from all the ones necessary to a real friction material and so a complete formula understanding.

To overcome these issues, this work is devoted to the understanding of the interactions among all the ingredients of a brake pad, focusing on the relationship between the main thermal/mechanical properties and the tribological behavior of the composite. First, in order to study the matrix-fillers interactions, monofiller systems composed by a basic mix and one filler are formulated. The basic mix is composed of phenol formaldehyde resin, the whole material binder, and aramid fibres in order to give a sufficient

mechanical strength to the sample. The filler content is chosen based on the optimized composition proposed by scientific articles, and two others concentrations (one inferior, the other superior) are considered in order to obtain a tendency of each measured property in respect of the filler content. This step is fully explained in the *Materials and methods* chapter. These three materials are fully characterized using thermal, mechanical, morphological and tribological tests. The results are presented by type property in the *Physico-mechanical properties of monocomponent samples*, *Thermal properties of monocomponent samples* and *Tribological properties of monocomponent samples chapters*. At the end of this first step, the material among the three presenting the best properties compromise has its filler content retained for the next step.

Then, two, three and more fillers are mixed together with the binder, at the respective optimal contents, and once again a full characterization is performed. For sake of clarity, we present in chapter *Tribological properties of multiple samples: role of chemico-physical characteristics* the tribological results together with the main properties affecting them, to the purpose with simplifying the explaining of the material features affecting friction and wear properties.

The fillers incorporated in the resin matrix are the ones considered the most indispensable and commonly used in brake pad formulations. The final composition toward which evolves the systems is a simplified brake pad formula. This material was not optimized with respect to best brake performance, but it contains the most important ingredients which are normally applied in conventional automotive braking systems nowadays.

CHAPTER I

MATERIALS AND METHODS

I - MATERIALS: SYSTEM COMPOSITION

A deep bibliographical research has been done in order to select a total of ten ingredients to compose the friction material. For each of them all the papers dealing with the effect of the content on the general properties (tribological, mechanical or thermal) have been gathered together and for each studied article, an "index" (from 0 to 5) has been attributed which values, arbitrary, have been used as indication for the relevance of the presented work with the study conducted here. The paper with the maximum index determines the intermediate content value to take as reference. The main data of the analyzed papers are all in the *Appendix* part. In order to have a tendency of the tested material characteristics, two other monocomponent materials are formulated, at a lower and at a higher filler content. In a second time, the formulation of the multicomponent samples is done considering the best filler content regarding the whole performance of the corresponding monocomponents.

The data collected from literature for the fillers are mainly from the Handbook of Fillers (Fourth Edition), G. Wypych (ISBN: 978-1-895198-91-1), but also from Advances in Composite Tribology, Composite Materials Series, Vol. 8, G. Crosa and I. J. R. Baumvol and from the raw materials' producers technical datasheets.

1.1. BINDER: PHENOL FORMALDEHYDE RESIN

The chosen binder is a phenol formaldehyde resin usually and traditionally used in brake pad friction material. The chemical structure is presented in FIGURE 1.1, and as presented by the manufacturer it is phosphorous and boron modified adding some P and B particles to the powdered neat resin.

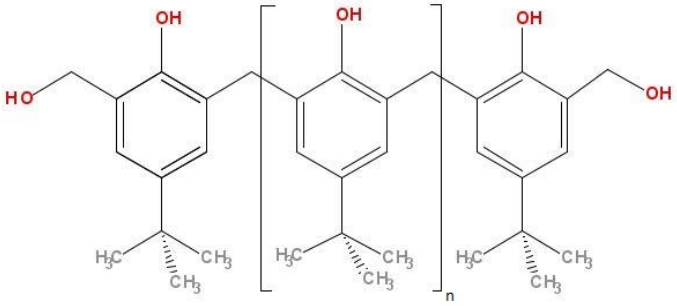

FIGURE 1.1 CHEMICAL STRUCTURE OF THE PHENOLIC RESIN

The data collected on this raw material from supplier and obtained as routine characterization in ITT laboratory are summarized on TABLE 1.1.

TABLE 1.1 DATA FORM FOR PHENOLIC RESIN RAW MATERIAL

Literature data		Laboratory data	
Density	1.25 g/cm^3	Granulometry	D50 = 33 µm
		Humidity content	2-3 %wt
		Volatile part	0-6 %wt

1.2. REINFORCING FIBRES

Among many ingredients currently used in the friction materials, reinforcing fibres play crucial role in the determination of the friction features during braking process. Usually, the reinforcing fibres used for automotive brake materials are metallic fibre, aramid pulp, ceramic fibre, acrylic fibre, glass fibre. In the majority of the friction materials, there is a total of 5–25 %vol of ingredients under fibres form and their natures, morphologies and amounts affect many aspects of brake performance and the wear life of the product.

1.2.1. Aramid fibres

One type of fibres has particularly attracted attention: the aramid pulp. Due to its crystal structure, it presents high anisotropic properties with strong covalent bonds in the fibre direction and a weak bonding (H-bonding) in the transverse direction (29) (30). Aramid fibres such as Kevlar® fibres are the most used in the reinforcing fibres category. This generic name denotes fibres made by the condensation of m- or p-phenylenediamine and isophthalic or terephthalic acids (31). They have a very low weight, and exhibit excellent thermal stability. According to Smith and Boyd (32), aramid fibres exhibit better anti-fade properties than its historical concurrent asbestos. They also present a very good

stiffness–weight ratio. Aramid fibres are of prior importance to maintain the integrity and uniformity of the brake pad material during the process (33). A very important property they have for the present use is their high wear resistance (34). However, because of their relative softness, there would most probably be other harder fibres present in the mixture such as metallic fibres to support the braking load (35).

Aramid fibres can present different morphologies: fibre powder or pulp. In this study an aramid pulp is chosen (see FIGURE 1.2) with a fibrillary structure.

Data form of these aramid fibres is presented in TABLE 1.2.

TABLE 1.2 DATA FORM FOR ARAMID FIBRES RAW MATERIAL

Literature data		Laboratory data	
Chemistry		Granulometry	D50 = 1 mm
Absorbed moisture	5-8 %wt	Volatile part	4 – 10 %wt
Physical properties			
Density	1.44 g/cm^3		
Thermal conductivity	0.04 - 0.05 W/K.m		
Thermal expansion coefficient	-3.5x10-6 1/K		
Tensile strength	2500 MPa		
Elongation	2 – 3 %		
BET	7-15 m^2/g		
Fibre length	0.75 – 1.30 mm		

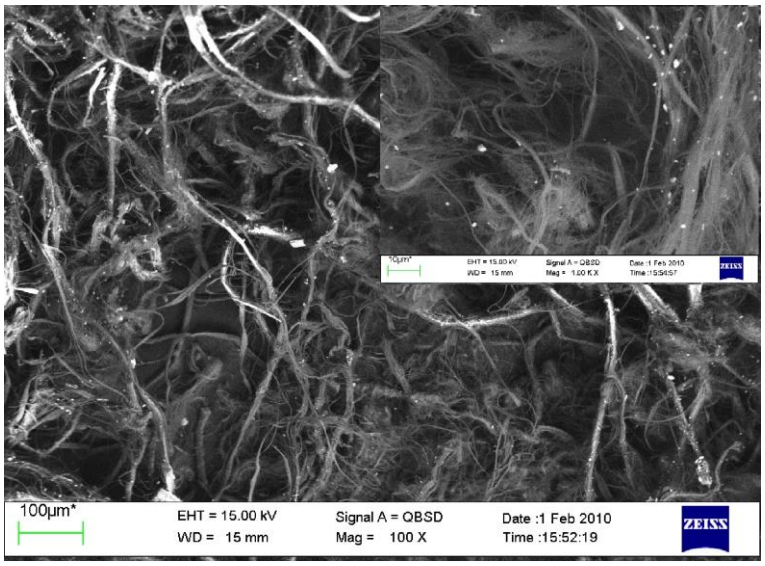

FIGURE 1.2 SEM PICTURE OF ARAMID FIBRE AT 100X USING BACKSCATTERED ELECTRON ANALYSIS (BS)

The results of the bibliographic research are presented on TABLE 1.3.

TABLE 1.3 BIBLIOGRAPHIC RESEARCH REFERENCES OBTAINED FOR ARAMID FIBRE

	Index	Content	Tested Properties
Paper 1 (36)	3	10%vol.	µ, Hardness, Porosity, Wear
Paper 2 (37)	4	12%vol.	µ, Noise, Wear
Paper 3 (38)	3	3:1 for aramid:potassium titanate	µ, Wear
Paper 4 (39)	4	30%wt.	µ, Wear
Paper 5 (22)	4	30%wt.	µ, Wear, Hardness, Thermal conductivity

The paper about aramid fibres dispersed in a phenolic resin matrix most compatible with this study indicates an optimal value of 30%wt (equal to 27.1%vol), so this content value is kept to formulate the first sample. Then the smallest considered concentration is equal to 10%vol and as a superior content would lead the material very difficult to process, an intermediate content in aramid fibre is done, equal to 17.8%vol. These compositions are presented in TABLE 1.4.

TABLE 1.4 BASIC MIXES COMPOSITIONS

Sample name	[Aramid fibres], %vol	[Resin], %vol
$BM._{10}$	10 (from literature (36))	90
$BM._{17.8}$	17.8	82.2
$BM._{27.1}$	27.1 (from literature (39))	72.9

1.2.2. Steel fibres

In order to improve some fundamental properties as thermal diffusivity, wear resistance and strength of the friction materials, metallic ingredients are incorporated in the friction material mixtures which could be steel, iron, bronze, copper, brass, or aluminum under fibres or particle form. Since they provide excellent wear pad resistance and maintain the friction effectiveness even at high temperature (high fade resistance with fast recovery process), steel fibres are often used in the friction material industry (40). However, steel fibres present some disadvantages such as excessive disc wear, and can be the cause of brake vibration. This aggressiveness against the brake disc is due to their high hardness and the metallic adhesion between steel and gray cast iron.

SEM observation of the chosen steel wool is presented in FIGURE 1.3 and the data available are shown in TABLE 1.5.

TABLE 1.5 DATA FORM FOR STEEL FIBRES RAW MATERIAL

Literature data	
Physical properties	
Density	7.89 g/cm^3
Composition	Fe: 98.6%

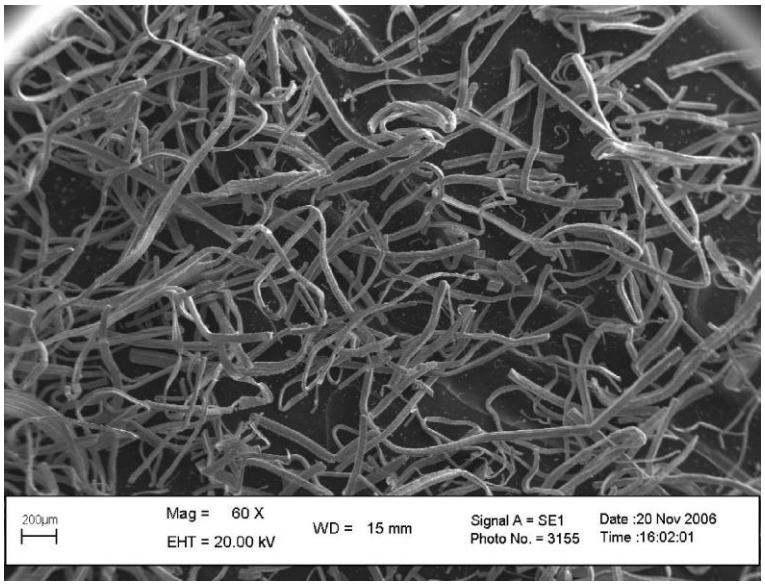

FIGURE 1.3 SEM PICTURE OF STEEL FIBRES AT 60X USING BACKSCATTERED ELECTRON ANALYSIS (BS)

The results of the bibliographic research are presented in TABLE 1.6.

TABLE 1.6 BIBLIOGRAPHIC RESEARCH REFERENCES OBTAINED FOR STEEL FIBRES

	Index	Content	Tested Properties
Paper (41)	3	15%vol.	Friction, Wear, Fade

The concentrations of steel fibres are presented in TABLE 1.7.

TABLE 1.7 STEEL FIBRES MIXES COMPOSITIONS

Sample name	[Steel fibres], %vol	[Basic mix], %vol
$St._{8}$	8	92
$St._{15}$	15 (from literature (41))	85
$St._{30}$	30	70

1.2.3. Potassium hexatitanate fibres

In the group of ceramic fibres the potassium titanate whiskers ($K_2O{\cdot}6TiO_2$) demonstrated to be of great interest thanks to their thermal stability and very good compatibility with the binder. In fact, they maintain thermal stability at elevated temperatures thanks to their high melting point at 1250–1310°C (42) (43). Their chemical structure consists of fine poly-crystalline whiskers and is a tunnel form with high strength and modulus. Potassium titanate has been used mainly as heat insulator, ion exchanger, filter, photocatalyst, anode material, pigment, abrasive, and reinforcing agent for polymeric or metallic composites (44). Potassium hexatitanate fibres have been taken on as reinforcing components for friction materials, as substitutes for asbestos: these fibres give to the friction material good characteristics related to wear friction noise, resistance and fading (45) (46).

Data available about the selected potassium hexatitanate are presented in TABLE 1.8 and a SEM observation in FIGURE 1.4.

TABLE 1.8 DATA FORM FOR POTASSIUM HEXATITANATE RAW MATERIAL

Literature data		Laboratory data	
Physical properties		Granulometry	D50 = 30 µm
Density	3.6 g/cm^3	Volatile part	0.17 %wt
BET	1.5 m^2/g		
Humidity	< 0.4 %wt		
Mohs hardness	3 - 5		

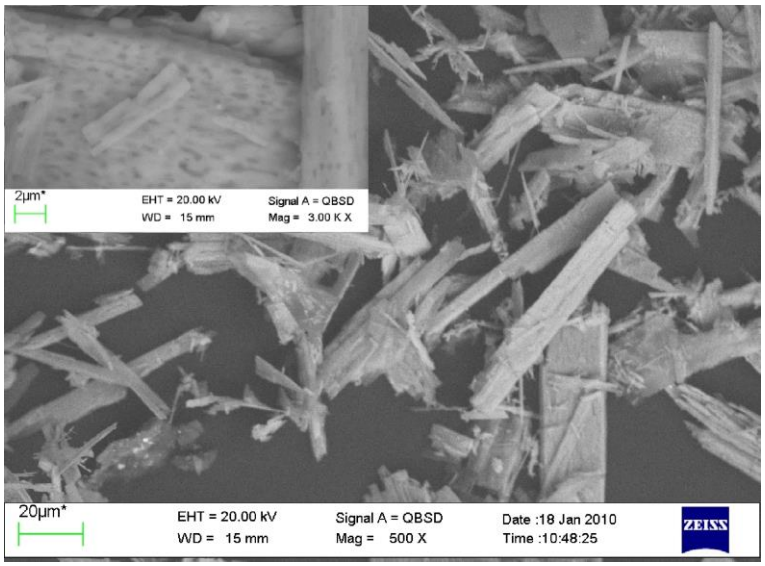

FIGURE 1.4 SEM PICTURE OF POTASSIUM HEXATITANATE FIBRES AT 500X USING BACKSCATTERED ELECTRON ANALYSIS (BS)

The results of the bibliographic research are presented in TABLE 1.9.

TABLE 1.9 BIBLIOGRAPHIC RESEARCH REFERENCES OBTAINED FOR POTASSIUM HEXATITANATE

	Index	Content	Tested Properties
Paper 1 (47)	2	20%vol.	µ, Wear
Paper 2 (48)	4	5:1 for Potassium titanate:aramid fibre	Fade

The concentrations used in the composites are presented in TABLE 1.10.

TABLE 1.10 POTASSIUM HEXATITANATE FIBRES MIXES COMPOSITIONS

Sample name	[Potassium hexatitanate], %vol	[Basic mix], %vol
$Ti._{10}$	10	90
$Ti._{20}$	20 (from literature (47))	80
$Ti._{50}$	50 (from literature (48))	50

1.3. FILLERS

1.3.1. Friction dust

Cashew nut shell liquid (CNSL) is a product from nature origin, obtained from the cashew nut shells, mainly grown in Brazil or India. The main component of raw CNSL is anacardic acid, a hydroxy carboxylic with an alkyl substituent meta to the hydroxy functionality. During heating, decarboxylation of anacardic acid occurs. This process yields distilled CNSL which is composed of: cardanol, a meta-substituted phenol (>86%); cardol, a meta-substituted resorcinol (2-5%) and other minor components (<6%) including 2-methyl cardol (49). In addition to ring heterogeneity, the alkyl chains contain 15 carbons but consist of mixtures of saturated (<1%), monoene (39%), diene (16%) and triene (45%). The percentages are based on the work of Tyman and Jacobs (50) but considering the original nature of this component, important variations can be observed in different CNSL benches, corresponding to variations in the percentages of each component (51). Their chemical structures are presented in FIGURE 1.5.

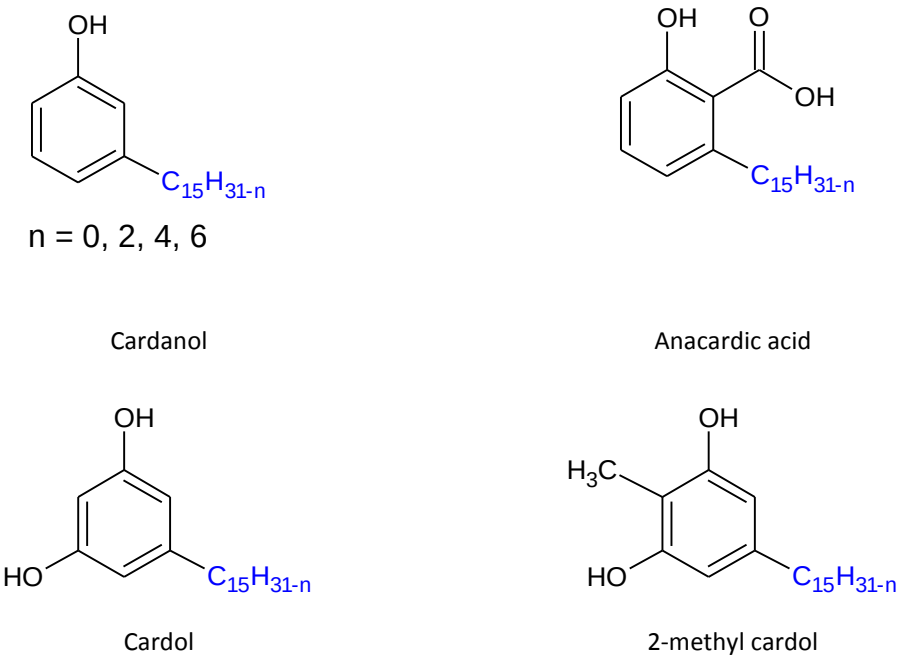

FIGURE 1.5 CHEMICAL COMPOSITIONS OF DIFFERENT COMPONENTS OF CNSL

Thanks to its phenolic nature and the unsaturation present in the side chain, cardanol component offers reaction sites both on the aromatic ring and on the side chain, which makes it a good candidate to undergo a variety of reactions (52) (53). Via the hydroxyl group, cardanol may react with formaldehyde species or hexamethylene tetramine to form cardanol-formaldehyde resins (54) (55). The aliphatic side chains of cardanol usually carry one to three double bonds, making cardanol a mixture of four ingredients varying in the degree of side-chain unsaturation (56) (57), which allows cardanol to undergo addition polymerization through these double bonds. In conclusion, a variety of resins can be synthesized starting with cardanol molecules (58).

About the chosen raw material, the data at disposal from laboratory characterization are in TABLE 1.11.

TABLE 1.11 DATA FORM FOR FRICTION DUST RAW MATERIAL

Literature data		Laboratory data	
Physical properties		Morphological properties	
Density	1.06 g/cm^3	Sieve analysis	425 µm: 11%wt 250 µm: 27%wt 150 µm: 28%wt <150 µm: 34%wt

The results of the bibliographic research are presented in TABLE 1.12.

TABLE 1.12 BIBLIOGRAPHIC RESEARCH REFERENCES OBTAINED FOR FRICTION DUST

	Index	Content	Tested Properties
Paper 1 (59)	3	16%vol.	Compressibility, Hardness, Porosity, µ, Wear
Paper 2 (52)	2	75:25 for phenol:friction dust	Hardness, Tensile strength

The amount used for preparing the composites are presented in TABLE 1.13.

TABLE 1.13 FRICTION DUST MIXES COMPOSITIONS

Sample name	[Friction dust], %vol	[Basic mix], %vol
$F._8$	8	92
$F._{16}$	16 (from literature (59))	84
$F._{32}$	32	68

1.3.2. Barium sulfate

One of the most commonly used fillers in brake pad materials is barium sulphate, also called barite. It gives heat resistance to the brake friction material and at the same time improve the friction characteristics of the brake pad (60).

Barium sulfate is obtained from a common mineral substance, from which it is chemically purified. It can be extracted from a variety of natural rocks, including limestone and sandstone (61). Chemically, $BaSO_4$ is an inorganic salt composed of a lattice of ions, Ba^{2+} and $SO4^{2-}$.

Laboratory and literature data about the selected barium sulfate filler are presented in TABLE 1.14, and a SEM picture of the selected barite is shown in FIGURE 1.6.

TABLE 1.14 DATA FORM FOR BARIUM SULFATE RAW MATERIAL

Literature data		Laboratory data	
Physical properties		Granulometry	D50 = 5 µm
Density	4.3 g/cm^3	Volatile part	0.05 %wt
BET	0.4 m^2/g		
Humidity	0.2 %wt max		
Mohs hardness	2.5		
Conductivity	200-300 µS/cm		

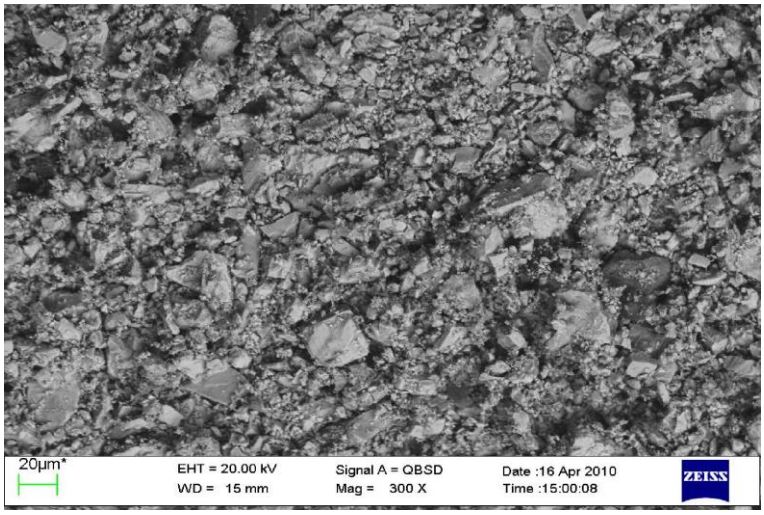

FIGURE 1.6 SEM PICTURE OF BARIUM SULFATE AT 300X USING BACKSCATTERED ELECTRON ANALYSIS (BS)

The results of the bibliographic research are presented in TABLE 1.15.

TABLE 1.15 BIBLIOGRAPHIC RESEARCH REFERENCES OBTAINED FOR BARIUM SULFATE

	Index	Content	Tested Properties
Paper (62)	3	70:30 for barite:novolac resin vol	μ, worn surface morphology

The compositions of the barium sulfate samples are presented in TABLE 1.16.

TABLE 1.16 BARIUM SULPHATE MIXES COMPOSITIONS

Sample name	[Barium sulfate], %vol	[Basic mix], %vol
$B._{30}$	30	70
$B._{50}$	50	50
$B._{70}$	70 (from literature (62))	30

1.4. LUBRICANTS

1.4.1. Graphite

The english word “graphite”, which is originated from the greek word graphein, means to write. Thus, it was first known for its possible use as pencil, considering the facility with which it can be transferred to a substrate during a rubbing motion (63). It dates back one hundred years ago when it was discovered that graphite surface exhibits a very low frictional force (64) and due to this unusual low friction, graphite has been used as a solid lubricant (65).

As exposed by Yu. N. Vasilev et al (66), in graphitic materials the crystallite size is comprised over a wide range from 2.5 nm in high-strength fibre to 1 μm in natural graphite. A graphite crystallite presents a laminar structure, and in each layer carbon atoms form a regular network of regular hexahedrons (67) (68). Each of these C atom in the base plane is bound with three adjacent ones at a distance of 0.14 nm. The bond energy is equal to 710 kJ/mol. The adjacent planes interact thanks to dispersion forces. The bond energy between the planes is in the range of 4.2–18.2 kJ/mol and the distance between them is 0.34 nm (see FIGURE 1.7). Given that the bond energy between the atoms

in the same plane significantly exceeds the bond energy between adjacent planes, free movement of the layers during friction are possible.

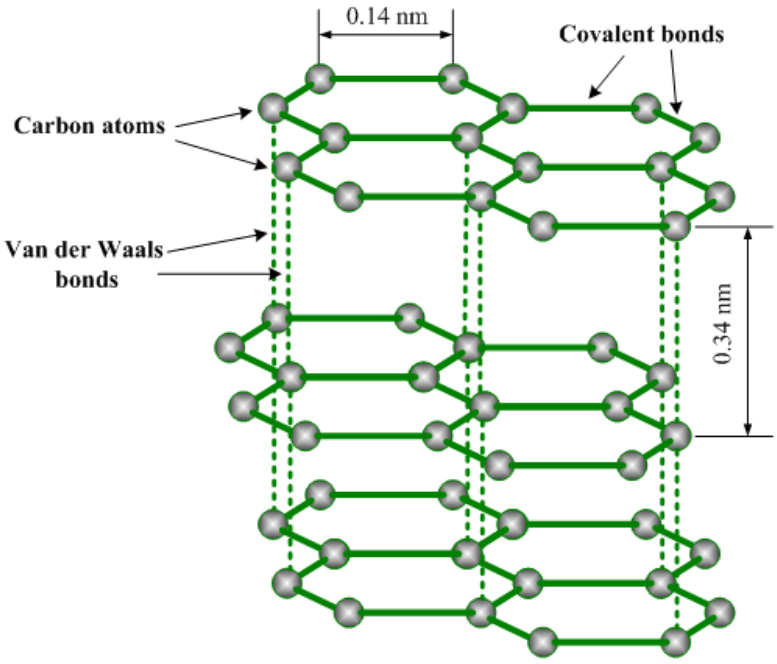

FIGURE 1.7 GRAPHITE MOLECULAR STRUCTURE (69)

The main purpose of a lubricant in a pad material is the stabilization of the friction coefficient during sliding, particularly at high temperature. The most commonly used lubricants are graphite and various metal sulphides. Graphite is wider employed because it is able to form a lubricant layer on the opposing counterface in a short time (70). This self-sustaining layer ensures a strong stability to the friction coefficient. The graphite used in brake friction materials is in flake or powder form, but in the flake form it demonstrates improved lubrication properties (71), while in the powder form it is able to better dissipate the heat generated during braking (72).

The data about the synthetic graphite available are presented in TABLE 1.17, and a SEM observation is shown in FIGURE 1.8.

TABLE 1.17 DATA FORM FOR GRAPHITE RAW MATERIAL

Literature data		Laboratory data	
Physical properties		Sieve analysis	212 µm: 2%wt 106 µm: 18%wt 75 µm: 20%wt <75 µm: 60%wt
Density	2.2 g/cm^3	Volatile part	0.08 %wt
Thermal conductivity	110-190 W/K-m		
BET	6.5-20 m^2/g		
Mohs hardness	1 - 2		

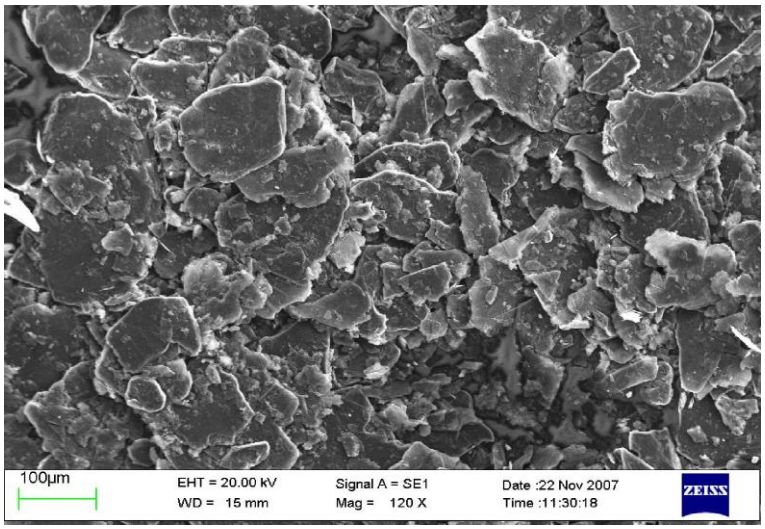

FIGURE 1.8 SEM PICTURE OF GRAPHITE AT 120X USING BACKSCATTERED ELECTRON ANALYSIS (BS)

The results of the bibliographic research are presented in TABLE 1.18.

TABLE 1.18 BIBLIOGRAPHIC RESEARCH REFERENCES OBTAINED FOR GRAPHITE

	Index	Content	Tested Properties
Paper (73)	3	10%vol.	Friction stability, Fade resistance, Lubricating capability, Wear

The compositions of graphite monocomponent samples are presented in TABLE 1.19.

TABLE 1.19 GRAPHITE MIXES COMPOSITIONS

Sample name	[Graphite], %vol	[Basic mix], %vol
$G._5$	5	95
$G._{10}$	10 (from literature (73))	90
$G._{20}$	20	80

1.4.2. Petroleum coke

Among inorganic particles the petroleum coke is widely used in brake pad materials as friction modifiers to improve the mechanical and tribological properties of the friction material. It is mainly composed of graphite fragments and amorphous carbon.

Characterization data about the selected petroleum coke are presented in TABLE 1.20 and a SEM observation is presented in FIGURE 1.9.

TABLE 1.20 DATA FORM FOR PETROLEUM COKE RAW MATERIAL

Literature data		Laboratory data	
Physical properties		Granulometry	D50 = 500 µm
Density	2.06 g/cm^3		
Humidity	0.10 %wt		

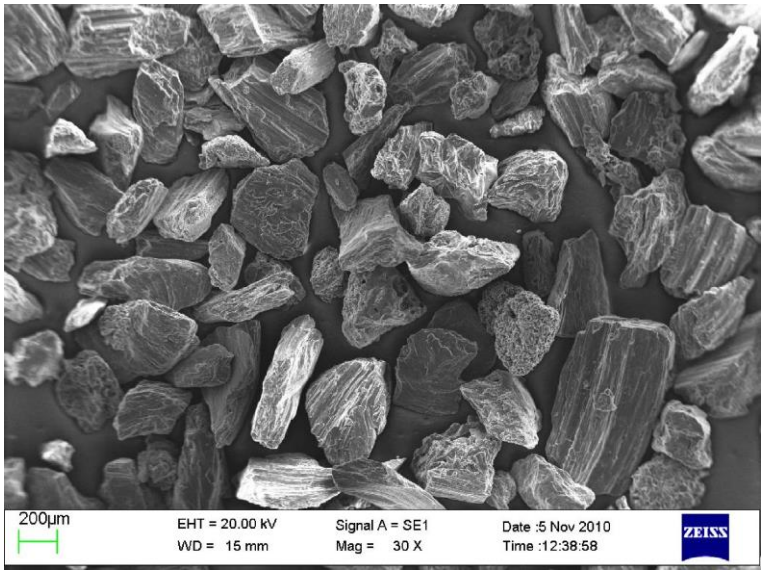

FIGURE 1.9 SEM PICTURE OF PETROLEUM COKE AT 30X USING BACKSCATTERED ELECTRON ANALYSIS (BS)

The results of the bibliographic research are presented in TABLE 1.21.

TABLE 1.21 BIBLIOGRAPHIC RESEARCH REFERENCES OBTAINED FOR PETROLEUM COKE

	Index	Content	Tested Properties
Paper (74)	4	10%vol.	Hardness and Bending Strength, μ, Wear

The compositions of the petroleum coke monocomponent samples are presented in TABLE 1.22.

TABLE 1.22 PETROLEUM COKE MIXES COMPOSITIONS

Sample name	[Coke], %vol	[Basic mix], %vol
$C._5$	5	95
$C._{10}$	10 (from literature (74))	90
$C._{20}$	20	80

1.5. ABRASIVES

1.5.1. Aluminum oxide

Aluminum oxide, or alumina (Al_2O_3) is one of the most attractive ceramics that has found many applications in various industries. It is commonly uses in its crystalline polymorphic phase α-Al_2O_3. It can be used to produce aluminum, as an abrasive thanks to its hardness, or as a refractory material thanks to its high thermal stability (75).

The collected data on the α-Al_2O_3 chosen raw material are presented in TABLE 1.23, and a SEM observation is reported in FIGURE 1.10.

TABLE 1.23 DATA FORM FOR ALUMINUM OXIDE RAW MATERIAL

Literature data		Laboratory data	
Physical properties		Granulometry	D50 = 29 μm
Volume resistivity	>1014 Ω-cm	Volatile part	0.6 %wt
Density	3.9 g/cm³		
BET	9-17 m²/g		
Thermal	20.5-29.3 W/K.m		

conductivity	
Mohs hardness	9
Compressive strength	2000 MPa
Moisture content	4.5 %

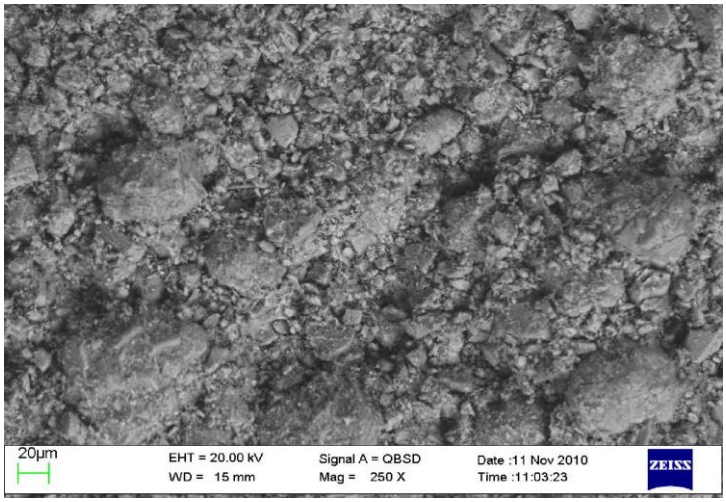

FIGURE 1.10 SEM PICTURE OF ALUMINUM OXIDE AT 250X USING BACKSCATTERED ELECTRON ANALYSIS (BS)

The results of the bibliographic research are presented in TABLE 1.24.

TABLE 1.24 BIBLIOGRAPHIC RESEARCH REFERENCES OBTAINED FOR ALUMINUM OXIDE

	Index	Content	Tested Properties
Paper 1 (76)	3	5%wt.	Tensile strength, Tg, tan δ
Paper 2 (77)	5	5.6%vol.	µ stability, Wear

The compositions of the alumina monocomponent samples are presented in TABLE 1.25.

TABLE 1.25 ALUMINUM OXIDE MIXES COMPOSITIONS

Sample name	[Aluminum oxide], %vol	[Basic mix], %vol
$A._{3}$	3	97
$A._{5.6}$	5.6 (from literature (77))	94.4
$A._{12}$	12	88

1.5.2. Silicon carbide

Today, silicon carbide material has been developed into a high quality technical grade with very high mechanical properties. Its most considered properties are: high strength, low density, low thermal expansion, high thermal conductivity, high hardness, high elastic modulus, excellent thermal resistance, and good chemical inertness. Silicon carbide exists in more than 70 crystalline forms, among which the most commonly encountered polymorphs are the alpha silicon carbide (α-SiC), with a hexagonal crystal structure and the beta modification (β-SiC), with cubic crystal structure (78).

Collected data on the α-SiC selected for this study are displayed in TABLE 1.26 and a SEM picture is presented in FIGURE 1.11.

TABLE 1.26 DATA FORM FOR SILICON CARBIDE RAW MATERIAL

Literature data		Laboratory data	
Physical properties		Volatile part	0.77%wt
Density	3.21 g/cm^3	Granulometry	D50 = 4.5 µm
Mohs hardness	9		

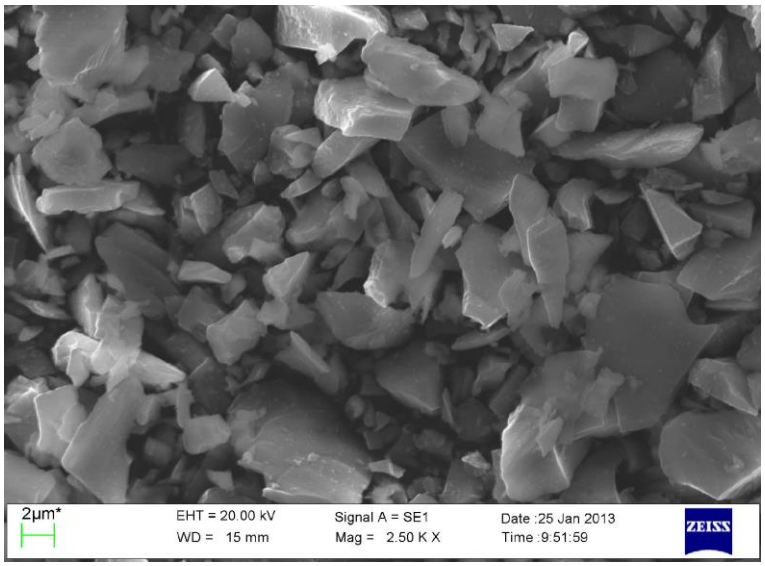

FIGURE 1.11 SEM PICTURE OF SILICON CARBIDE AT 2500X USING BACKSCATTERED ELECTRON ANALYSIS (BS)

The results of the bibliographic research are presented in TABLE 1.27.

TABLE 1.27 BIBLIOGRAPHIC RESEARCH REFERENCES OBTAINED FOR SILICON CARBIDE

	Index	Content	Tested Properties
Paper (79)	5	3.4%vol.	Wear, Friction Coefficient

The compositions of silicon carbide monocomponent samples are presented in TABLE 1.28.

TABLE 1.28 SILICON CARBIDE MIXES COMPOSITIONS

Sample name	[Silicon carbide], %vol	[Basic mix], %vol
$Si._{2}$	2	98
$Si._{3.4}$	3.4 (from literature (79))	96.6
$Si._{7}$	7	93

II - METHODS

2.1. PROTOCOL FOR SAMPLES PREPARATION

Chronologically, in the first part of this work a lab-scale process is set up to prepare the monocomponent samples (formulated using the "resin + aramid fibres" basic mix together with one of the eight other fillers) varying the filler content according to the most performant materials reported in literature. This way the basic mix and the monocomponent samples are prepared and tribologically tested.

The second part of the work concerns more complex materials (basic mix with at least two fillers) fabrication and testing, and in order to get closer to real friction materials, the samples are produced with the friction material press used in the prototype area of ITT. An analogous protocol to the lab-scale previously used is set up, with slightly different parameters, as presented in TABLE 1.29. The fundamental change is the basic mix composition: in order to avoid swelling during moulding the resin content must be lower than 90%vol, and is fixed at 72.9%vol.

TABLE 1.29 COMPARISON AND DETAILS OF THE MOLDING PROCESSES

	Friction material press	Lab press
Basic Mix composition	Resin : aramid fibres = 72.9:27.1vol. "BM"	Resin : aramid fibres = 90:10vol. "$BM._{10}$"
Mixing parameters	Total of 4 kg in a 8L capacity Eirich R02E mixer for 15 min	Total of 0.5 kg in a 5L capacity Lödige mixer for 15 min
Pressing time	5 cycles: 13' pressing + 15' outgassing and finally 60' pressing	> 74 min (pressing in oven)
Pressing load	150 kg/cm^2	70 kg/cm^2
Pressing Temperature	150°C	160°C
Heating cycle in oven	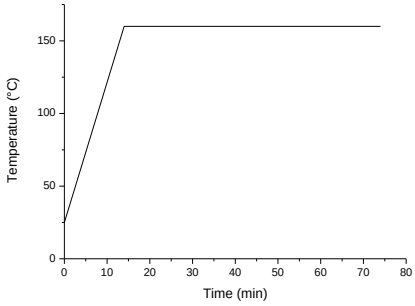	
Heating modality	Free samples in oven	Samples under pressing in oven
Sample geometry		
	7 - 13 mm thickness for around 100 g	2 – 3.5 mm thickness for 5 – 7 g
Nomenclature	S/*%vol*, T/*%vol*...	$BM_{\%vol1}$, ..., $BM_{\%vol3}$, ..., $S_{\%vol}$, $T_{\%vol}$...

Some characterization tests have been performed on samples produced by both methods and the results are reported herein below. The aim of this comparison is to verify that both methods allow to obtain samples with similar features, or at least that the properties vary in the same way. To this purpose, the chosen materials are the

monocomponents containing steel fibres, petroleum coke as lubricant, aluminum oxide and silicon carbide as abrasives. The data are stiffness, hardness and density for physical properties, residual weight at 950°C and maximum resin decomposition temperature for thermal properties and COF and wear factor for tribological properties. All are presented and explained in the *Characterization tests* part.

In FIGURE 1.12, the values of the physical properties for the four monocomponent samples are presented. Stiffness and hardness values are higher for the industrial samples, because of the higher pressing load applied (150 kg/cm^2 versus 70 kg/cm^2). On the other hand, density for the lab-scale manufactured samples is slightly higher, the sample is thinner, so during curing process gas produced by resin crosslinking is more easily drained away, that leads to a lower porosity and then to a higher density value.

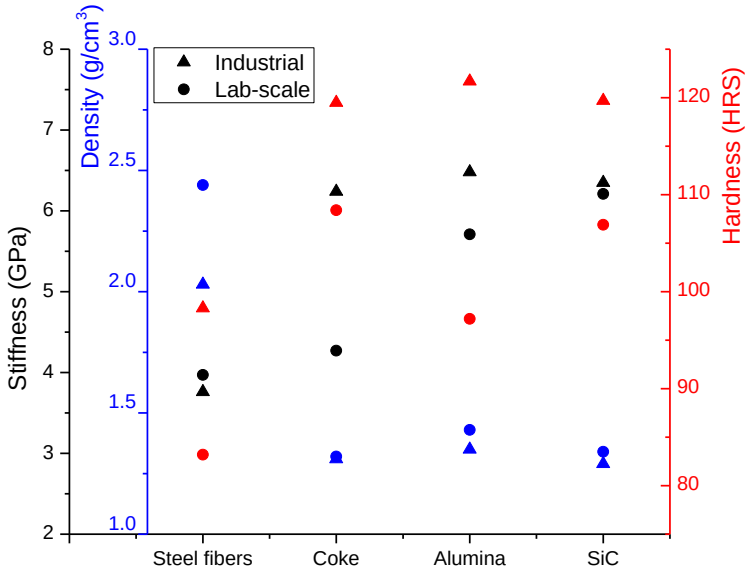

FIGURE 1.12 STIFFNESS, HARDNESS AND DENSITY VALUES OF SAMPLES PRODUCED USING BOTH INDUSTRIAL AND LAB-SCALE PROCESSES, FOR MONOCOMPONENT SAMPLES CONTAINING STEEL FIBRES, PETROLEUM COKE, ALUMINA AND SILICON CARBIDE

In FIGURE 1.13 thermal features are plotted. The first is the residual weight at 950°C obtained using TGA results; all the materials present very similar values. The industrial materials values are higher due to the higher aramid fibres content in the industrial composite (see TGA study in chapter III, 1.3 section). The temperature of maximum resin

decomposition is higher for the four materials produced by industrial process; in fact the higher aramid fibre content leads to have a denser network inside the matrix, so more interaction between the components and more thermal stability.

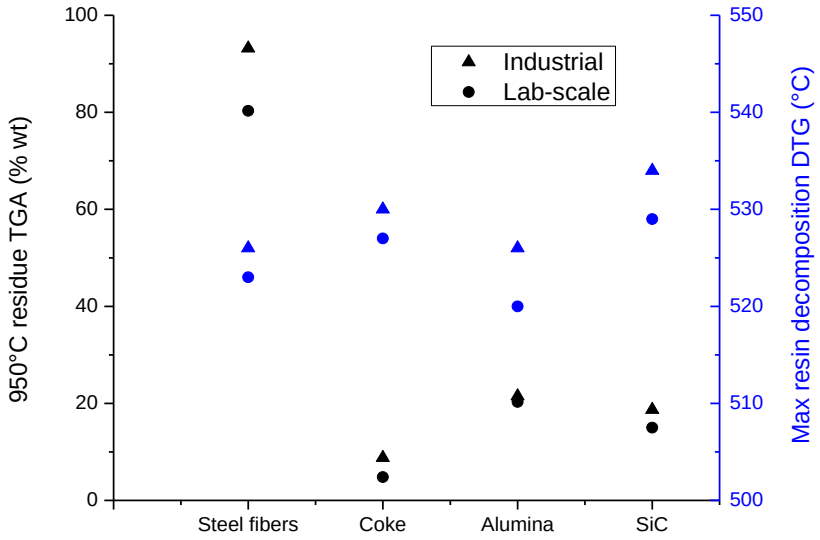

FIGURE 1.13 WEIGHT RESIDUE AT 950°C FROM TGA CURVE AND RESIN DECOMPOSITION PEAK MAXIMUM TEMPERATURE FROM DTG CURVE VALUES OF SAMPLES PRODUCED USING BOTH INDUSTRIAL AND LAB-SCALE PROCESSES, FOR MONOCOMPONENT SAMPLES CONTAINING STEEL FIBRES, PETROLEUM COKE, ALUMINA AND SILICON CARBIDE

In FIGURE 1.14 the two main parameters of tribological tests are represented: COF and wear factor. For both, the lab scale specimen exhibits the highest values, which means more friction and less resistance to wear, indicating a weaker structure due to the lower aramid fibres content (10%vol against 27.1%vol).

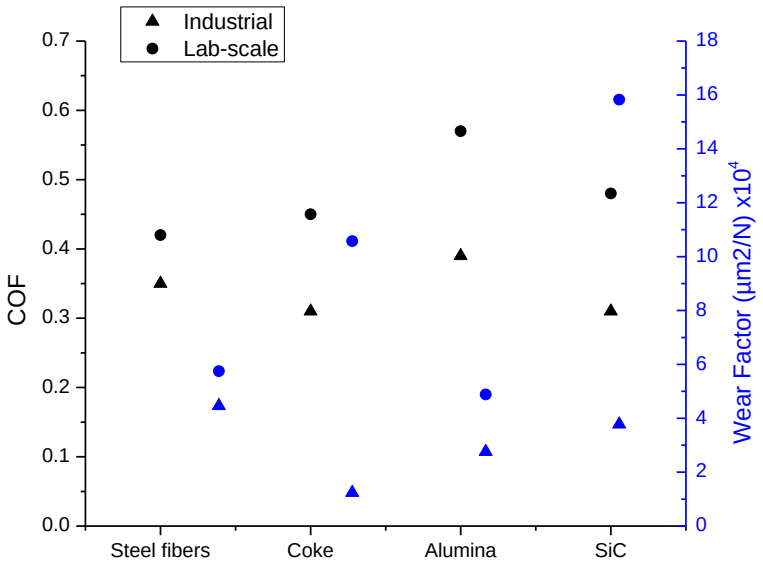

FIGURE 1.14 COF AND WEAR FACTOR VALUES OF SAMPLES PRODUCED USING BOTH INDUSTRIAL AND LAB-SCALE PROCESSES, FOR MONOCOMPONENT SAMPLES CONTAINING STEEL FIBRES, PETROLEUM COKE, ALUMINA AND SILICON CARBIDE

It is possible to conclude that as the considered thermal, mechanical, physical and tribological properties vary following the same trend for the studied monocomponent samples from one process to the other, the similarity between these two processes is verified. It allows to present in the whole work the friction-material pressed samples results, closer to the real brake pad materials, holding the initial tribological tests performed on the lab scale specimen. For sake of clarity the nomenclature is different. The samples are all called after the first letter of the component mixed with the basic mix (as presented in TABLE 1.30). For the lab-scale prepared samples this letter is followed by the component content in %vol; while for a friction-press process prepared sample the letter is followed by a "/" symbol and in the same way the component content in %vol present in the material.

TABLE 1.30 MONOCOMPONENT SAMPLES GENERAL NOMENCLATURE

	Sample description	Lab-scale sample name	Industrial sample name
	Basic Mix	BM_{10} – $BM_{17.8}$ – $BM_{27.1}$	BM/10 – BM/17.8 – BM/27.1 (=BM)
Monocomponent	Steel fibre	St_8 – St_{15} – St_{30}	St/8 – St/15 – St/30
	Potassium hexatitante fibre	Ti_{10} – Ti_{20} – Ti_{50}	Ti/10 – Ti/20 – Ti/50
	Friction dust	F_8 – F_{16} – F_{32}	F/8 – F/16 – F/32
	Barium sulphate	B_{30} – B_{50} – B_{70}	B/30 – B/50 – B/70
	Graphite	G_5 – G_{10} – G_{20}	G/5 – G/10 – G/20
	Petroleum coke	C_5 – C_{10} – C_{20}	C/5 – C/10 – C/20
	Aluminum oxide	A_3 – $A_{5.6}$ – A_{12}	A/3 – A/5.6 – A/12
	Silicon carbide	Si_2 – $Si_{3.4}$ – Si_7	Si/2 – Si/3.4 – Si/7

2.2. CHARACTERIZATION TESTS

2.2.1. Morphology

2.2.1.1. SEM

The Scanning Electron Microscope (SEM) pictures are taken with a Zeiss LEO 1450VP in high vacuum; potential difference used is equal to 20 keV for all the pictures and the working distance is maintained at 15 mm to allow the simultaneous use of the microprobe. EDS instrument is an INCA of Oxford Instruments, with a 10 mm^2 sensor.

2.2.1.2. FTIR

2.2.1.2.1. Single beam

The instrument used is Spectrum One, Perkin Elmer.

The measurements are done in transmission mode. The FTIR spectra are collected with a resolution of 4 cm^{-1} for 64 scans in the medium infrared range (4000-800 cm^{-1}).

2.2.1.2.2. Mapping

The instrument used is Spectrum Spotlight 300, Perkin Elmer.

The mappings are collected using Attenuated Total Reflectance (ATR) mode. The mapping consists of 26 × 26 points with 16 spectral scans per pixel, resulting in a spatially resolved dataset of 676 individual point analyses. Every point on these maps records a full range infrared spectrum (4000–800 cm^{-1} with 8 cm^{-1} resolution). Maps are produced by selecting a specific absorption band, in our case a characteristic peak of the raw material to recognize on the observed material surface and then displaying the intensity of absorption (or transmission) within each spectrum recorded at each point in the area mapped. All spectra and maps were background subtracted.

2.2.2. Physical properties

2.2.2.1. Density

The density of the samples are calculated using the weight of the obtained sample, knowing its geometric dimensions, from the following equation:

$$\rho = \frac{m}{V}$$

with m: measured mass of the sample
V: volume of the sample

In order to identify some interaction effects, the theoretical density value is calculated as the weighted sum of the components density, following the equation:

$$d_{th} = \sum_i d_i\,[i]$$

with d_i : density of component i
[i]: component i content in the sample, in %vol.

The porosity of the sample is calculated as follow:

$$P = \frac{d_{th} - d_{exp}}{d_{air}}$$, in %vol

with d_{exp}: measured density of the sample

d_{air}: air density

2.2.2.2. Elastic Constant Determination

The instrument used is ETEK 3000, IMS (Elevated Temperature Elastic Konstant Measurement System), and its basic principle is the determination of modulus based on Hooke's law. The stiffness is determined through measurements of time-of-flight of an ultrasonic wave, on 5 points (see FIGURE 1.15) and the kept value is the mean.

FIGURE 1.15 LOCATIONS OF THE FIVE MEASUREMENT POINTS FOR ELASTIC CONSTANT DETERMINATION ON A PAD

The formula to obtain the stiffness of the material C is:

$$C = \rho \, . S^2$$

with ρ the density;

S the velocity transfer.

2.2.2.3. Hardness

Hardness is measured to examine the resistance of composites to indentation. The determination of the Rockwell hardness of a material involves the application of a minor load followed by a major load. The minor load establishes the zero position. The major load is applied, then removed while still maintaining the minor load. The depth of penetration from the zero datum is measured from a dial, on which a harder material gives a higher number. That is, the penetration depth and hardness are inversely proportional.

Hardness of the friction material specimen was measured using a Rockwell hardness tester (ARK 600 Akashi) in S scale which corresponds to the 100 kg load or 981 N, with a 12.70 mm steel sphere diameter. For each sample three measurements are performed on different points. The given value is the mean of the three and the error bars correspond to the standard deviation.

2.2.3. Thermal properties

2.2.3.1. Thermal conductivity

The instrument used is LFA 447/2 (Netzsch). For solids, the laser flash thermal technique is one of the most widely used techniques for the determination of the thermal diffusivity and conductivity. Using this method, the front side of a plane-parallel sample with a well-defined thickness (here 2 mm thickness) is heated by a laser pulse. The resulting temperature increase on the opposite surface is measured with respect to time using an infrared detector. Analyzing this resulting signal with appropriate mathematical models, information on thermal diffusivity and specific heat of the material is obtained. Using the density of the material the thermal conductivity can be determined. The flash method is a standardized technique (ASTM E 1461). A scheme of the instrument is presented in FIGURE 1.16. The determination of specific heat is done by means of a comparative method (in our case the graphite is used as reference). The temperature range is RT-250°C. The sample diameter is equal to 25.4 mm.

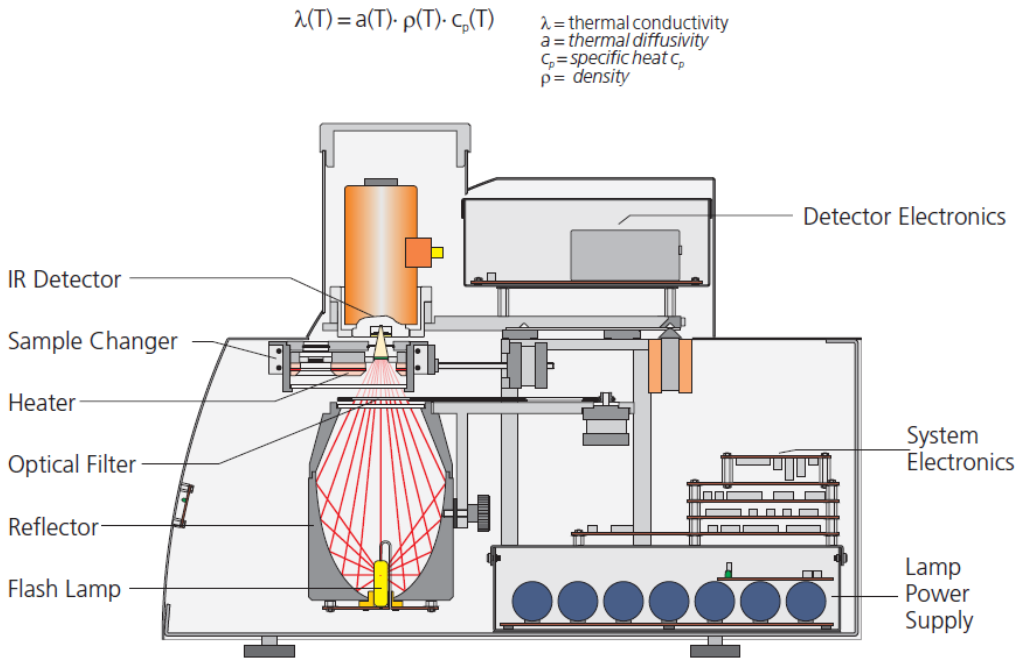

FIGURE 1.16 SCHEME OF THE LASER FLASH THERMAL ANALYSIS INSTRUMENT

2.2.3.2. Thermogravimetric analysis (TGA) / Differential scanning calorimetry (DSC)

In order to permit an optimal comparison between a sample and the raw materials forming it, the raw materials are thermally treated following the same heating cycle of the oven than the samples (14 min ramp from RT to 160°C, 60 min at 160°C and cooling in the open-air). For the composites, a powder sample is taken off using a diamond saw.

DSC measurements are achieved using a DSC821e, Mettler Toledo apparatus equipped with a low temperature probe, at a heating rate of 10°C.min^{-1} in air. An empty aluminum pan serves as a reference. Sample weight is around 10 mg. When the measurement is performed under nitrogen gas, it is clearly specified (the heating rate of 10°C.min^{-1} remains unchanged).

The glass transition temperature (Tg) is chosen as the temperature at the middle point of the glass transition obtained in the heating process. When it is followed by a relaxation, the glass transition presents a peak shape and in this case the Tg is chosen at the inflexion point as shown in FIGURE 1.17.

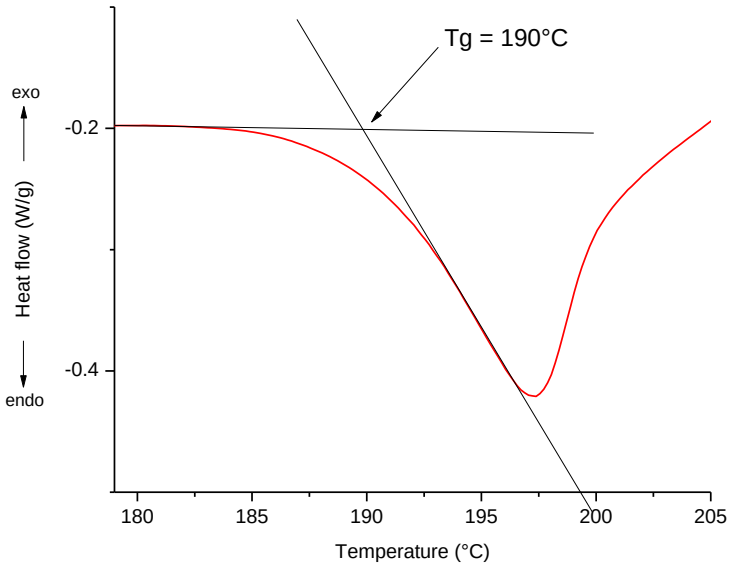

FIGURE 1.17 GLASS TRANSITION DETERMINATION TEMPERATURE ON DSC CURVE

In general the temperature of the different studied phenomena such as crystallization (T_c), degradation (T_d) or crosslinking (T_{cross}) are chosen as the temperature at the peak maximum.

For the TGA analysis a TGA/sDTA 851e, Mettler Toledo is used in the temperature range RT-970°C at a heating rate of 10°C.min^{-1} in air. Following the works of R. A. Shanks et al. (80), an useful way to compare TGA or DTG of mixtures is to calculate theoretical TGA or DTG curves (indicated with the mention "th" after the curve name) by summing the curves of components in the ratio they are present in the mixture, and compare it with the experimental curve of the mixture. This comparison reveals synergism or antagonism between ingredients.

2.2.3.3. Dynamic mechanical thermal analysis (DMTA)

The instrument used is DMA+150, Metravib.

In polymers, the viscoelastic behavior corresponds to the observable macroscopic consequences of molecular movements. The mobility of polymeric chains depends on temperature which in turn affects the values of storage and loss modulus, thus damping

factors too. Dynamic mechanical thermal measurements are used to identify, follow and characterize the variation of certain material properties such as glass transition temperature, crystallinity level, polymer crosslinking degree and the storage modulus. The latter measures the energy stored during a sinusoidal cycle, while the damping factor is defined as the ratio between the loss modulus (E'') and the storage modulus (E') per cycle, and corresponds to the tangent of the phase angle:

$$\tan \delta = E''/E'$$

The tan δ value which is also called damping factor quantifies the way in which a material absorbs and disperses energy. It corresponds to the out-of-phase time relationship between the sinusoidal force applied on the material and the resultant force that is transmitted. Materials that effect the most the phase shift, approaching 90°, have the highest tan δ values. These materials demonstrate a great capability to dissipate energy under another form as heat. The tan δ is also known as loss factor due to this loss of energy. Thus, it can be considered that the tan δ is an indicator of the effectiveness of a material's damping capabilities. The higher the tan δ value, the greater the damping coefficient, the more efficient the material will be in absorbing and dispersing energy. Tan δ can be related to the impact resistance of the material. Since the damping peak occurs in the region of the glass transition where the material changes from a rigid to a more viscous state, it is associated with the movement of small groups and chains or portion of chains of polymeric molecules. In a composite system, damping is affected by the incorporation in the mixture of new ingredients as fibres or fillers.

The DMA 3-points bending tests (see geometry in FIGURE 1.18) are done at a frequency of 10 Hz and heating rate of 1.5°C/min over a temperature range of RT to 400°C. The data collected consisted of storage modulus, loss modulus, and damping factor (tan δ).

The DMA tests are performed on friction material press because of tests requirements (sample geometry: 70*10*3 mm^3).

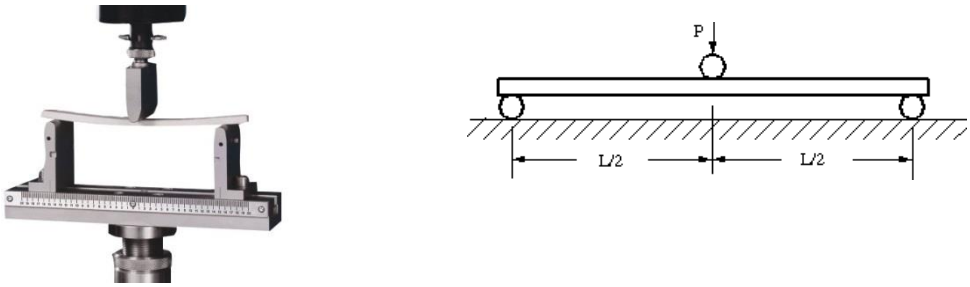

FIGURE 1.18 3-POINTS BENDING TEST PLAN

The Cole-cole plot

The complexity of the relaxation phenomenon existing inside a polymer material can be attributed to factors such as chemical differences or structural changes in the polymer unity of repetition, different environments for the chains, or heterogeneities in molecular weight distribution or free volume distribution for example, and thermo-mechanical history. If reinforcing agents such as fibres are introduced into the polymeric matrix, the mobility of the chains is limited by both the physical presence of the fillers and by any eventual chemical interaction filler/matrix. The magnitude of the changes occurring during the relaxation phenomena due to the presence of the interface is related to the degree of interaction between phases of the composite (in this case fillers and the binder resin).

Although as described before, a serie of relaxation times is a more realistic conception of the relaxation processes occurring in a polymer material, to simplify a model that uses only two relaxation times can be considered (81) (82) (83) (84) (85). An equation such as the one below can usually give a good correlation between theory and experimental data.

$$E^* = E_r + \frac{E_{u-} E_r}{1 + (iw\tau_1)^{-h} + (iw\tau_2)^{-k}}$$

with:

E*= complex modulus;

E_r = relaxed modulus;

E_u = instantaneous or unrelaxed modulus;

τ_1 and τ_2 = relaxation times;

w = frequency;

h = long time parameter;

k = short time parameter.

The relaxed and unrelaxed modulus can be obtained from a Cole-cole plot where the storage modulus is plotted against the loss modulus, by extrapolating the data to near the zero loss value equivalent to E" = 0. h and k parameters are used to fit the model to the data: they are calculated as $h = 2\theta_r/\pi$ and $k = 2\theta_u/\pi$, both from angles in which the curves reach the E' axis of the Cole-Cole plot with h the long time parameter and k is the short time parameter. The angles θ_r and θ_u are defined in the insert on the top of FIGURE 1.19. Both h and k parameters can be related to heterogeneities within the material that can potentially disturb the relaxation processes. In terms of a composite, the interface is a type of heterogeneity that can lower the values of k and h, by interfering in the relaxation phenomena.

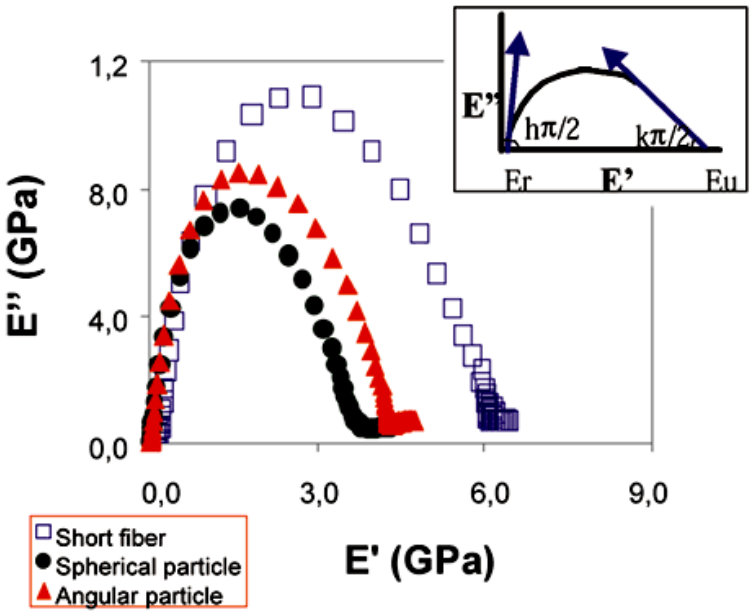

FIGURE 1.19 EXAMPLE OF COLE-COLE PLOT FOR POLY (ARYL) SULPHONE WITH REINFORCING AGENTS (86)

The imperfect semicircular shape indicates the heterogeneity of system and good fibre/matrix bonding. In the present study, all composites show imperfect semicircular curve suggesting heterogeneity of composite and relatively good fibre/matrix interfacial

bonding (87), depending on the filler nature and content. Nevertheless, some differences can be distinguished between the composites.

2.2.4. Tribological tests

The wear test is done using a tribometer ball-on-disc (CSEM tribometer), as presented in FIGURE 1.20. The principle is the following: the sample spin round, in contact with an alumina sphere linked with a transducer on which a load of 10N is applied. The transducer measures the sliding resistance on the surface sample using a software able to calculate the coefficient of friction. The wear resistance is calculated analyzing the created track on the surface, in terms of depth and lost volume. Thanks to this test, it is possible to study the wear and friction behavior of solid materials with or without lubrication. Moreover, the possibility to control the different test parameters (spinning speed, contact pressure and environmental conditions) permits to study how they affect friction and wear resistance, then allowing to hypothesize the behavior in real conditions. The chosen speed is 25 cm/s held for 100 000 laps at a pressure of 10N.

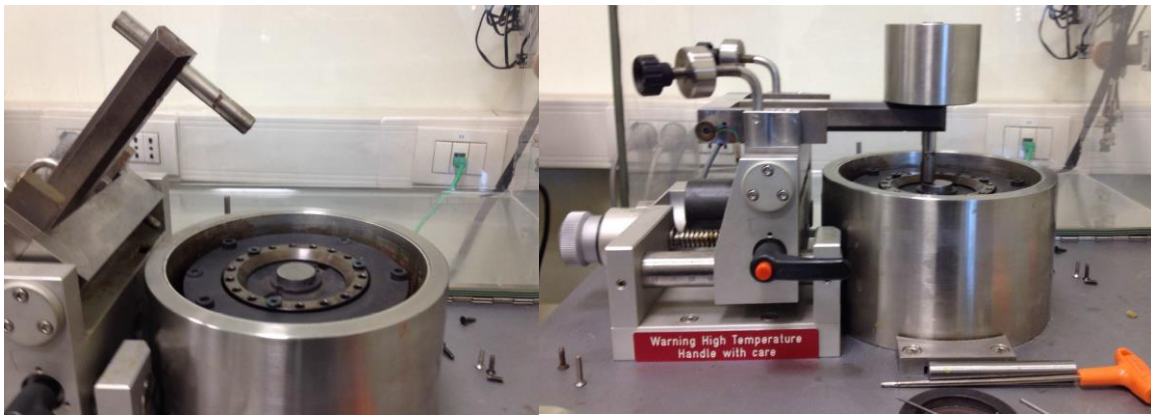

FIGURE 1.20 TRIBOMETER BALL-ON-DISK

The wear factor K gives indication on the wear resistance, expressed as the lost material volume normalized in respect of the load and the total path.

$$K = \frac{V}{F \,.\, d}$$

with V: lost volume

F: load

d: path

The reported data about the COF are:

- The friction coefficient medium value, calculated from 20 000 laps to the end of the test in order to let to the sample the time to get stabilized. In fact as explained by Bowden (88), in the total force of friction F (defined as $F = COF\ x\ L$, with L the load applied), there are alternately shear forces and interaction forces at the contact. As a consequence until the contact area is not stabilized, the asperities control the sliding motion, friction and wear characteristics, and the COF value is not stabilized but in transition. Once the two counterfaces have overstepped this running-in, the COF value can be measured.
- The standard deviation as an indication of the "vibration" of the COF curve.

LIST OF FIGURES

LIST OF TABLES

CHAPTER II

PHYSICO-MECHANICAL PROPERTIES OF MONOCOMPONENT SAMPLES

INTRODUCTION

Some of the most important requirements for a friction material are physical and mechanical properties, as strength integrity of the product with increasing temperature, mechanical resistance especially with the normal forces applied to the pad surface, and resistance to shear stress induced by the tangential forces caused by rotation movement (89).

These characteristics are important because are correlated to other phenomena: for instance if the matrix is not cohesive enough, the friction contact against the counterpart can induce high amount of particles ejection, so an excessive wear rate. The stiffness of the material is also to consider as it mediates friction force and contributes to brake squeal. It is tightly linked with the damping property which is decisive for the noise generated during braking.

In this chapter, the physical and mechanical properties studied are density, elastic constant through ultrasonic wave speed measurement from a surface to the opposite one of the material, storage modulus from DMTA measurements and Rockwell hardness. The considered samples are the monocomponent ones, made of the basic mix together with one of the eight fillers of the simplified formulation.

PREAMBLE - BASIC MIX MECHANICAL PERFORMANCES

The basic mix composed of phenol formaldehyde resin and aramid fibres is fully characterized in order to be the reference on which the further monocomponents samples are compared to. Materials containing different ratio resin:fibres are analyzed to

observe the influence of aramid fibres content on the final properties. Density values are reported in TABLE 2.1.

TABLE 2.1 GEOMETRICAL DENSITY VALUES OF BASIC MIXES SAMPLES.

	Raw material		Sample			
	Resin	Aramid fibres	$BM._{10}$	$BM._{17.8}$	$BM._{27.1}$	BM
Density, g/cm³	1.25	1.44	1.30±0.03	1.24±0.03	1.32±0.02	1.30±0.06
Aramid fibre content, % vol	-	-	10	17.8	27.1	27.1
Theoretical density, g/cm³	-	-	1.27	1.28	1.30	1.30

The material density is stable when the aramid fibre concentration increases. Following the study of P. Cai et al (90) from 0%vol to 18%vol of aramid fibre, the density decreases and it corresponds to porosity presence, also measured by S. J. Kim et al (91) for aramid pulp content from 0%vol to 20%vol; in this study as demonstrated by the theoretical density value of $BM._{27.1}$ there is no porosity, so no density change. This is a further check of the process validity. Besides, density values for $BM._{27.1}$ and BM samples are strictly the same, which confirms the good match between samples prepared by the two different protocols.

Stiffness values obtained by ETEK instrument tests of the phenol formaldehyde resin – aramid fibres materials are reported in TABLE 2.2. The stiffness increases with aramid fibre content, which ensure a good chemical unity and strength of the material. This is in total agreement with the theory: aramid fibres reinforce the material strength and make it stiffer. It is noteworthy that BM sample exhibits a different stiffness value than its homologue $BM._{27.1}$, because of the process change.

Table 2.2 STIFFNESS VALUES OF BASIC MIXES SAMPLES

	Sample			
	$BM._{10}$	$BM._{17.8}$	$BM._{27.1}$	BM
Aramid fibre content, % vol	10	17.8	27.1	27.1
Stiffness value, GPa	6.18±0.52	6.44±0.60	7.08±0.36	6.01±0.31

From the DMTA tests, storage (E') and loss modulus (E'') are measured during heating from RT to 400°C. The plot of E' as a function of the temperature of sample BM is presented in FIGURE 2.1. Because of required geometry specimen it has not been possible to perform DMTA on lab-scaled materials. The $\log_{10}$ scale is conventionally used to plot the storage modulus as a function of the temperature. In this case, due to the limited variation of E', this scale is not suitable, so the linear scale is preferred. After the glass transition phenomenon at around 190°C, at 230°C there is a light increase of E' corresponding to the 2nd step of crosslinking reaction. In the book Polymer Composites, Macro and Microcomposites (92), it is reported that aramid fibres dispersed in a polymeric matrix show a higher storage modulus than the neat polymer due to the reinforcement imparted by fibres that allows stress transfer from the matrix to the dispersed fibres.

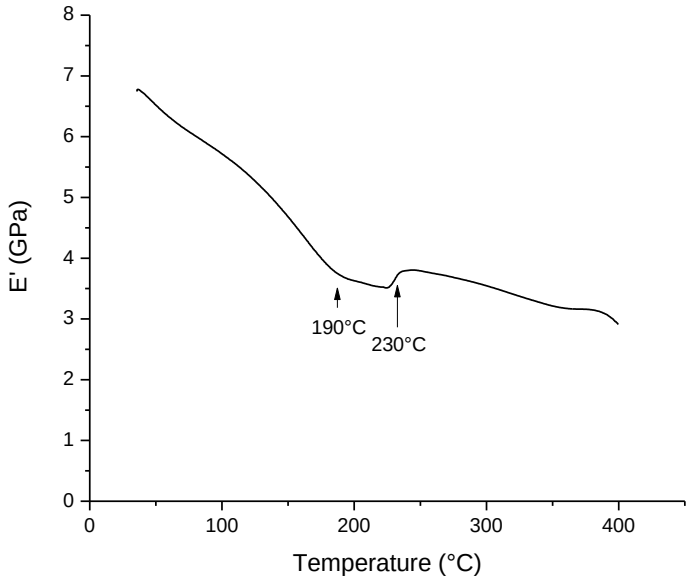

FIGURE 2.1 STORAGE MODULUS E' IN FUNCTION OF TEMPERATURE FOR BM SAMPLE IN LINEAR SCALE

Hardness values of the basic mix samples are reported in TABLE 2.3. There is a light increase of hardness with the aramid fibre content increase. This result is in contradiction with literature which predicts a decrease of hardness with aramid pulp content (91) (93). Considering the light increase of hardness and the absence of a wear

decrease until 27.1 %vol of aramid pulp (see chapter IV, *Preamble*), it can be hypothesized that there is for the basic mixes a particularly good dispersion quality.

Table 2.3 HARDNESS VALUES OF BASIC MIXES SAMPLES

	Sample		
	$BM._{10}$	$BM._{17.8}$	$BM._{27.1}$
Aramid fibre content, % vol	10	17.8	27.1
Hardness, HRS	103±2.0	108±3.5	107±2.9

After the study of the mechanical properties of the basic mixes, monocomponent samples mechanical properties have been tested, and the results compared to the basic mix in order to evaluate the single filler influence. It appears that among the chosen fillers, two families are distinguishable in respect of the influence the filler has on the final material stiffness: some of them present the ability to increase this property while the others don't have a clear influence on it.

I - FILLERS WITH ABILITY TO INCREASE MATERIAL STIFFNESS

1. POTASSIUM HEXATITANATE FIBRES

The results of density, stiffness and hardness for the basic mix and potassium hexatitanate based mixes are compared in TABLE 2.4.

TABLE 2.4 DENSITY, STIFFNESS AND HARDNESS VALUES OF BASIC MIX AND TI/X MIXES SAMPLES

Sample name	BM	Ti/10	Ti/20	Ti/50
Potassium hexatitanate content, % vol	0	10	20	50
Density, g/cm^3	1.30±0.03	1.49±0.04	1.71±0.02	2.03±0.08
Theoretical density, g/cm^3	1.30	1.53	1.77	2.45
Stiffness, GPa	6.01±0.31	7.30±0.35	7.91±0.36	7.32±0.32
Hardness, HRS	111.7	123.3 ± 0.2	117.4 ± 2.2	109.2 ± 3.1

The potassium hexatitanate fibre density is equal to 3.6 g/cm^3, so an increase of the composites density in respect of their potassium hexatitanate content is expected and

verified, see results in TABLE 2.4. The density of all the composites except Ti/50 approaches the theoretical value, indicating the absence of a significant amount of porosities. About stiffness, the maximum is observed for 20%vol of fibres content; the decrease after the addition of potassium titanate whiskers at 50%vol is attributed to insufficient binder resin and aramid pulps to support excess potassium titanate. This hypothesis is in agreement with the reduced density with respect to theoretical value observed. A similar decrease of the composite properties has been observed from 24%vol of potassium hexatitanate fibres by Y.C. Kim et al (59). As far as the hardness results are concerned, the value increases for the lowest filler content (10%vol), then progressively decreases. The hardness seems to show an optimum potassium hexatitanate value at around 10%vol, lower than the 20%vol observed in respect of stiffness property.

The plot of storage modulus in respect of temperature is presented in FIGURE 2.2. Storage modulus drastically increases with potassium hexatitanate whiskers content, with the same amplitude in glassy and rubber states. E' increase following the glass transition gets more important with the filler content: it could be attributed to the second step of the crosslinking reaction. In fact the filler presence makes the chemical groups contact more difficult, so the reaction proceeds in less extent during the sample preparation heating. This phenomenon is less pronounced for the 50%vol filler sample (Ti/50) because the number of the reaction sites is minor.

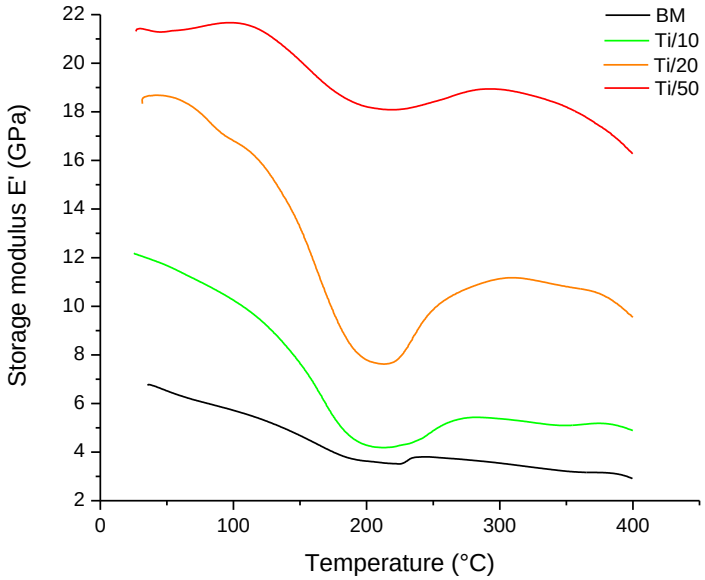

FIGURE 2.2 STORAGE MODULUS E' IN FUNCTION OF TEMPERATURE FOR BM, TI/10, TI/20 AND TI/50 SAMPLES

In the works of S.J. Kim et al (38), the synergistic effect of aramid fibre pulp and potassium hexatitanate fibres, providing friction stability and wear resistance, is attributed to the better filler retention of aramid pulp and the heat resistance of potassium titanate whiskers. It explains the good mechanical performances of the samples containing potassium hexatitanate fibres: higher stiffness, higher storage modulus until the optimum content of around 20%vol. Thus this content is believed as the optimal one, and it will be used to build the more complex samples in this study.

2. BARIUM SULPHATE

The obtained results of density, stiffness and hardness for basic mix and B/x mixes are shown in TABLE 2.5.

TABLE 2.5 DENSITY, STIFFNESS AND HARDNESS VALUES OF BASIC MIX AND B/X MIXES SAMPLES

Sample name	BM	B/30	B/50	B/70
Barium sulphate content, % vol	0	30	50	70
Density, g/cm^3	1.30±0.03	2.23±0.06	2.62±0.03	2.89±0.03
Theoretical density, g/cm^3	1.30	2.20	2.82	3.40
Stiffness, GPa	6.01±0.31	9.42±0.43	12.02±0.54	10.93±0.45
Hardness, HRS	111.7	113.6 ± 3	104.7 ± 2.52	99.6 ± 0.58

The barium sulphate density is equal in literature to 4.3 g/cm^3, so it is expected to observe an increase of the material density with this filler. As in the previous case, a decrease in density is observed for high percentage of filler, probably because of a binder content insufficient to insure a good fibres wetting.

As seen in the work of H.J. Hwang et al. (94), the stiffness gradually increases with the barium sulphate content, here from 6 GPa to 12 GPa at 50%vol. At 70%vol of barite the sample stiffness is minor with respect to the 50%vol sample (10.93 GPa versus 12.02 GPa), indicating that this filler content is too high and leads to physical properties deterioration. In fact, as explained by G. Yi and F. Yan (95) an excessive content leads to severe structural inhomogeneity of the blend and hence to depletion of the mechanical strength of the final composite.

The hardness values are stable until 30%vol then decrease, according to the aforementioned loss of mechanical properties.

The storage modulus plot of the barium sulphate monocomponent samples is presented in FIGURE 2.3.

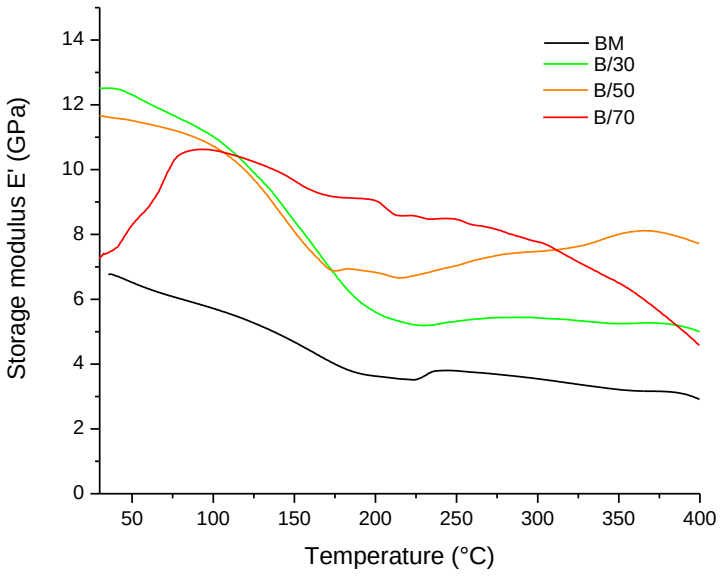

FIGURE 2.3 STORAGE MODULUS FOR BM AND B/X MIXES AS A FUNCTION OF TEMPERATURE

The barium sulfate leads to a general storage modulus increase in respect to the basic mix as noticed by A. Tiwari et al (96). B/30 sample presents a higher storage modulus but with the same trend of the basic mix. Then the sample containing 50%vol of barite presents similar E' values for the glassy state but higher for the rubber state, increasing from 250°C to 370°C. It could corresponds to a partial and progressive post curing reaction: the resin content is low, so the groups need more energy and time to react.

It is readily recognized that storage modulus increases over the whole temperature range as $BaSO_4$ concentration increases: this is in agreement with the change of stiffness observed, as both stiffness and storage modulus are measurements of the material elasticity.

3. GRAPHITE

The results of density, stiffness and hardness for basic mix and G/x mixes are listed in TABLE 2.6.

TABLE 2.6 DENSITY, STIFFNESS AND HARDNESS VALUES OF BASIC MIX AND G/X MIXES SAMPLES

Sample name	Basic mix	G/5	G/10	G/20
Graphite content, % vol	0	5	10	20
Density, g/cm³	1.30±0.03	1.31±0.04	1.42±0.07	1.42±0.04
Theoretical density, g/cm³	1.30	1.35	1.39	1.48
Stiffness, GPa	6.01±0.31	6.89±0.32	6.54±0.32	8.28±0.39
Hardness, HRS	111.7	120.7 ± 0.7	112.3 ± 3.2	113.6 ± 0.6

The graphite density is equal to 2.2 g/cm³, so higher the graphite content, higher the density. Hardness values are not affected by the graphite presence, except for the 5%vol sample for which hardness is sensitively higher (120 instead of 112 for basic mix).

The storage modulus (E') as a function of the temperature, obtained by DMTA, is displayed in FIGURE 2.4.

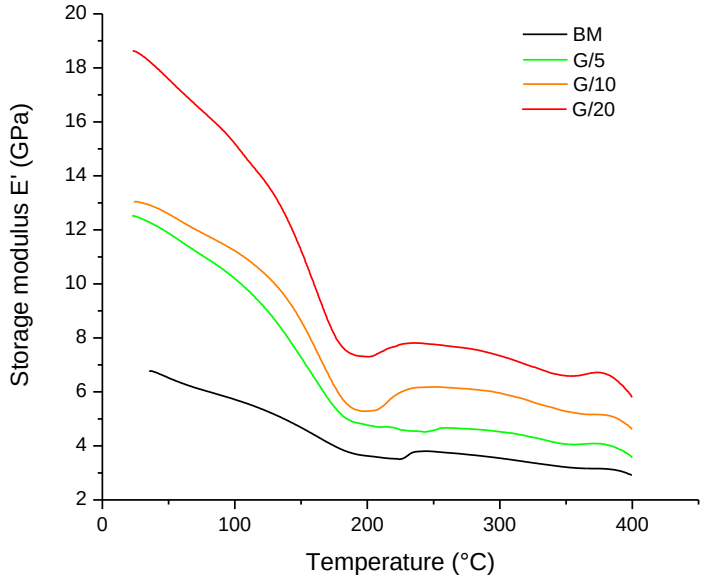

FIGURE 2.4 STORAGE MODULUS E' IN FUNCTION OF TEMPERATURE FOR BM, G/5, G/10 AND G/20 SAMPLES

Storage modulus increases with graphite content, holding the same curve shape than the basic mix one. It is in complete agreement with the stiffness value increase with graphite content. It is noteworthy that in the storage modulus plot in function of temperature for a reinforced material, the part of the curve to analyze is the post glass transition portion,

called rubbery plateau. In fact at lower temperature the material is in glassy state, and studying the influence of additive particles is less relevant. In the present case, the progressive increase of the storage modulus with filler content is clearly visible, perfectly fulfilling its reinforcing filler role.

4. SILICON CARBIDE

The results of density, stiffness and hardness for basic mix and Si/x mixes are summarized in TABLE 2.7.

TABLE 2.7 DENSITY, STIFFNESS AND HARDNESS VALUES OF BASIC MIX AND SI/X MIXES SAMPLES

Sample name	BM	Si/2	Si/3.4	Si/7
Silicon carbide content, % vol	0	2	3.4	7
Density, g/cm^3	1.30±0.03	1.30±0.03	1.29±0.04	1.31±0.08
Theoretical density, g/cm^3	1.30	1.34	1.37	1.44
Stiffness, GPa	6.01±0.31	6.56±0.30	6.35±0.29	7.58±0.31
Hardness, HRS	111.7	122.3 ± 0.6	119.7 ± 2.9	122.3 ± 1.5

Often, the addition of particles leads to porosity and, therefore, to lower densities due to wetting and mixing problems. The silicon carbide density is equal to 3.2g/cm^3; the stability of the density values for Si/x samples let think that concurrently to SiC particles introduction in the mix the sample porosity increases, as it has been observed by J. Abenojar et al (97). The porosity value found in their work is equal to 5–6%vol, which has a significant impact on composite properties. Here, the comparison between experimental and theoretical density leads to identical porosity range values of 3, 6 and 9% respectively for Si/2, Si/3.4 and Si/7.

According to the literature (97), the addition of abrasion-resistant fillers leads to significantly increase composite hardness. In literature (98) (99) a linear correlation between hardness value and SiC volume fraction in an epoxy matrix is found, which follows the equation:

$$Hardness = 10.659\, Vf + 156.28 \quad (99)$$

The results obtained here do not present this dependency: the authors of the cited work established this equation considering the lowest SiC content equal to 9%vol. Thus it is

hypothesized that for samples with low silicon carbide content, the hardness variation is lower: a minimum content is required to have a relevant influence on the macroscopic properties of the material.

The curves of storage modulus as a function of the temperature are presented FIGURE 2.5. The curve trends are similar for all Si/x samples, except for the glassy state: higher is the storage modulus for the 2%vol and 3.4%vol SiC containing samples. It may be related to the stress accumulation created by the SiC particles presence in the composite; on the contrary, the most concentrated sample Si/7 could contain too much fillers and that leads to fillers segregation. In fact, it is known that the enhancements in thermomechanical properties are related to the good dispersion and adhesion of the particles inside and with the matrix, so at the opposite, a decrease of these properties in respect of the expected trend is synonym of bad quality dispersion.

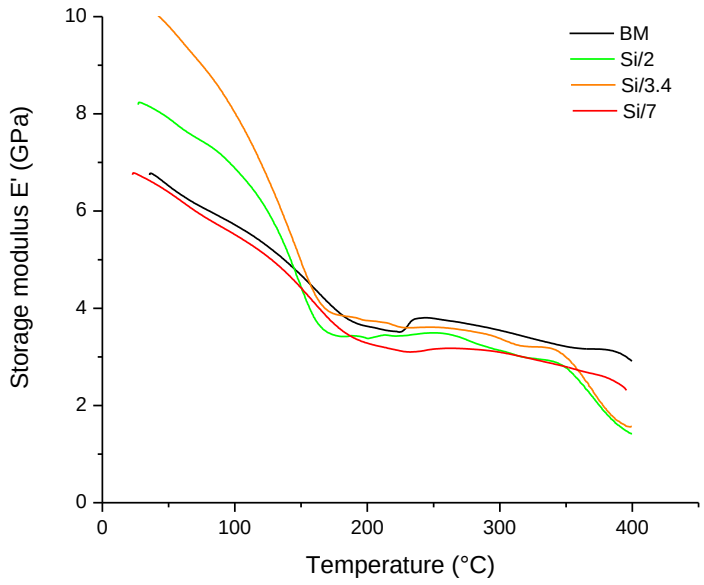

FIGURE 2.5 STORAGE MODULUS OF BM AND SI/X MIXES IN FUNCTION OF TEMPERATURE

5. ALUMINUM OXIDE

The results of density, stiffness and hardness for basic mix and alumina monocomponent mixes are displayed in TABLE 2.8.

TABLE 2.8 DENSITY, STIFFNESS AND HARDNESS VALUES OF BASIC MIX AND A/X SAMPLES

Sample name	BM	A/3	A/5.6	A/12
Aluminum oxide content, % vol	0	3	5.6	12
Density, g/cm^3	1.30±0.03	1.32±0.03	1.35±0.01	1.66±0.06
Theoretical density, g/cm^3	1.30	1.38	1.45	1.61
Stiffness, GPa	6.01±0.31	6.21±0.24	6.48±0.29	9.11±0.45
Hardness, HRS	111.7	121 ± 0.58	121.7 ± 1.5	125.5 ± 1.2

The aluminum oxide density is equal to 3.09 g/cm^3, so its addition to the basic mix leads to an increase of the density value.

As it is widely reported in literature (100), alumina develops a strong interaction with the matrix, leading the samples to present better mechanical properties as high hardness, stiffness and storage modulus. This bonding is partially due to the hydroxy groups chemisorbed at the surface of alumina particles, as observed via FT-IR technique by H. Etemadi et al (100). Hydroxyls are able to interact with the phenol formaldehyde macromolecules, for instance via hydrogen bonding. About the mechanical properties presented in TABLE 2.8, no upper limit has been reached which would correspond to the development of stress concentration caused by the presence of aggregates in the matrix. It confirms that, as seen via SEM observations presented in FIGURE 2.6 the fillers quality dispersion here is very satisfying.

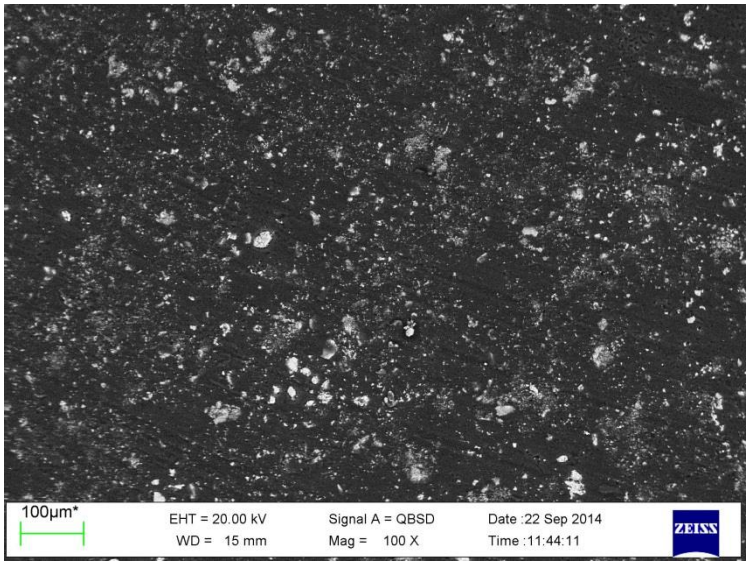

FIGURE 2.6 SEM PICTURE OF A/12 SAMPLE SURFACE AT 100X USING BACKSCATTERED ELECTRON ANALYSIS

The variations of storage modulus (E') with temperature are presented in FIGURE 2.7.

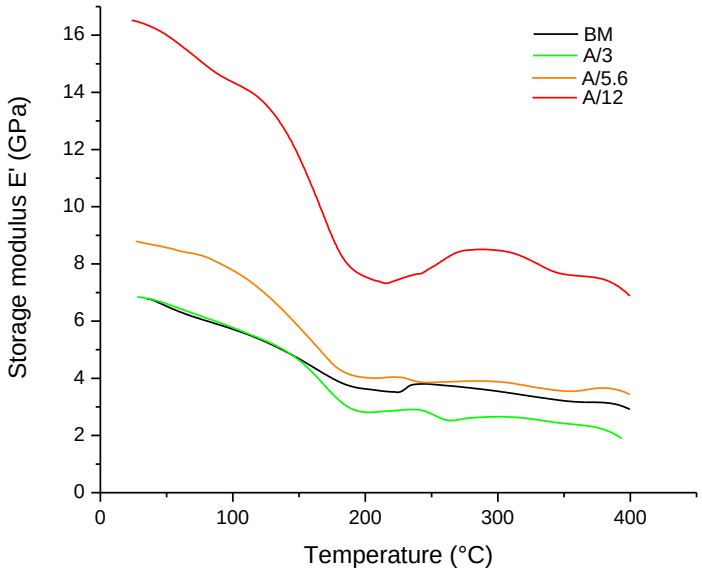

FIGURE 2.7 STORAGE MODULUS OF BM AND A/X MIXES IN FUNCTION OF TEMPERATURE

Stiffness and storage modulus values have the same trend: their values increase with alumina content and there is a particular leap between 5.6%vol and 12%vol.

In this first part, some of the studied fillers have been identified as influencing agents on the material stiffness, in the monocomponent samples: potassium hexatitanate fibres, barium sulphate, graphite, silicon carbide and aluminum oxide. The other fillers do not present the same trend on stiffness property, but participate to the material mechanical changes in function of concentration, as presented in the second part of this chapter.

II - FILLERS WITHOUT CLEAR INFLUENCE ON MATERIAL STIFFNESS

1. STEEL FIBRES

The obtained results of density, stiffness and hardness for the steel fibres monocomponent samples are compiled in the TABLE 2.9**.**

TABLE 2.9 DENSITY, STIFFNESS AND HARDNESS VALUES OF BASIC MIX AND ST/X SAMPLES

Sample name	BM	St/8	St/15	St/30
Steel fibre content, % vol	0	8	15	30
Density, g/cm^3	1.30±0.03	1.69±0.10	2.03±0.04	2.76±0.03
Theoretical density, g/cm^3	1.30	1.83	2.31	3.28
Porosity, %vol	0	8	12	16
Stiffness, GPa	6.01±0.31	4.64±0.19	3.76±0.15	5.69±0.24
Hardness, HRS	111.7	120 ± 0.1	98.3 ± 17.1	108 ± 1.0

The density increases by increasing the steel fibre content. Being the density value of the pure steel fibre 7.89 g/cm^3, such phenomenon is expected, but porosity up to 16% for St/30 makes the composite density lower than the theoretical one.

The addition of steel fibres inside the material leads to the decrease of the material stiffness, but a final increase from 3.76 to 5.69 GPa for 15%vol to 30%vol samples is observed. About hardness data, there is a slight increase from 0%vol to 8%vol, then a decreasing step at 15%vol and an increase again at 30%vol. It is noteworthy that the increase of the general mechanical properties between 15%vol and 30%vol of steel fibres content seem in contradiction with the conclusions obtained by M. Kristkova et al. (101) according to which at steel content superior to 25%vol in phenol formaldehyde resin bulk there is polymer degradation catalization by metal during the curing step. In fact this phenomenon would lead to a drastic loss of physical characteristics of the sample. This trend suggests that a particular phenomenon occurs between 8%vol and 15%vol of steel fibres inside the matrix, leading to a decrease of the initial material hardness and stiffness.

SEM observations of St/15 material are presented in FIGURE 2.8: an important quantity of whiskers around the steel fibres, with some gas bubbles, are present on the sample surface. It is noteworthy that the same result has been observed for St/30 sample.

(a) (b)

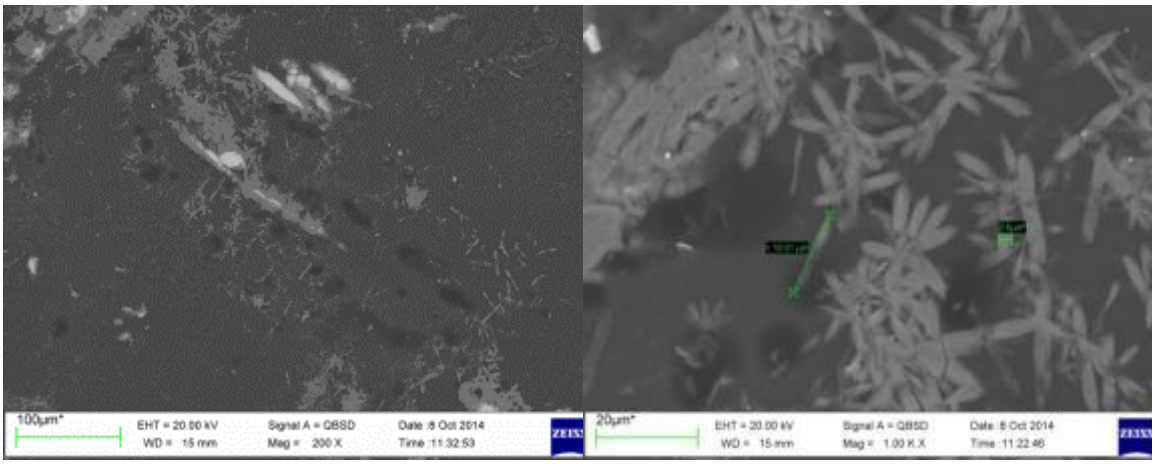

FIGURE 2.8 SEM PICTURES OF ST/15 SAMPLE SURFACE AT (A) 200X AND (B) 1000X (BS)

Further SEM observations with corresponding EDS mapping have been done (FIGURE 2.9) that permit to identify the phosphorous as main component of these whiskers.

(a) (b)

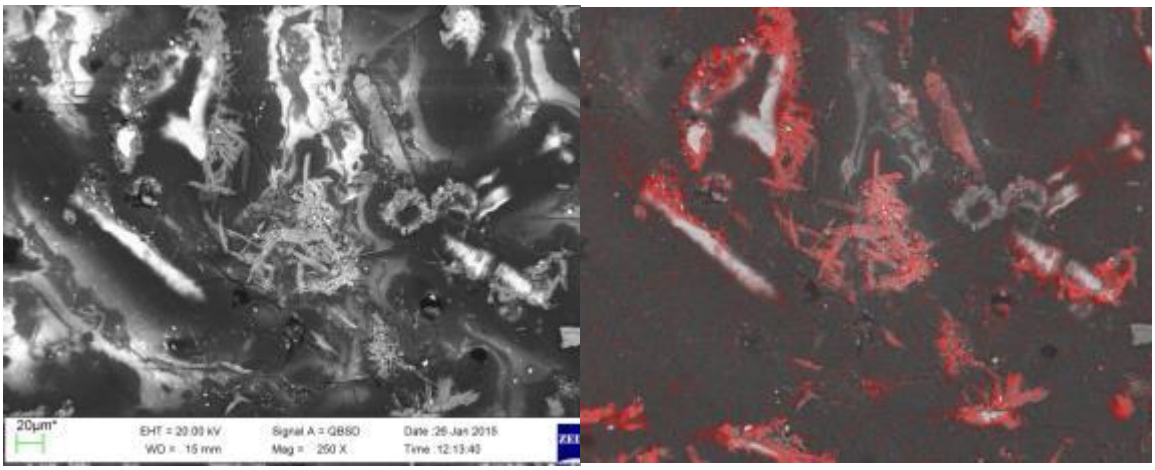

FIGURE 2.9 SEM PICTURES OF ST/15 SAMPLE SURFACE AT (A) 250X USING BACKSCATTERED ELECTRON ANALYSIS; (B) WITH PHOSPHOROUS EDS MAPPING AND IDENTIFICATION OF TWO P-RICH DIFFERENT PHASES LABELED 1 AND 2

Two zones rich in phosphorous are visible one these pictures: the first consists of whiskers (see zone 1 in FIGURE 2.9B) and the second against steel fibre is a phase without detectable crystalline structure (see zone 2 in FIGURE 2.9B). It can be hypothesized that one of these conformations is the precursor of the other. Other observations have been performed on the fracture surface (see FIGURE 2.10 and FIGURE 2.11) and section (see FIGURE 2.12 and FIGURE 2.13 respectively) of the sample.

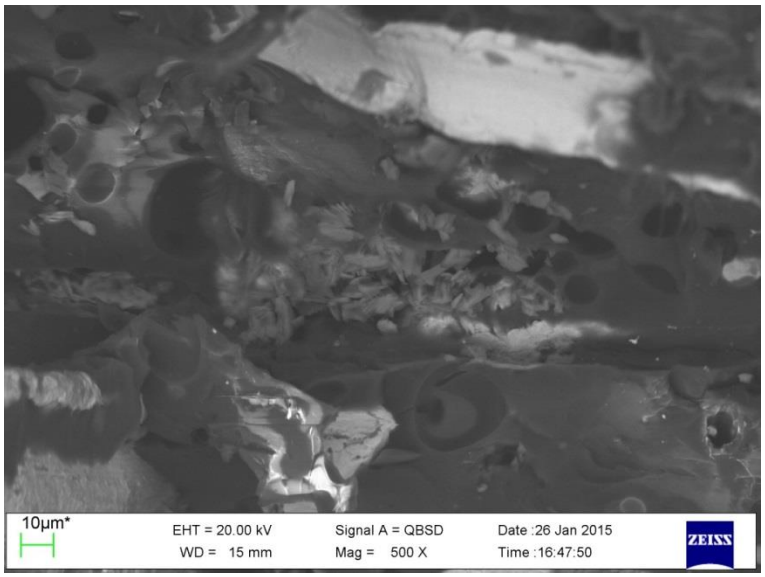

FIGURE 2.10 SEM PICTURE OF FRACTURE SAMPLE AT X500 USING BACKSCATTERED ELECTRON ANALYSIS

This fracture view highlights the formation of whiskers even in the bulk, not only in surface (see the center of the picture in FIGURE 2.10). Further analysis of the fracture surface are reported in FIGURE 2.11.

(a) (b) (c)

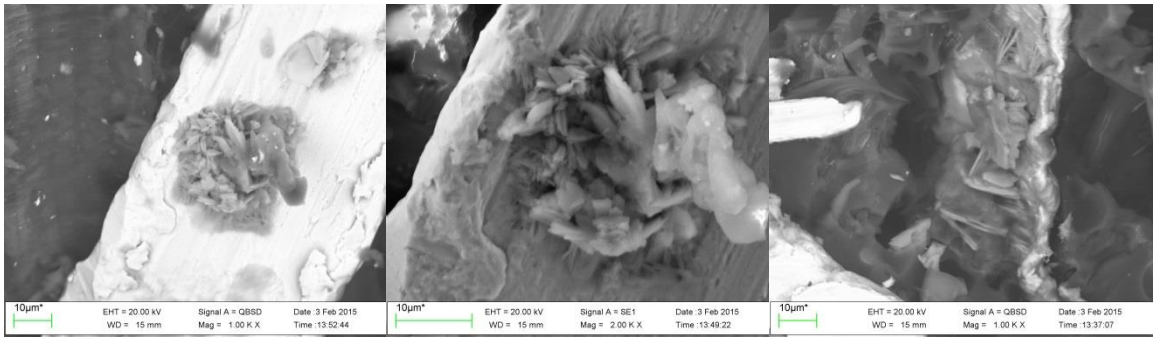

FIGURE 2.11 SEM PICTURES OF A P-RICH ZONE ON A STEEL FIBRE SURFACE AT (A) X1000 ; (B) X2000; AND OF (C) A STEEL FIBRE CARRYING A LARGE FORMATION OF P-RICH PHASE AT X500 USING BACKSCATTERED ELECTRON ANALYSIS

This set of pictures point out a morphology more similar to platelets than whiskers. Around the steel fibres, shapes corresponding to a different phase than the bulk are visible on the sectioned material (see FIGURE 2.12). A magnification of one of these zones highlights that this different shape is dendritic; this would be the initiation of the whiskers formation. A deeper study of this zone is presented in FIGURE 2.13.

(a) (b)

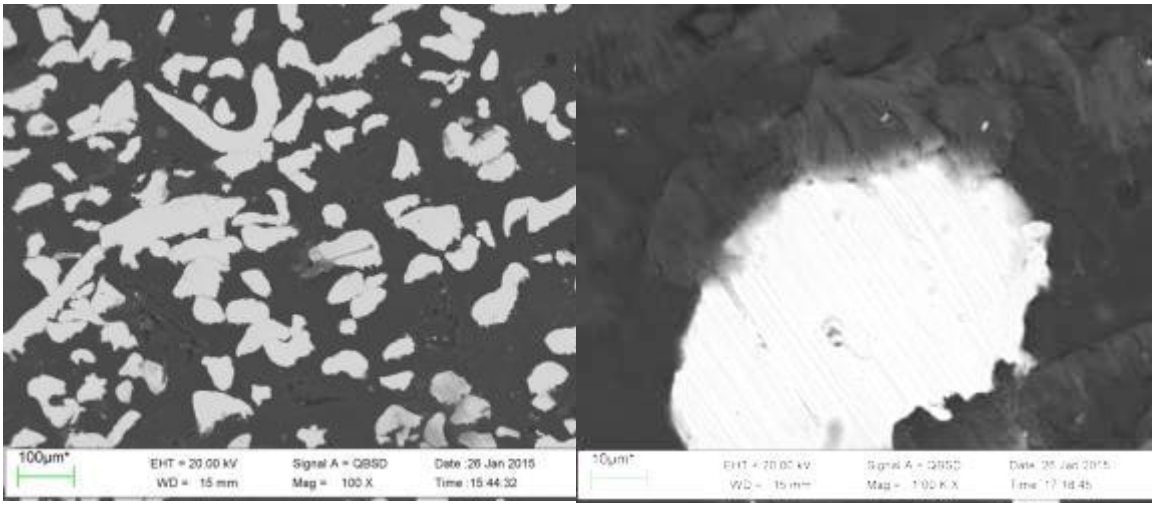

FIGURE 2.12 SEM PICTURE OF SAMPLE SECTION AT (A) 100X USING BACKSCATTERED ELECTRON ANALYSIS AND (B) X1000 USING SECONDARY ELECTRON ANALYSIS

(a) (b) (c)

FIGURE 2.13 SEM PICTURES OF A STEEL FIBRE INSIDE ST/15 SAMPLE IN THE SECTION X1000 USING SECONDARY ELECTRON ANALYSIS : (A) NEAT PICTURE, (B) PHOSPHOROUS EDS MAPPING PICTURE, (C) PHOSPHOROUS IN RED AND OXYGEN IN GREEN EDS MAPPING PICTURE

From the farthest to the closest side of the steel fibre a gradient of phosphorous amount is observed, while an oxidised zone is present on the border of the steel fibre. It has been found in literature that the observed phosphorous-rich phase in these samples could correspond to an hydrated iron phosphate mineral called Vivianite (102), which formula is $Fe^{2+}Fe_2^{2+}(PO_4)_2.8H_2O$.

It can be concluded that whiskers presence leads to a decrease of stiffness and hardness.

Storage modulus plot in function of temperature is presented in FIGURE 2.14.

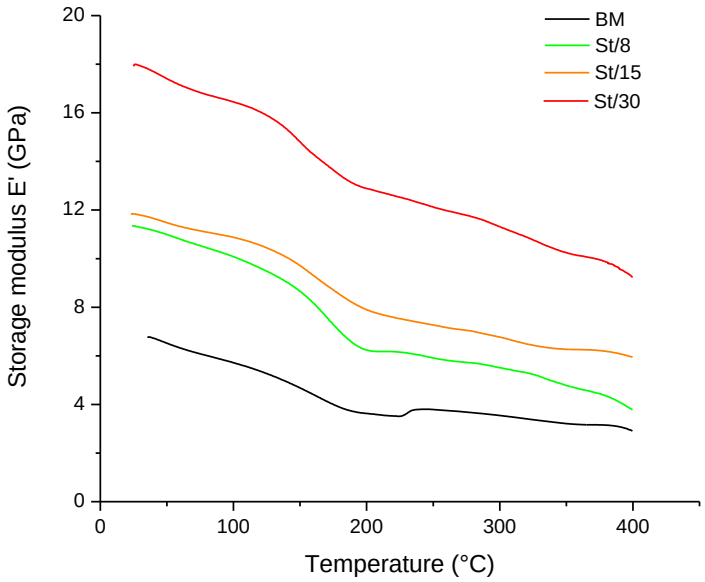

FIGURE 2.14 STORAGE MODULUS E' IN FUNCTION OF TEMPERATURE FOR BM, ST/8, ST/15 AND ST/30 SAMPLES

An increase for storage modulus is observed for steel fibres containing samples, with similar values for St/8 and St/15 but much higher for St/30. This rupture in the results between St/15 and St/30 has already been observed for the stiffness test data and can be the results of several factors as the formation of the whiskers or the increased porosity. It is important to note that later phenomena are correlated in the sense that pores were observed in proximity of the whiskers, as the result of their formation reaction.

2. FRICTION DUST

Friction dust, as explained in *Materials and methods* chapter mainly contains cardanol, a meta-substituted phenol. Due to its phenolic nature and the unsaturation in its side chain, it offers possible reaction sites, which makes it a potential component for various reactions (103) (104). Cardanol molecule reacts with formaldehyde or hexamethylene tetramine via the hydroxyl group to create cardanol-formaldehyde resins (54) (55). The side chain of cardanol can carry one, two or three double bonds (57), which permits it to undergo addition polymerization through these double bonds. As a conclusion different types of resins can be obtained from cardanol, and also from all the chemically modified

cashew nut shell raw materials (105). FT-IR analyses have been performed and attest that these reactions occur in the system basic mix + friction dust (see chapter III, section 1.4.1.).

Moreover, as reported by Cardona et al (106), the crosslinking density values of the resins are significantly lower than the value for the neat phenol formaldehyde resin. The presence of cardanol decreases the crosslinking density making the resin less brittle. The resulting polymer shows flexibility, due to internal plasticization resulting from the presence of the long alkyl side-chain. The partial substitution of phenol with cardanol in the synthesis of the resins drastically reduces the crosslinking density, producing a phenolic resin less brittle and tougher (106). Reducing the crosslinking density, the general material density also decreases, and as toughness increases, stiffness decreases (see TABLE 2.10).

Table 2.10 DENSITY, STIFFNESS AND HARDNESS VALUES OF BASIC MIX AND F/X MIXES SAMPLES

Sample name	BM	F/8	F/16	F/32
Friction dust content, % vol	0	8	16	32
Density, g/cm^3	1.30±0.03	1.22±0.02	1.16±0.03	1.07±0.03
Theoretical density, g/cm^3	1.30	1.29	1.27	1.24
Stiffness, GPa	6.01±0.31	5.10±0.24	4.28±0.17	3.39±0.14
Hardness, HRS	111.7	115.2 ± 4.6	116.8 ± 4.2	114.6 ± 0.6

Friction dust density, as reported in literature, is 1.06 g/cm^3. So the decrease observed of the material density in respect of friction dust content is expected.

Hardness remains almost unaffected as P.A. Mahanwar observed in his study (52) in similar measurements conditions.

Storage modulus representation in function of temperature is presented in FIGURE 2.15. Friction dust addition slightly decreases storage modulus in both glassy and rubber regions. As explained by Brijnaresh R. Sinha et al (49), substitution on the phenolic ring with an alkyl group "soften" the resins, as happens for cardanol in respect of phenol formaldehyde resin. Even in its crosslinked state, the long alkyl chains confer flexibility to the material (49). These crosslinked polymers tend to be "softer" as compared to the classical phenol with no aliphatic side chains due to the molecular motions of the latters.

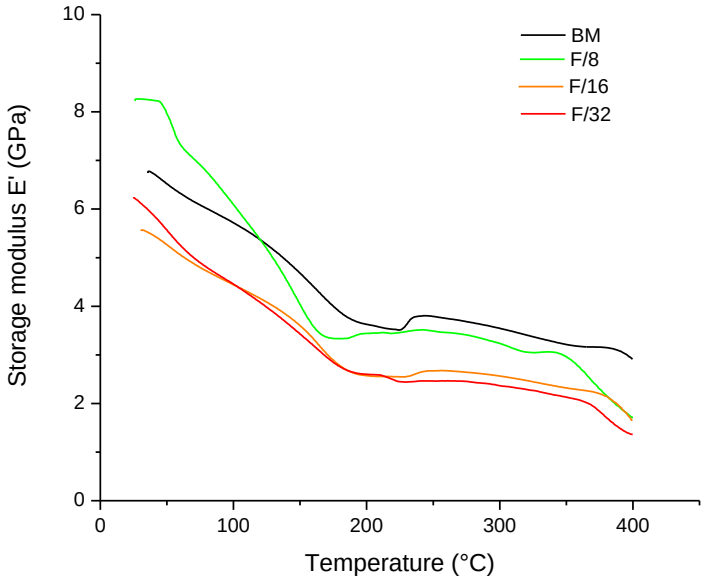

FIGURE 2.15 STORAGE MODULUS E' IN FUNCTION OF TEMPERATURE FOR BM, F/8, F/16 AND F/32 SAMPLES

3. PETROLEUM COKE

The results of density, stiffness and hardness for basic mix and petroleum coke monocomponent mixes are listed in TABLE 2.11.

TABLE 2.11 DENSITY VALUES OF BASIC MIX AND C/X MIXES SAMPLES

Sample name	BM	C/5	C/10	C/20
Coke content, % vol	0	5	10	20
Density, g/cm^3	1.30±0.03	1.33±0.04	1.31±0.04	1.39±0.05
Theoretical density, g/cm^3	1.30	1.34	1.38	1.48
Stiffness, GPa	6.01±0.31	6.24±0.28	6.24±0.27	6.57±0.30
Hardness, HRS	111.7	122.6 ± 0.6	119.5 ± 6.2	122.0 ± 1.0

The coke density is equal to 2.06 g/cm^3, so its addition to the basic mix leads to a slight density increase.

There is a light stiffness increase between 10 and 20%vol of petroleum coke as observed by G. Yi et al (107). It is claimed that the filler develops interaction with the matrix during the process, where application of compression at elevated temperature contributed to

greatly increase the bending strength and hardness of the phenolic resin-based composites. In another work, G. Yi reported that hardness increases linearly with petroleum coke content (95) until a concentration of 25%vol. Here, these values are stable from 5%vol to 20%vol; however, stiffness, storage modulus and hardness values are higher for C/x samples with respect to basic mix.

Storage modulus plot in function of temperature is presented in FIGURE 2.16.

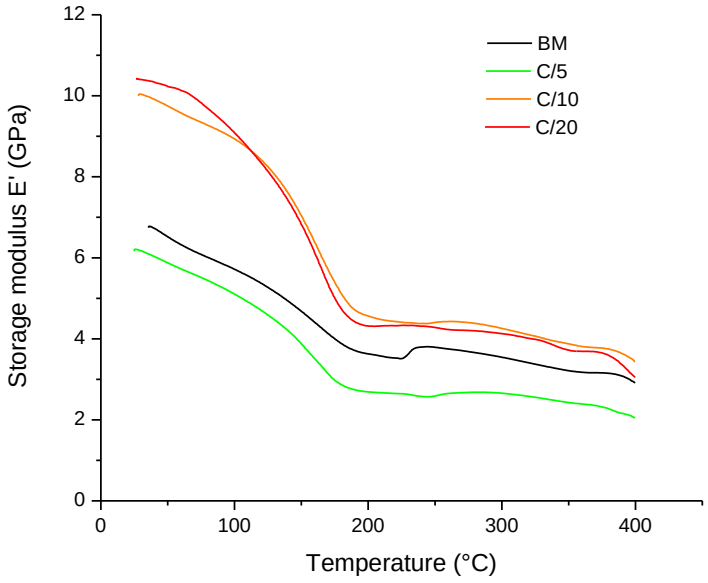

FIGURE 2.16 STORAGE MODULUS E' IN FUNCTION OF TEMPERATURE FOR BM, C/5, C/10 AND C/20 SAMPLES

There is first a decrease of stiffness from basic mix to C/5 sample, then the two most concentrated samples present the same storage modulus values in the 25-400°C range, slightly higher than the BM one.

CONCLUSION

While it is commonly admitted that fibres and abrasives are the most influencing fillers regarding the material stiffness and general mechanical properties (89), this work suggests that such classification presents some limitations.

It has been seen that aramid fibre increases the material stiffness, thus it is an indispensable component to ensure a good chemical unity and strength to the material. Then two classes of ingredients have been identified. First the one with a clear ability to increase the material stiffness as potassium hexatitanate fibres or barium sulphate, both presenting optimal physico-mechanical properties at the intermediate considered content (equal to 20 %vol and 50%vol respectively for fibres and barite); but also graphite and silicon carbide for which a content increase is accompanied by an increased porosity but stiffness as hardness increase anyhow. The last filler is aluminum oxide, which generates a progressive increase in stiffness, hardness and global storage modulus trend thanks to hydrogen bonds formed between the matrix the hydroxyl groups at the alumina particles surface. The second component category gather together the fillers which exhibit on stiffness a different kind of effect. For example, steel fibres lead to formation around themselves of particular whiskers or platelets which affect the material characteristics and generate stiffness and hardness decrease. In this second filler family also the friction dust is included, which leads to stiffness and hardness decrease due to the reaction between cardanol and formaldehyde; the petroleum coke keeps the properties unchanged.

LIST OF FIGURES

LIST OF TABLES

CHAPTER III

THERMAL PROPERTIES OF MONOCOMPONENT SAMPLES

INTRODUCTION

In the previous chapter, the influence of the fillers on the physico-mechanical properties has been deeply investigated. The final product must demonstrate a good strength and a good integrity first of all the other characteristics. Also the thermal properties are of paramount importance, inasmuch during braking the local temperature of the friction material can reach even more than 600°C.

The phenomenon of braking effectiveness loss at high temperatures is called fade and it is due to a reduction of the friction coefficient value. The successive return to acceptable levels of friction at low temperatures is called recovery (108). It is known that fade is highly-dependent on the tribological history of the material (109) (110) (111). In a classical brake pad the phenol formaldehyde resin degrades thermo-oxidatively leading to formation of organic components at temperatures superior to 250°C. Thus, it would be better to limit at the maximum this degradation in order to preserve the material integrity in the operating range of pressures, sliding speeds, and temperatures. The influence of friction material additives on thermal properties has been widely reported. Few papers deal with the effects of various fibres on both fade and recovery behaviour (110) (112) (113). Very little has been also reported on the influence of resins and their possible modifications. Bera et al. (114) modified a cashew nut shell liquid polymer (called friction dust if under powder form) with ortho-phosphoric acid and fabricated composites: it was reported that wear performances in general improved due to the resin modification.

To study the thermal behavior of the samples, different analyses are performed as Differential Scanning Calorimetry (DSC) and Thermo-Gravimetric Analysis (TGA) for the thermal stability, Dynamic Mechanical Thermal Analysis (DMTA) for the thermal

transformations and Laser Flash Thermal technique (FLA) for the thermal conductivity measurement. For each monocomponent sample the DSC and TGA measurements are first performed on the single raw materials thermally treated as the samples are (as explained in the *Materials and methods* chapter in section *II-2.2.3.2.*).

First of all, the basic mix containing only the phenol formaldehyde resin with aramid fibres reinforcement is studied. Then eight monocomponent samples, each containing only one filler at a time are created and the effect of each filler on the global thermal stability of the material is analyzed. A first division is done to separate the fillers presenting some interaction with the basic mix from the ones which don't. This difference is based on the variation of the glass transition temperature of the resin polymer with respect to its value in the basic mix material. In fact, if the dispersed fillers interact with the resin, the movement capacity of the polymeric chains gets limited and the passage from glassy to rubber state occurs at higher temperatures, because the molecules need more energy to break the bonds.

PREAMBLE - BASIC MIX THERMAL BEHAVIOR

1. DSC AND TGA

1.1. Aramid fibres

DSC, TGA and DTG curves of aramid fibres are shown in FIGURE 3.1.

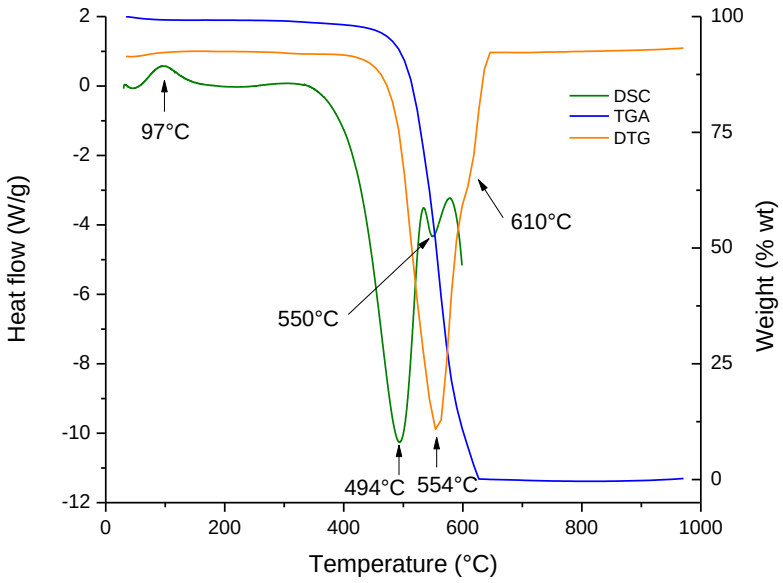

FIGURE 3.1 DSC, TGA AND DTG CURVES OF ARAMID FIBRE PERFORMED IN AIR, AT A HEATING RATE OF 10°C/MIN

The enthalpic change centered at 97°C is due to the initial weight loss to the release of absorbed water (115). If order within the polymeric network is decreased as a result of thermal treatment (as for the polymer melting), an endothermic event occurs. Therefore, the destruction of hydrogen bonds among adjacent chains is considered as an endothermic phenomenon within the DSC spectra, clearly visible at 494°C. Conversely, an exotherm is observable when crosslinking occurs (opposite phenomenon) within the polymer chain; here absent. It is possible that an endo- and an exothermic events are occurring simultaneously, and only the dominant thermodynamic change is detected by the DSC. At 550°C, a large endotherm was observed in the DSC scan, most likely corresponding to degradation of the aramid fibres and the formation of pyrolytic products such as hydrogen cyanide, benzene, toluene and benzonitrile (116). H.-T. Zhang et al (117) studied the aramid fibres degradation using FT-IR spectra to identify the decomposition products. Following his observations, the DTG peak at 554°C in FIGURE 3.1 corresponds to a small amount of weak aromatic heterocyclic bonds break into fibres; H_2O, HCN, CO_2 and CO absorption peaks appear on the FT-IR spectra. The DTG signal shoulder at around 610°C corresponds to all kinds of small molecule fragments, in which the FT-IR absorption peak of CO_2 is the strongest.

The same measurement has been performed under nitrogen (see FIGURE 3.2). The aramid fibres decomposition begins after 353°C in nitrogen and 323°C in air. In both scans, we interpret the inflection in the decomposition peak to be a melting transition that is superimposed on decomposition.

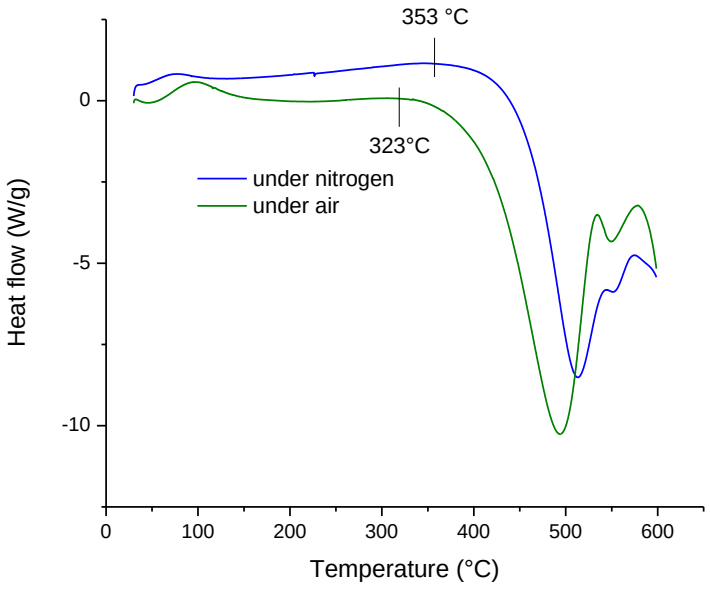

FIGURE 3.2 DSC MEASUREMENT OF ARAMID FIBRES UNDER AIR AND UNDER NITROGEN, AT BOTH HEATING RATE OF 10°C/MIN

As a conclusion, in the temperature range of 400-600°C, complex depolymerization, random rupture, hydrolysis, restructuring and other chemical reactions occur.

1.2. Phenol formaldehyde resin

As explained by Korosec et al. (118) phenol formaldehyde resins are divided into two categories: resoles and novolacs. They are both obtained through polycondensation reaction from phenols and aldehydes. If aldehyde is in excess in alkaline media resoles are formed, while if phenol is in excess under acidic conditions novolacs are formed. During the pressing process and its successive heating in oven a polycondensation reaction occurs between the novolac oligomers (see FIGURE 3.3), in the presence of

hexamethylenetetramine (HMTA) (the curing agent). The first step of the curing reaction occurs within a short time (around 2 min) at around 150°C.

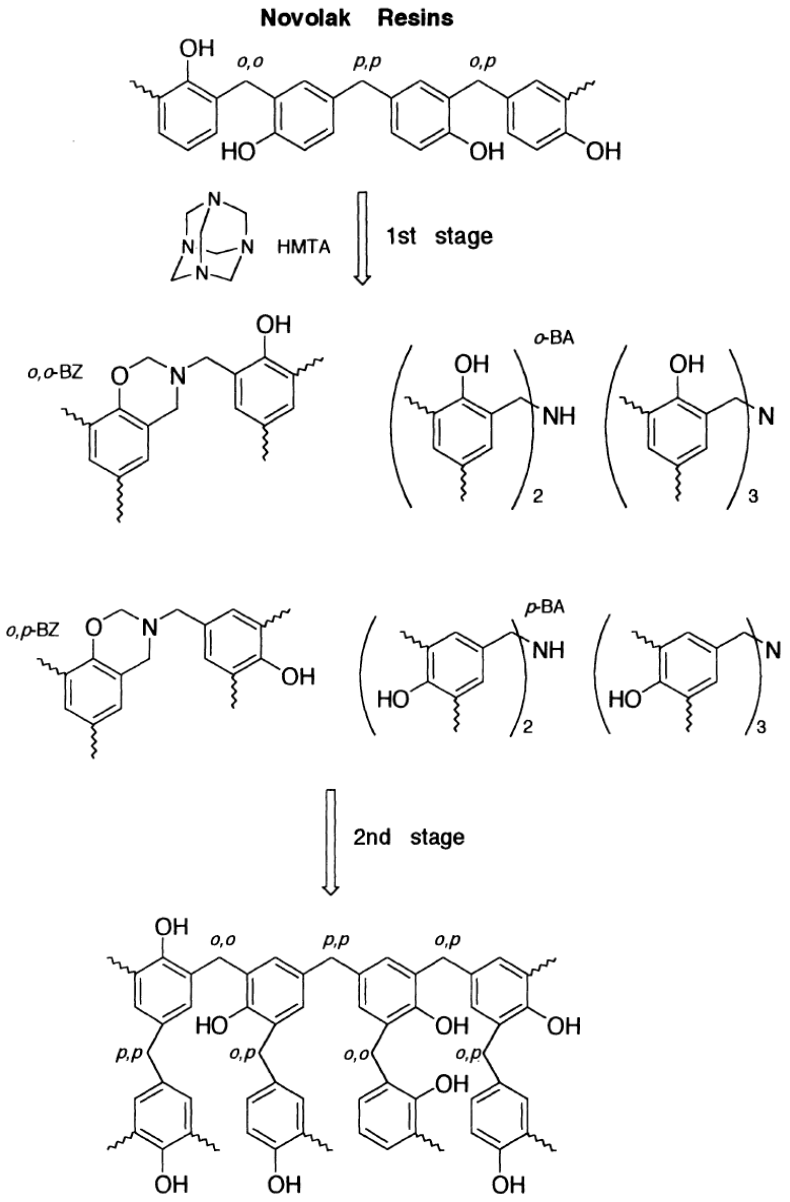

FIGURE 3.3 CROSSLINKING REACTION OF PHENOLIC RESIN WITH HMTA

During the second reaction, also called post-curing process, the structure crosslinks 3-dimensionally. This process takes several hours and occurs at temperatures up to 200°C. Afterwards, the final thermosetting material is obtained with its intrinsic dimensional, thermal, chemical and insulating properties (119) (120). The materials in this study are

all treated in the same way, as explained in the *Materials and methods* chapter, the product is heated in oven for around 1h at 160°C, which corresponds to the 1st stage crosslinking reaction temperature. It then can be hypothesized that the 2nd stage is not carried out, or only partially. The phenol formaldehyde resin which is used in this study is already mixed with 10% of hexamethylenetetramine (HMTA). Phenolic resin as raw material needs to be characterized before and after the heating treatment at 160°C, used for all others raw materials, in order to understand its behavior as crosslinked binder of the material.

DSC, TGA and DTG curves of neat resin are plotted in FIGURE 3.4. A glass transition of the raw material occurred at around 50°C. A broad peak positioned at 154°C appeared due to the 1st step of the curing reaction. During this step various substituted benzoxazines and benzylamines were produced as well as ammonia and formaldehyde and the corresponding loss weight is identified at 151°C on the DTG curve. The decomposition of these products, oxidation and/or further reactions of these initial curing intermediates produced methylene linkages between phenolic rings (121). The second step, in which various amide and imide structures with aromatic ring –CO–N< bonds were formed (121) is difficult to separate from the general exothermic process occurring at temperatures higher than 200°C in air ; anyway the exothermic signal centered at 287°C can correspond to this partial reaction. After that, the signal did not return to the baseline, but increased further in the exothermic direction corresponding to the organic degradation of the material.

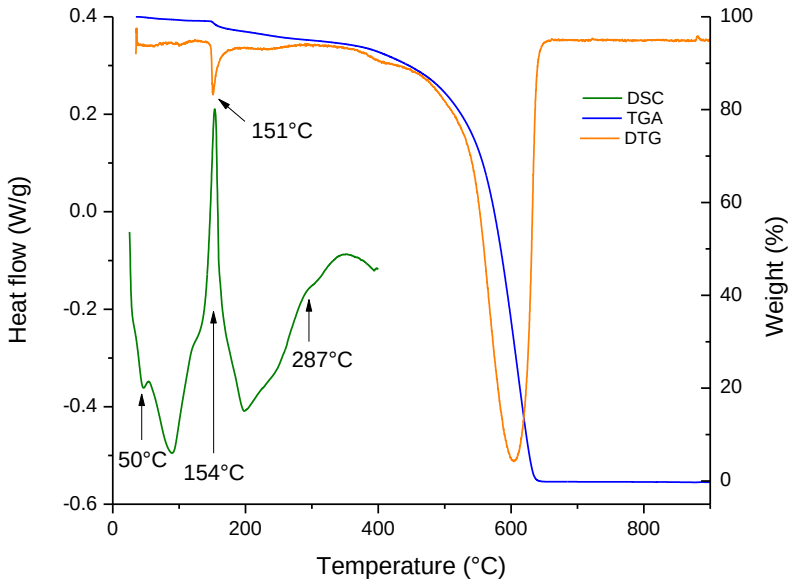

FIGURE 3.4 DSC, TGA AND DTG CURVES OF NEAT PHENOLIC RESIN PERFORMED IN AIR, AT A HEATING RATE OF 10°C/MIN

The same measurements are performed for the previously heated phenol formaldehyde resin (following the usual protocol). The results are presented in FIGURE 3.5.

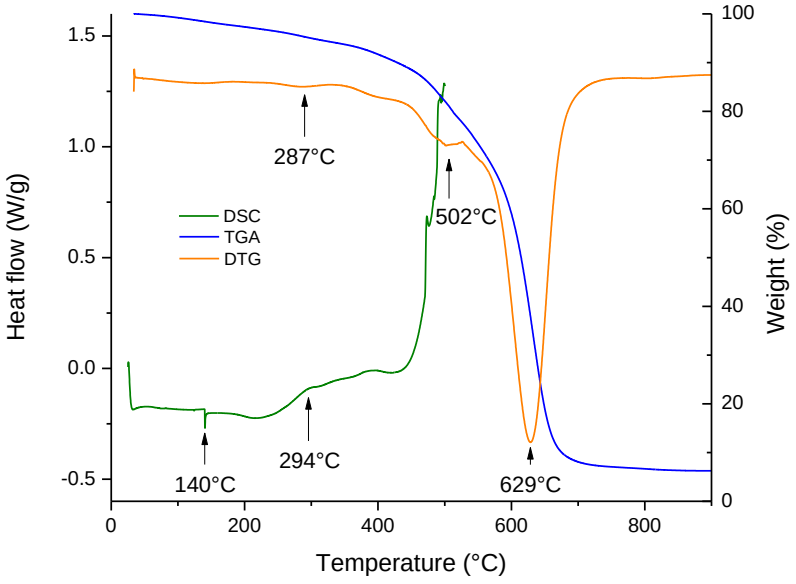

FIGURE 3.5 DSC, TGA AND DTG CURVES OF CURED PHENOLIC RESIN PERFORMED IN AIR, AT A HEATING RATE OF 10°C/MIN

On the DSC curve there is no peak located at around 150°C, so the 1st step of the curing reaction is completed during the oven treatment. The glass transition of the cured material is clearly visible at 140°C. In the DSC curve, the first maximum exothermic signal beyond 200°C is centered at 294°C and could correspond to the first weight loss visible on the DTG curve at 287°C. It corresponds to the partial 2nd step of phenolic resin curing reaction and is attributed to the generation of NH_3, as analyzed by TGA FT-IR on an analogous phenol-formaldehyde resin (see FIGURE 3.6A) in a parallel ITT study, and demonstrated by Guo et al (122). It is worthy to note that oxidation itself could prevent the curing reaction from proceeding, as these events happen at the same time (at temperatures up to 200°C). The second peak at 502°C in the DTG curve in FIGURE 3.5 is caused by the post-curing together with thermo-oxidative degradation of the phenolic resin with the evolution of H_2O, CO_2, and CO, as visible on the TGA FT-IR analysis on FIGURE 3.6B (H_2O and CO_2 release). The third peak at 629°C is due to the evolution of CH_4 (123).

It can be concluded that the resin once heated is mainly composed of polycondensated novolac oligomers with some aromatic ring bond (-CON<), as studied by D. Santamaria Razo (124).

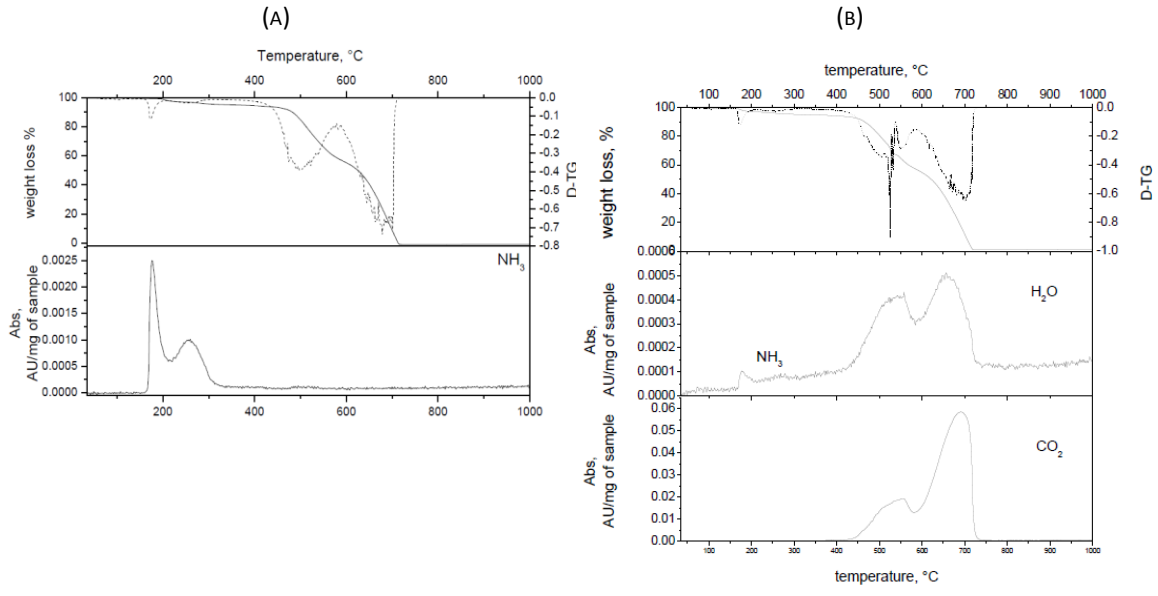

FIGURE 3.6 TGA, DTG AND FT-IR OF A PHENOL FORMALDEHYDE RESIN IN TEMPERATURE RANGE RT-1000°C

1.3. Basic mixes

DSC measurements have been performed for the basic mix samples, as presented in FIGURE 3.7.

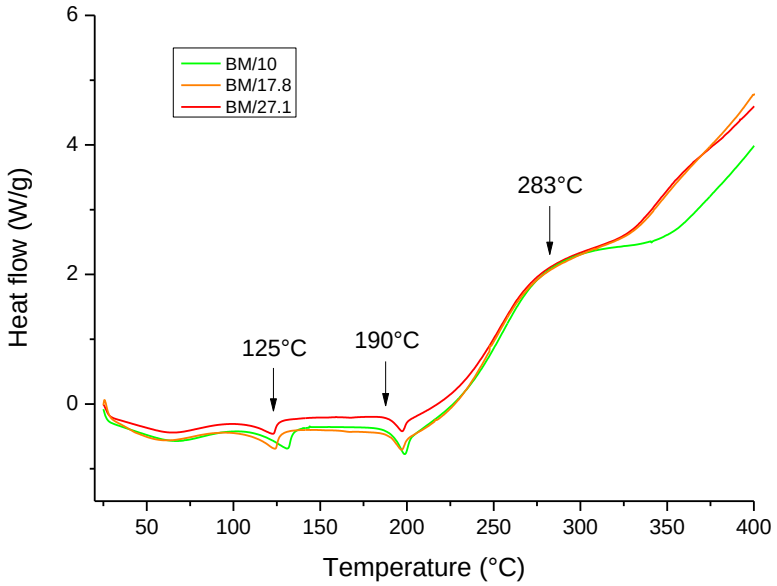

FIGURE 3.7 DSC MEASUREMENTS OF THE THREE BASIC MIXES BM/10, BM/17.8 AND BM/27.1

For the three samples the endothermic peak at around 125°C is due to water evaporation. This peak can easily disappear using a hermetically sealed pan, as shown on FIGURE 3.8A, and will not be considered later in this study. The 1st glass transition temperature is the same for the three samples, equal to 190°C, which is higher than the Tg value measured on the phenolic cured resin, equal to 140°C (see FIGURE 3.8B). The aramid fibres create a complex 3D network in the material that contributes to the mechanical integrity, and then decrease the polymer chains mobility, which significantly increase its glass transition. The broad signal centered at 283°C corresponds to the 2nd crosslinking reaction, but it happens simultaneously with the exothermic organic chain degradation, so is difficult to be observed.

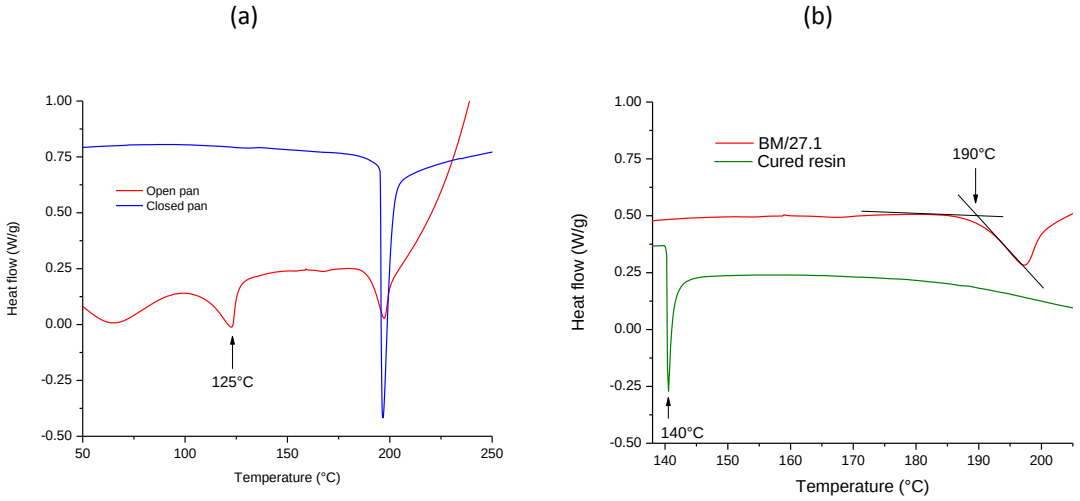

FIGURE 3.8 DSC CURVES OF (A) MIX BM/27.1 IN OPEN AND CLOSED PAN IN THE TEMPERATURE RANGE 50-250°C, (B) CURED RESIN AND BM/27.1 SAMPLE

The TGA curve for the basic mixes BM/10, BM/17.8 and BM/27.1 are reported in FIGURE 3.9. The previous phenomena observed in the temperature range 25-400°C are clearly visible on the TGA curves (see in FIGURE 3.9a): until 130°C the weight loss corresponds to water evaporation, as observed in DSC measurements. The second broad signal is visible from 190°C to 310°C and corresponds to the 2nd crosslinking reaction and the evaporation of the associated volatile products. The three samples decompose at the same temperature, namely 545°C as shown in FIGURE 3.9b, which corresponds to the aramid fibres temperature degradation. The phenolic resin degradation happens simultaneously (see FIGURE 3.5), and its peak is not clearly visible.

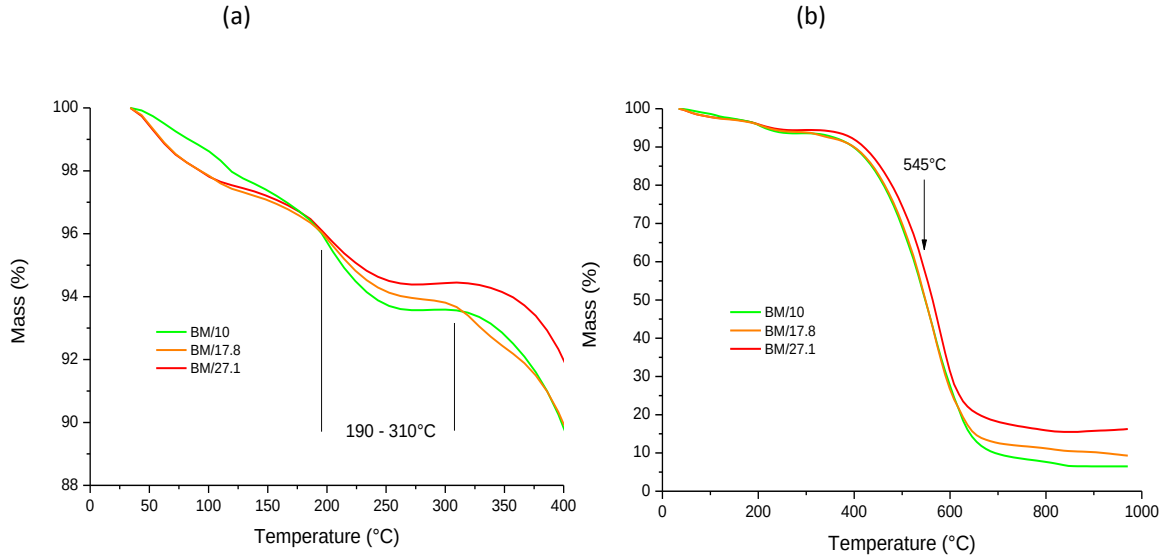

FIGURE 3.9 TGA CURVES OF BM SAMPLES (A) IN TEMPERATURE RANGE 25-400°C, (B) IN TEMPERATURE RANGE 25-950°C

2. DMTA

Due to the sample preparation process and sample geometry required for DMTA analysis, only BM/27.1 sample has been analyzed by DMTA, the result is presented in FIGURE 3.10.

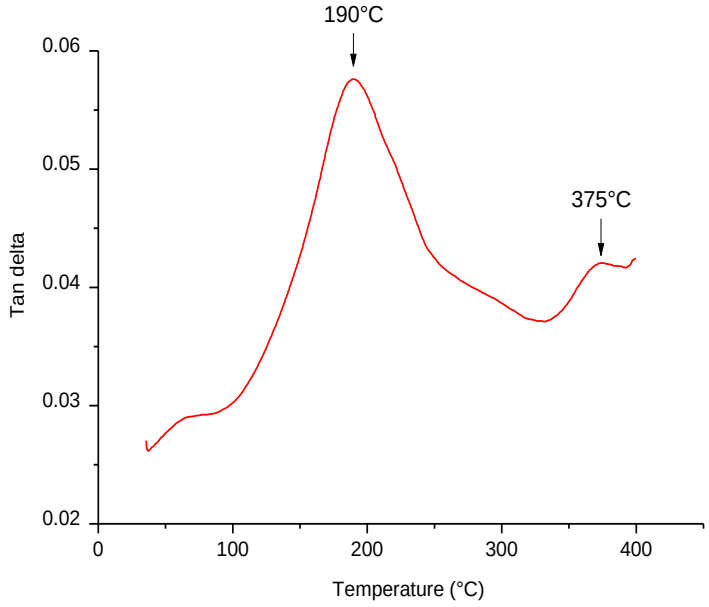

FIGURE 3.10 DMTA CURVE OF BM/27.1 SAMPLE

Two glass transitions are visible at 190°C and 375°C. The first one at 190°C has already been observed through DSC analysis (see on FIGURE 3.7) at the same temperature, while the second one at 375°C was not clearly observed because of simultaneous exothermic phenomena (oxidation and 2nd crosslinking reaction). It corresponds to the mobility of polymer chain segments having undergone the 2nd crosslinking reaction, which could be considered as the "fully cured polymer" (125). When running the sample in the DMTA, the 1st glass transition region is reached; thermal energy provides enough molecular mobility so that chemical reaction can continue, leading to an increase in the crosslinking degree and the appearance of the 2nd glass transition peak, corresponding to the fully cured material.

3. FLA

Thermal conductivity values for the three basic mix samples as a function of aramid fibre content is shown in FIGURE 3.11. There is a light increase of thermal conductivity of the composite in the range 10-27%vol of aramid fibre as expected considering the thermal conductivities of the raw materials.

Thermal conductivity of aramid fibre: 8.05 W/(K.m) at 300K (126);
Thermal conductivity of phenolic resin: 0.15 W/(K.m) at 298K (127).

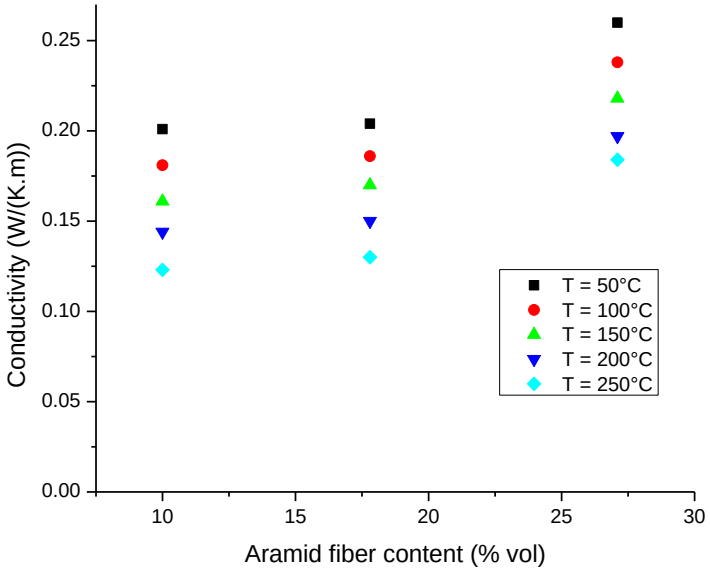

FIGURE 3.11 LASER FLASH THERMAL ANALYSIS FOR MIXES BM/10, BM/17.8 AND BM/27.1 CONDUCTIVITY IN FUNCTION OF ARAMID FIBRE CONTENT

In this preamble, the thermal behavior of the basic mix, phenol formaldehyde resin and dispersed aramid fibres, has been studied in the range RT-950°. At neat state the phenolic resin exhibits a glass transition at 50°C, and then two crosslinking reactions at 150°C and 287°C corresponding to the two successive steps of the complete network formation of a novolac resin. On cured phenol formaldehyde resin, there is no glass transition at 50°C but at 140°C, shifted until 190°C in the basic mix due to aramid fibre network that limit polymer chain movements. The 150°C crosslinking peak is absent in sign of complete 1st step reaction, but then the second step of crosslinking is still present at around 283°C considering the fact that the material is composed for majority of novolac oligomers. At higher temperature organic degradation starts and the DMTA measurements show the 2nd glass transition corresponding to the whole crosslinked polymer at 375°C.

I - FILLERS PRESENTING INTERACTION WITH RESIN

1. STEEL FIBRES

1.1. DSC and TGA

DSC, TGA and DTG curves of previously heated steel fibres (following the protocol detailed in the *Materials and methods* chapter, section *II-2.2.3.2.*) are presented in FIGURE 3.12. In the TGA curve two gains of weight are present: the first one centered at 508°C would correspond to the exothermic DSC signal beginning at 326°C, and the second centered at 898°C with a final weight at 970°C equal to 142% of the initial sample weight. Both are weight gain due to oxidation reactions: with the oxygen present in air flowing, iron forms Fe_3O_4 and Fe_2O_3. The first step centered at 508°C could be the formation at the interface powder/air of an oxide layer acting as a shield, then the reaction stops after only 5%wt gain until around 830°C.

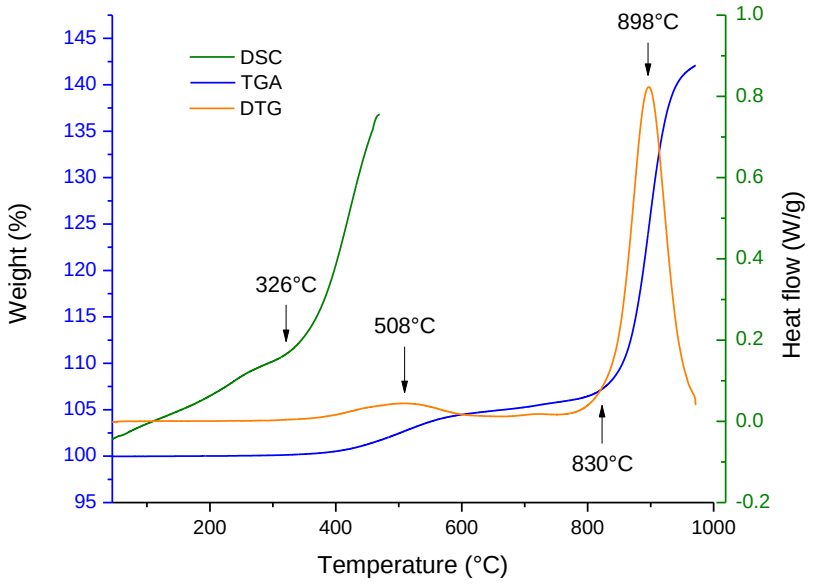

FIGURE 3.12 DSC, TGA AND DTG CURVES OF STEEL FIBRES PERFORMED IN AIR, AT A HEATING RATE OF 10°C/MIN

It is known that at 60% of the metal fusion temperature (equal to 1538°C, 1811K for Fe (128)) the diffusion phenomenon inside the material becomes important, which permits

to the oxidation to go further and reach the heart of the alloy. This temperature is equal to 813°C for pure iron, and in fact it is the starting temperature for the massive oxidation step as seen in FIGURE 3.12. In literature the successive iron oxides layers are, from surface to heart: Fe_2O_3, Fe_3O_4, and FeO as visible on FIGURE 3.13.

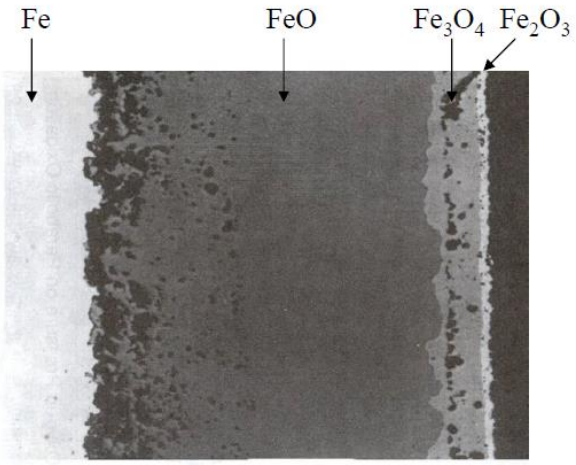

FIGURE 3.13 TRANSVERSAL SECTION OF OXIDIZED FE SAMPLE (129)

The TGA curves performed on the three steel fibres based samples are plotted in FIGURE 3.14.

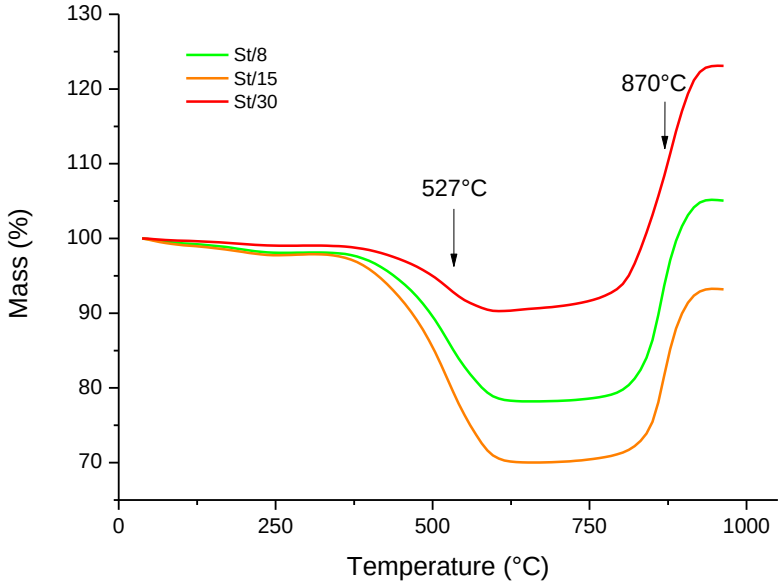

FIGURE 3.14 TGA MEASUREMENTS OF ST/8, ST/15 AND ST/30 MIXES

Two phenomena are clearly identifiable: the aramid fibres degradation appears at 527°C for the three samples, with the simultaneous resin degradation. At 870°C the weight gain corresponding to the steel fibre oxidation is observed. To interpret these curves it can be interesting to consider the "theoretical TGA curves" obtained for each material (see *Materials and methods* chapter, section *II-2.2.3.2.)*, adding the single raw material curves. The results are presented in FIGURE 3.15. The main observation is the difference between experimental and theoretical curves: before 500°C, which is the temperature of degradation of the basic mix components, the couples of curve move apart. It is possible to conclude that the degradation of the organic part of the mixes is limited or at least slowed down when mixed and pressed with steel fibres. As studied by R. Vijay et al (130), higher the steel fibre content, higher the thermal stability of the material. About the oxidation step, the experimental increase is more important than the theoretical one. It would mean that someway the oxidation rate is higher when fibres are in the mix than when they are alone. It may be due to the fact that the aspect ratio of these fibres is lower when picked up from the mix because of the sampling process that may have broken them up. As a consequence there are more free steel surface, so there is more oxidation.

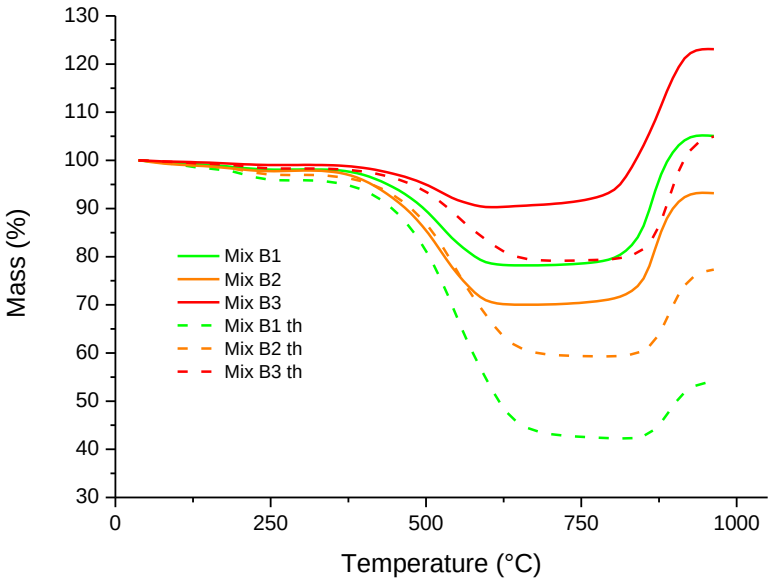

FIGURE 3.15 TGA MEASUREMENTS OF THE THREE ST/X MIXES AND THEIR THEORETICAL CURVES

1.2. DMTA

DMTA measurements are performed on the St/x samples, and the results are presented in FIGURE 3.16, together with those of BM sample. For clarity, the observed temperatures are not shown on the graphic itself but the values are reported in TABLE 3.1.

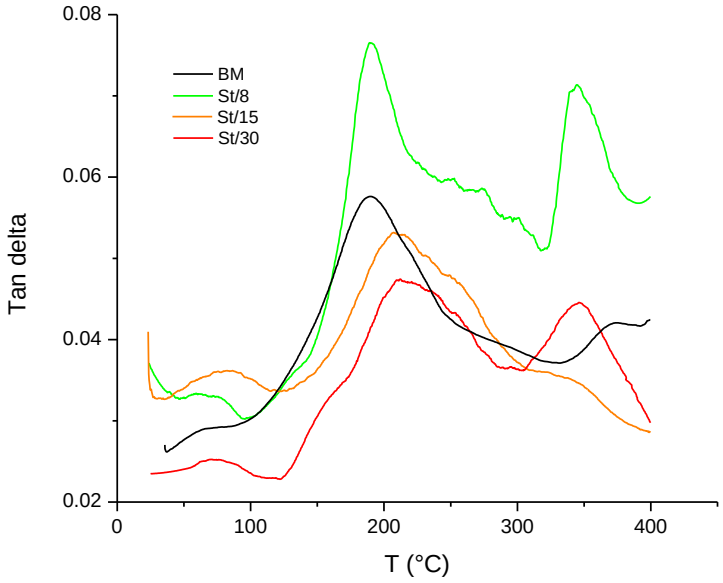

FIGURE 3.16 DMTA MEASUREMENTS FOR BM, ST/8, ST/15 AND ST/30 SAMPLES

TABLE 3.1 GLASS TRANSITION VALUES FOR ST/X SAMPLES

Sample	BM	St/8	St/15	St/30
1st Tg temperature	190°C	190°C	207°C	212°C
2nd Tg temperature	375°C	343°C	344°C	347°C

The 1st glass transition (Tg_1) temperature shifts to higher temperatures, that is, from 190°C for composite BM to 212°C for composite St/30. A strong fibre/matrix interfacial bonding acts as a barrier that restricts the mobility of polymeric chains; thus, reduction in damping factor occurs in rubbery region (131), as verified by Chua (132). The 2nd glass transition temperature presents a different behavior: for St/x samples it is shifted to lower temperatures and its height is higher. Because of the high content of fibres dispersed through the material, there is proportionally less resin so the 2nd crosslinking

reaction happens in minor quantity, so the network density is initially lower, which corresponds to a higher damping amplitude. The 2nd Tg temperature is lower for steel fibres containing samples because the 2nd crosslinking reaction happens in minor quantity during the previous thermal treatment so it is facilitated during the heating of the DMTA measurement.

The Cole-cole plots of samples St/x presented in FIGURE 3.17 indicate some positive interaction between steel fibres and matrix. In fact the representation of loss modulus in function of storage modulus is reported to be indicative of the homogeneity of the system: more perfect the circle shape more homogeneous the system and weaker the bonding filler/matrix (see theorical consideration in the *Materials and methods* chapter in section *II-2.2.3.3.*). From St/8 to St/30 with the increase content in steel fibres the shape of the curve is sharper, sign of a stronger system heterogeneity, thus of a stronger interface and bonding fibre/matrix.

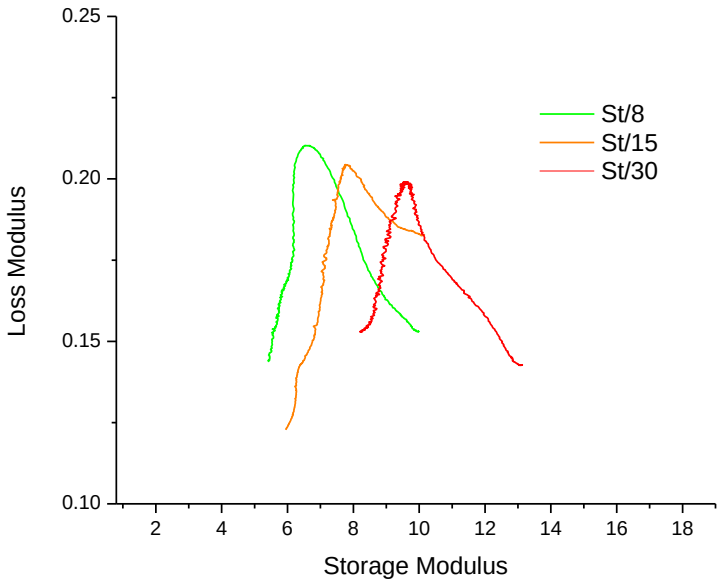

FIGURE 3.17 COLE-COLE PLOT OF ST/X SAMPLES

1.3. FLA

The graphic presenting the thermal conductivity variations in function of temperature for steel fibre components is in FIGURE 3.18.

Steel thermal conductivity: 50.2 W/(K.m) (133).

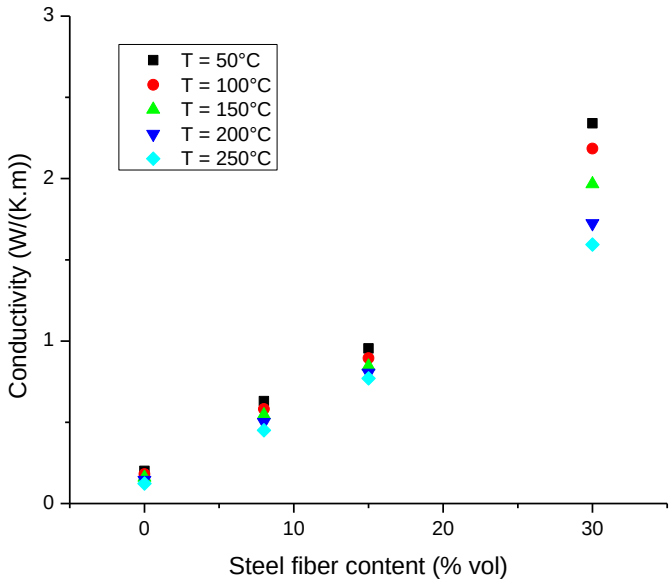

FIGURE 3.18 GRAPHIC OF THERMAL CONDUCTIVITY IN FUNCTION OF STEEL FIBRE CONTENT

Steel fibres are metallic, so because of their conductive nature, higher their content in the material higher is the resulting conductivity. Conductivity increases with temperature thanks to the free movements of charge carriers electrons. It is worthy to note that the thermal conductivity value for the more concentrated sample is much less than the steel conductivity found in literature. In fact, during the sample preparation process, at the pressing step the fibres inside the material get oriented in the parallel direction to the sample surface; this way there is few conductive path created through the matrix from one surface to another, so the percolation threshold is not reached. The percolation threshold is a basic characteristic of a conductive composite which is characterized by a sharp drop in the electrical resistance when the conductive filler content reaches a special value corresponding to the formation of a continuous path through the matrix.

Many theoretical percolation models have been developed to define the conditions at which a network is formed. In the most notable geometrical models created by Kirkpatrick (134) and Zallen (135), a regular array on which particles (with spherical shape) are distributed statistically is examined. In these models, the required minimum network of touching particles is 16%vol. This value is in approximate agreement with most experimental determinations since for most polymers filled with powdery materials the critical volume fraction for percolation is between 5 and 20 %vol. Nevertheless it has been shown that the percolation threshold not only depends on the particle size and fractal dimension but also on all the process parameters used to synthesize the sample (136).

2. ALUMINUM OXIDE

2.1. DSC and TGA

Aluminum oxide is thermally treated following the usual protocol; it is stable in the temperature range 30-970°C: there is no weight loss on the TGA curve and no exo-endo signals on the DSC curve.

DSC measurements on the alumina monocomponent samples are shown in FIGURE 3.19, while the values are summed up in TABLE 3.2.

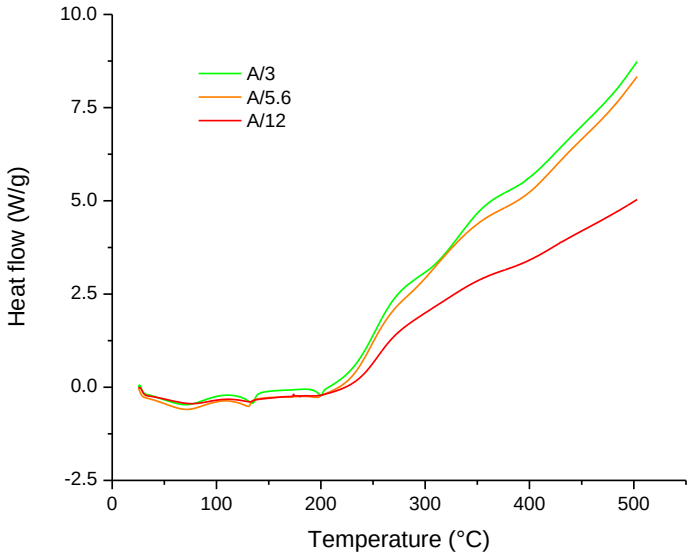

FIGURE 3.19 DSC MEASUREMENTS OF A/3, A/5.6 AND A/12 MIXES

TABLE 3.2 DSC VALUES FOR BM AND A/X SAMPLES

Sample	Aluminum oxide content	Tg_1 temperature	T_{cross2}	Tg_2 temperature
BM	0%vol	190°C	283°C	N.A
A/3	3%vol	192°C	276°C	357°C
A/5.6	5.6%vol	185°C	275°C	346°C
A/12	12%vol	N.A	N.A	N.A

DSC signals are not precise in this case and no clear tendency is visible. TGA measurements have been performed on the alumina monocomponent samples, and are presented in FIGURE 3.20.

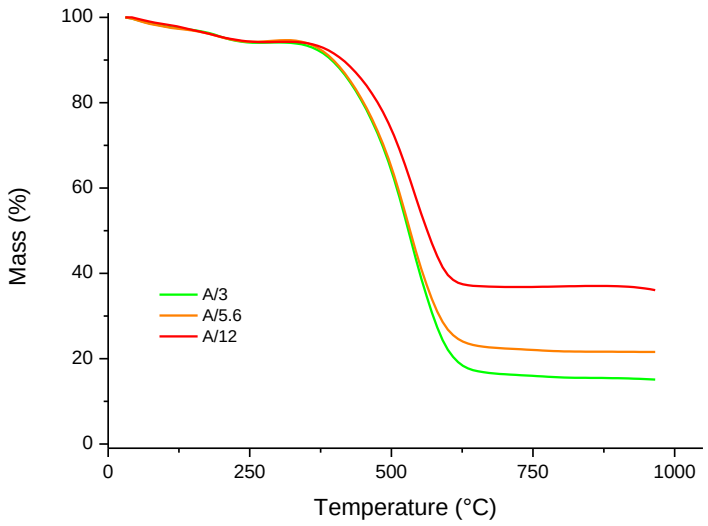

FIGURE 3.20 TGA MEASUREMENTS OF A/3, A/5.6 AND A/12 SAMPLES

The A/3 and A/5.6 mixes degrade at low temperatures whereas the most concentrated sample degrade at higher temperature in respect of basic mix sample, this behavior rupture is the sign of an optimal concentration for the system, equal to 5.6%vol.

2.2. DMTA

DMTA measurements are performed for the A/x samples; the curves are presented in FIGURE 3.21 and the noted values are reported in TABLE 3.3. Tg_1 temperature is higher for

A/x mixes with respect to the basic mix, especially for the most concentrated sample (Tg_1 = 211°C instead of 190°C). It can be concluded that alumina oxide interacts with the basic mix matrix. A/3 sample presents a peak at 316°C which could correspond to the 2nd crosslinking reaction occurring at higher temperature compared to BM at 283°C, due to the developed interaction fillers/matrix.

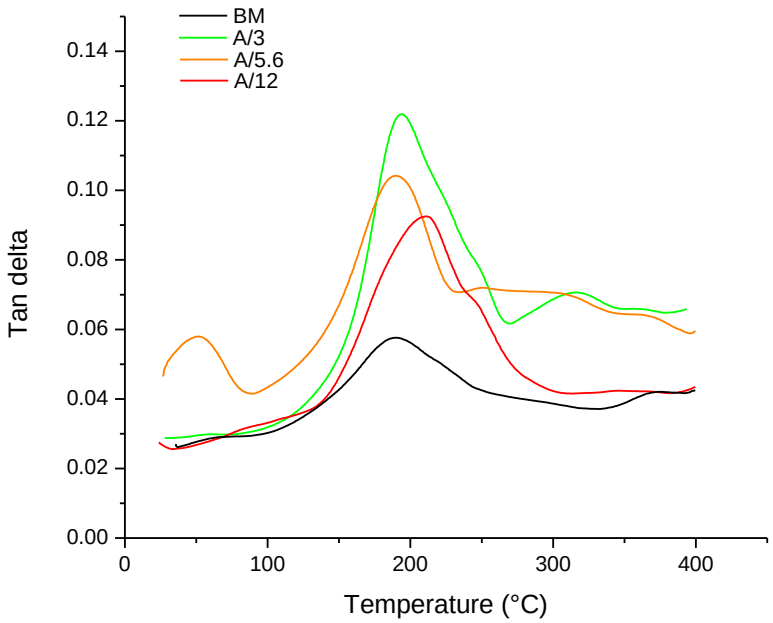

FIGURE 3.21 DMTA MEASUREMENTS FOR BM, A/3, A/5.6 AND A/12 SAMPLES

TABLE 3.3 GLASS TRANSITION VALUES FOR A/X SAMPLES

Sample	BM	A/3	A/5.6	A/12
1st Tg temperature	190°C	194°C	191°C	211°C
2nd Tg temperature	375°C	≈365°C	≈371°C	≈346°C

2.3. FLA

Laser flash thermal analysis are performed on the A/x samples and the results are presented in FIGURE 3.22.

Thermal conductivity of aluminum oxide: 30 W/(K.m) (137)

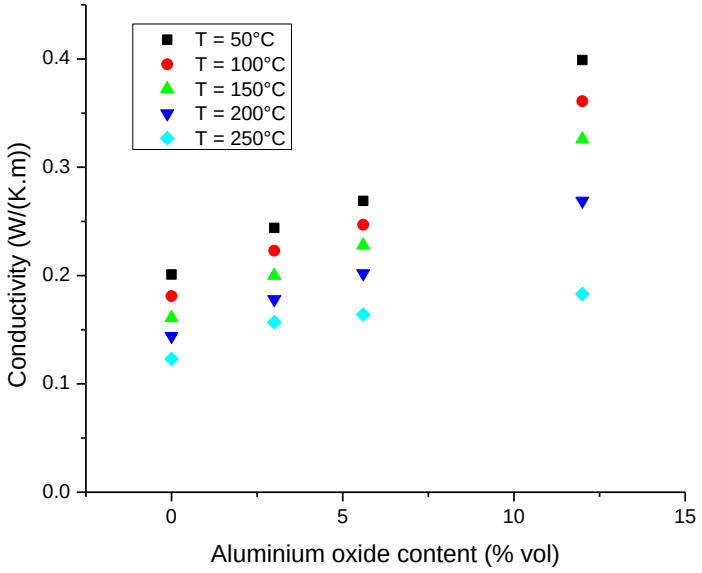

FIGURE 3.22 GRAPHIC OF THERMAL CONDUCTIVITY IN FUNCTION OF ALUMINUM OXIDE CONTENT FOR A/X MIXES

The conductivity increase with alumina content is in agreement with the observations of L.C. Sim et al. (138) in the range 0.2-0.4 W/(K.m) for a filler content until 12%vol. In his work, theoretical models (the Maxwell–Eucken, Bruggeman and Cheng–Vochan models (139)) were used to predict the thermal conductivity of the Al_2O_3 filled pads, as presented in FIGURE 3.23. The results obtained were then compared with the experimental data. It can be observed that the predictions of the Maxwell–Eucken and Bruggeman models significantly deviate from the experimental data, while the Cheng–Vochan model overestimated at filler loading inferior to 8 vol.% for Al_2O_3.

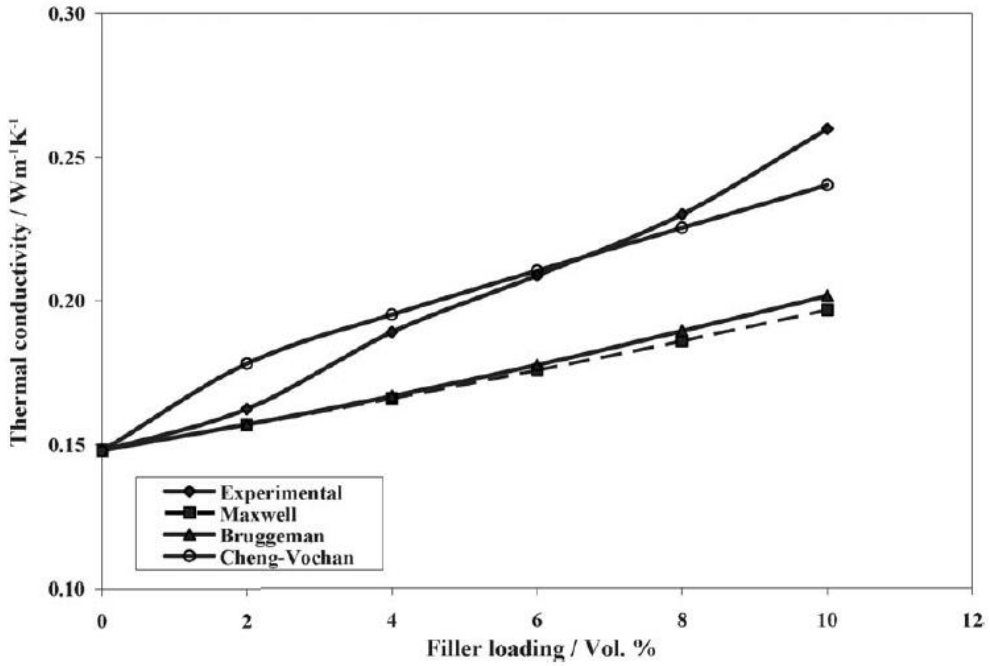

FIGURE 3.23 COMPARISON OF THERMAL CONDUCTIVITY OF Al_2O_3 FILLED THERMAL PADS WITH THEORETICAL PREDICTIONS (139)

The deviations arise from the fact that the theoretical models didn't take in account the filler quality dispersion in the bulk, especially for composites with low filler content (140). However, by fitting the experimental data into the Agari model (represented by the equation herein below), a possible explanation of the state of filler dispersion in the composites studied could be obtained:

$$\log K = V_f \, C_2 \log K_f + v_p \log(C_1 K_p)$$

with K : composite thermal conductivity;
V_f and V_p : volume fraction of fillers and polymer;
C_1 : crystallinity of the matrix;
C_2 : factor indicating the possibility to form conductive chains for the fillers (complex parameter including for instance the filler shape)

According to Agari, the values of C_1 and C_2 are between 0 and 1 (141) (142) (143). The more easily particles are gathered to form conductive chains, the more thermal conductivity composite changes, and the C_2 value becomes closer to 1. It has been reported that, during the composite preparation process, particles can influence the

polymer crystallinity and thus change the resulting thermal conductivity. This effect is taken in consideration into C_1 parameter. The values found by L.C. Sim et al. (138) are C_1 = 0.8159; C_2 = 0.9647. It is observed that the alumina addition into the matrix affects the C_2 values more strongly than the C_1 values, that means it does not affect the polymer crystallinity, but a conductive path through the material should be easily formed. This equation, with the C1 and C2 parameters found by L.C. Sim et al., is plotted using the measurements performed on the A/x samples and presented in FIGURE 3.24 where both theoretical and experimental curves dealing with log K are shown. The similarity between these two curves confirms that the model used and the conclusion drawn by the author of the aforementioned paper are correct.

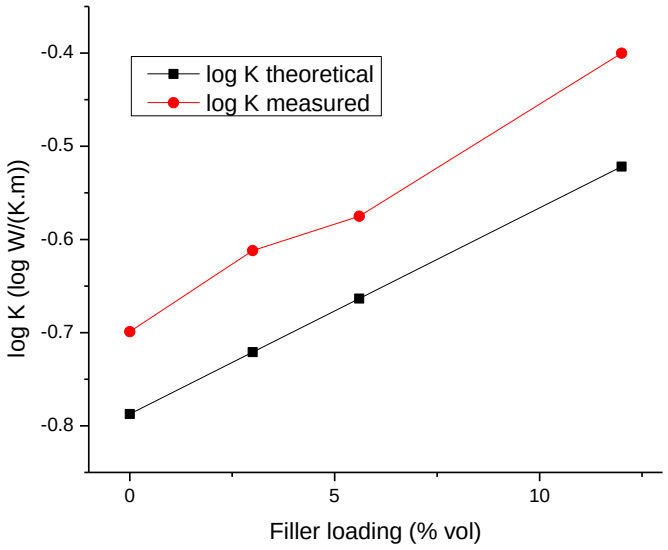

FIGURE 3.24 THEORETICAL AND EXPERIMENTAL GRAPHIC REPRESENTATION OF LOG K IN FUNCTION OF ALUMINUM OXIDE CONTENT

3. PETROLEUM COKE

3.1. DSC and TGA

DSC, TGA and DTG curves of previously thermally treated petroleum coke are plotted in FIGURE 3.25. Since the petroleum coke had been calcinated at temperatures around 1100 °C, most of the volatile matter and moisture had already been removed, and as expected

there is no weight loss for petroleum coke until 537°C, then the organic degradation of the filler occurs with a maximum rate at 756°C, as highlighted on the DTG curve. On the DSC the onset of the oxidation reaction is visible at around 340°C.

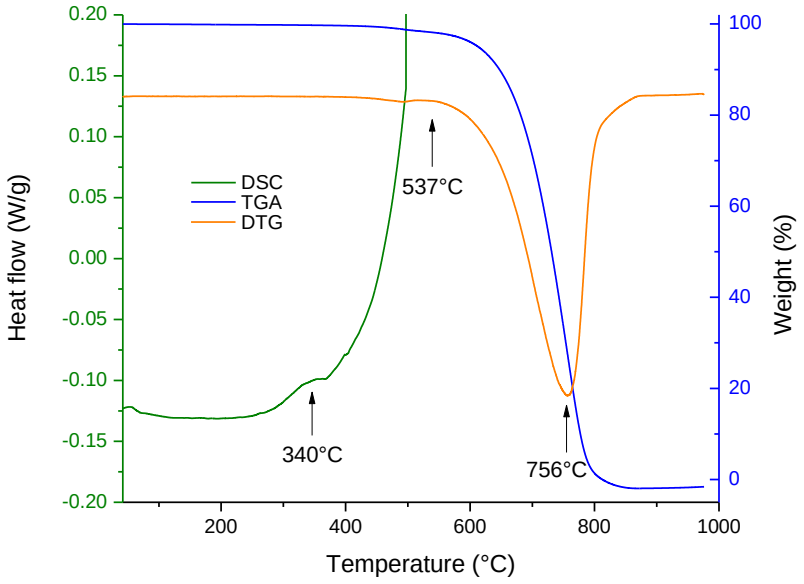

FIGURE 3.25 DSC, TGA AND DTG CURVES OF PETROLEUM COKE PERFORMED IN AIR, AT A HEATING RATE OF 10°C/MIN

The analogous measurements are performed on the petroleum coke based samples, and the resulting curves are presented in FIGURE 3.26; for clarity the values are compiled in TABLE 3.4. The light T_{g1} temperature increase could be explained by the interaction coke/resin, which implies a higher energy input to reach the glass transition. The 2nd crosslinking temperature is roughly the same for the C/x mixes. As the exothermic signal is broad and happens simultaneously to the beginning of oxidative degradation process of the organic matter, its measure is not very precise and a difference of $\Delta T = 4°C$ is not relevant.

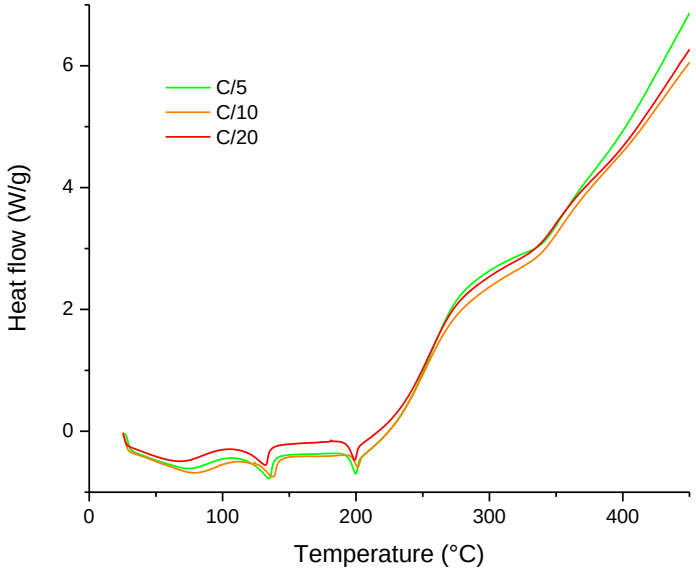

FIGURE 3.26 DSC MEASUREMENTS OF C/5, C/10 AND C/20 MIXES

TABLE 3.4 DSC VALUES FOR C/X SAMPLES

Sample	Tg_1 temperature	T_{cross2}
BM	190°C	283°C
C/5	194°C	280°C
C/10	196°C	279°C
C/20	193°C	279°C

The TGA curves of petroleum coke monocomponent samples are presented in FIGURE 3.27.

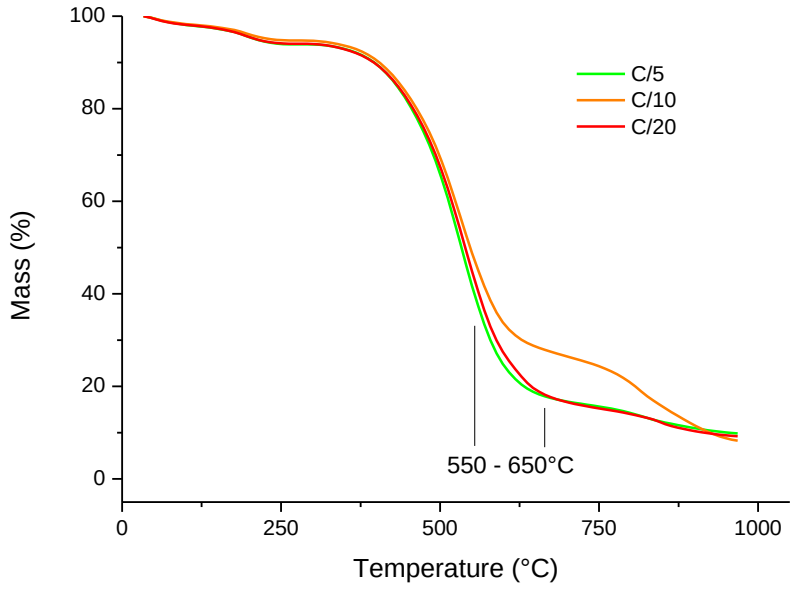

FIGURE 3.27 TGA CURVES PERFORMED IN AIR AT HEATING RATE OF 10°C/MIN OF C/X MIXES

Until 550°C the three curves are superimposed, sign that there is no effect of petroleum coke presence on the thermal stability of the materials.

3.2. DMTA

DMTA curves of coke monocomponent samples are plotted in FIGURE 3.28 and the particular values are compiled in TABLE 3.5.

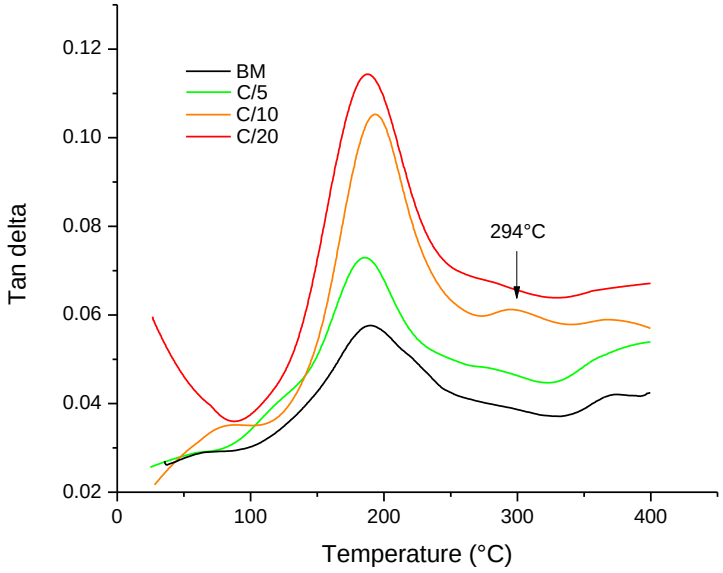

FIGURE 3.28 DMTA MEASUREMENTS FOR BM, C/5, C/10 AND C/20 SAMPLES

TABLE 3.5 GLASS TRANSITION VALUES FOR C/X SAMPLES

Sample	BM	C/5	C/10	C/20
1st Tg temperature	190°C	187°C	194°C	196°C
2nd Tg temperature	375°C	371°C	372°C	370°C

There is a peak for C/10 sample at 294°C that corresponds to the 2nd crosslinking reaction unachieved during the heating treatment. On the DSC curves, T_{g1} temperature slightly increases, which reflects a bonding filler/matrix; while it is here the case only for C/10 and C/20 samples. In agreement with G. Yi et al (144) it can be concluded that petroleum coke has a light interfacial bonding strength with the phenolic resin matrix. However, as seen for steel fibres mixes, the Tg_2 temperature is lower than the basic mix sample because this reaction is achieved in minor quantity during the previous thermal treatment, so it is facilitated with the energy provided by the measurement.

3.3. FLA

The measurements of thermal conductivity with respect to temperature and coke content are presented in FIGURE 3.29. The thermal conductivity of C/x samples increases with the

petroleum coke content to reach the filler value at around 0.4 W/K.m: so it can be considered that at 20%vol of coke the percolation is reached.

Thermal conductivity of petroleum coke: 0.4 W/(K.m) at RT (145).

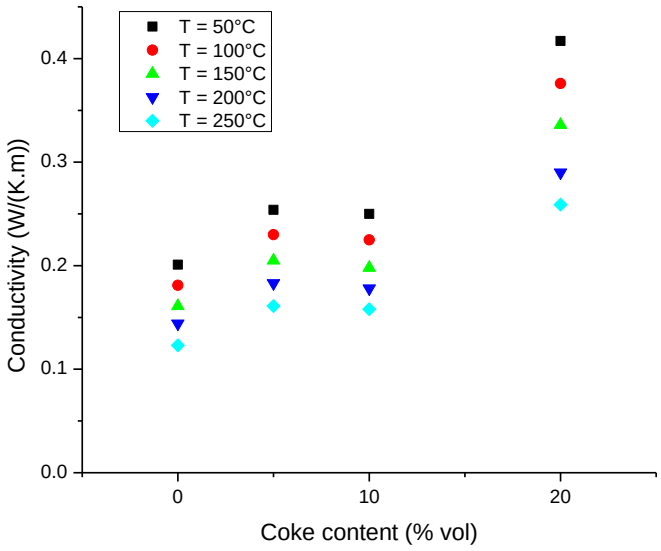

FIGURE 3.29 GRAPHIC OF THERMAL CONDUCTIVITY IN FUNCTION OF PETROLEUM COKE CONTENT FOR C/X SAMPLES

4. FRICTION DUST

4.1. DSC and TGA

DSC, TGA and DTG curves of friction dust beforehand thermally treated are plotted in FIGURE 3.30.

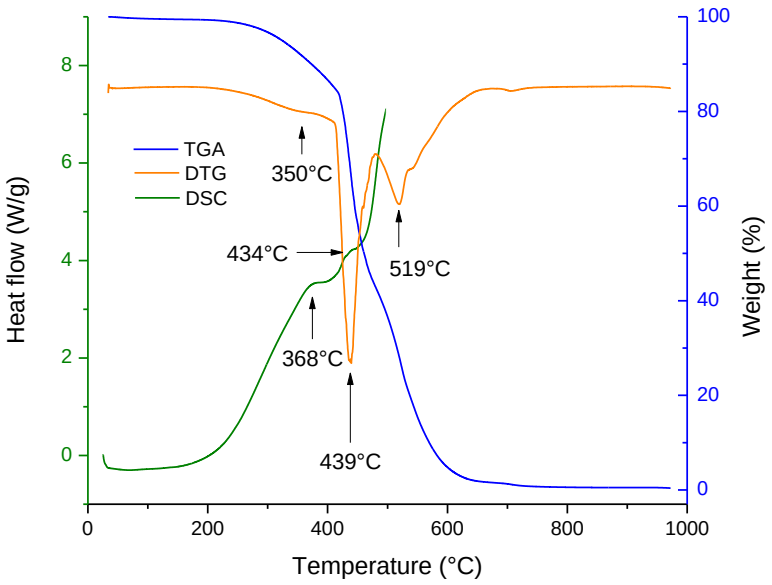

FIGURE 3.30 DSC, TGA AND DTG CURVES OF FRICTION DUST PERFORMED IN AIR, AT A HEATING RATE OF 10°C/MIN

As the friction dust is a mix of phenolic resins, the interpretation of FIGURE 3.30 is similar and based on the same dynamics than heated phenol formaldehyde resin study (see *Preamble section 1.*). On the DSC curve, at 368°C the exothermic peak corresponds to the 2nd crosslinking reaction and is visible on the DTG curve at 350°C; then a degradation peak is present at around 434°C and centered at 439°C on the DTG curve that could correspond to a breakdown of the methylene linkages of the alkyl chain of cardanol (146). A second degradation signal is identifiable on the DTG curve at 519°C; it could correspond to the organic degradation, which occurs at 629°C for cured phenolic resin (see FIGURE 3.5) as it is assumed than friction dust is a mix of different phenolic chains which don't necessary degrades at the same temperature, with various impurities decreasing the cohesion and the chains interaction and thus facilitating the degradation.

Same measurements have been performed on F/x samples, and are presented in FIGURE 3.31. Important values are reported in TABLE 3.6. About the phenolic resin dynamics, there is a slight T_{g1} temperature increase, but too low to conclude about an interaction filler-resin, and a 2nd crosslinking temperature decrease. For the two most concentrated

samples in friction dust (F/16 and F/32), a signal centered at 339°C and 350°C appears, corresponding to the 2nd glass transition of phenolic chains; its amplitude is high considering the phenolic nature of friction dust and its content in the material.

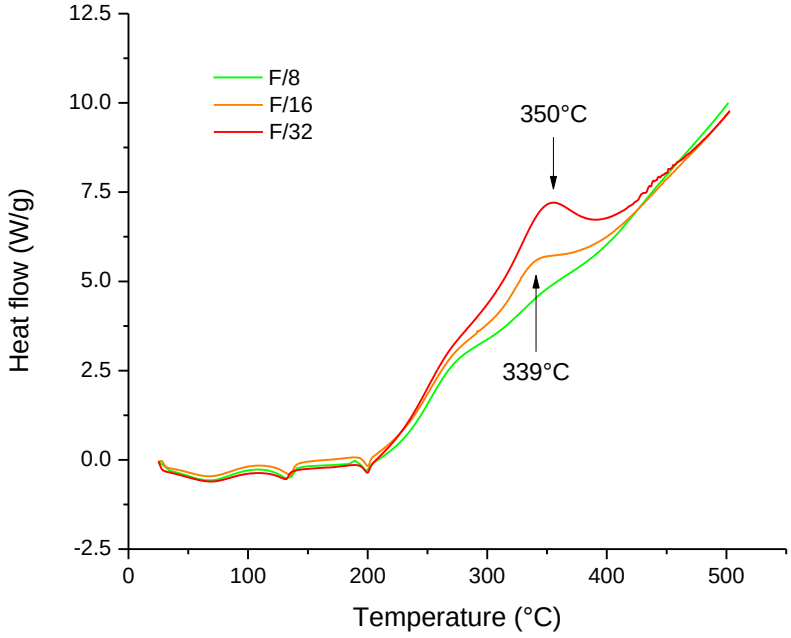

FIGURE 3.31 DSC MEASUREMENTS OF F/8, F/16 AND F/32 SAMPLES

TABLE 3.6 DSC VALUES FOR BM AND F/X SAMPLES

Sample	Tg_1	$T_{cross2\ resin}$	Tg_2
BM	190°C	283°C	N.A
F/8	192°C	≈274°C	N.A
F/16	193°C	≈273°C	339°C
F/32	193°C	≈270°C	350°C

Some FT-IR measurements have been performed on phenol formaldehyde resin, friction dust, and the mixture of both. The spectra are presented in FIGURE 3.32.

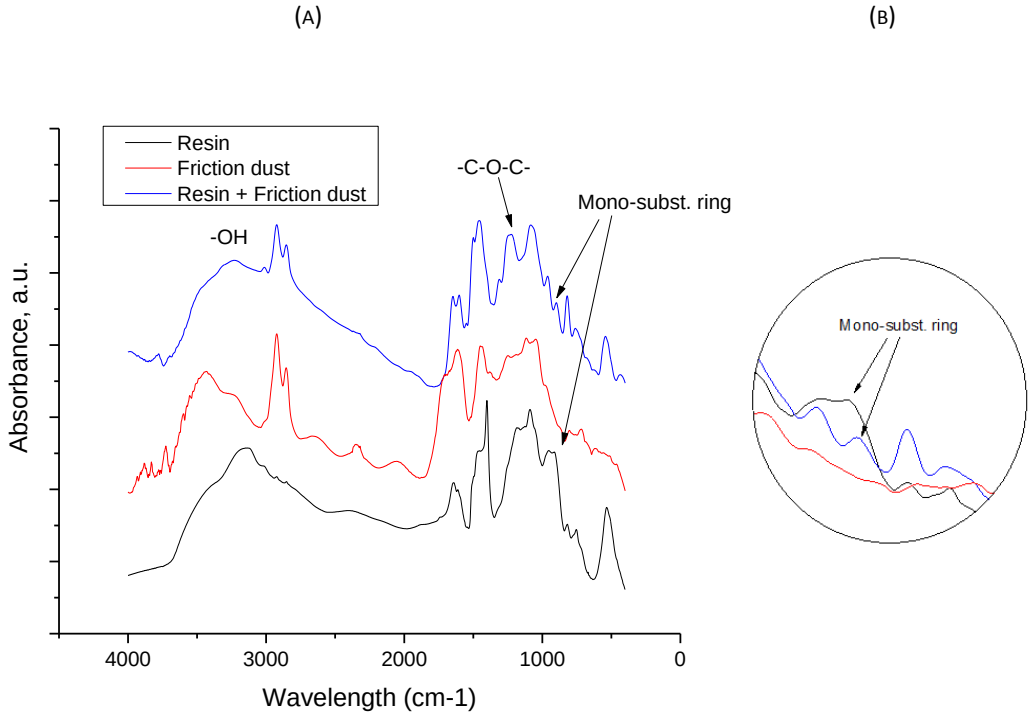

FIGURE 3.32 FT-IR SPECTRA OF PHENOLIC RESIN, FRICTION DUST AND PHENOLIC RESIN + FRICTION DUST SAMPLES, ALL PREVIOUSLY HEATED AT 160°C FOR 60 MIN

The peak associated with the OH- group attached to the phenyl ring in the polymeric resin repeat unit is observed in the region 3290 cm^{-1} to 3370 cm^{-1}. The peak at 1200 cm^{-1} in the infrared spectrum of the mix is associated with the presence of ether linkages. The peaks associated with the methylene groups at 2921 cm^{-1}, 2851 cm^{-1} in the neat friction dust and 2922 cm^{-1} and 2853 cm^{-1} in the mix are due to the cardanol side chain and also to etherification reactions. The peak for mono-substitution at 752 cm^{-1} in the phenyl ring are significantly decreased in the mix. This confirms that the polymerization has taken place through the ortho and/or para positions between phenol formaldehyde resin and friction dust (105). This way, it can be stated that reaction between friction dust and phenol formaldehyde occurs, but the molecular weights of friction dust components are too low so this filler has a plasticizing behavior. At the same time, the fact that the glass transition temperature stays equal to basic mix indicates that two opposite effects occur: classical plasticizing effect (leads to a Tg decrease) and interaction via direct chemical reaction and hydrogen bonds (leads to a Tg increase).

4.2. DMTA

DMTA results for the three friction dust monocomponent samples are presented in FIGURE 3.33 and the particular values are compiled in TABLE 3.7.

For F/16 the Tg_2 is not clearly visible, the peak is not well defined so it is not possible to give a value. At 289°C a peak is visible for F/32. This temperature corresponds to the 2nd crosslinking temperature of phenolic chains. It could be hypothesized for this sample that all the binder didn't react during sample preparation heating and the network get formed during the DMTA measurement.

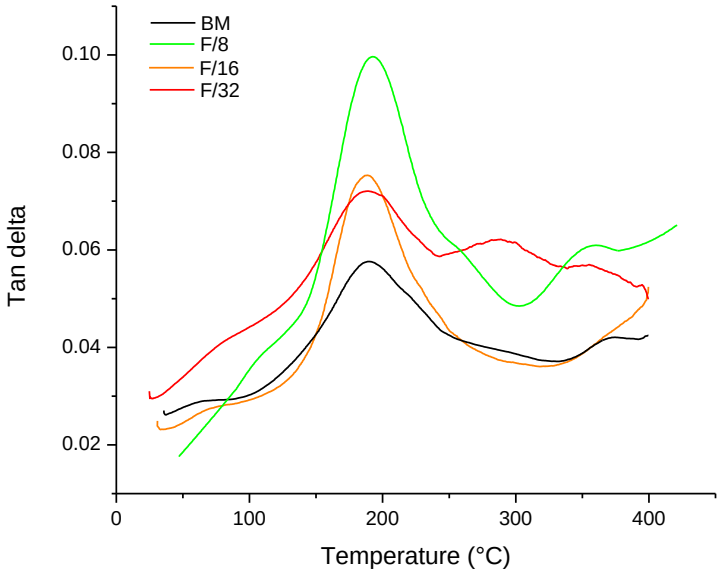

FIGURE 3.33 DMTA MEASUREMENTS FOR SAMPLES BM, F/8, F/16 AND F/32

TABLE 3.7 GLASS TRANSITION VALUES FOR BM AND F/X SAMPLES

Sample	BM	F/8	F/16	F/32
1st Tg temperature	190°C	191°C	193°C	193°C
2nd Tg temperature	375°C	353°C	N.A	355°C

The tendency observed on DSC curves of a slight increase of Tg_1 with friction dust content is confirmed here.

4.3. FLA

The variations of thermal conductivity with respect to temperature in the range 50-250°C are plotted for the F/x samples in FIGURE 3.34. The conductivity of the samples slightly decreases in function of the friction dust content: in fact the friction dust thermal conductivity is equal to the phenolic one (0.15 W/(K.m) at 298K (147)) whereas it is of 8.05 W/(K.m) at 300K (126) for aramid fibre.

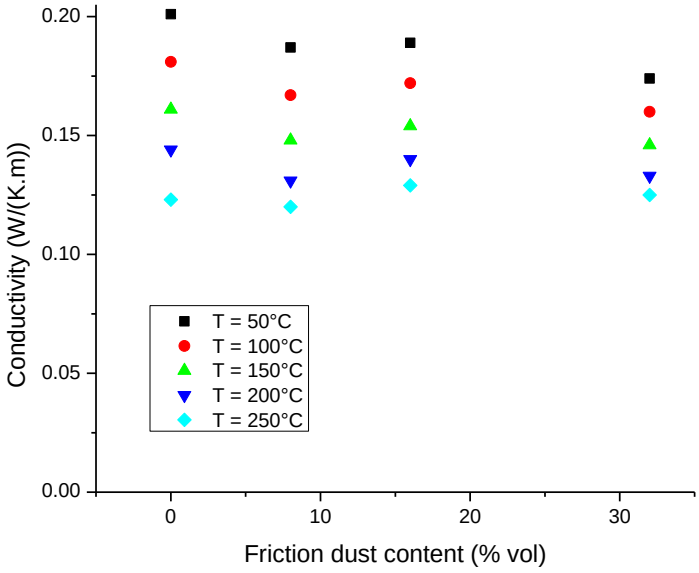

FIGURE 3.34 GRAPHIC OF THERMAL CONDUCTIVITY IN FUNCTION OF TEMPERATURE FOR SAMPLES F/X

Through DSC and DMTA measurements, four of the eight fillers belonging to the present study, develop a good interaction with the matrix (made of aramid fibres dispersed in the resin). As a consequence, an increase of the glass transition temperature is observed, sign that the polymeric chains are blocked by bonding with added component. The other four components do not exhibit the same kind of result and show an inert behavior towards the polymeric chain: they act as plasticizer in the mixture.

II - FILLERS WITHOUT INTERACTION WITH RESIN: PLASTICIZERS

1. POTASSIUM HEXATITANATE FIBRES

1.1. DSC and TGA

The DSC obtained for the previously thermally treated potassium hexatitanate fibres does not present any peak; TGA curve of thermally treated filler shows that potassium hexatitanate is stable in the 30-970°C temperature range.

DSC curves obtained for the potassium hexatitanate fibres monocomponent samples are presented in FIGURE 3.35 and the important values are reported in TABLE 3.8. The 1st glass transition temperature is slightly lower for potassium hexatitanate containing samples: the oligomers are less in contact with aramid fibres which block their movements; so the glass transition is easier and the Tg_1 temperature lower. The fillers act as plasticizer inhibiting interaction inside the basic mix. The broad signal centered at around 272°C corresponds to the 2nd crosslinking reaction of the phenolic resin; it is clearly visible for Ti/10 mix, but considering the resin content decreasing for Ti/20 and Ti/50 samples, this signal gets lower and is not distinguishable.

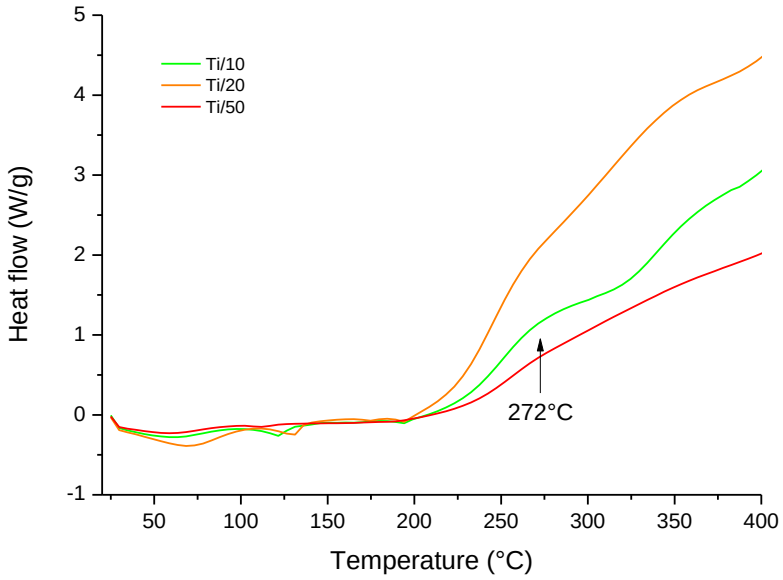

FIGURE 3.35 DSC MEASUREMENTS OF TI/10, TI/20 AND TI/50 MIXES

TABLE 3.8 DSC VALUES FOR BM AND TI/X SAMPLES

Sample	Tg_1 temperature	T_{cross2}
BM	190°C	283°C
Ti/10	188°C	≈272°C
Ti/20	188°C	N.A.
Ti/50	184°C	N.A.

TGA curves of potassium hexatitanate fibres monocomponent samples are presented in FIGURE 3.36.

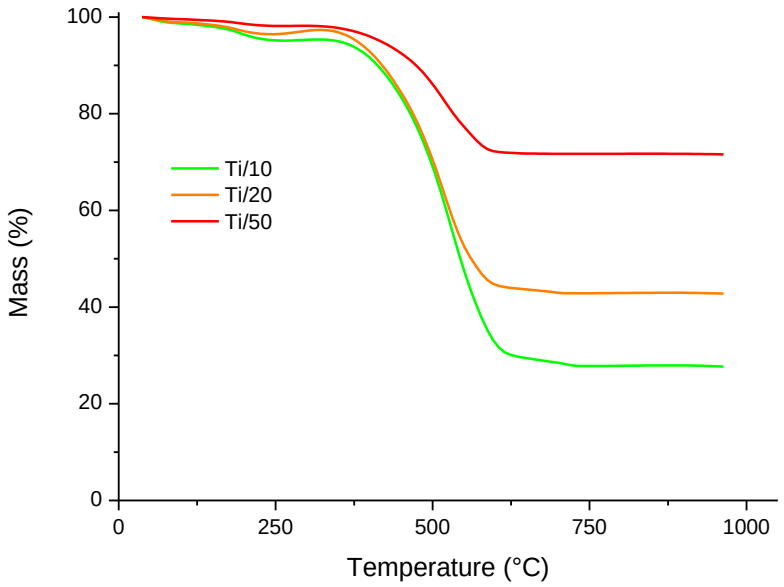

FIGURE 3.36 TGA CURVES OF TI/10, TI/20 AND TI/50

The degradation of basic mix is clearly shifted towards higher temperature with potassium hexatitanate fibres addition. It is due to the shield effect: the fillers protect the matrix from degradation, isolating it in some way from the high temperature of the environment. More fibres in the bulk, more this effect is important: the degradation shift is much higher at 50%vol of fibres content than at 10%vol and 20%vol.

1.2. DMTA

The DMTA curves of Ti/x samples are plotted in FIGURE 3.37 and the noted values are reported in TABLE 3.9.

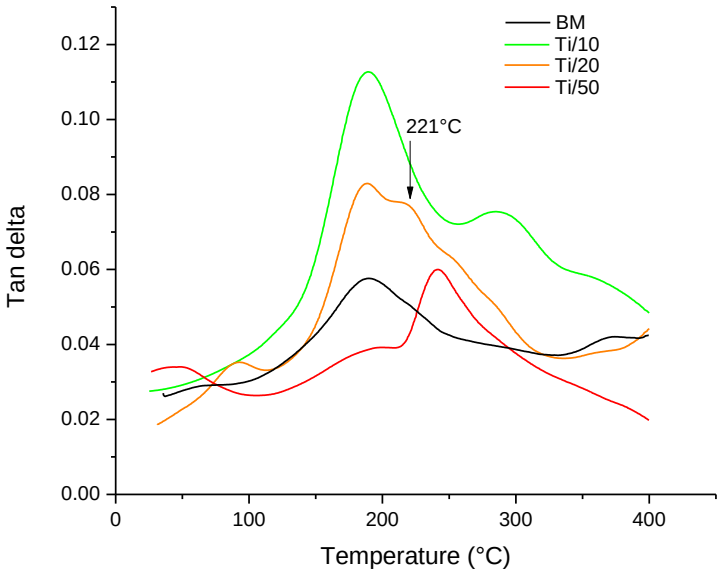

FIGURE 3.37 DMTA MEASUREMENTS FOR BM, TI/10,TI/20 AND TI/50 SAMPLES

TABLE 3.9 GLASS TRANSITION VALUES FOR BM AND TI/X SAMPLES

Sample	BM	Ti/10	Ti/20	Ti/50
1st Tg temperature	190°C	188°C	188°C	N.A
1st Tg damping amplitude	0.028	0.087	0.062	N.A
2nd Tg temperature	375°C	362°C	N.A	N.A

Ti/50 sample, containing 50%vol of potassium hexatitanate does not show the same behavior than samples Ti/10 and Ti/20; it is assumed that is contains too much filler to be considered and compared to them; the resin content could not be high enough to bind all the fillers. Ti/20 sample exhibits a second peak at around 221°C, which can be due to the interaction between the phenolic chains and the whiskers: the "bulk" polymer presents a glass transition at 188°C, and the chains in contact with the fibres need more

energy to pass the glass transition and shift it to 221°C. For Ti/x mixes the glass transition temperature is roughly equal to the basic mix one (188°C instead of 190°C for BM) while tan δ height increases when potassium titanate whiskers are incorporated. Damping of materials is actually evaluated by the rate of dissipate energy (148). As explained by S. Chen et al. (149), the internal friction of a polymer matrix is a measure of the rate of dissipating energy. When potassium titanate whiskers are incorporated, additional friction between the whiskers and the polymer chains as well as friction between whiskers increase the rate of dissipating energy. Thus, the damping properties of the materials improved, and the 1st Tg damping amplitude increase as visible in TABLE 3.9. In addition, the hexatitanate whiskers exhibit a relatively high specific surface area. So the friction between whiskers and matrix is stronger than for traditional fibres. However, the interaction between fillers and matrix is poor, as the addition of potassium hexatitanate lets the Tg value unchanged showing that the filler has only a plasticizing effect.

1.3. FLA

The thermal conductivity measurements of Ti/x samples are presented in FIGURE 3.38. Potassium hexatitanate thermal conductivity: 1.7 W/(m.K) at RT (150).

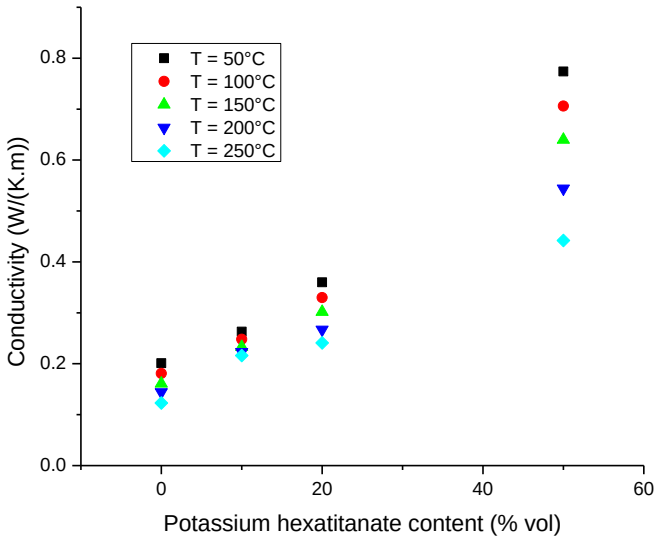

FIGURE 3.38 GRAPHIC OF THERMAL CONDUCTIVITY IN FUNCTION OF TEMPERATURE FOR TI/X MIXES

There is a linear relation between thermal conductivity and potassium hexatitanate content. It is noteworthy that even when the filler content is equal to 50%vol, the thermal conductivity of 0.8 W/(m.K) is far from the one of the filler (1.7 W/(m.K) at RT).

2. BARIUM SULFATE

2.1. DSC and TGA

DSC and TGA tests are performed on barium sulfate filler previously thermally treated; this filler exhibits high thermal stability at temperatures as high as 970°C as the TGA and DSC curves are flat.

DSC of B/x mixes are presented in FIGURE 3.39, the important values for clarity are compiled in TABLE 3.10. The signal at 348°C and 351°C for mixes B/50 and B/70 respectively can be identified as the 2nd glass transition of the phenolic network. The 1st glass transition is unchanged.

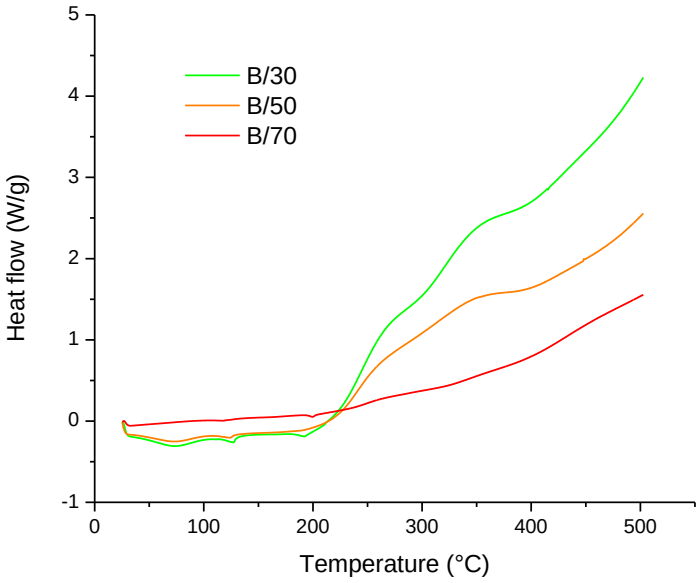

FIGURE 3.39 DSC MEASUREMENTS OF B/X MIXES

TABLE 3.10 DSC VALUES FOR BM AND B/X SAMPLES

Sample	Tg_1 temperature	T_{cross2}	Tg_2 temperature
BM	190°C	283°C	N.A
B/30	182°C	271°C	348°C
B/50	N.A	N.A	351°C
B/70	192°C	N.A	N.A

TGA measurements are performed on the barium sulphate monocomponent materials and presented in FIGURE 3.40. The degradation of basic mix is shifted towards higher temperature due to the shield effect, already observed for the potassium hexatitanate fibres samples. The weight loss evolution of mixes B/x is equal to the basic mix one, as barium sulfate does not degrade in this temperature range. As presented in TABLE 3.11, the residue at 970°C is equal to barium sulfate weight, as expected.

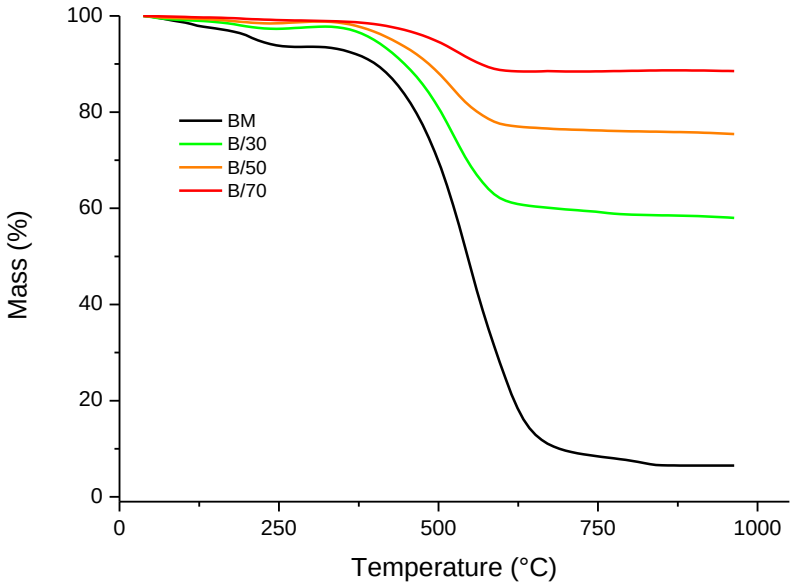

FIGURE 3.40 TGA OF BM AND MIXES B/30, B/50 AND B/70

TABLE 3.11 WEIGHT RESIDUE AND BARIUM SULFATE CONTENT IN WEIGHT IN MIXES B/X

Sample	Barium Sulfate, %wt	Residue at 970°C, %wt
B/30	59.2	58
B/50	77.2	75
B/70	88.8	88.5

2.2. DMTA

The tan δ variations are plotted in function of temperature in FIGURE 3.41 for the B/x samples.

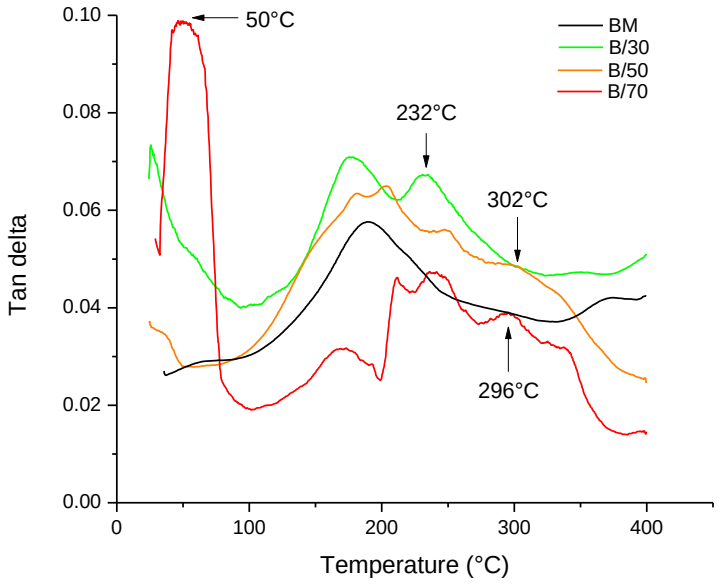

FIGURE 3.41 DMTA MEASUREMENTS FOR BM, B/30, B/50 AND B/70 SAMPLES

TABLE 3.12 GLASS TRANSITION AND DAMPING VALUES FOR BM AND B/X SAMPLES

Sample	BM	B/30	B/50	B/70
1st Tg temperature	190°C	177°C	183°C – 202°C	171°C – 214°C
1st Tg damping amplitude	0.028	0.030	0.035	0.012
2nd Tg temperature	375°C	351°C	N.A	≈341°C

For B/70 sample the very high tan δ peak centered at 50°C corresponds to the neat resin glass transition (see FIGURE 3.4). This would mean that the resin did not react; but as its DSC curve does not present any signal at 154°C (see FIGURE 3.39) which is the crosslinking temperature of the phenolic resin, it is possible to conclude that a partial resin curing occurs. In fact the barium sulfate of B/70 is equal to 70%vol, thus the oligomers are isolated from each other and can't react. As a conclusion B/70 mix is too poor in resin content to be considered as a composite and its DMTA curve is not relevant.

For mix B/30 a peak appears at 232°C, and corresponds to the 250°C and 239°C ones for mixes B/50 and B/70. They correspond to secondary α transitions, mainly due to some sample heterogeneities, with formation of different zones (mainly bulk and interface matrix/filler) which present different behaviors. As explained by A. Tiwary et al. (151), the peak general broadening and its irregularities may be caused by various relaxation mechanism associated with slippage of fillers on surrounding polymer chains, slippage of polymer chains on one another, slippage of filler on one another or breakage of the filler network with an increase in temperature (152) (153). Another peak is newly present for B/50 and B/70 at 302°C and 296°C respectively, which corresponds to the 2nd crosslinking reaction as already observed for other samples (C/10 for example). For B/50 mix Tg_1 peak seems to split and the 2nd peak is centered at 202°C and is identifiable at 214°C for B/70. It can be due to the presence of two distinct phases: the polymeric chains in conformation bulk and the segments in contact with the particles. A too high content of fillers generally leads to this separation, as explained by L.A. Pothan et al (154).

Barium sulfate particles act as plasticizer, as their addition decreases the 1st glass transition (from 190°C for basic mix BM to 177°C and 183°C for B/30 and B/50) and increases the damping amplitude (from 0.028 for basic mix BM to 0.030 and 0.035 for B/30 and B/50), as observed by S. Manoharan et al (131) for more complex friction system varying the barium sulfate content from 0 to 20%wt. This may be partially explained by the fact that particle aggregates are gradually formed due to strong filler–filler interaction or closer interparticle distances as barite concentration increases. These aggregates act as steric hindrance of chain mobility for the entire molecular chains of the polymer (155).

2.3. FLA

Thermal conductivity measurements are performed and the results are presented in FIGURE 3.42.

Thermal conductivity of barium sulfate: 1.72 W/(K.m) at RT (156).

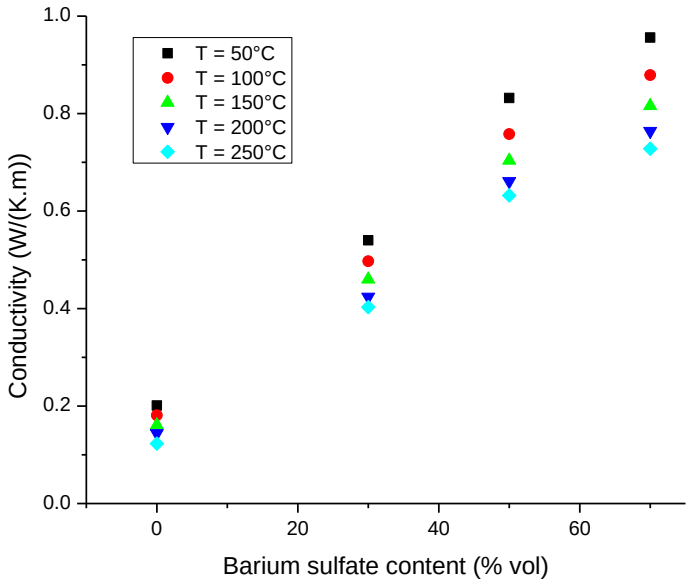

FIGURE 3.42 GRAPHIC OF THERMAL CONDUCTIVITY IN FUNCTION OF BARIUM SULFATE CONTENT FOR B/X SAMPLES

Higher the barium sulfate content, higher the conductivity value, in a linear trend. The increase of this parameter with barium sulfate content has already been observed by H.J. Hwang (94).

3. GRAPHITE

3.1. DSC and TGA

DSC and TGA analysis are performed on thermally treated graphite, the resulting curves in function of temperature are plotted in FIGURE 3.43.

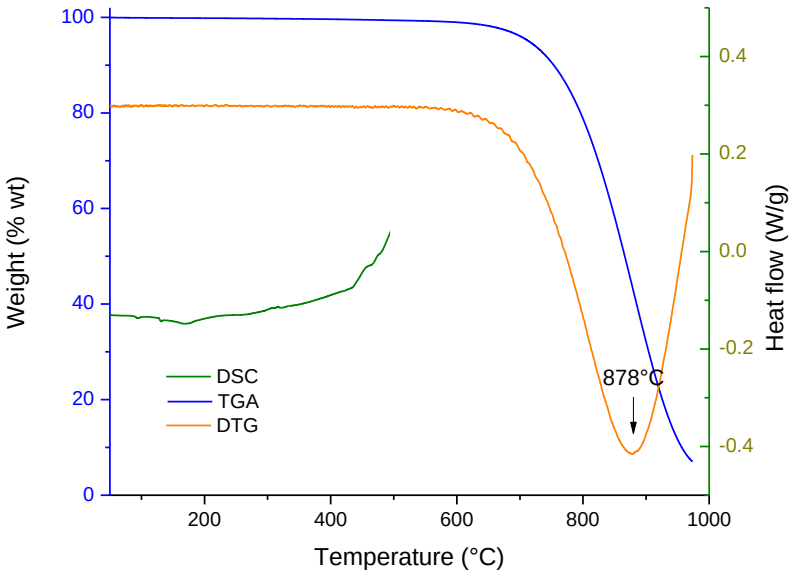

FIGURE 3.43 DSC, TGA AND DTG CURVES OF GRAPHITE PERFORMED IN AIR, AT A HEATING RATE OF 10°C/MIN

Graphite particles are thermally stable until 600°C, then with a maximum reaction rate centered at 878°C, graphite oxidation starts, producing CO and CO_2. The DSC measurement performed on the same material in the temperature range 30-400°C does not exhibit significant reaction.

DSC measurements of G/x samples are presented in FIGURE 3.44 and the notable values are reported in TABLE 3.13. The 1st glass transition temperature is constant and not influenced by graphite presence. As observed for other samples, 2nd crosslinking reaction temperature is lower than the basic mix one.

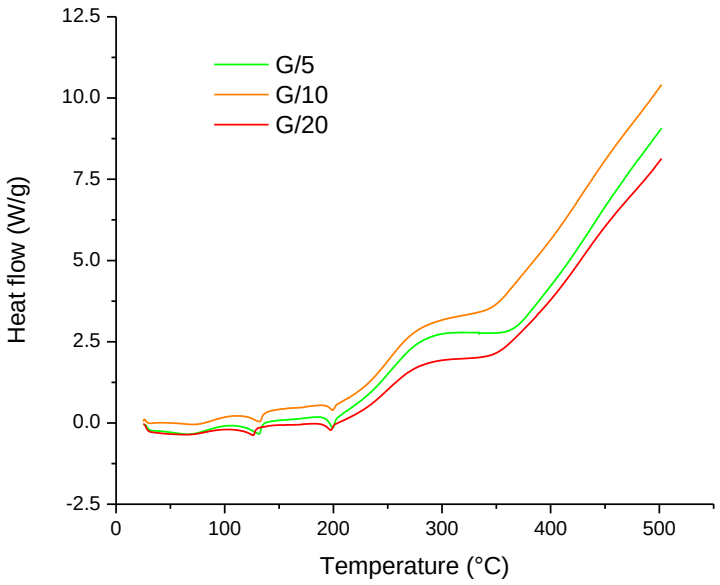

FIGURE 3.44 DSC MEASUREMENTS OF G/X MIXES

TABLE 3.13 DSC VALUES FOR BM AND G/X SAMPLES

Sample	Tg_1 temperature	T_{cross2}
BM	190°C	283°C
G/5	190°C	284°C
G/10	191°C	277°C
G/20	189°C	278°C

TGA measurements are performed on G/x samples and their plot in function of temperature are presented in FIGURE 3.45a. The important weight losses are easily distinguishable for the three samples: the first correspond to the basic mix degradation (mainly aramid fibres) at 545°C, and the other over 800°C is the graphite decomposition as visible in FIGURE 3.45b. The G/x sample curves are all superimposed for the basic mix step degradation: there is no thermal stability due to graphite addition in the bulk. The difference in the graphite step degradation observed for G/20 sample is due to different graphite carbonization dynamics at high temperature, not studied here.

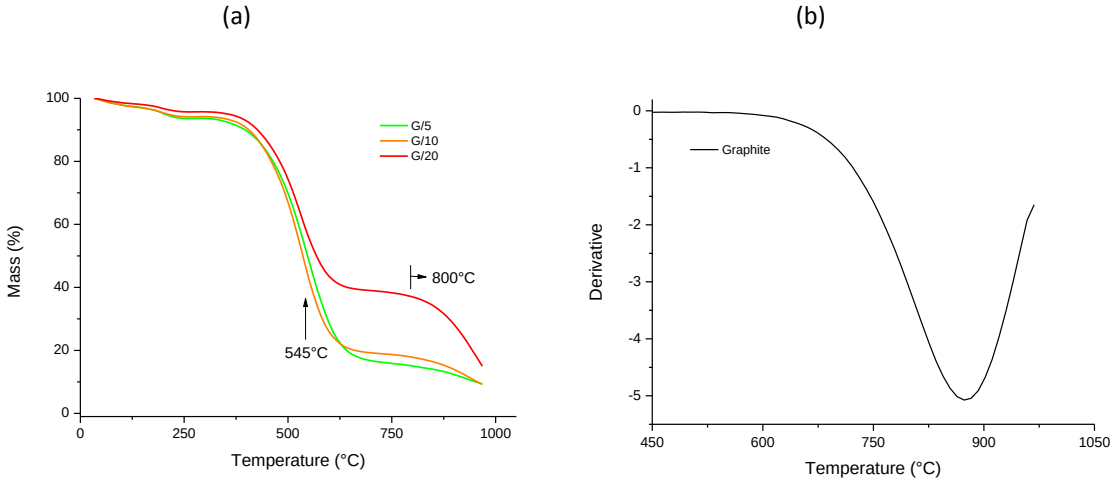

FIGURE 3.45 (A) TGA OF G/X MIXES, (B) DTG PLOT OF GRAPHITE

3.2. DMTA

DMTA results of the graphite monocomponent samples are presented in FIGURE 3.46 and the important values are reported in TABLE 3.14.

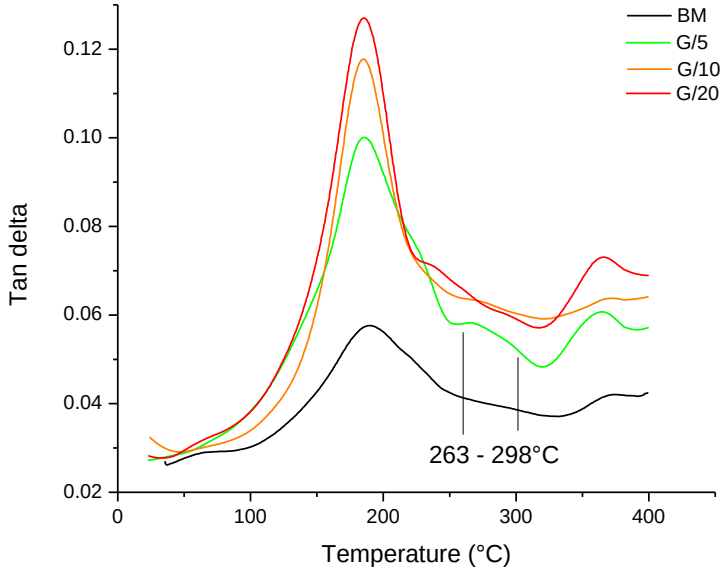

FIGURE 3.46 DMTA MEASUREMENTS FOR BM, G/5, G/10 AND G/20 SAMPLES

TABLE 3.14 GLASS TRANSITION AND DAMPING VALUES FOR BM AND G/X SAMPLES

Sample	BM	G/5	G/10	G/20
1st Tg temperature	190°C	185°C	185°C	185°C
1st Tg damping amplitude	0.028	0.073	0.089	0.100
2nd Tg temperature	375°C	366°C	373°C	366°C

G/5 sample presents a broad and weak peak between 263°C and 298°C which corresponds to the 2nd crosslinking step reaction of phenolic resin. The 1st glass transition for all graphite containing samples is centered at 185°C. This light T_{g1} temperature decrease means that the oligomers in contact with graphite particles and, as a consequence, less in contact with aramid fibres are less entangled so they can move more easily, which is expressed here by a Tg temperature decrease. The damping amplitude is higher because of the minor crosslinking density. As reported by T. Komori et al (157), the bonding strength between graphite and phenolic resin is very weak, so the graphite fillers act as plasticizers, as they decrease the chain interaction; the T_{g1} temperature decrease and the damping increase are the DMTA signs of this phenomenon.

The more graphite dispersed in the sample, the higher damping is observed. In fact the fillers prevent the oligomers to react and form the network; so the crosslinking density is lower, the chains have more mobility once they pass the glass transition which appears here as higher damping values. This phenomenon presents an upper limit, as demonstrated by the plot of 1st glass transition temperature damping in function of graphite content in the G/x samples, presented in FIGURE 3.47.

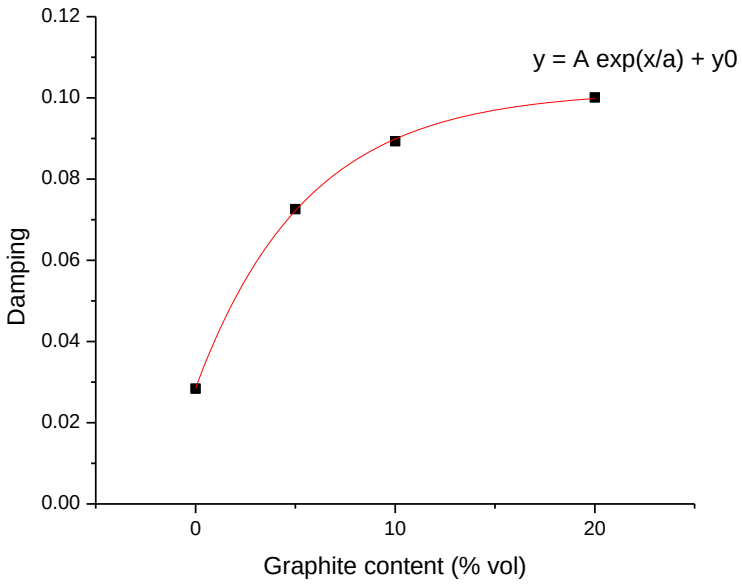

FIGURE 3.47 GRAPHIC OF DAMPING VALUE OF 1ST GLASS TRANSITION VERSUS GRAPHITE CONTENT FOR G/X SAMPLES

The fitting of the curve representing the damping versus graphite content corresponds to the following exponential equation:

$$y = A\ exp\frac{x}{a} + y_0$$

with:

A = -0.073;

a = -5.51;

y_0 = 0.1.

As a conclusion, at 20%vol of graphite, the composite has reached its maximum damping value.

The non-interaction between matrix and graphite is confirmed by two techniques: the FT-IR mapping using correlation treatment to identify the different components arrangement presented in FIGURE 3.48 (see *Materials and methods* chapter, section *2.2.1.3.2*) and the Cole-cole plot presented in FIGURE 3.49.

(a)

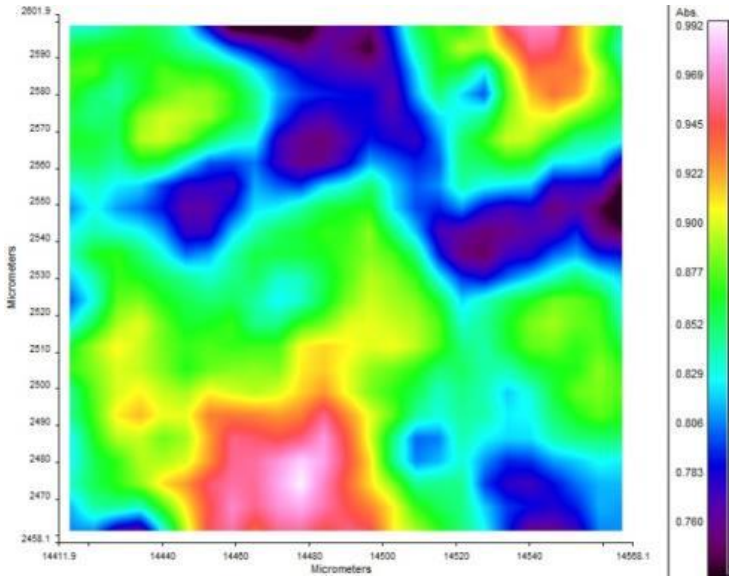

(b) (c) (d)

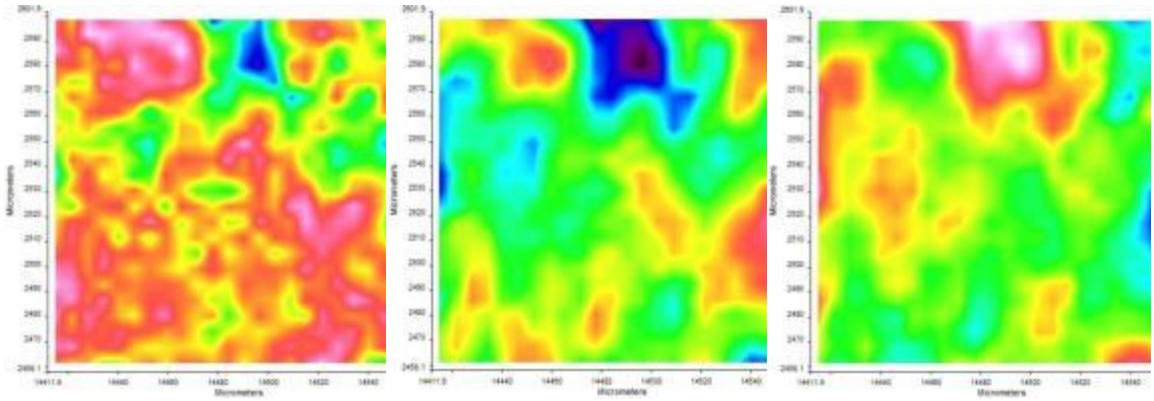

FIGURE 3.48 (A) FT-IR MAPPING OF G/20 SAMPLE, SQUARE OF 150 µM SIDE. FTIR MAPPING OF G/20 SAMPLE WITH CORRELATION WITH (B) RESIN, (C) ARAMID FIBRE AND (D) GRAPHITE SPECTRA

Considering the FIGURE 3.48c and d, the phenolic resin seems to be well distributed but don't hide all the elements present in the material. On the right side of the picture there is an aramid fibre and on the top a graphite particle. Both are very well identifiable and do not seem to be particularly linked or cover by the resin. By these observations, no interaction between the different elements is discovered.

On the Cole-cole plot the circular shape of the curves Loss modulus = function (Storage modulus) for the G/x composites is more regular than the basic mix one, sign that the

bonding (considered as an heterogeneity in the composite) between graphite and the matrix is very poor.

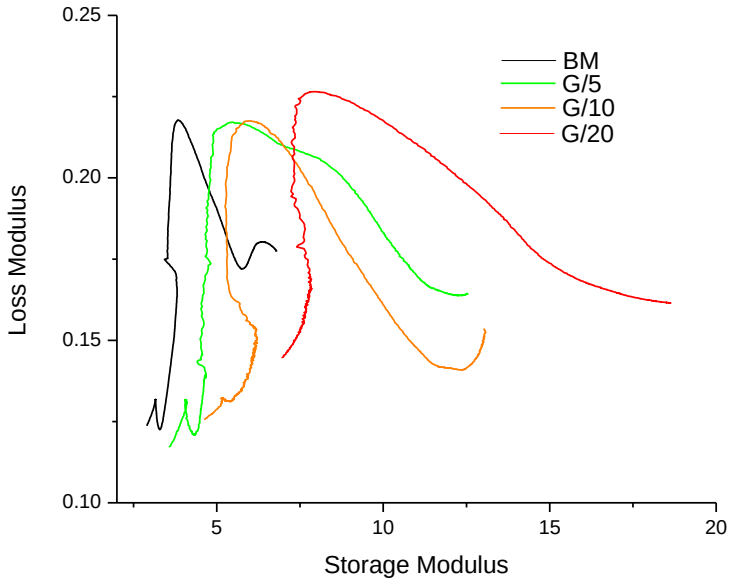

FIGURE 3.49 COLE-COLE PLOT OF BASIC MIX AND G/X SAMPLES

3.3. FLA

Thermal conductivity in function of temperature and graphite content for the G/x samples is presented in FIGURE 3.50.

Thermal conductivity of graphite: 110-190 W/(K.m) (158).

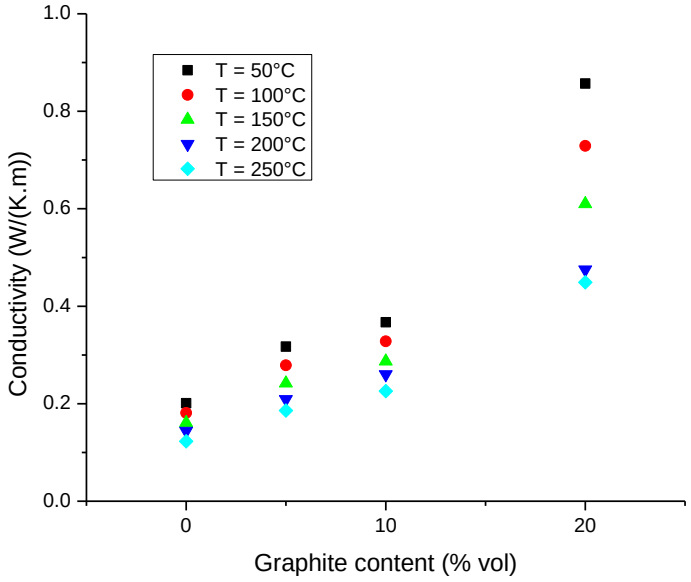

FIGURE 3.50 GRAPHIC OF THERMAL CONDUCTIVITY IN FUNCTION OF GRAPHITE CONTENT FOR G/X SAMPLES

Higher the graphite content higher is the conductivity, which is logical considering the excellent conductivity in the parallel direction of the sp^2 graphite particles plans, reported in literature equal to 1000 W/(K.m). There is a change in the curve slop between 10%vol and 20%vol, as thermal conductivity from 0.38 W/(K.m) reaches 0.89 W/(K.m): it could be the beginning of the percolation threshold sharp increase but, as explained before, during the press process the platelets get oriented alongside to the others. Thus, a much higher fillers content is required to reach the percolation threshold.

4. SILICON CARBIDE

4.1. DSC and TGA

DSC and TGA measurements have been performed on the thermally treated silicon carbide. As expected, in the temperature range of 30-970°C there is no weight loss and no reaction observed by the DSC curve; in fact silicon carbide is one of the most promising high-temperature structural materials resistant in harsh environment.

The results of the DSC measurements carried out on the SiC monocomponent composites are plotted in FIGURE 3.51, and the significant values are reported in TABLE 3.15.

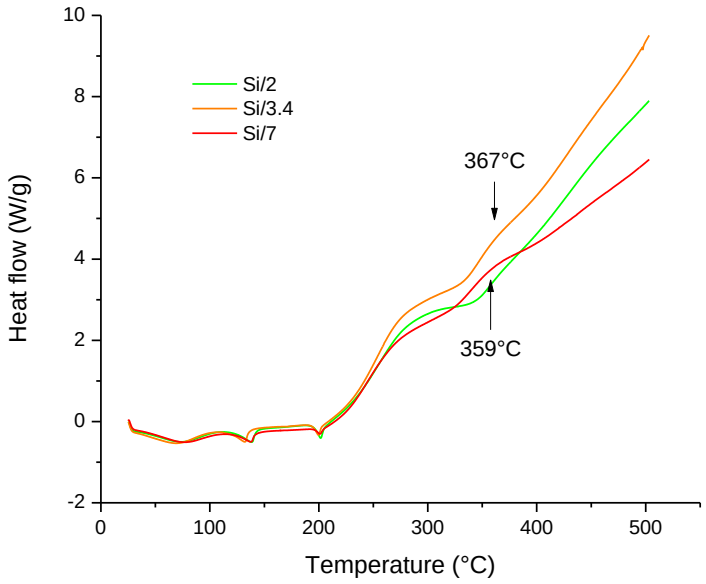

FIGURE 3.51 DSC MEASUREMENTS OF SI/X MIXES

TABLE 3.15 DSC VALUES FOR BM AND SI/X SAMPLES

Sample	Tg_1 temperature	T_{cross2}	Tg_2 temperature
BM	190°C	283°C	N.A
Si/2	195°C	279°C	N.A
Si/3.4	194°C	275°C	362°C
Si/7	195°C	274°C	363°C

T_{g1} temperature slightly increases, which could be sign of a good interaction matrix/fillers. The 2nd crosslinking reaction temperature decreases; as observed for other samples it may be due to a facilitated reaction happening during the DSC measurement itself. As for aluminum oxide based samples, a signal appears simultaneously to the oxidizing degradation of the basic mix (at 367°C and 359°C for respectively Si/3.4 and Si/7) and corresponds to the 2nd glass transition step of the phenolic chains network.

There is no particular observation to make about the TGA curves of the Si/x samples, as there is no weight loss observed for SiC on this temperature range.

4.2. DMTA

The DMTA measurements results for Si/x samples are presented in FIGURE 3.52 and the significant values are reported in TABLE 3.16.

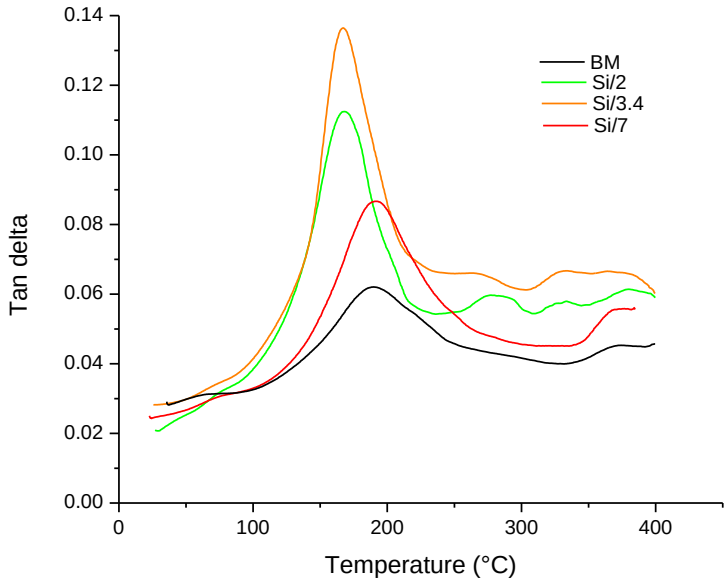

FIGURE 3.52 DMTA MEASUREMENTS FOR SAMPLES BM, SI/2, SI/3.4 AND SI/7

TABLE 3.16 GLASS TRANSITION AND DAMPING VALUES FOR BM AND SI/X SAMPLES

Sample	BM	Si/2	Si/3.4	Si/7
1st Tg temperature	190°C	168°C	167°C	190°C
1st Tg damping amplitude	0.028	0.079	0.094	0.052
2nd Tg temperature	375°C	380°C	365°C	≈376°C
2nd crosslinking step	N.A	277°C	263°C	N.A

Tg_1 temperature values of the composites are lower than for the basic mix, but for the most concentrated sample Si/7 the behavior appears very different and the T_{g1} temperature value is equal to the basic mix one. It could be the sign of a bad dispersion quality. Considering mixes Si/2 and Si/3.4, SiC particles clearly hinder polymer-chain growth and crosslinking. As conclusion, SiC is considered as plasticizer, as it is reported in literature (97). The tan δ intensity peak values of the composites are higher for Si/x mixes in respect of the basic mix, as the tan δ values in the rubbery phase. It should be noticed, however, that the width of tan δ Tg_1 peak increases with the SiC content, proof of heterogeneity gain in the material.

4.3. FLA

FLA results for SiC monocomponent samples are presented in FIGURE 3.53.

Thermal conductivity of silicon carbide: 63 W/(m.K) as specified by supplier, as the SiC thermal conductivity depends a lot on the synthesis process and geometry (159).

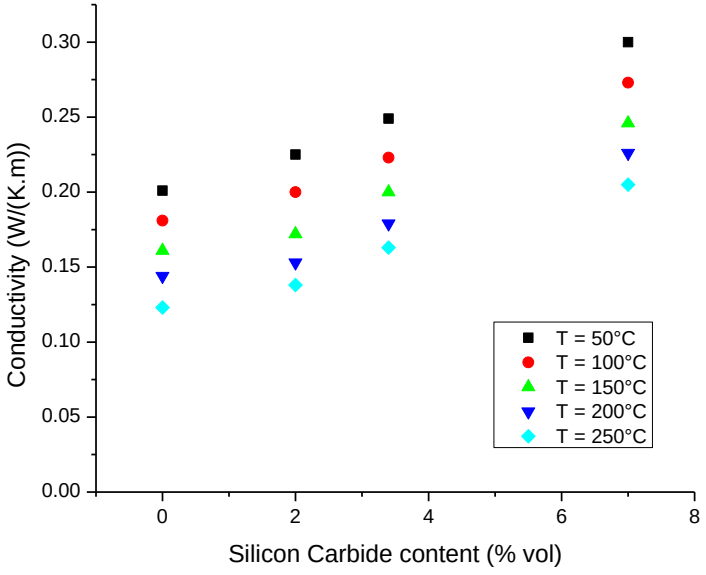

FIGURE 3.53 GRAPHIC OF THERMAL CONDUCTIVITY IN FUNCTION OF SILICON CARBIDE CONTENT FOR SI/X SAMPLES

The thermal conductivity of the composites varies linearly with SiC volume fraction in the range 0-7%vol. Since the large volume fraction of phenolic resin plays a leading role, and the thermal conductivity of the basic mix is poor (0.12-0.20 $W/K^{-1}m^{-1}$ in temperature range 50-250°C), the heat transfer is hindered in the material. With the continuous increase of SiC volume fraction, the thermal conductivity of the fabricated composites has a little change from 0.20 to 0.32 at 50°C in the SiC content range [0-7%vol]. In fact with the increase of SiC volume fraction, the thermal conductivity of the fabricated composites showed growth trend, for little effects on the heat transfer performance. As example, Cong Wu et al (160) show that for SiC particles of 50 µm around (nearly ten times bigger than the particles used in this study), a peak of thermal conductivity is reached when the SiC content is equal 40%vol, corresponding to the percolation threshold.

CONCLUSION

In this chapter the thermal stability of each singular filler has been investigated through different techniques as DSC, TGA, DMTA and FLA, as the corresponding monocomponent samples. The study allows to divide the fillers into two categories, based on the bonding they develop with the phenol formaldehyde resin. This separation relied on the polymer glass transition temperature value. In fact, the bonding between a filler and the resin in which it is dispersed is "measurable" considering the necessary energy to permit to the polymeric chains to move from glassy state to rubber state.

The first family of fillers developing interaction with the resin consists of steel fibres, friction dust, petroleum coke and aluminum oxide. For steel fibre an interaction appears in the fact that the degradation of the organic part in the mix is limited: the higher the steel fibre content, the higher the thermal stability of the material. For this filler, the good interaction resin/filler is confirmed by the Cole-cole plot. For friction dust, FT-IR spectroscopy was used to confirm the polymerization reaction of resin and cardanol, insuring a perfect interaction. For petroleum coke, the intermediate content presents major thermal stability due to interaction at the matrix/filler interface (enough contacts between resin and fillers but not excessive filler content which leads to their aggregation and a general loss of the properties). Otherwise, the thermal conductivity measurements evidenced a percolation value at 20%vol. The alumina monocomponent samples showed a strong Tg increase with alumina content and some theoretical models found in literature explain the thermal conductivity trend and confirm the excellent quality dispersion.

The second family of fillers corresponds to the ones which do not develop interaction with the matrix. Potassium hexatitanate fibres have shown a slight decrease in the glass transition temperature value, due to the fact that oligomers are less in contact with aramid fibres. The fillers act as plasticizers, inhibiting interaction inside the basic mix. The barium sulphate based materials present a lower Tg than the basic mix. At the highest content of fillers (equal to 70%vol) various relaxation mechanism associated with slippage of fillers occur, and the Tg peak is split, sign of the presence of two distinct phases in the polymer: the polymeric chains in bulk conformation and the segments in contact with the particles. For graphite composites, the glass transition temperature is

constant and not influenced by the filler presence; this non-interaction has been observed by FT-IR mapping and Cole-cole plot. About silicon carbide, its plasticizer role is verified, according to data reported in literature. SiC particles clearly hinder polymer-chain growth and crosslinking.

LIST OF FIGURES

LIST OF TABLES

CHAPTER IV

TRIBOLOGICAL PROPERTIES OF MONOCOMPONENT SAMPLES

INTRODUCTION

Wear and friction coefficient are more system responses than system properties (161). The main objective of tribology is to understand and minimize surface damage and wear. As reported by M. Atarian et al (162), briefly, wear mechanism may be classified into three classes: mechanical, chemical and thermal wear. In many cases, the difference and limit between two modes of wear is not clear and these phenomena occur simultaneously. For composites, special fillers are known to be able to improve the weak load-carrying capacity of neat polymers. Many studies have been performed to understand the interaction between these fillers, and predict in some way the tribological material properties of the resulting composites, but without success: there is no single answer because of the complexity of filler mechanisms and their reciprocal actions. In the composite industry, for instance, reinforcing fibres or lubricating fillers may be added to polymers to improve their tribological behaviors, e.g. lubricating fillers to lower the friction coefficient and surface energy in materials. In the case of friction materials, a transfer film, also called third body, is formed on the counterface surface with a consequent diminution of the friction coefficient. Reinforcing fillers, lubricants and fibres binded by a phenol formaldehyde resin are usually used to modulate the friction coefficient, surface energy and the strength of materials. Generally speaking, friction materials contain many ingredients and considerable research has been focused on the effects of each ingredient on improving friction performance (163). Some ceramic fillers such as aluminum oxide, silicon or titanium dioxide play important roles thanks to their high temperature and wear resistance (164) (165) (166).

As already written, tribological properties as wear and friction coefficient are the final and most important features for a friction material as a brake pad, and are largely determined by physical, mechanical and thermal properties. In this part, results of the

ball-on-disc tests are presented and explained based on the properties extensively described in the previous chapters. The studied samples are, as previously, the monocomponent based ones.

PREAMBLE - BASIC MIX TRIBOLOGICAL BEHAVIOR

Tribology tests are performed on the three basic mixes, which COF variations during the test are presented in FIGURE 4.1, and the corresponding specific wear rates are reported in TABLE 4.1.

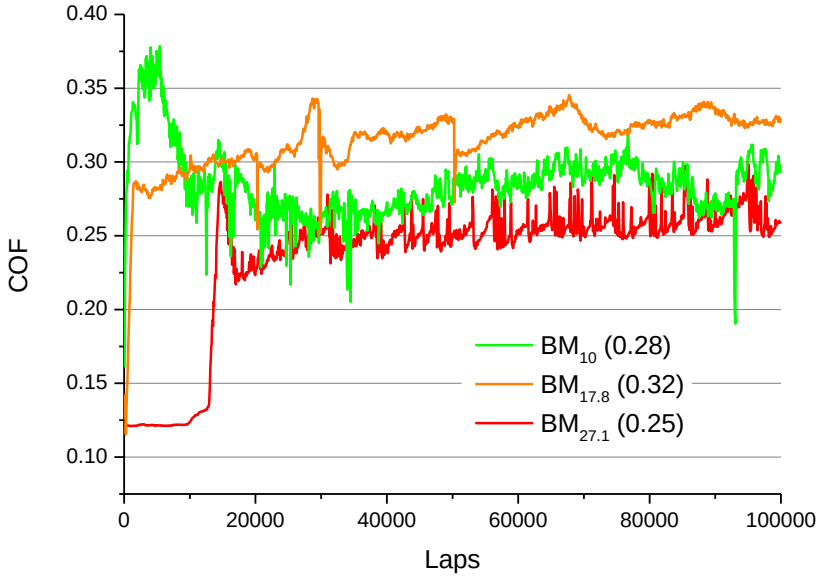

FIGURE 4.1 COEFFICIENT OF FRICTION IN FUNCTION OF THE NUMBER OF CYCLES, FOR SAMPLES BM_{10}, $BM_{17.8}$ AND $BM_{27.1}$. THE AVERAGE COF IS WRITTEN IN PARENTHESIS

TABLE 4.1 SPECIFIC WEAR RATE K FOR BM_x SAMPLES

Sample	BM_{10}	$BM_{17.8}$	$BM_{27.1}$
Aramid fibre content, %vol	10	17.8	27.1
K , x 10^4 $\mu m^3/Nm$	7.00	2.20	1.18

In general, at the beginning of a friction test, the change of the friction coefficient during sliding is due to the changes of the real contact area at the friction interface, the strength

of the binder resin, and the frictional properties of mixture components (36). The higher COF (0.32) is presented by the sample containing the intermediate aramid fibre content. It is reported by P. Cai (167) that fibrillary aramid fibre as the one used in this work may adhere better to the matrix comparing to a fibre or a particle shape, but the load-carrying capacity of microfibril might be low. This aspect implies that such kind of fibre could not protect the worn surface effectively by forming primary plateaus. This could explain the high standard deviation/vibration of the COF values for the three samples. Since the friction coefficient stability is essential, the best sample for this criterium is the one containing 17.8%vol. of fibres, result close to the 22.5%vol. found by S.J. Kim et al (38). It is known that the addition of aramid fibres greatly improves the friction performance (38). In a study conducted by P. Cai et al (167), for the free aramid fibres based specimen, the worn surface indicated that the material was peeled off from the matrix under flakes fragments; while in the aramid fibres based samples the fibres prevent the materials from being peeled off in flakes, and the materials were worn in the form of fine grains This observation indicates that the wear mechanism is deeply affected by the presence of aramid fibre. However, it is noteworthy that morphologies of the surface samples of the fibres reinforced friction materials are different with respect to the geometry of the aramid fibres. Indeed, any contact plateaus can be seen on the worn surface of the composite, as it is the case in the present study. This is because the fibrils constituting aramid pulp are embedded into the matrix and do not directly contribute to build up plateaus.

The wear results are presented in TABLE 4.1: thanks to the mechanical strength due to aramid pulp, wear resistance increase with pulp content.

As seen before in Chapter II *Preamble* section, hardness increases when aramid fibres content increases (36), so in agreement with Archard equation ($Wear \propto Hardness^{-1}$) we observe here a decrease of wear with respect to the filler concentration (also reported by M.H. Cho et al (73), when the main wear mechanism is the abrasive one). According to T. Kato et al (22), there is an optimum for an aramid content included in the range 25-35%vol, while for P. Cai et al (167) this value is equal to 10%vol. The motivation for avoiding higher percentages lies in an expected aggregation of the fibres that cannot be well-dispersed, thus causing an increase of the wear rate. In the present study, the

optimal aramid fibre content is taken equal the highest one studied (27.1%vol), according to the Kato findings, as the wear doesn't exhibit a sharp increase but conversely a continuous decrease.

In this preamble, the tribological characterization of basic mix is presented, and thanks to the well dispersed network formed by aramid pulp through the resin, the wear resistance of the three samples increases with the fibres content. Hence, the more concentrated material (at 27.1%vol) is taken as basis to form the other samples (called BM in the following). The eight other components are divided into two families: the ones increasing the wear resistance and the ones which don't.

I. FILLERS WITH ABILITY TO INCREASE THE WEAR RESISTANCE

1. FRICTION DUST

The COF evolution and the wear values obtained for the friction dust monocomponents are presented in FIGURE 4.2 and TABLE 4.2 respectively.

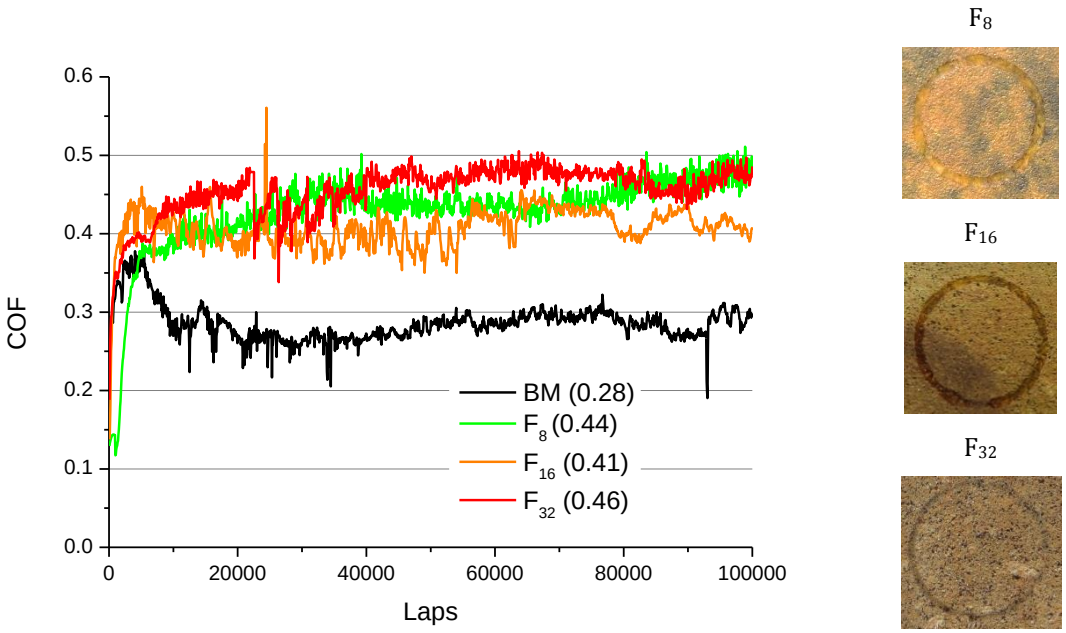

FIGURE 4.2 COEFFICIENT OF FRICTION IN FUNCTION OF THE NUMBER OF CYCLES, FOR BM AND SAMPLES F_8, F_{16} AND F_{32}

TABLE 4.2 WEAR FACTOR K FOR F_X SAMPLES

Sample	Basic Mix	F_8	F_{16}	F_{32}
Friction dust content, %vol	0	8	16	32
K, x10^4 µm^3/Nm	7.00	22.75	3.96	31.62

The samples containing friction dust present higher COF values with respect to BM in agreement with literature data (168). The COF curves for the three samples are all as irregular as the basic mix one. The F_{16} material mix (16%vol friction dust) has the lowest mean COF value.

Wear increases with friction dust content. It has been seen by J. Bijwe et al (169) that the worn surfaces of samples containing friction dust showed few secondary plateaus in the third body and a high level of deterioration in the filler/matrix bonding. The important debonding of additive particles to the matrix could be the main cause for the poor wear performance of these materials. Even if wear increases with friction dust presence, at 16%vol this phenomenon seems reduced as wear rate is even lower than the basic mix one. It could correspond to the optimal content: enough to be efficient but not too much to weaken the material. In fact, at low content, there is few surface contact between filler and matrix, so the positive interaction studied in chapter III section I.4 is not exploited; while at high content the cardanol and derivates lead to a network density decrease and weaken the material. This hypothesis is supported by the stiffness value of 3.39 GPa of F/32, while BM value is equal to 6.01 GPa.

As reported in literature (93), the best performances correspond to the intermediate formulation, with 16%vol of friction dust. For this sample the wear resistance is increased compared to BM.

2. GRAPHITE

Graphite, as most of the solids, consists of polycrystals formed by adjacent crystallites separated by boundaries, and defined as an uniform yet finite space. During sliding against another material, the contact with the latter breaks when the crystallite boundaries and other structure defects are hit. The work of the friction force is spent on the breakage of adhesive bonds on the friction surface and cohesive bonds beneath the

friction surface in the zone of maximum tangential stresses. Therefore for friction on graphite based materials two processes separated in space take place (170).

Tribology results for graphite monocomponent samples are reported in FIGURE 4.3 (COF variations) and TABLE 4.3 (specific wear rate).

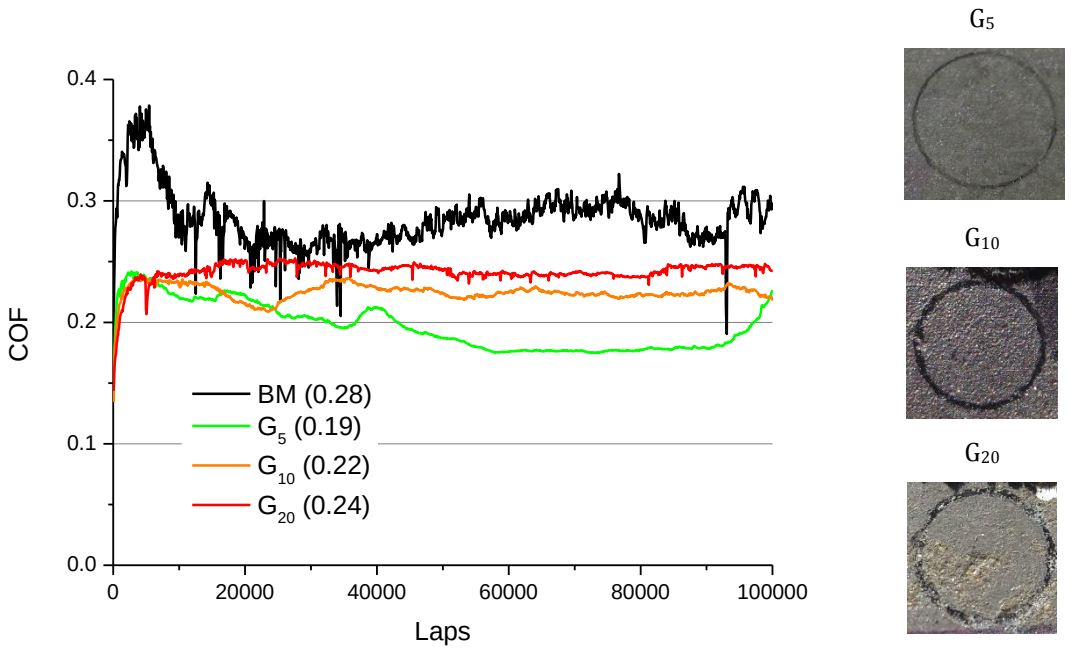

FIGURE 4.3 COEFFICIENT OF FRICTION IN FUNCTION OF THE NUMBER OF CYCLES, FOR BM AND G_x SAMPLES

TABLE 4.3 SPECIFIC WEAR RATE K FOR F SAMPLES

Sample	BM	G_5	G_{10}	G_{20}
Graphite content, %vol	0	5	10	20
K, x10^4 µm^3/Nm	7.00	0.09	0.41	1.03

Graphite addition to the basic mix induces low COF values: as it is largely reported in literature (171) (172) graphite has a strong lubricating action since it is able to form a self-sustaining lubricant layer (173). G_5 sample has the lowest mean COF value, slightly irregular in the first half of the test: considering the low graphite content, more time is required to create and maintain the friction film. Osterle et al. (174) performed a pin-on-disc test on graphite powder only and evidenced that it tooks a long time to form the third body layer because of the high grain size of the original graphite particle (around 40 µm) that is grinded into finer particles. There is a running-in period during which the

COF decreases until its final low and stable value. Besides, to join Osterle's work and the present study, it has to be mentioned the similarity between the stabilized COF obtained for a powder test and a friction material containing 50%vol of graphite: the created film is assumed to be similar considering the high graphite content, so the final stabilized COF value is equal in both cases (175). Then, G_{10} and G_{20} samples exhibit higher COF values and the wear track gets bigger and more irregular. So more the graphite dispersed in the material, higher the COF. It should partly be because of graphite aggregates formation inside the matrix: beyond a certain value, graphite is not dispersed homogeneously and leads to opposite effects as aggregates are pulled out from the surface and the contact surface is more irregular.

The hypothesized lack of cohesion is in agreement with the increase of the specific wear rate with the graphite concentration. The loss of friction properties with graphite increasing content from 5 to 20%vol could be also due to microcracks propagation which occurs more easily in high graphite content composites (176). Therefore, wear due to pull out of the grains phenomenon takes place and debris are generated in large extent as the cracks grow to connect with the surface. On the worn surface irregular cavities and microcracks perpendicular to the sliding direction are present ; a cavity may be the original location of a graphite particle that get ejected from the surface as the closed materials delaminate as shown in FIGURE 4.4. The delamination phenomenon not only reduces the wear resistance of the composites, but also leads to a higher friction coefficient.

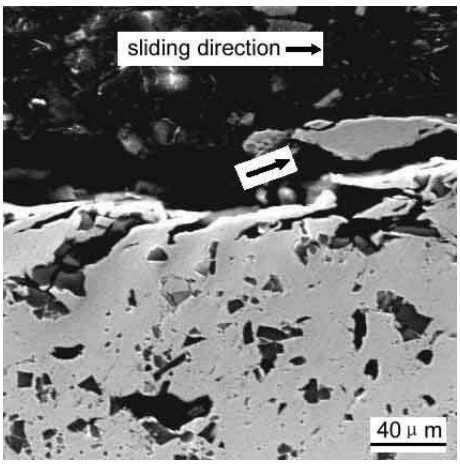

FIGURE 4.4 SEM PICTURE ILLUSTRATING DELAMINATION PROCESS (176)

In literature a concentration of 10%vol of graphite is recognized to bring the best performances (73). G_5 sample seems to be the more efficient composition in our case especially in accordance with the tribological performances.

3. STEEL FIBRES

Friction coefficient variations and wear results obtained for steel fibres based monocomponent samples are presented in FIGURE 4.5 and TABLE 4.4 respectively.

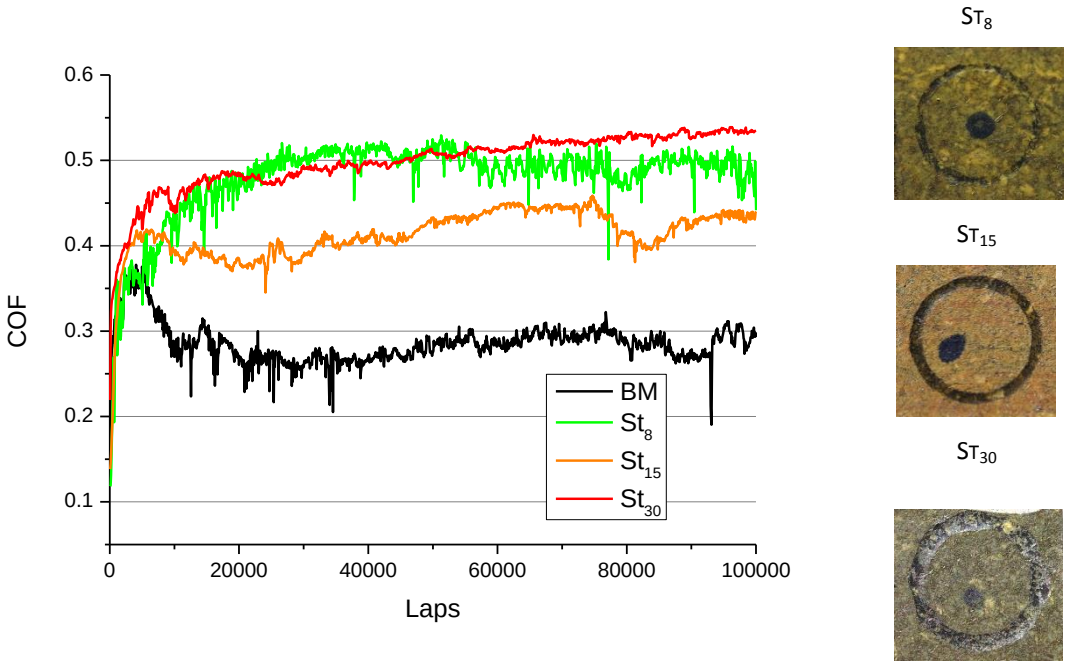

FIGURE 4.5 COEFFICIENT OF FRICTION IN FUNCTION OF THE NUMBER OF CYCLES, FOR BM, ST_8, ST_{15} AND ST_{30}

TABLE 4.4 SPECIFIC WEAR RATE K FOR BM AND ST_x SAMPLES

Sample	BM	St_8	St_{15}	St_{30}
Steel fibre content, %vol	0	8	15	30
K, $x10^4$ $\mu m^3/Nm$	7.00	10.92	5.75	7.48

Friction coefficient values are higher for St_x samples than for the basic mix: steel fibres present an abrasive behavior. The lowest and the highest concentrated samples in steel fibres present a medium COF value of 0.5, while the intermediate material St_{15} exhibits a medium value of around 0.42. This first observation could be the sign of an optimal

content at 15%vol. The COF curve is more stable when steel fibres are present in the material, and higher the steel content more stable the COF. Metallic fibres in general are the main actors of the transfer layer formation, insuring a stable and continuous friction behavior of the braking system (177). In fact fibres protrude from the material surface and the formed wear debris can cluster against them acting as retention zones. These zones constitute primary zones of contact; their existence allow the mechanical formation of more extended and compacted zones made by sintered debris (see FIGURE 4.6). In the work of Eriksson et al (178), friction layers are discontinuous and comprise primary and secondary contact patches called 'plateaus'; while Godet called them "screens" (179).

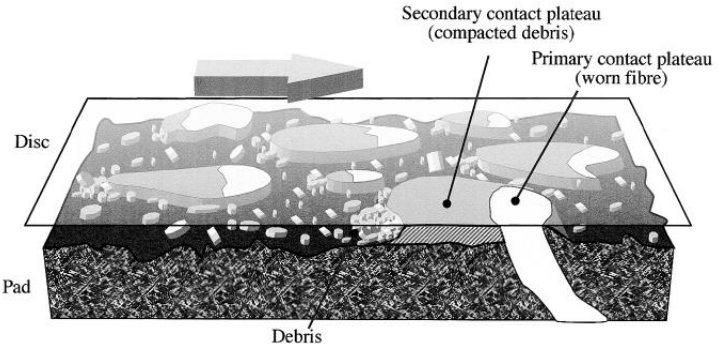

FIGURE 4.6 CONTACT SITUATION BETWEEN THE COUNTERFACES CONSTITUTING A BRAKE SYSTEM, INVOLVING CONTACT PLATEAUS WITH PRIMARY (LIGHTER) AND SECONDARY PLATEAUS, AND A FLOW OF PILED UP DEBRIS. A STEEL FIBRE ALLOWS THE FORMATION OF A STABLE PRIMARY PLATEAU AND A SECONDARY PLATEAU FORMED IN FRONT OF THE FIBRE. THE FRICTIONAL ENERGY HELPS TO COMPACT AND SINTER THE DEBRIS FORMING THE SECONDARY PLATEAUS (177)

Following the conclusion of R. Vijay et al (130), a wear decrease in function of steel fibres content is expected, as the steel wool presence leads to more efficient dissipation of frictional heat. The higher the dissipation, the lower the surface temperature and hence the lower the degradation of the organic components in the composites, which hence helped to maintain a stable and consistent friction level. In the present case, a lower wear, associable to a lower degradation, is observed for the sample with the intermediate concentration. Studying glass fibres based materials, G. Crosa et al (18) conclude that they can break during testing and generate wear debris. These debris increase the ploughing action and so increase the friction coefficient, having a bad consequence on the amount of wear. Steel fibres don't get broken, but tend to lift off, increasing the angle

formed with the rotor disc surface, increasing the ploughing action. Thus, it is logical to observe friction coefficient and wear increase by increasing steel fibres content.

As a conclusion, the action of the steel wool is of primary importance for the third body layer formation, and it also strengthens the composite body. More content of steel wool causes more fibres to appear on the friction surface, increasing the true contact area between the fibres and the rotor disk, then enhancing the friction coefficient (180). Steel wool has a relatively high resistance to sliding wear against the disc. Thus, after a short running-in period, the metal fibres stand slightly higher than less wear resistant constituents, forming the heart of the contact plateaus (181). Therefore, due to the softer components filling the friction material volume, the contact situation is dominated by metal-to-metal contact. In literature the best composition is reported to be St_{15} (15%vol steel fibre), according to the present results: it presents intermediate behavior and the better properties compromise.

4. ALUMINUM OXIDE

Results of tribology tests performed on alumina monocomponent samples are presented in FIGURE 4.7 for COF variations and in TABLE 4.5 for wear data.

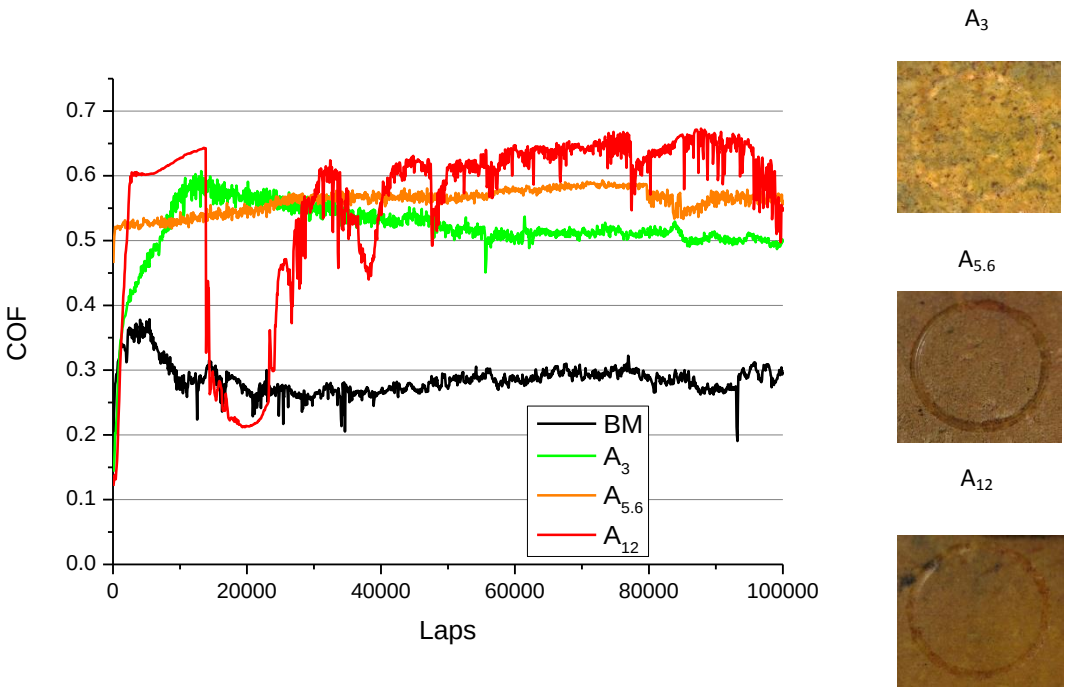

FIGURE 4.7 COEFFICIENT OF FRICTION IN RESPECT OF THE NUMBER OF CYCLES, FOR BM AND A_x MIXES SAMPLES

TABLE 4.5 SPECIFIC WEAR RATE K FOR BM AND A_x SAMPLES

Sample	BM	A_3	$A_{5.6}$	A_{12}
Aluminum oxide content, %vol	0	3	5.6	12
K, x10^4 µm^3/Nm	7.00	4.62	4.88	1.42

As it is well known, aluminum oxide acts as an abrasive: higher the aluminum oxide content higher the mean friction coefficient value. A_3 and $A_{5.6}$ samples have regular COF curves while A_{12} sample performance is very irregular and the tribological track let on the surface presents waved delimitations. It confirms what V. Tomasek et al (77) wrote in their article: the friction stability is optimal for an aluminum oxide content close to 6%vol.

The wear factor K is lower for all the A_x samples with respect to the reference basic mix sample, indicating a higher wear resistance. A_3 and $A_{5.6}$ samples present similar results, while A_{12} shows the half of their values. Here again the obtained results are in agreement with the study of V. Tomasek (77) for whom wear is minimal for an alumina content superior to 3%vol (friction material tested against cast iron disc). In fact, in the present study, the aluminum oxide sphere (the tribometer ball) gets in contact with the aluminum oxide particles dispersed on the material and doesn't create wear against itself. Literature indicates as better composition the one corresponding to $A_{5.6}$. The performed tests do not permit to rank the samples: $A_{5.6}$ has the better friction coefficient curve but it is important to follow the common filler contents typically used in a brake pad formula, besides A_{12} sample exhibits a too high friction coefficient value and too strong vibrations. As a result $A_{5.6}$ alumina content is retained to carry on the study.

In this first part about tribological measurements on monocomponent samples, it has been studied the positive influence that graphite, steel fibres, aluminum oxide and friction dust demonstrate when dispersed in the matrix at a precise content (the concentration then held to form the more complex samples). The second part hereinbelow present the results obtained for the other four fillers, which demonstrates a null or negative influence on the monocomponent material wear.

II. FILLERS WITHOUT OR WITH NEGATIVE INFLUENCE ON WEAR

1. POTASSIUM HEXATITANATE FIBRES

Tribology test results for potassium hexatitanate monocomponents Ti_{10}, Ti_{20} and Ti_{50} are presented in FIGURE 4.8 and TABLE 4.6.

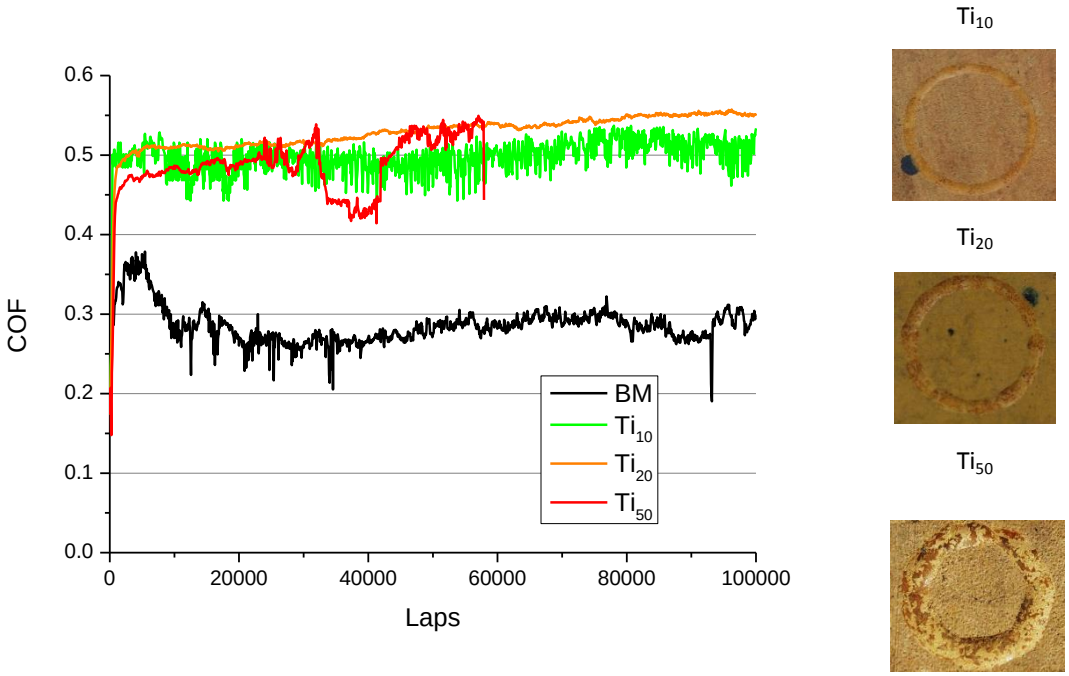

FIGURE 4.8 COEFFICIENT OF FRICTION IN FUNCTION OF THE NUMBER OF CYCLES, FOR BM AND SAMPLES MIX Ti_{10}, Ti_{20} AND Ti_{50}

TABLE 4.6 SPECIFIC WEAR RATE K FOR Ti_x SAMPLES

Sample	BM	Ti_{10}	Ti_{20}	Ti_{50}
Potassium hexatitanate fibre content, %vol	0	10	20	50
K, $x10^4$ $\mu m^3/Nm$	7.00	11.00	9.66	30.84

Potassium hexatitanate increases the coefficient of friction, so it presents an abrasive behaviour. Ti_{10} sample (10%vol hexatitanate potassium) presents a very irregular COF (standard deviation of 0.019); while Ti_{20} sample continuously increases and the Ti_{50} mix

gives a very irregular curve. In fact in SEM pictures (see FIGURE 4.9) a percolation threshold is perceived between the Ti_{20} and the Ti_{50} sample fibres concentration.

(a) (b) (c)

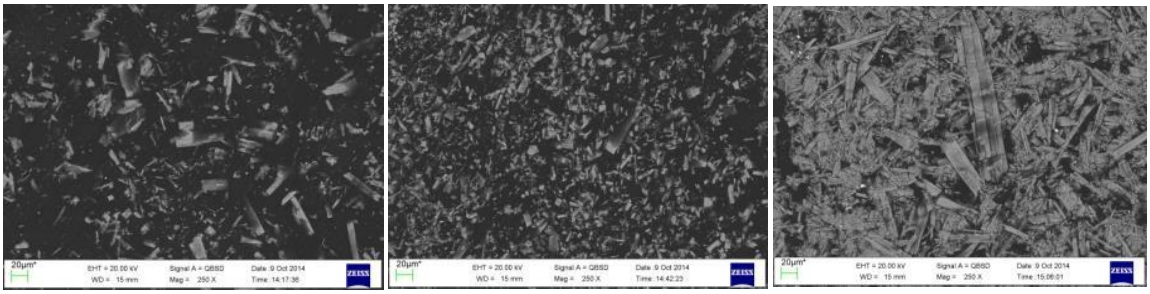

FIGURE 4.9 SEM PICTURES OF MIXES (A) TI_{10}, (B) TI_{20} AND (C) TI_{50} AT 250X USING BACKSCATTERED ELECTRON ANALYSIS (BS)

The wear increases with potassium hexatitanate fibres content, and as presented in FIGURE 4.8, this phenomenon is associated with a high COF level. Then, for 50%vol of filler the tribological track depth and area are very high, the material gets friable and visibly degrades, probably due to the too low resin content. The potassium hexatitanate shape determines the tribological properties of the material. As explained by K. H. Cho et al. (47), the splinter shape of potassium hexatitanate helps to form contact plateaus which offset the polymer degradation, so at 20%vol (reference content in this article) the wear is divided by two with respect to whiskers or platelets potassium hexatitanate one. It has been demonstrated by S. J. Kim et al (38) that aramid pulp and potassium hexatitanate fibres develop beneficial synergistic effect, in particular due to their contribution to the transfer film formation (layer of compacted wear particles) at the friction surface.

The literature indicates as the best the Ti_{20} and Ti_{50} compositions; considering the results obtained during this study the best sample seems to be Ti_{20}, the intermediate one.

2. BARIUM SULPHATE

Tribology test results are presented in FIGURE 4.10 and TABLE 4.7 respectively for friction coefficient variations and wear data of barite monocomponent materials.

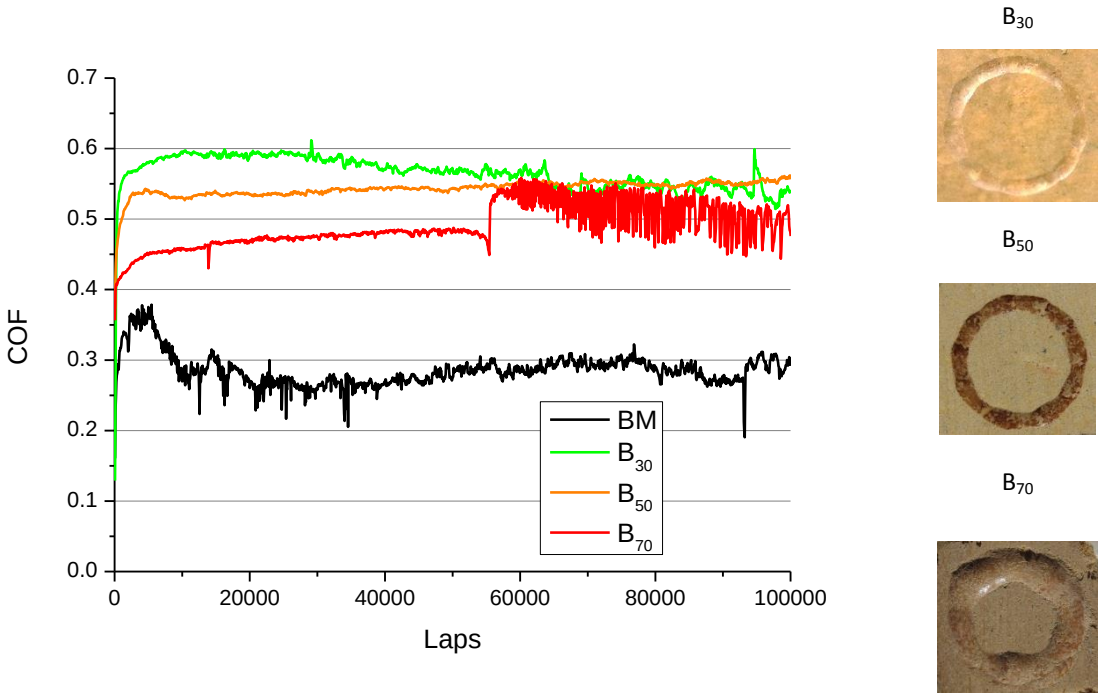

FIGURE 4.10 COEFFICIENT OF FRICTION IN FUNCTION OF THE NUMBER OF CYCLES, FOR BM, B_{30}, B_{50} AND B_{70} SAMPLES

TABLE 4.7 SPECIFIC WEAR RATE K FOR B_x SAMPLES

Sample	BM	B_{30}	B_{50}	B_{70}
Barium sulphate content, %vol	0	30	50	70
K, x10^4 µm^3/Nm	7.00	8.48	12.32	48.12

Friction coefficient values are higher when barium sulphate is dispersed in the sample but its value decreases from B_{30} to B_{70} (respectively from 0.56 to 0.49). The COF is particularly stable for B_{50} sample. Once again B_{70} sample exhibits too anarchic results to be taken in account: considering the COF curve variation and the strong irregularity of the track design, it is possible to hypothesize the pull out of barite grains from a wide area during friction and the successive high vibration in the contact ball/surface sample.

Wear increases with barium sulphate addition; as explained by S.J. Kim (62) barite particles are easily ejected from the matrix and undergo rolling and scratching at the contact with the counterface during sliding, that leads to a poor wear resistance.

3. SILICON CARBIDE

Tribology tests have been performed on the Si_x samples, containing silicon carbide: the COF variations is shown in FIGURE 4.11, while the wear data are reported in TABLE 4.8.

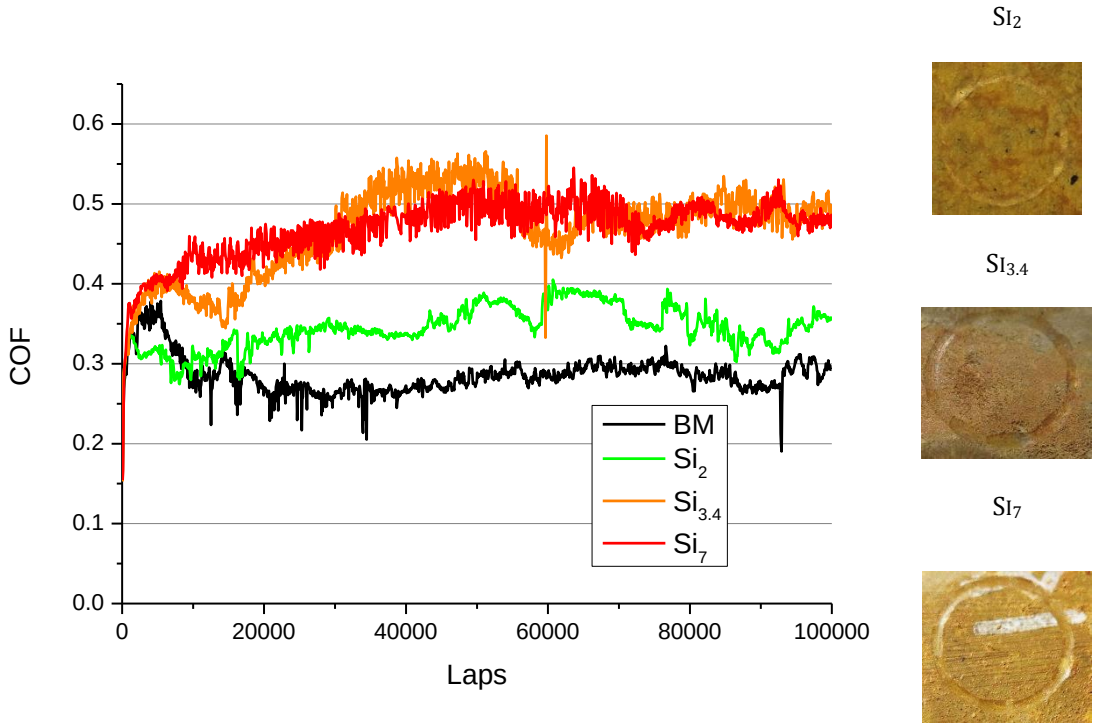

FIGURE 4.11 COEFFICIENT OF FRICTION IN FUNCTION OF THE NUMBER OF CYCLES, FOR BM AND Si_x MIXES SAMPLES

TABLE 4.8 SPECIFIC WEAR RATE K FOR Si_x SAMPLES

Sample	BM	Si_2	$Si_{3.4}$	Si_7
Silicon carbide content, %vol	0	2	3.4	7
K, $x10^4$ $\mu m^3/Nm$	7.00	31.72	15.83	24.66

The three samples present a higher COF than the basic mix one, so silicon carbide presents an abrasive action, as expected and COF curves are irregular. The one much more different from the others is the Si_2 one with the lowest COF mean value and a major friction stability; $Si_{3.4}$ and Si_7 are very similar and both vibrate a lot. At naked eye the three track designs are similar.

Higher wear rates with SiC presence with respect to the basic mix one are found. The addition of 2%vol of SiC leads to higher mechanical properties (6.56 GPa of stiffness against 6.01 GPa for basic mix and a hardness of 122.3 HRS against 11.7 HRS for basic mix, as presented in chapter II section I.4) so a first wear increase can be expected, due to the embrittlement of the material. Afterwards, wear rate as well as physical properties significantly decrease for a SiC content of 3.4%vol, which corresponds to the transition between abrasive and adhesive wear mechanisms. Then, as studied by J. Abenojar et al (97) increasing SiC content, the adhesive wear becomes the dominating wear mechanism so at 12%vol of fillers the wear rate is particularly high. Furthermore, the existence of the third body (from detached SiC particles) favors abrasive wear. Unbonded particles can act as a third-body agent and as centres of stress accumulation (see FIGURE 4.12).

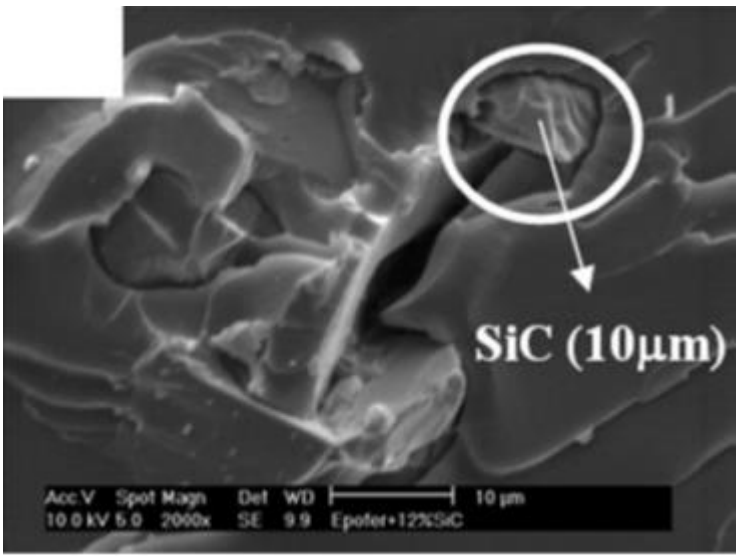

FIGURE 4.12 FRACTURE SURFACE BY SEM: DETAIL EPOXY + 12%VOL SIC 10 µM (97)

Following these observations it is expected to have a wear increase beyond 6%vol (see TABLE 4.8).

$Si_{3.4}$ is the sample which presents the littler track depth, so the best wear resistance, then come Si_7 and Si_2 samples. This result is in agreement with what has been found in literature: according to V. Matejka et al (79), a silicon carbide content of 3.4%vol gives the best wear resistance of the material.

4. PETROLEUM COKE

The results of tribology tests obtained for petroleum coke containing samples are presented in FIGURE 4.13 for COF data and TABLE 4.9 for wear data.

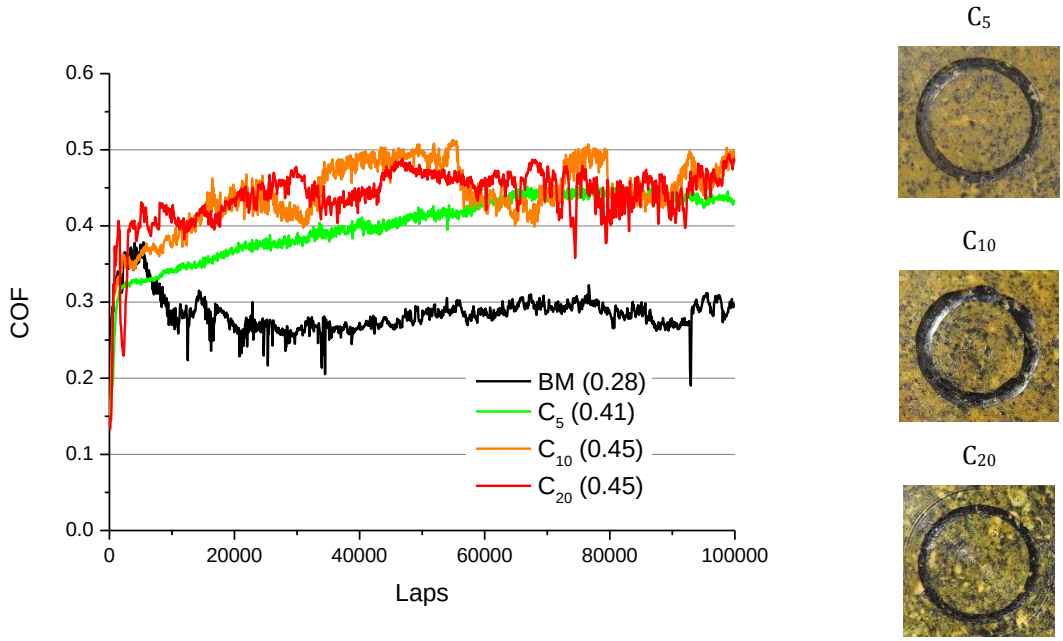

FIGURE 4.13 COEFFICIENT OF FRICTION IN FUNCTION OF THE NUMBER OF CYCLES, FOR BM AND C_X MIXES SAMPLES

TABLE 4.9 SPECIFIC WEAR RATE K FOR BM AND C_X SAMPLES

Sample	BM	C_5	C_{10}	C_{20}
Coke content, %vol	0	5	10	20
K, x10^4 µm^3/Nm	7.00	3.92	10.58	2.14

All the petroleum coke monocomponent based samples exhibit a higher friction coefficient than the basic mix, so the coke presents an abrasive behavior. C_5 sample exhibits a relatively regular COF value but it continually increases until it gets stabilized after 65 000 laps around, while C_{10} and C_{20} samples curves show high vibrations with higher and lower segments. This could be due to periods of destruction followed by periods of reconstruction of the friction layer. The COF value fluctuates a lot for the three samples, as already noticed by G. Yi et al. (95).

C_{10} sample presents the lower wear resistance, then comes C_5 sample and finally C_{20}. There is a discontinuity of these values with respect to petroleum coke content in the material. Considering both friction coefficient measurements and wear test, C_5 is the most efficient sample. G. Yi et al (95) explained that a non-uniform and patchy transferred film is created on the cast iron disc surface sliding against the friction material. This suggests that little part of composite was transferred from the friction composite onto the rubbing cast iron surface to form the third body layer, and that's why together with the continuous construction and destruction of the third body layer irregular tribological results are obtained.

CONCLUSION

In this chapter a detailed analysis of the tribological features of the monocomponent samples has been carried out.

The friction dust exhibits an abrasive behavior as its presence in the basic mix increases the friction coefficient value; only for the intermediate content of 16%vol the wear resistance is increased, then this concentration is held to proceed with the more complex systems. The graphite filler presents a strong lubricant action due to its ability to form a self-sustaining lubricant layer on the friction surface. The best sample is the lowest concentrated, since for higher content cracks, aggregation and delamination occur. Steel fibres present an abrasive behavior, nevertheless they stabilize the friction coefficient as they have a primordial role in the transfer layer formation: they are the base of the first and second plateaus, from which the transfer layer can grow. Alumina exhibits an abrasive behavior as largely reported in literature. Its presence in the mix preserves the material as wear value is much lower than the basic mix one. The presence of the potassium hexatitanate fibres in the bulk leads to an increase of wear and friction coefficient, partially due to the loss of cohesion because of the low resin content. The composite containing barium sulphate presents an abrasive behavior, induces a wear deterioration except for the intermediate concentration of 50%vol. Silicon carbide, which is a strong abrasive, implies higher friction coefficient and wear, whose main mechanism passes from abrasive to adhesive. The petroleum coke presents an abrasive behavior and the corresponding monocomponent samples exhibit irregular tribological performances, due to patchy transfer layer zones.

LIST OF FIGURES

LIST OF TABLES

CHAPTER V

TRIBOLOGICAL PROPERTIES OF MULTIPLE SAMPLES: ROLE OF CHEMICO-PHYSICAL CHARACTERISTICS

INTRODUCTION

After the chapter about monocomponent samples tribological characterization, it is essential to keep on this work with the multi-components samples study. With this aim in mind, firstly fillers presenting similar effect on wear or, at the opposite, antagonist effect on wear are dispersed together in the same material in order to see how they interact and which are the resulting tribological properties. Then the intermediate steps are done between bicomponent materials towards the full system formulation with the samples at three and four ingredients. A division is done between the samples containing graphite and the one containing steel fibres, as it has been demonstrated in the previous chapter that they both have a great importance in the third body formation and composition. Graphite is able to form a self-sustaining lubricating film which is perpetually consumed and renewed; while steel fibres promote the formation of plateaus from wear debris generated during friction.

I - FROM MONO TO BICOMPONENT SYSTEMS

1. COMPONENTS WITH SIMILAR EFFECT ON WEAR

1.1. Components increasing wear resistance

1.1.1. Friction dust + aluminum oxide (F/16-A/5.6 → F-A)

The chemical formulation of F-A mix is presented in TABLE 5.1.

TABLE 5.1 F-A SAMPLE COMPOSITION

	Resin	Aramid fibre	Friction dust	Aluminum oxide	Sum
Content, in %vol	57.2	21.2	16	5.6	100
Content, in %wt	49.6	21.3	13.7	15.4	100

Tribology tests have been performed on the F-A sample, and the results as COF variations and wear data are compared to the monocomponent ones (see FIGURE 5.1 and TABLE 5.2).

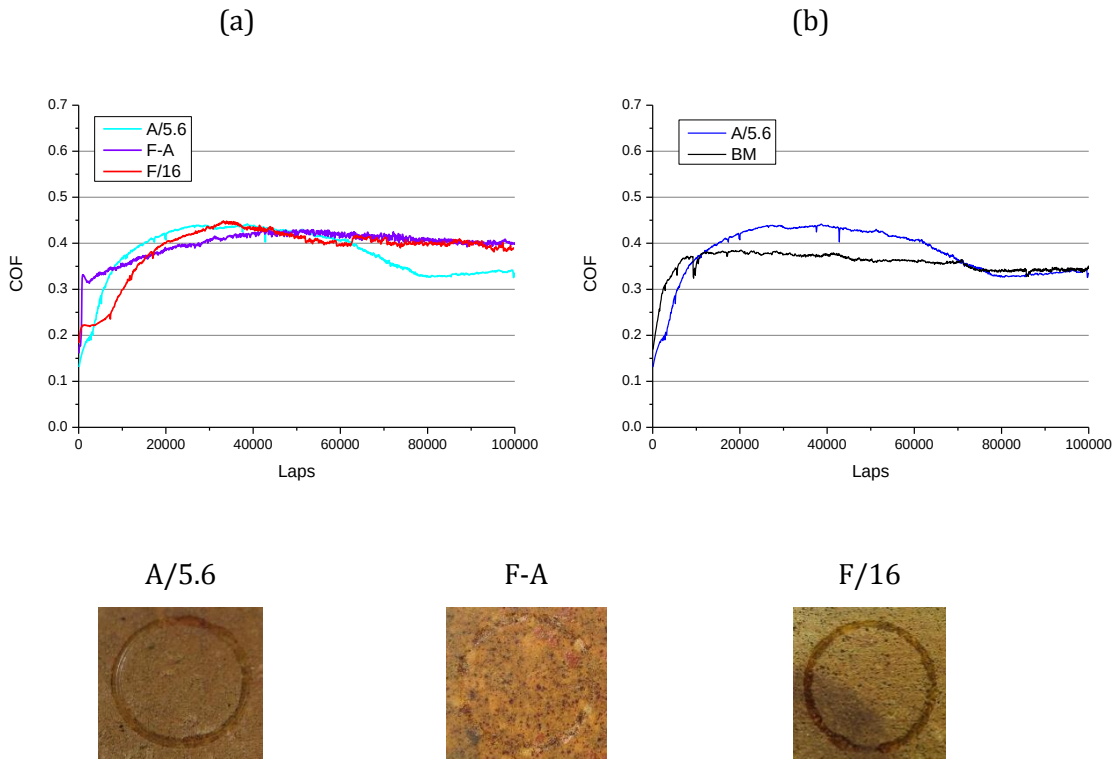

FIGURE 5.1 COF VARIATIONS OF (A) A/5.6 (5.6%VOL ALUMINUM OXIDE), F/16 (16%VOL FRICTION DUST) AND F-A (16%VOL FRICTION DUST-5.6%VOL ALUMINUM OXIDE) SAMPLES; (B) A/5.6 AND BM (BASIC MIX) SAMPLES

TABLE 5.2 SPECIFIC WEAR RATE K VALUES FOR F/16 (16%VOL FRICTION DUST), F-A (16%VOL FRICTION DUST-5.6%VOL ALUMINUM OXIDE) AND A/5.6 (5.6%VOL ALUMINUM OXIDE) SAMPLES

Sample	F/16	F-A	A/5.6
K, $x10^4$ $\mu m^3/Nm$	3.47	3.19	2.76

As presented in TABLE 5.2**,** the wear values observed for monocomponent samples F/16 and A/5.6 (respectively containing friction dust and alumina) are very similar, so as the one of F-A sample (16%vol friction dust - 5.6%vol aluminum oxide) as well as the tracks designs. The tribological features of this bicomponent mix are intermediate to the binary mixes ones. As visible in FIGURE 5.1, both monocomponent COF curves start at around 0.2 and increase gradually to a maximum at around 35 000 laps and then decrease; while bicomponent sample has a higher initial COF value of 0.32 and increases slower to finally get stabilized at 40 000 laps. This initial increase until a stable value corresponds to the bedding process: it is linked with the transfer of an even layer of brake pad material onto the counterface (in general the brake rotor and in this case the aluminum oxide ball), the third body.

The A/5.6 sample presents in the second half of the test a decrease and then a stabilization, as presented in FIGURE 5.1b at the basic mix level: it means that in some way, aluminum oxide disappears from the surface or at least the particles get covered up by in situ liquefied and spread resin due to the local temperature increase.

It can be concluded that there is no particular interaction between friction dust and aluminum oxide developed in this material, as the tribological performances, as well as the other characteristics as stiffness, hardness and absence of porosity (see in TABLE 5.3) are similar to the monocomponents ones.

TABLE 5.3 DENSITY, STIFFNESS, HARDNESS VALUES FOR F/16 (16%VOL FRICTION DUST), A/5.6 (5.6%VOL ALUMINUM OXIDE) AND F-A (16%VOL FRICTION DUST-5.6%VOL ALUMINUM OXIDE) SAMPLES

Sample	F/16	A/5.6	F-A
Friction dust content, %vol	16	0	16
Aluminum oxide content, %vol	0	5.6	5.6
Density, g/cm^3	1.26±0.03	1.46±0.05	1.41±0.01
Theoretical density, g/cm^3	1.24	1.42	1.41
Stiffness, GPa	4.28±0.17	6.48±0.29	6.43±0.17
Hardness, H-RS	116.8 ± 4.2	121.7 ± 1.53	120.0 ± 0.6

1.1.2. Steel fibres + friction dust (St/15-F/16 → St-F)

The chemical formulation of St-F mix is presented in TABLE 5.4.

TABLE 5.4 ST-F SAMPLE COMPOSITION

	Resin	Aramid fibre	Steel fibre	Friction dust	Sum
Content, in %vol	50.3	18.7	15	16	100
Content, in %wt	23.8	10.2	52.3	13.7	100

The tribology test results for St-F sample and the corresponding monocomponent materials St/15 and F/16 are presented in FIGURE 5.2 for COF curves and TABLE 5.5 for wear data.

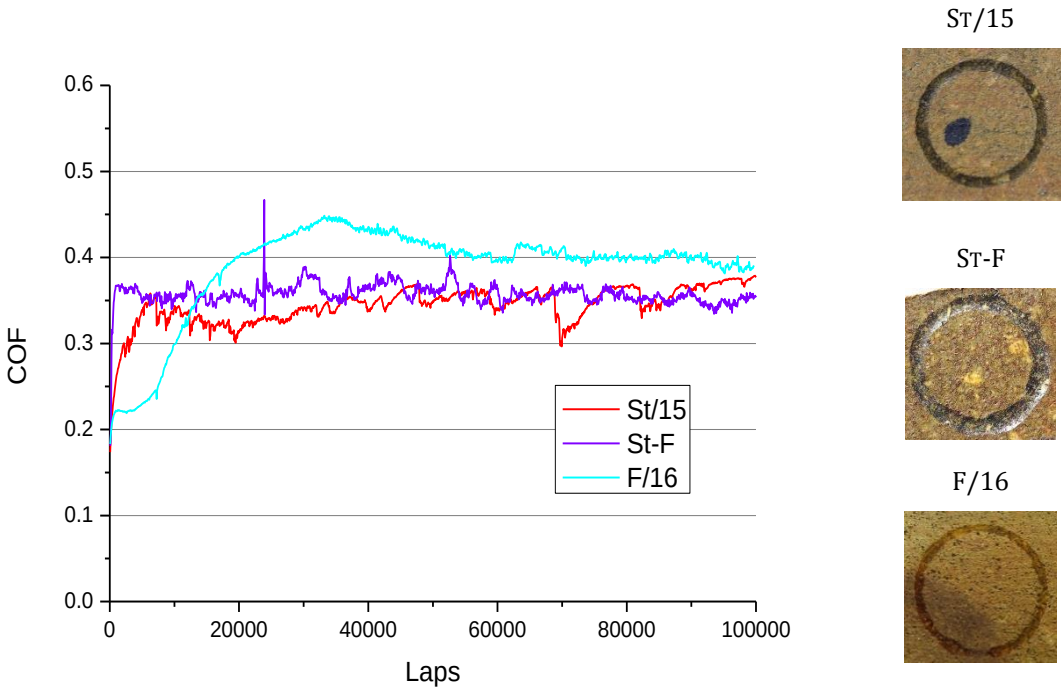

FIGURE 5.2 COEFFICIENT OF FRICTION IN FUNCTION OF THE NUMBER OF CYCLES, FOR ST/15 (15%VOL STEEL FIBRE), F/16 (16%VOL FRICTION DUST) AND ST-F (15%VOL STEEL FIBRE-16%VOL FRICTION DUST) SAMPLES

TABLE 5.5 SPECIFIC WEAR RATE K AND DENSITY VALUES FOR ST-F (15%VOL STEEL FIBRE-16%VOL FRICTION DUST), ST/15 (15%VOL STEEL FIBRE) AND F/16 (16%VOL FRICTION DUST) SAMPLES

Sample	St/15	St-F	F/16
K, $x10^4$ $\mu m^3/Nm$	4.46	8.92	3.47
Density, g/cm^3	2.29±0.05	1.98±0.02	1.25±0.02
Theoretical density, g/cm^3	2.26	2.26	1.24
Porosity, %vol	0	12	0

St-F sample COF curve is similar as medium value and vibrations to the St/15 sample one (steel fibres monocomponent), which is an expected result considering the importance of steel fibres in the friction mechanism. Due the chemical similarity between friction dust and phenolic resin, a limited influence of this filler on the results is expected. Wear value is higher for the St-F bicomponent than for monocomponent mixes, as it is easily visible just observing the tracks in FIGURE 5.2. In fact, considering the density values of these three samples, it appears than St-F sample presents high porosity (see in TABLE 5.5). Porosity can have an influence on the sample thermal conductivity since it is expected to reduce it, then causing heat accumulation during sliding. Based on these statements, for St-F sample, porosity induces severe heat accumulation which deteriorates the materials and produces more wear. As explained by S.J. Kim et al. (36), porosity of the friction material is an important factor for brake performance such as noise damping and fade resistance (182).

Among the St-F mix components, only steel fibres are conductive, so as their content is maintained in St-F in respect of St/15 mix, it is expected to observe the same thermal conductivity values for these two mixes. Experimentally, as visible in FIGURE 5.3a, St-F sample thermal conductivity is 40% lower than F/16 one, according to the expected diminution based on the porosity level.

On the TGA curves (see FIGURE 5.3b), it is visible that for St-F sample the final weight at ≈ 970°C is lower than the theoretical one: this means that in some way the oxidation of steel fibres is facilitated in the St-F mix in presence of friction dust. St-F mix contains friction dust which corresponds to phenolic chains previously thermally treated, so St-F could be considered as similar from the chemical point of view to St/15 mix with less

aramid fibres. It implies less cohesion of the material and as a consequence, oxidation phenomena can be facilitated and occurs at lower temperature. The porosity too should play an essential role and facilitates oxidation in this material.

Another consequence of this high porosity content is the important part of phenolic chains which remain uncured during the process: it is visible on the DMTA curve, in FIGURE 5.3c. The peak located at 282°C could correspond to the 2nd phenolic resin crosslinking step: as previously seen it indicates the partial post-curing reaction during sample preparation. The decrease of phenolic resin content in the material together with the porosity presence explain the minor rate of post curing reaction: the phenolic chains are less in contact with each others so the thermal treatment does not provide enough energy to allow the completion of this step.

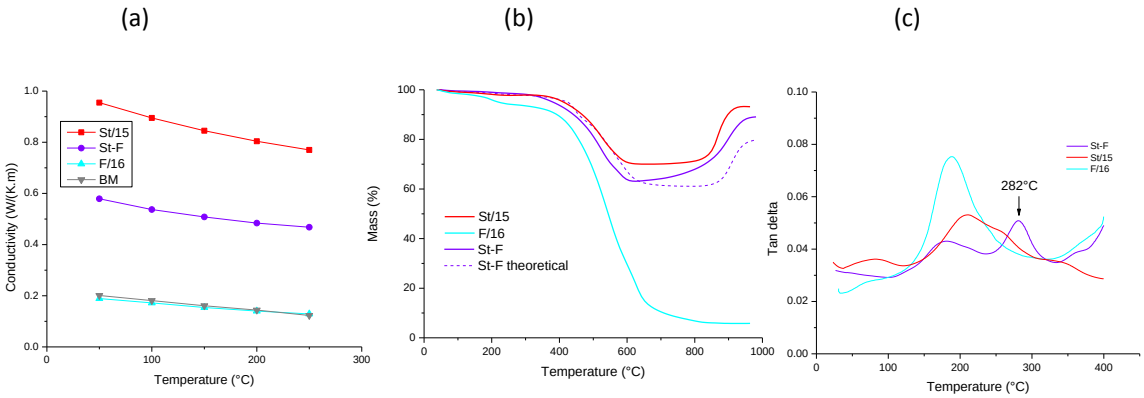

FIGURE 5.3 GRAPHICS OF (A) THERMAL CONDUCTIVITY, (B) TGA AND (C) TAN DELTA IN FUNCTION OF TEMPERATURE OF ST/15 (15%VOL STEEL FIBRE), F/16 (16%VOL FRICTION DUST), ST-F (15%VOL STEEL FIBRE-16%VOL FRICTION DUST) MIXES AND THE BASIC MIX

1.1.3. Steel fibres + aluminum oxide (St/15-A/5.6 → St-A)

St-A sample contains steel fibres and the aluminum oxide. St-A composition is presented in TABLE 5.6 and the respective tribological test results in FIGURE 5.4 and TABLE 5.7.

TABLE 5.6 ST-A SAMPLE COMPOSITION

	Resin	Aramid fibre	Steel fibre	Aluminum oxide	Sum
Content, in %vol	57.9	21.5	15	5.6	100
Content, in %wt	22.6	9.7	52.3	15.4	100

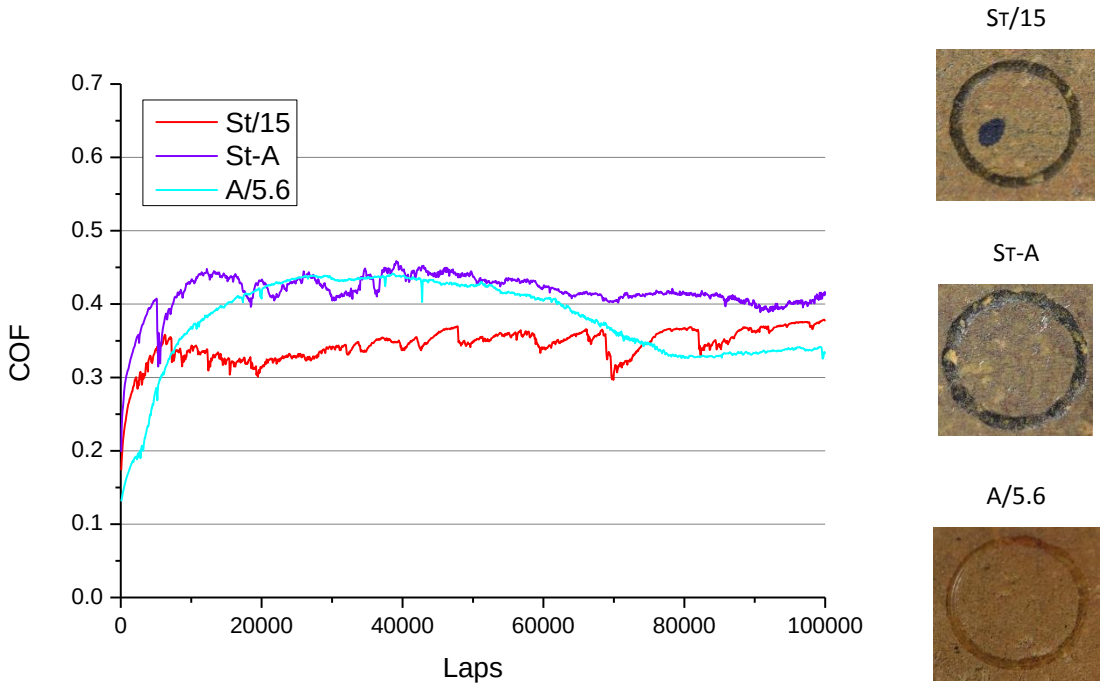

FIGURE 5.4 COF IN FUNCTION OF THE NUMBER OF CYCLES, FOR ST/15 (15%VOL STEEL FIBRE), A/5.6 (5.6%VOL ALUMINUM OXIDE) AND ST-A (15%VOL STEEL FIBRE-5.6%VOL ALUMINUM OXIDE) SAMPLES

TABLE 5.7 SPECIFIC WEAR RATE K, DENSITY AND STIFFNESS VALUES FOR ST-A (15%VOL STEEL FIBRE-5.6%VOL ALUMINUM OXIDE), ST/15 (15%VOL STEEL FIBRE) AND A/5.6 (5.6%VOL ALUMINUM OXIDE) SAMPLES

Sample	St/15	St-A	A/5.6
K, x10^{4} µm^{3}/Nm	4.46	7.28	2.76
Density, g/cm^{3}	2.03±0.04	2.58±0.02	1.35±0.01
Theoretical density, g/cm^{3}	2.31	2.44	1.45
Porosity, %vol	12	0	7
Stiffness, GPa	3.76±0.15	8.84±0.23	6.48±0.29

In the second half of the test, St-A COF value slightly decreases and gets stabilized, as well as the A/5.6 sample one: the high COF level is similar to that of alumina in the first part of the test: it is probably due to the exposed alumina particles in contact with the ball, that at some point disappear from the track and lead to the COF stabilization at a lower value.

A decrease of the wear resistance for the binary mix St-A (15%vol steel fibre-5.6%vol aluminum oxide) with respect to the monocomponent mixes is observed. According to Y. Lu (183), packing model analysis proved that if different-diameter fibres or fillers are mixed together, the packing space is more dense than that of mixed identical-diameter fibres or fillers (184). In fact the two raw materials introduced in the bicomponent St-A have different sizes and shape and the quality dispersion is good, as seen by SEM pictures (FIGURE 5.5), which leads to a density increase from the two monocomponents to the bicomponent, as presented in TABLE 5.7 (density equal to 2.58 g/cm^3 for the bicomponent, 2.03 g/cm^3 for St/15 and 1.35 g/cm^3 for A/5.6). It should lead to a wear resistance increase of the material (28), but results show the opposite trend. A possible explanation for this high wear rate would be that both fillers steel fibres and aluminum oxide create a strong interaction with the matrix, as demonstrated by the DMTA analysis (FIGURE 5.6a). But for St-A sample, the tan δ peak maximum is located at 219°C rather than 207°C for St/15 and 191°C for A/5.6. This demonstrates a synergistic effect, as the maximum peak is shifted towards higher temperatures. This strong interaction leads to high stiffness and storage modulus values (see in TABLE 5.7 and FIGURE 5.6b). Thus during friction, the material struggles against deformation, adopts a fragile behavior and the friction leads to important losses of debris. As a consequence, the strong interaction matrix/filler highlighted here has a negative effect on the tribological features.

Another complementary explanation is the fact that the material doesn't present porosity (see TABLE 5.7), and its density is high: there is no possibility to fill the surface pores with the crumbled debris, so the wear rate is high.

(a) (b)

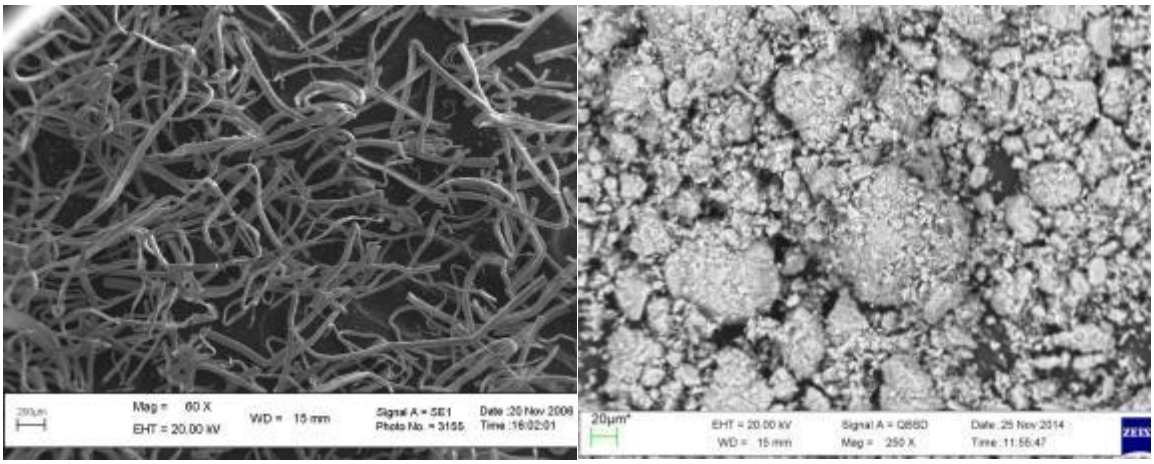

(c)

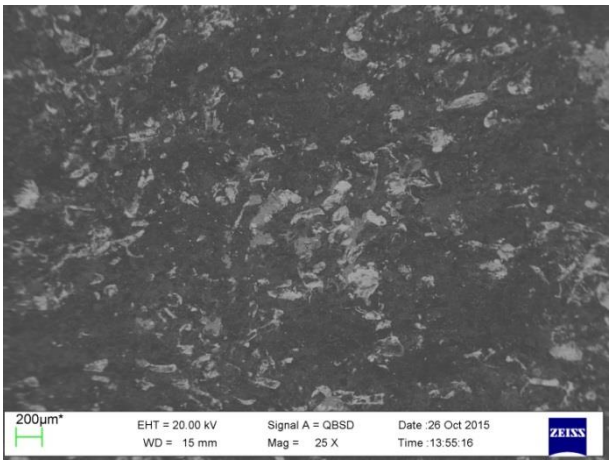

FIGURE 5.5 SEM PICTURES USING BACKSCATTERED ELECTRON ANALYSIS OF (A) STEEL FIBRE AT 60X (BAR EQUAL TO 200 µM), (B) ALUMINUM OXIDE AT 250X (BAR EQUAL TO 20 µM) AND (C) ST-A SAMPLE SURFACE AT 25X (BAR EQUAL TO 200 µM)

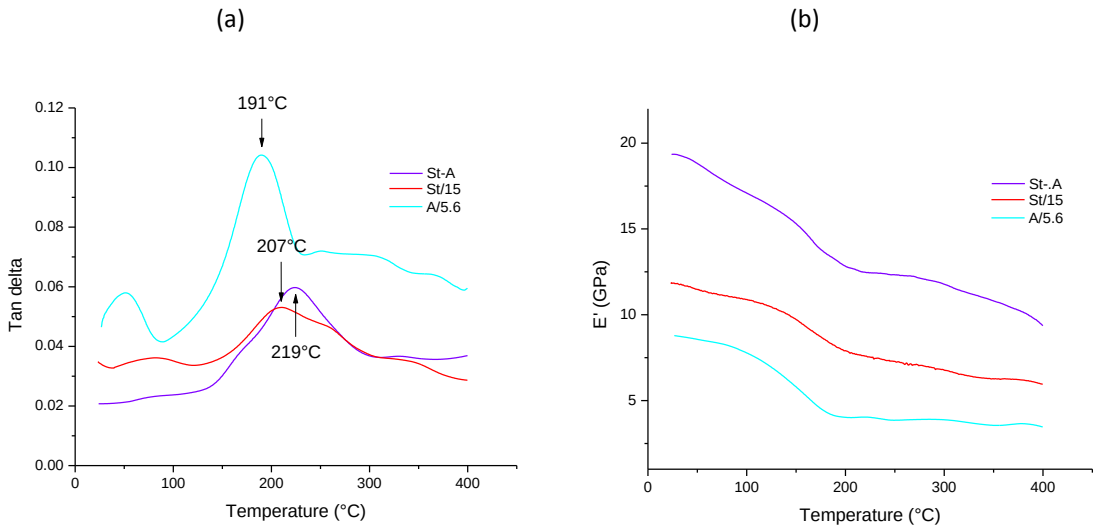

FIGURE 5.6 (A)TAN DELTA AND (B) STORAGE MODULUS VARIATIONS OF ST/15 (15%VOL STEEL FIBRE), A/5.6 (5.6%VOL ALUMINUM OXIDE) AND ST-A (15%VOL STEEL FIBRE-5.6%VOL ALUMINUM OXIDE) MIXES WITH TEMPERATURE

1.2. Components decreasing wear resistance

1.2.1. Barium sulphate + petroleum coke (B/50-C/10 → B-C)

The chemical formulation of B-C sample is presented in TABLE 5.8.

TABLE 5.8 B-C SAMPLE COMPOSITION

	Resin	Aramid fibre	Barium sulfate	Coke	Sum
Content, in %vol	29.2	10.8	50	10	100
Content, in %wt	12.7	5.4	71.5	7.2	100

COF variations and wear values of tribology tests are presented respectively in FIGURE 5.7 and TABLE 5.9.

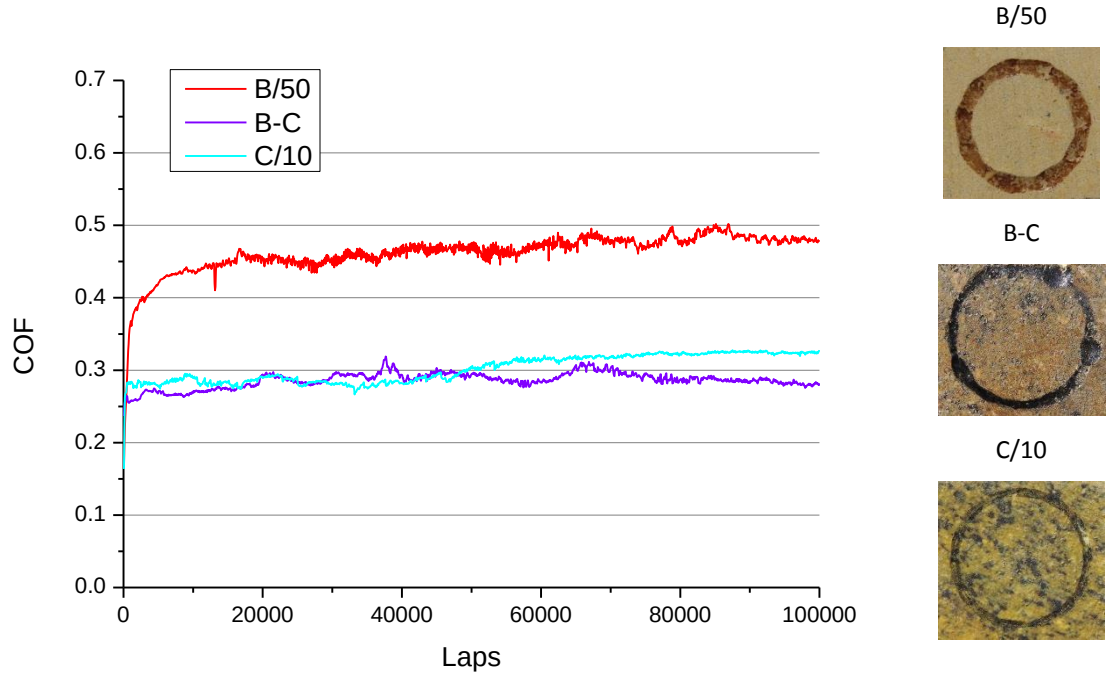

FIGURE 5.7 COF IN FUNCTION OF THE NUMBER OF CYCLES, FOR B/50 (50%VOL BARIUM SULFATE), C/10 (10%VOL COKE) AND B-C (50%VOL BARIUM SULFATE-10%VOL COKE) SAMPLES

TABLE 5.9 SPECIFIC WEAR RATE K, DENSITY AND HARDNESS VALUES FOR B-C (50%VOL BARIUM SULFATE-10%VOL COKE), B/50 (50%VOL BARIUM SULFATE) AND C/10 (10%VOL COKE) SAMPLES

Sample	B/50	B-C	C/10
K, x10^4 µm^3/Nm	12.33	4.67	1.24
Density, g/cm^3	2.74±0.03	2.25±0.02	1.38±0.04
Theoretical density, g/cm^3	2.78	2.88	1.35
Porosity, %vol	1	22	0
Hardness, H-RS	104.7 ± 2.52	96.0 ± 7.6	119.5 ± 8

COF values of binary mix B-C (50%vol barium sulfate-10%vol coke) are similar to the petroleum coke sample (around 0.3) as presented in FIGURE 5.7. As visible in FIGURE 5.8, some SEM observations have been performed in order to better understand the tribological features of B-C sample, at different enlargements and electron energy. Looking at the picture in FIGURE 5.8a and at the corresponding EDS analysis, it seems that the contact surface is mainly composed of barium sulfate, but using lower electron beam

energy on the track (FIGURE 5.8d) both barite and coke are present on the transfer layer in a grinded state. In the presented pictures barium sulphate particles are the clearer ones and the darker zones correspond to coke. Two interpretations can be proposed to explain the low wear rate of this bicomponent sample. The first is that energy is dissipated grinding the third body, and forming a thick layer that protects the material from wear, which explains the high wear resistance of B-C sample (50%vol barium sulfate-10%vol coke), intermediate between the two mono-filler samples B/50 (50%vol barium sulfate), and C/10 (10%vol petroleum coke). The second explanation can be proposed observing the data in TABLE 5.9**:** B-C sample presents a very high level of porosity of 22%. In fact, thanks to its low density, both petroleum coke and barium sulphate crumble apart and during friction they fill the pores at the surface: as a result the wear factor is low.

B-C sample has a low COF and a quite low wear rate, thus constitutes a good example of positive interaction between ingredients.

(a)

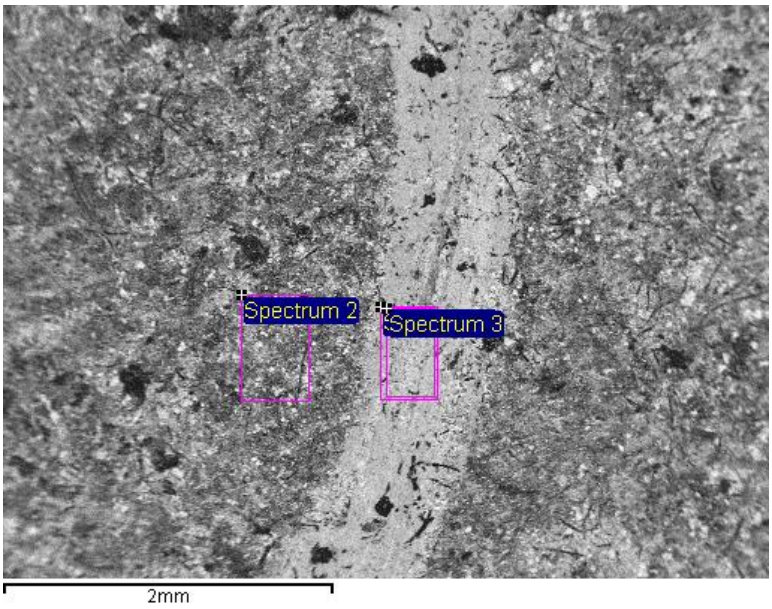

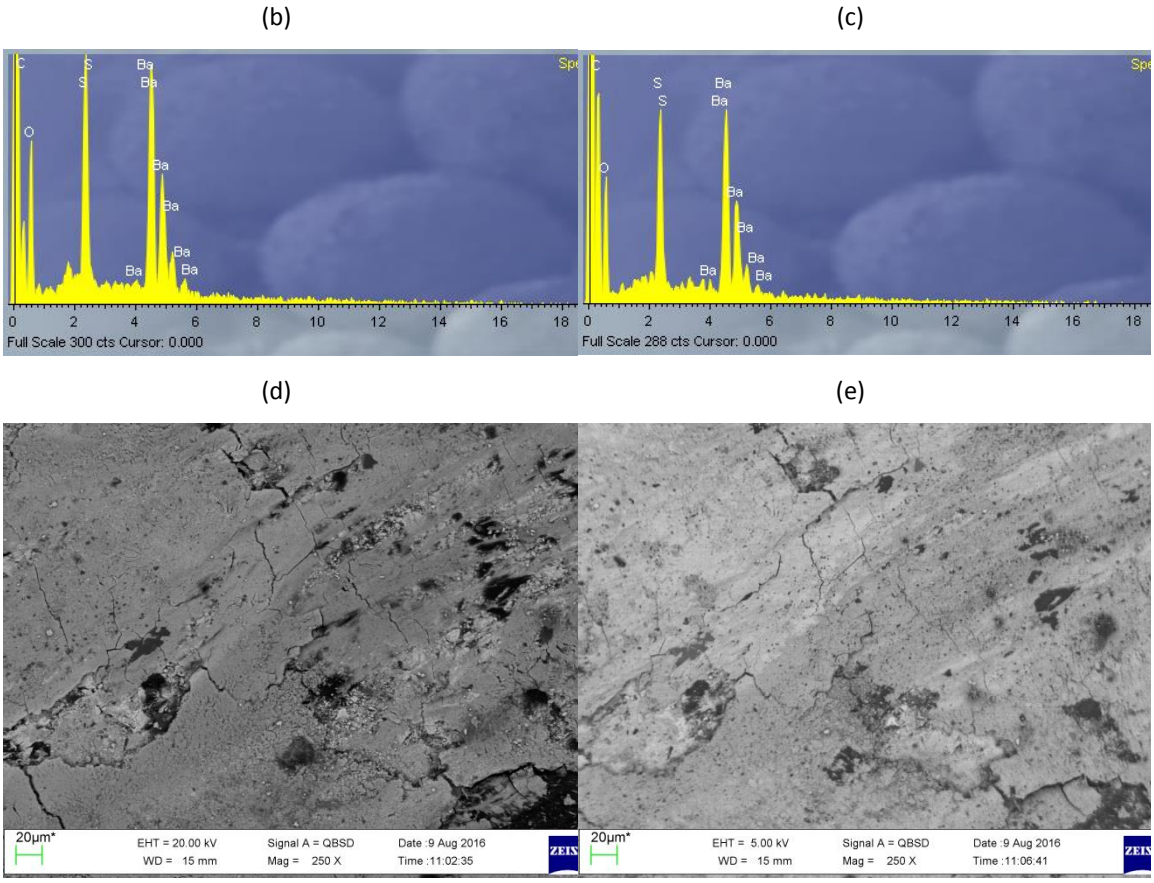

FIGURE 5.8 SEM OBSERVATIONS (USING BACK SCATTERING ELECTRONS): (A) B-C SAMPLE (50%VOL BARIUM SULFATE-10%VOL COKE) TRACK SURFACE AT 25X AND (B) ESDS ANALYSIS ASSOCIATED TO THE BULK; (C) ESDS ANALYSIS ASSOCIATED TO THE TRACK; (D) B-C SAMPLE INSIDE THE TRACK AT 250X, E=20KV AND (E) SAME ZONE AT 250X, E=5KV

Considering the DMTA storage modulus and tan δ curves in FIGURE 5.9, a surprising behavior is observed. In fact the storage modulus curve increases from 43°C to reach its maximum at 109°C. In the tan δ curve this variation matches with the 58°C peak. It corresponds to the glass transition of the neat resin located at 50°C in chapter III *Preamble*: the major part of oligomers are absolutely uncured in this sample. The peak located at 270°C corresponding to the 2nd crosslinking temperature of phenolic chains is high as well: this is in complete agreement with the fact that the entire resin get cured during the test heating. As a consequence, the 1st and the 2nd glass transition peaks centered at 190°C and 351°C are present but their amplitude is low. The curing of the sample is done little by little during the tribological test: this way the wear rate remains

low. In fact the resin gets transformed to build a strong polymer network and binds the components, instead of being degraded and fragmented under the friction effect and losing the contact ball/counterface under wear particles: this way the material gets stronger and presents a minor wear rate, despite the low physical-mechanical properties measured as seen in TABLE 5.9 (low hardness and high porosity).

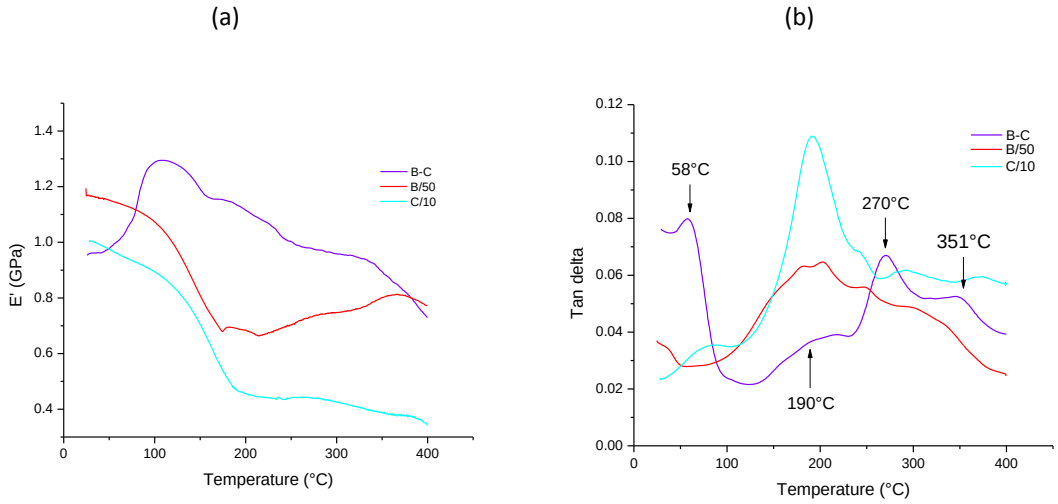

FIGURE 5.9 (A) STORAGE MODULUS AND (B) TAN DELTA VARIATIONS FOR B-C (50%VOL BARIUM SULFATE-10%VOL COKE), B/50 (50%VOL BARIUM SULFATE) AND C/10 (10%VOL COKE) SAMPLES IN FUNCTION OF TEMPERATURE

2. INTERMEDIATE CASES: TWO FILLERS WITH OPPOSITE EFFECT ON WEAR

2.1. Potassium hexatitanate fibres + graphite (Ti/20-G/5 → Ti-G)

The chemical formulation of Ti-G sample is presented in TABLE 5.10.

TABLE 5.10 TI-G SAMPLE COMPOSITION

	Resin	Aramid fibre	Potassium hexatitanate	Graphite	Sum
Content, in %vol	54.7	20.3	20	5	100
Content, in %wt	35.1	15	41.5	8.4	100

The Ti-G sample tribology test results are reported in FIGURE 5.10 for COF variations and TABLE 5.11 for wear values, together with the corresponding potassium hexatitanate fibres and graphite monocomponent ones.

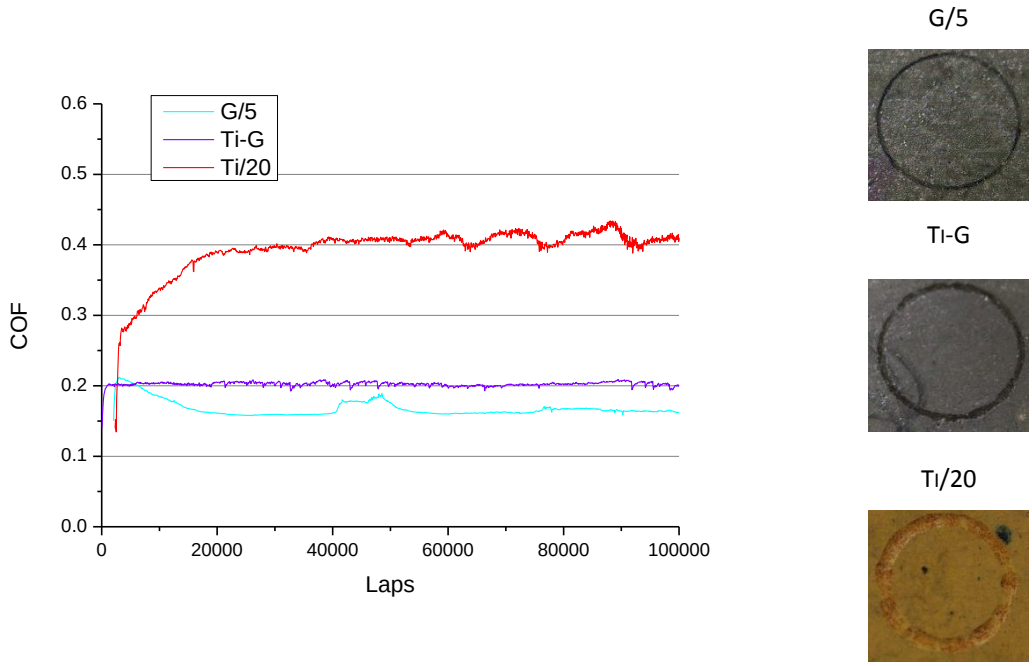

FIGURE 5.10 COF IN FUNCTION OF THE NUMBER OF CYCLES, FOR TI/20 (20%VOL POTASSIUM HEXATITANATE), G/5 (5%VOL GRAPHITE) AND TI-G (20%VOL POTASSIUM HEXATITANATE-5%VOL GRAPHITE) SAMPLES

TABLE 5.11 SPECIFIC WEAR RATE K, STIFFNESS AND DENSITY VALUES FOR TI-G (20%VOL POTASSIUM HEXATITANATE-5%VOL GRAPHITE), TI/20 (20%VOL POTASSIUM HEXATITANATE) AND G/5 (5%VOL GRAPHITE) SAMPLES

Sample	Ti/20	Ti-G	G/5
K, x10^4 µm^3/Nm	6.97	0.76	0.18
Stiffness, GPa	7.91±0.36	12.65±0.33	6.89±0.32
Density, g/cm^3	1.76±0.02	1.83±0.02	1.38±0.04
Theoretical density, g/cm^3	1.74	1.81	1.32
Porosity, %vol	3	0	3

The coefficient of friction of the Ti-G binary mix is particularly constant and stable, and its value is closer to the one of graphite sample: the lubricant behavior is dominating.

This is visually confirmed by the high similarity between G/5 and Ti-G samples tracks. The Ti-G sample (20%vol potassium hexatitanate-5%vol graphite) behaves more like G/5 (5%vol graphite) sample, so the wear resistance due to graphite prevails over the weakness of Ti/20 sample (20%vol potassium hexatitanate) evidenced by a high wear value. During shearing, there is delamination of the graphite honeycomb structured layers and a film tends to grow on the friction surface and increase the thickness thereof. This thickened graphite film hinders the abrasivity of the fibres and protects the material surface. As a result, tribological values as COF and wear are closer to graphite monocomponent sample ones.

In parallel to tribology, physical tests as stiffness measurements show that potassium hexatitanate fibres have a fundamental influence in the mechanical integrity of the material (see TABLE 5.11). The optimal compromise of properties between tribology and mechanical is also attributable to the absence of porosity in the sample. Besides, the presence of potassium hexatitanate in the mix substantially contributes to an optimal dispersion and mechanical delamination of graphite. The combination of fibres (potassium hexatitanate) and flakes (graphite) leads to a network formation revealed by thermal conductivity (see FIGURE 5.11). Thus, it can be concluded that this sample combined positive synergistic effects of tribology (COF stability and wear resistance of graphite), stiffness and thermal conductivity due to a strong network created by flakes and fibres.

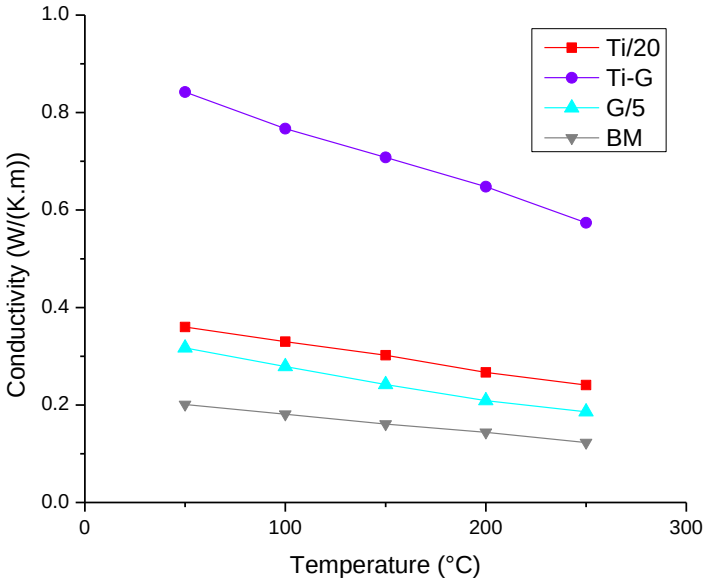

FIGURE 5.11 GRAPHIC OF THERMAL CONDUCTIVITY OF TI/20 (20%VOL POTASSIUM HEXATITANATE), G/5 (5%VOL GRAPHITE), TI-G (20%VOL POTASSIUM HEXATITANATE-5%VOL GRAPHITE) MIXES AND BASIC MIX IN FUNCTION OF TEMPERATURE

2.2. Graphite + silicon carbide (G/5-Si/3.4 → G-Si)

The chemical formulation of G-Si sample is presented in TABLE 5.12.

TABLE 5.12 G-SI SAMPLE COMPOSITION

	Resin	Aramid fibre	Graphite	Silicon carbide
Content, in %vol	66.8	24.8	5	3.4
Content, in %wt	58.4	25	8.4	8.2

Tribological tests results performed on G/5 (5%vol graphite), Si/3.4 (3.4%vol silicon carbide) and G-Si (5%vol graphite-3.4%vol silicon carbide) samples are reported in FIGURE 5.12 and TABLE 5.13.

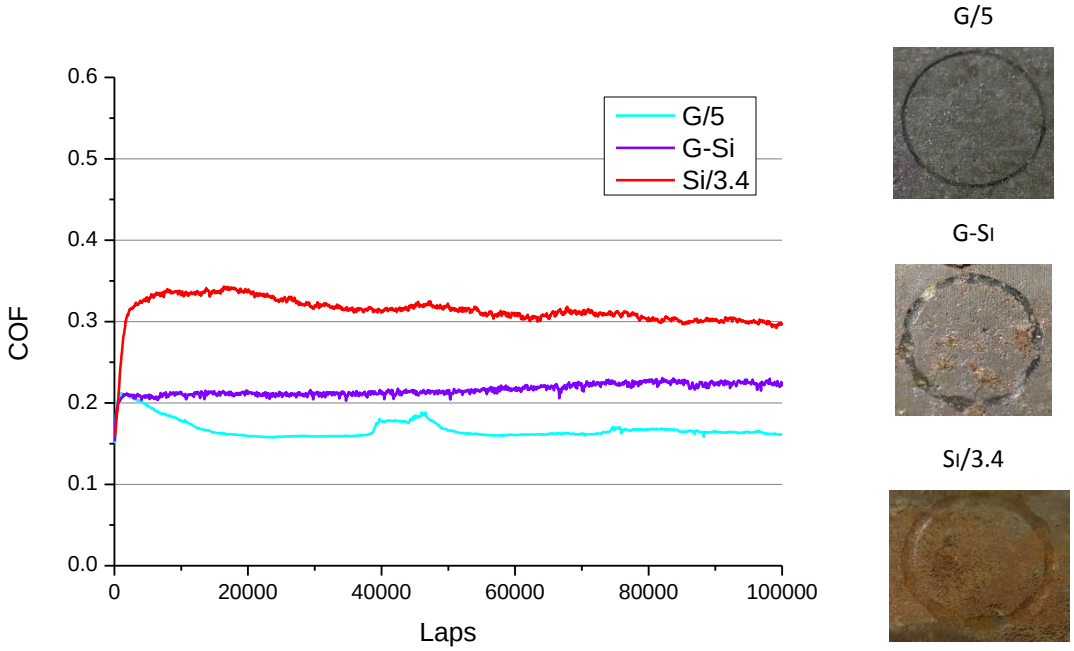

FIGURE 5.12 COF IN FUNCTION OF THE NUMBER OF CYCLES, FOR SI/3.4 (3.4%VOL SILICON CARBIDE), G/5 (5%VOL GRAPHITE) AND G-SI (5%VOL GRAPHITE-3.4%VOL SILICON CARBIDE) SAMPLES

TABLE 5.13 SPECIFIC WEAR RATE K, STIFFNESS AND HARDNESS VALUES FOR G-SI (5%VOL GRAPHITE-3.4%VOL SILICON CARBIDE), G/5 (5%VOL GRAPHITE) AND SI/3.4 (3.4%VOL SILICON CARBIDE) SAMPLES

Sample	G/5	G-Si	Si/3.4
K, x10^4 µm^3/Nm	0.18	3.70	3.78
Stiffness, GPa	6.89±0.32	3.48±0.24	6.35±0.29
Hardness, H-RS	120.7 ± 0.7	110.0 ± 5.1	119.7 ± 4.93

As observed for the other bicomponent sample Ti-G containing a lubricant and an abrasive (graphite and potassium hexatitanate fibres), G-Si sample COF curve is closer to the lubricant monocomponent sample one than to the abrasive one. In the present case, G-Si sample curve tends to increase while the Si/3.4 sample one decreases. G-Si sample presents COF values similar to the graphite monocomponent sample but wear rate similar to the abrasive silicon carbide mix. It can be hypothesized that during friction, once the lubricant transfer layer has been created from graphite fragments, it gets slowly consumed by the abrasive and cutting action of silicon carbide particles, considering its

sharp-edged shape (see SEM pictures in FIGURE 5.13). As a result, the graphite protective layer is perpetually consumed due to the pressure applied on it and to the abrasive action of silicon carbide dispersed inside the matrix.

(a) (b)

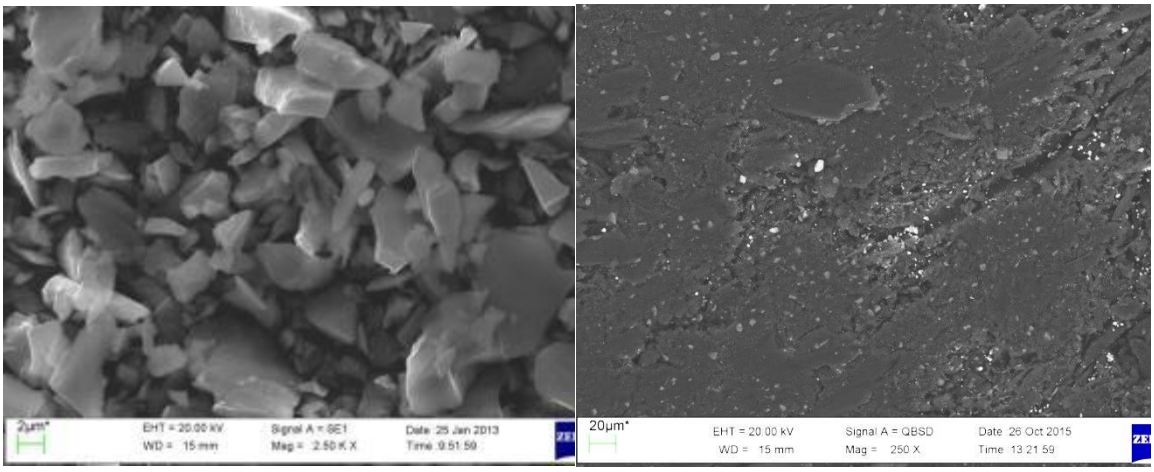

FIGURE 5.13 SEM PICTURES USING BACKSCATTERED ELECTRON ANALYSIS (BS): (A) SEM PICTURE OF SILICON CARBIDE FILLER AT 2500X; (B) SEM PICTURES OF G-SI SAMPLE SURFACE (5%VOL GRAPHITE-3.4%VOL SILICON CARBIDE) BEFORE TRIBOLOGICAL TEST AT 250X

Graphite and silicon carbide fillers as seen in chapter III in 2.3 and 2.4 sections don't develop interaction with the matrix and the behavior of the G-Si sample material is analogous, as shown by the DMTA results in FIGURE 5.14. It is interesting to notice the consequences on the physical properties: stiffness and hardness values are reported in TABLE 5.13. G-Si sample presents a stiffness reduced by half with respect to the two monocomponents mixes, and the hardness is slightly reduced too. In absence of interaction with the matrix, and without fibres (more than the aramid ones), the material gets fragilized when the binder content decreases. Considering a similar sample, the Ti-G material (containing potassium hexatitanate fibres and graphite), both monocomponents corresponding samples don't have interaction with the resin but the potassium hexatitanate fibres play a key role in the mechanical material properties.

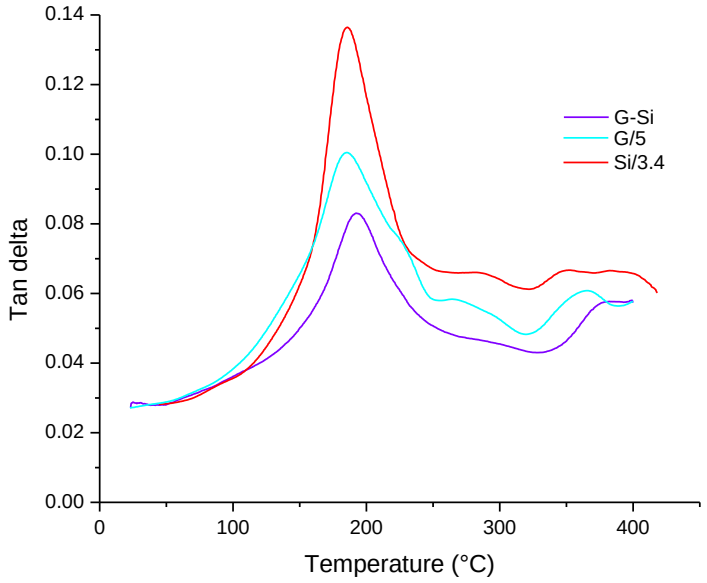

FIGURE 5.14 TAN DELTA VARIATIONS FOR G-SI (5%VOL GRAPHITE-3.4%VOL SILICON CARBIDE), G/5 (5%VOL GRAPHITE) AND SI/3.4 (3.4%VOL SILICON CARBIDE) SAMPLES IN FUNCTION OF TEMPERATURE

2.3. Potassium hexatitanate fibres + aluminum oxide (Ti/20-A/5.6 → Ti-A)

For the Ti-A sample, potassium hexatitanate fibres have been introduced together with aluminum oxide in the basic mix (see the chemical formulation of Ti-A sample in TABLE 5.14). From the composition point of view, this sample is close to St-A (steel fibres-aluminum oxide), only the fibres nature and content change.

TABLE 5.14 TI-A SAMPLE COMPOSITION

	Resin	Aramid fibre	Potassium hexatitanate	Aluminum oxide	Sum
Content, in %vol	54.2	20.2	20	5.6	100
Content, in %wt	30.2	12.9	41.5	15.4	100

The tribological test results are presented in FIGURE 5.15 and TABLE 5.15.

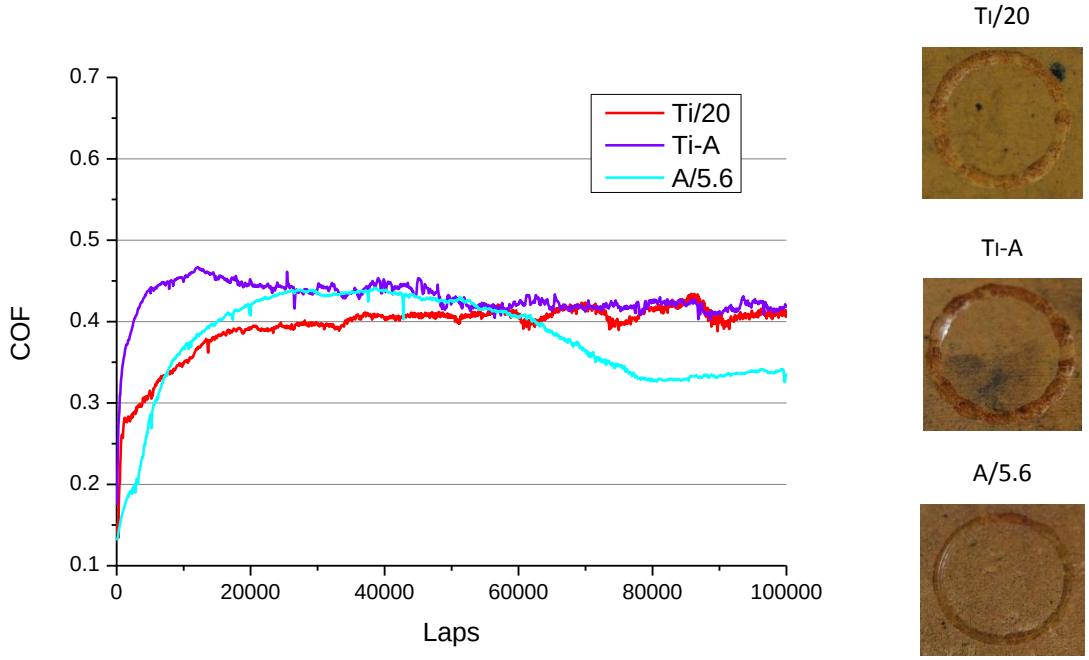

FIGURE 5.15 COF IN FUNCTION OF THE NUMBER OF CYCLES, FOR TI/20 (20%VOL POTASSIUM HEXATITANATE), A/5.6 (5.6%VOL ALUMINUM OXIDE) AND TI-A (20%VOL POTASSIUM HEXATITANATE-5.6%VOL ALUMINUM OXIDE) SAMPLES

TABLE 5.15 SPECIFIC WEAR RATE K, STIFFNESS AND HARDNESS VALUES FOR TI-A (20%VOL POTASSIUM HEXATITANATE-5.6%VOL ALUMINUM OXIDE), TI/20 (20%VOL POTASSIUM HEXATITANATE) AND A/5.6 (5.6%VOL ALUMINUM OXIDE) SAMPLES

Sample	Ti/20	Ti-A	A/5.6
K, x10^4 µm^3/Nm	6.97	8.36	2.77
Stiffness, GPa	7.91±0.36	14.76±0.41	6.48±0.29
Hardness, H-RS	117.4 ± 2.2	124.0 ± 7.2	121.7 ± 1.53

A similar behavior of St-A (steel fibres-aluminum oxide) mix can be observed: increased wear rate with respect to the monocomponents ones, and COF values decrease in the second half of the test, miming the aluminum oxide tendency. At the beginning of the test, both A/5.6 and Ti-A samples COF present a steep increase, while Ti/20 increases more slowly: the aluminum oxide presence leads to the abrasion of the material, so it has a more aggressive behavior. It can be hypothesized that the hexatitanate fibres create a so strong network that it fragilizes the material, decreasing its flexibility and capacity to get

deformed and adapted to the counterface, as demonstrated by the stiffness and hardness values in TABLE 5.15: the main consequence is an important wear rate.

Another explanation for the high wear value can be suggested by observing the ball-on-disc track on the material surface (FIGURE 5.16). Accumulation in some points of the track of organic fibres (aramid fibres) can be observed. The EDS analysis evidences that the third body is enriched in Al element. It can be explained by the fact that organic fibres get piled up in some points as visible in FIGURE 5.16a, but also by the aluminum oxide ball nature with a possible transfer from the ball to the material surface. The accumulation of organic fibres and the successive elimination of this pile partly explains the high wear rate.

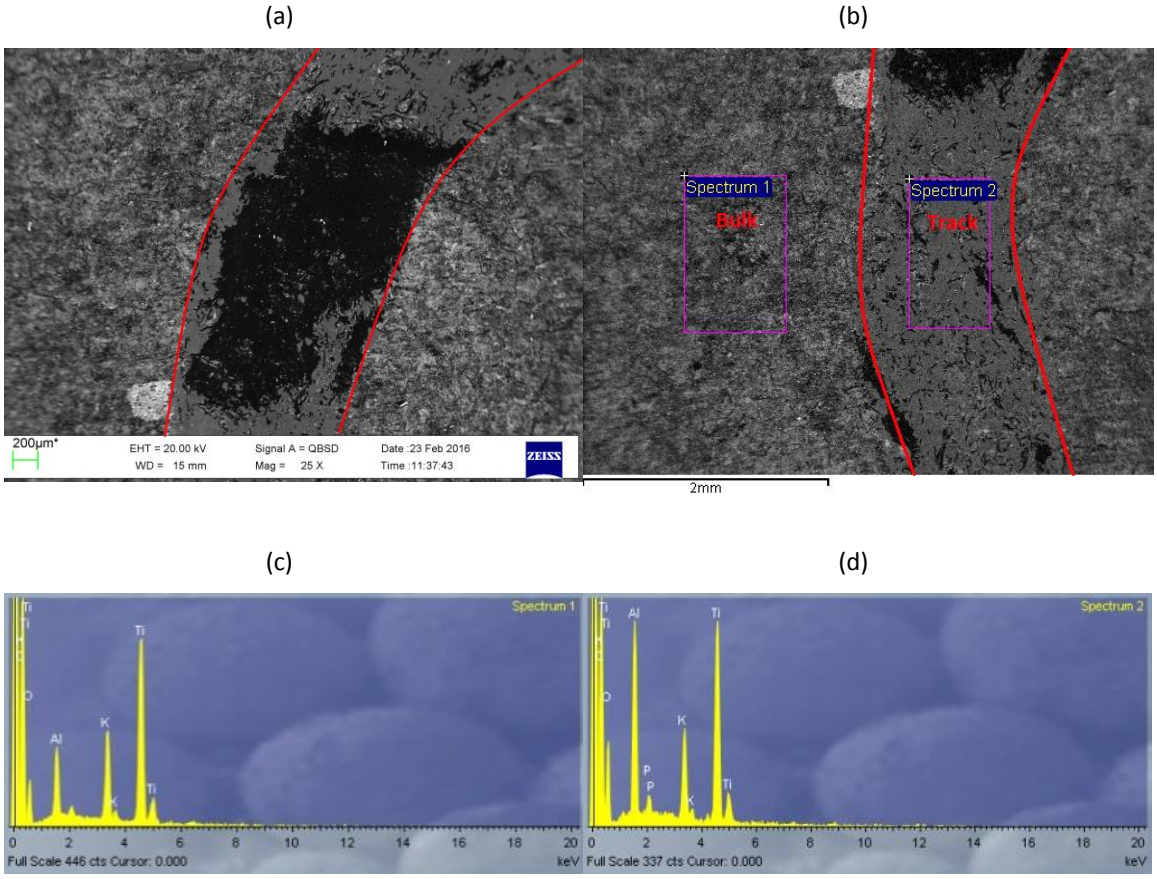

FIGURE 5.16 (A) AND (B) SEM OBSERVATIONS (25X, USING BACK SCATTERING ELECTRONS) OF BALL-ON-DISC TRACK OF TI-A SAMPLE (20%VOL POTASSIUM HEXATITANATE-5.6%VOL ALUMINUM OXIDE); (C) ESDS ANALYSIS ASSOCIATED ON THE BULK ZONE; (D) ESDS ANALYSIS ASSOCIATED ON THE TRACK ZONE

2.4. Steel fibres + barium sulphate (St/15-B/50 → St-B)

The chemical formulation of mix St-B is presented in TABLE 5.16.

TABLE 5.16 ST-B SAMPLE COMPOSITION

	Resin	Aramid fibre	Steel fibre	Barium sulfate	Sum
Content, in %vol	29.3	11.0	14.2	45.5	100
Content, in %wt	10.0	4.3	34.6	51.1	100

COF curve of steel and barite bicomponent sample is presented in FIGURE 5.17 together with the monocomponents ones; as well as track area left at the end of the test in FIGURE 5.18 and specific wear rate K in TABLE 5.17.

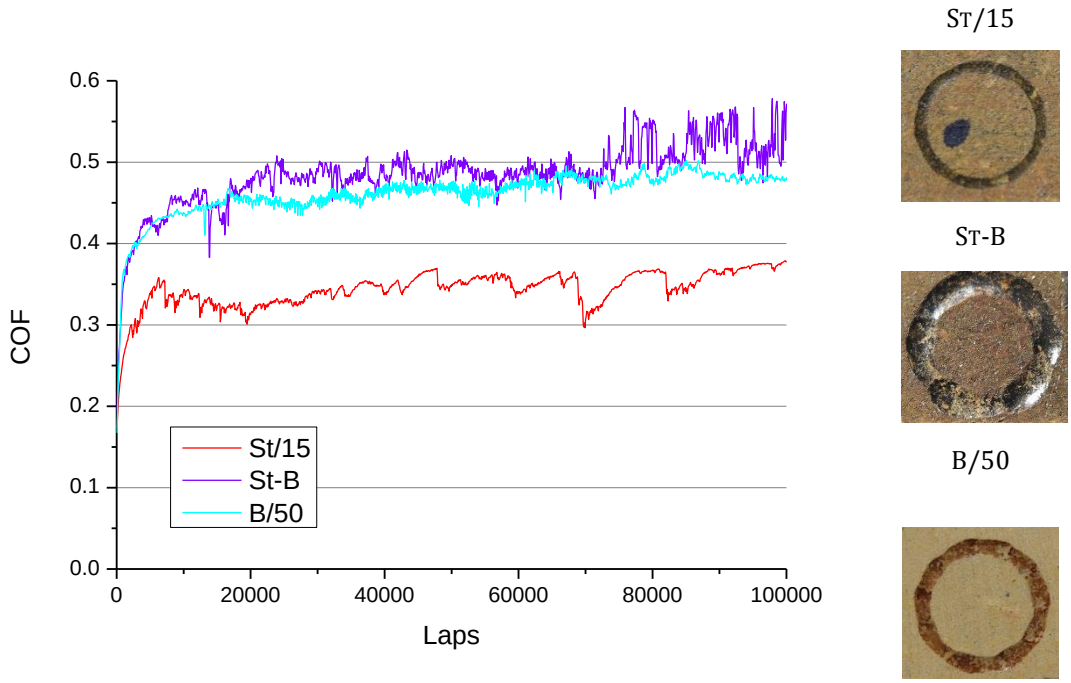

FIGURE 5.17 COF VARIATIONS OF ST/15 (15%VOL STEEL FIBRE), B/50 (50%VOL BARIUM SULPHATE) AND ST-B (15%VOL STEEL FIBRE-50%VOL BARIUM SULPHATE) SAMPLES

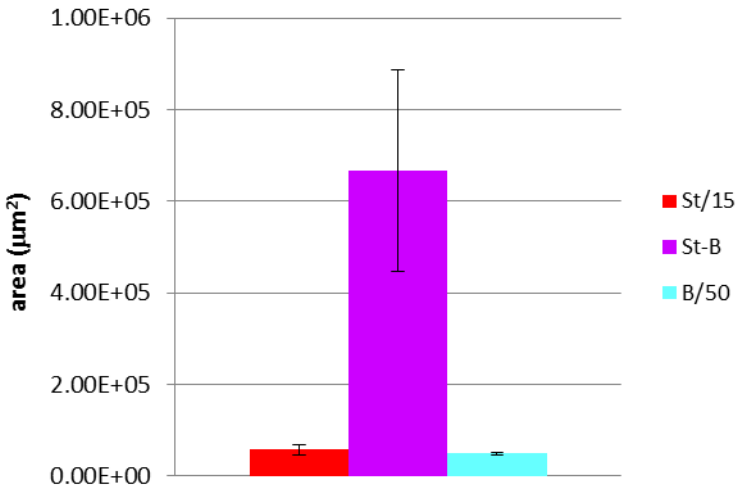

FIGURE 5.18 TRACK AREA LET AT THE END OF THE TEST FOR ST/15 (15%VOL STEEL FIBRE), B/50 (50%VOL BARIUM SULPHATE) AND ST-B (15%VOL STEEL FIBRE-50%VOL BARIUM SULPHATE) SAMPLES

TABLE 5.17 SPECIFIC WEAR RATE K AND DENSITY VALUES FOR ST/15 (15%VOL STEEL FIBRE), ST-B (15%VOL STEEL FIBRE-50%VOL BARIUM SULPHATE) AND B/50 (50%VOL BARIUM SULPHATE) SAMPLES

Sample	St/15	St-B	B/50
K, x10⁴ µm³/Nm	4.46	65.71	12.33
Density, g/cm³	2.23±0.04	3.21±0.03	2.74±0.03
Theoretical density, g/cm³	2.26	3.67	2.78
Porosity, %vol	1	12	1

There is a clear negative interaction for the St-B sample (15%vol steel fibre-50%vol barium sulphate) between barium sulfate and steel fibres: wear is 16 times higher than steel monocomponent sample and 5 times higher than barite sample. St-B track design is clearly the worst among the three materials. These wear results could partly be due to the fact that steel fibres get not easily compacted, and that the resin content is low so the fibres are quickly expelled by the sliding contact, leading a dramatic aspect of the track. It can be hypothesized that the high wear and the high error bar values in FIGURE 5.18 are partly due to the ejection of a high size fragment at 75 000 laps, explaining the sudden high friction coefficient vibration. This phenomenon happens because of the high level of porosity in the sample, that creates weak zones and permit the extraction of material fragments; the strong irregularities on the track edges confirm this theory.

Some SEM observations have been done (see in FIGURE 5.19): on the surface on which the tribological test is performed, there is no heterogeneity of the fillers dispersion able to explain the high wear rate. Looking at the tribological track (see FIGURE 5.20), some heterogeneities are visible in the third body layer, which is constituted by aggregates of aramid fibres, expelled during friction. This is confirmed by the difference of grey shade between the track zone and the bulk zone: the organic content results lower on the track. The third body layer is mainly constituted of barium sulphate, and few steel fibres are visible on the track (see FIGURE 5.20). Between steel fibres and barium sulfate, the respective contents in the bicomponent mix of 14.2%vol and 45.5%vol explain why barium sulfate controls the COF level, and considering the role during friction of the fibres, protruding from the surface it is expected to have similar COF vibrations for St-B and St/15.

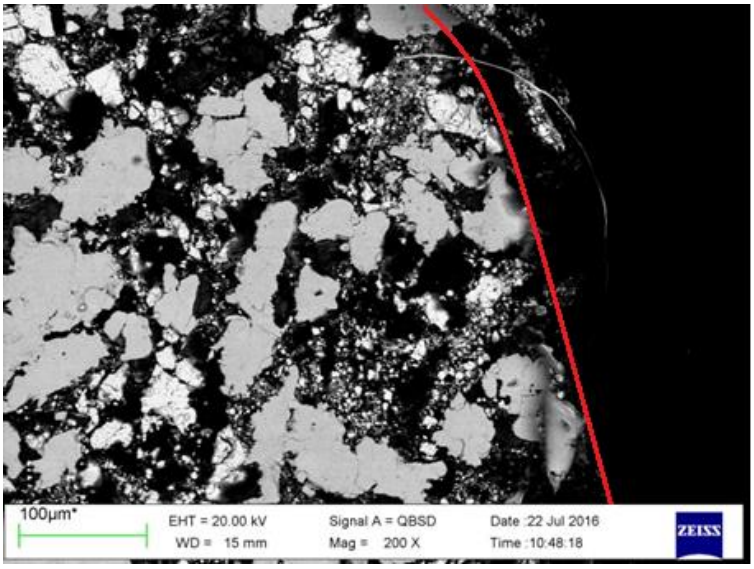

FIGURE 5.19 SEM PICTURE OF ST-B (15%VOL STEEL FIBRE-50%VOL BARIUM SULPHATE) SAMPLE SURFACE AT 200X USING BACKSCATTERED ELECTRON ANALYSIS (BS). GRAY ZONES: STEEL FIBRES; WHITE ZONES: BARIUM SULPHATE. NB: TESTED SURFACE IS ON THE RIGHT OF THE PICTURE

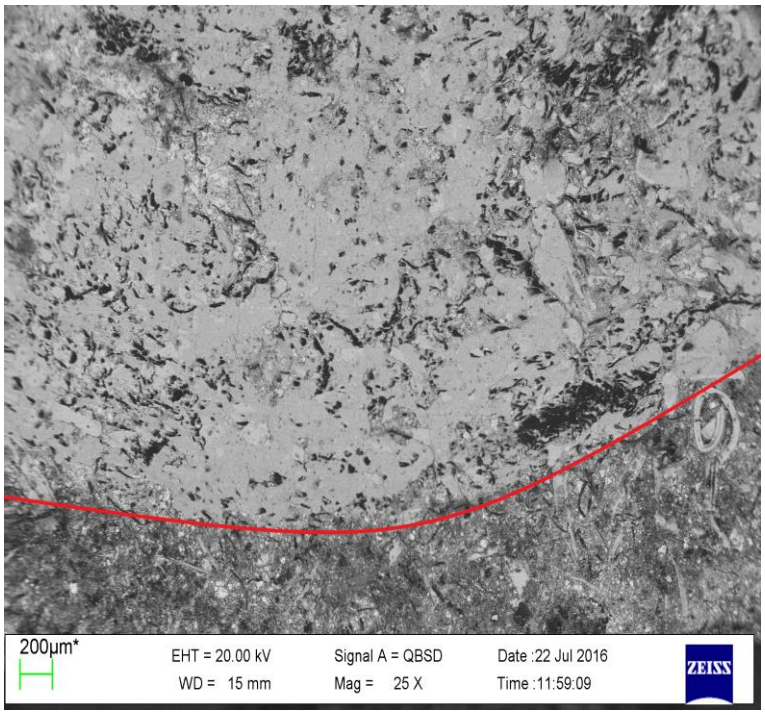

FIGURE 5.20 SEM PICTURE OF ST-B MIX (15%VOL STEEL FIBRE-50%VOL BARIUM SULPHATE) TRIBOLOGICAL TRACK SURFACE AT 200X USING BACKSCATTERED ELECTRON ANALYSIS (BS)

To explain the high wear rate of this sample, it would be right to consider the concept of thermal diffusivity. It corresponds to the relation between thermal conductivity and the product of density and specific heat of the studied material. To efficiently infuse the thermal wave, it is not sufficient for the material to be very conductive, it also has to be not too massive with a low specific heat value therefore the heat received at each single layer in which it is possible to divide the material, does not get trapped and hold in this layer (following the calorimetry rule) but engender a new thermal gradient between this layer and the successive one. According to this mechanism, thermal field spreads. If a material presents a high thermal conductivity but a high density and specific heat, once exposed to a thermal gradient the flow would be important in the first layers but would not succeed to go through the successive ones. In the present case, even if the thermal conductivity of the bicomponent sample (FIGURE 5.21) is relatively high, the high density of the sample together with the porosity presence (see in TABLE 5.17) could be the reasons of the heat accumulation leading to the excessive wear.

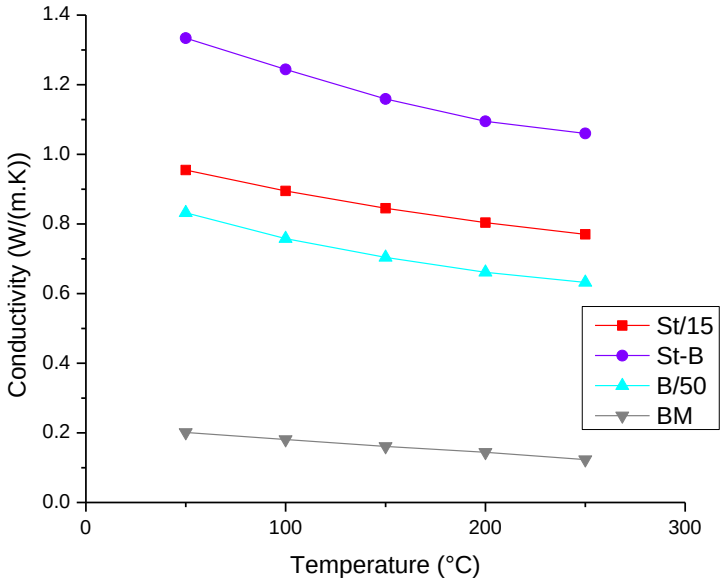

FIGURE 5.21 THERMAL CONDUCTIVITY FOR ST/15 (15%VOL STEEL FIBRE), B/50 (50%VOL BARIUM SULPHATE) AND ST-B (15%VOL STEEL FIBRE-50%VOL BARIUM SULPHATE) SAMPLES

Some general remarks can be done in light of these last results. All the bicomponent samples present a definitive friction coefficient plateau more quickly than the relative monocomponent samples: in fact the more complex samples contain less resin, so the third body gets enriched faster in fillers, the time needed to spread and rearrange the fillers on the track is lower. It is noteworthy that steel fibres presence always leads to increase the wear value and controls friction coefficient vibrations. In general, some couple of fillers show interaction, and the final tribological properties don't correspond to the intermediate of the monocomponent's ones; whereas in other cases particular mechanism come into play and new behaviors must be taken into account to explain the wear and friction coefficient variations. After this intermediate step between monocomponents and multiple systems, it is necessary to study the more complex materials with three to eight fillers in the basic mix.

II - FROM TERNARY TO COMPLETE MULTIPLE SYSTEMS

In the previous part about tribology tests on monocomponent samples, it has been seen the primordial role of two fillers in particular in the transfer layer formation mechanisms: graphite and steel fibres. In this last part about complex system analysis the materials have been divided into two categories, with respect to their composition: the steel fibres based and the graphite based ones.

1. STEEL FIBRES BASED MATERIALS

1.1. Steel fibres + Barium sulphate + Aluminum oxide (St/15-B/50-A/5.6 → St-B-A)

The chemical formulation of St-B-A mix is presented in TABLE 5.18.

TABLE 5.18 ST-B-A SAMPLE COMPOSITION

	BM	Steel fibre	Barium sulfate	Aluminum oxide	Sum
Content, in %vol	39.2	12.9	43.1	4.8	100
Content, in %wt	14.3	28.6	51.8	5.3	100

The tribological test results are presented in FIGURE 5.22 for COF and FIGURE 5.23 for wear values.

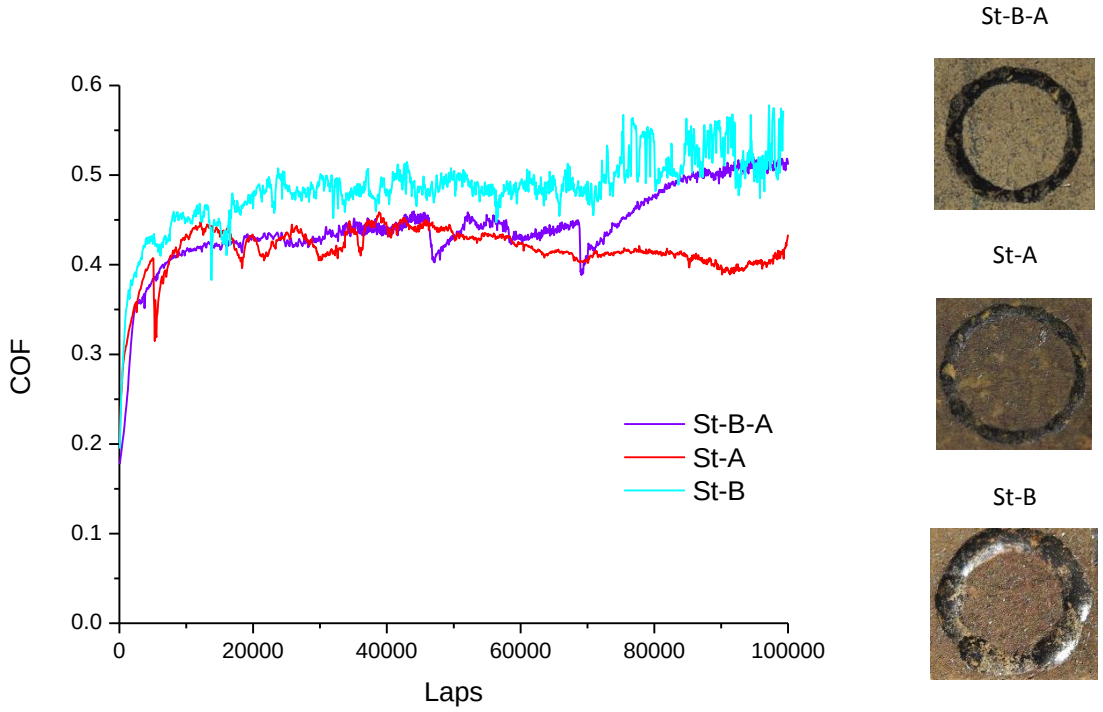

FIGURE 5.22 COEFFICIENT OF FRICTION IN FUNCTION OF THE NUMBER OF CYCLES, FOR ST-A (STEEL FIBRE-ALUMINUM OXIDE), ST-B (STEEL FIBRES-BARIUM SULPHATE) AND ST-B-A (STEEL FIBRE-BARIUM SULPHATE-ALUMINUM OXIDE) SAMPLES

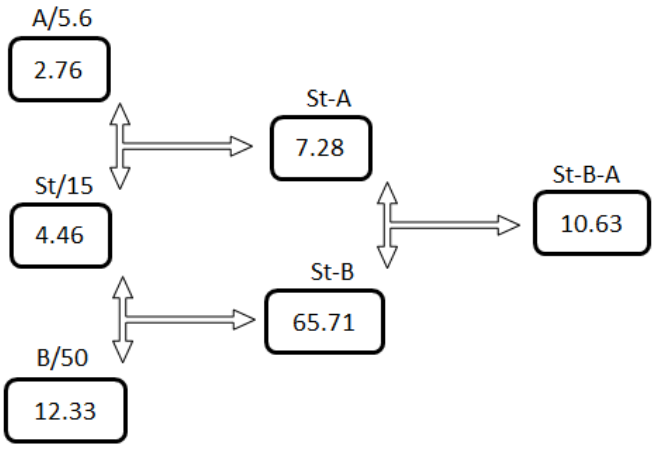

FIGURE 5.23 REPRESENTATION OF SPECIFIC WEAR RATE K FOR ST-B-A (STEEL FIBRE-BARIUM SULPHATE-ALUMINUM OXIDE), ST-A (STEEL FIBRE-ALUMINUM OXIDE), ST-B (STEEL FIBRES-BARIUM SULPHATE) SAMPLES AND THE CORRESPONDING MONOCOMPONENT SAMPLES, X10^4 $\mu M^3/NM$

In the friction coefficient curves, the starting phases of the three samples are similar. Then in the last part of the test the St-B-A COF value increases until reaching the St-B sample level one. In fact, as previously seen for the B-C sample, barium sulphate easily fell apart, and mainly contributes to build the third body, so the final COF value is dominated by its tribological characteristics.

About the wear rate, the value for St-B-A sample is higher than that of the St-A sample (steel fibres – aluminum oxide) but much lower than that of the St-B sample (steel fibres – barium sulphate) one. As seen for St-A sample, the interaction created between the components steel fibres and aluminum oxide together with the resin leads to a synergistic effect and the bicomponent presents a high glass transition temperature equal to 219°C. This phenomenon is the same for the tricomponent sample as visible by the DMTA results in FIGURE 5.24 (Tg temperature equal to 220°C), and by the stiffness and hardness high values (FIGURE 5.25). In this sense the addition of barium sulphate does not influence this phenomenon, even if it implies a minor resin quantity. This observation allows to draw as conclusion that the synergistic effect seen for the St-A sample could be due more to an additive interaction between the fillers themselves than between the fillers and the basic mix. On the other hand, compared to St-B sample characteristics, the tricomponent St-B-A presents a much lower wear rate. The aluminum oxide even if introduced at low content (5.6%vol) in the mix has a significant importance on the material performances: the COF curve for example is shifted to higher values. It can be easily explained by the fact that as seen before in chapter III, section I.2, alumina presents a positive interaction with the resin, which limits the wear.

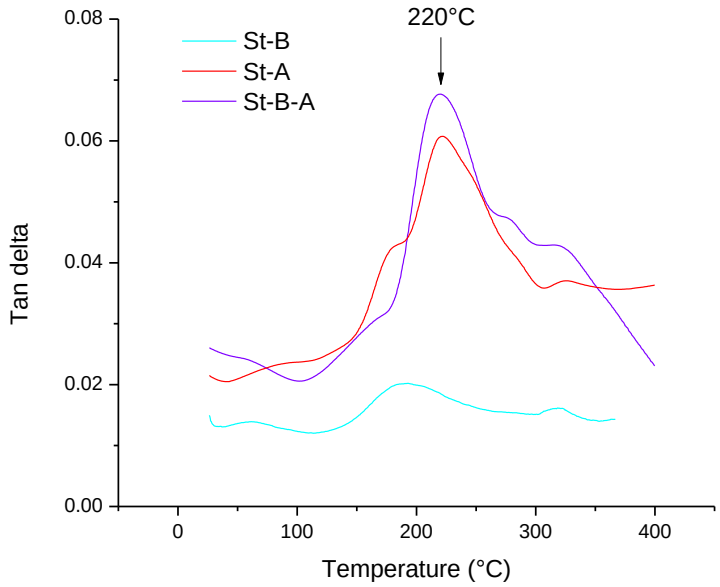

FIGURE 5.24 TAN DELTA VARIATIONS FOR ST-B (STEEL FIBRE-BARIUM SULPHATE), ST-A (STEEL FIBRE-ALUMINUM OXIDE) AND ST-B-A (STEEL FIBRE-BARIUM SULPHATE-ALUMINUM OXIDE) SAMPLES IN FUNCTION OF TEMPERATURE

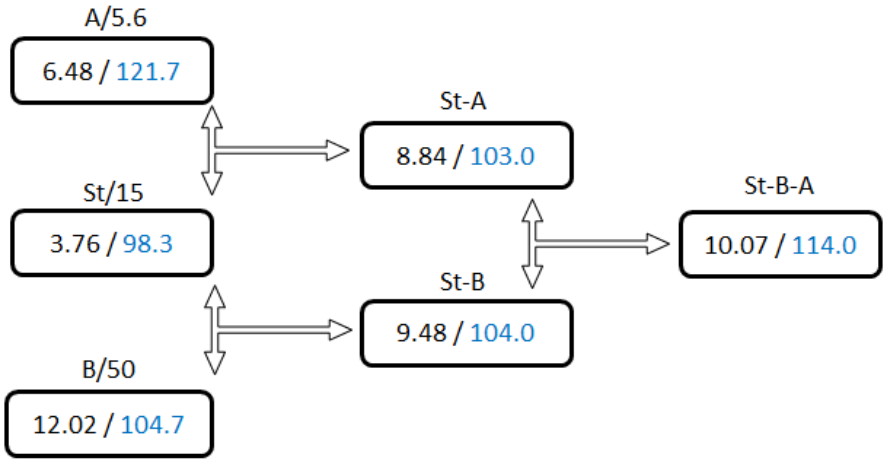

FIGURE 5.25 REPRESENTATION OF STIFFNESS (GPA, IN BLACK) AND HARDNESS (HRS, IN BLUE) VALUES FOR ST-B-A (STEEL FIBRE-BARIUM SULPHATE-ALUMINUM OXIDE), ST-A (STEEL FIBRE-ALUMINUM OXIDE), ST-B (STEEL FIBRES-BARIUM SULPHATE) SAMPLES AND THE CORRESPONDING MONOCOMPONENT SAMPLES

1.2. Steel fibres + Friction Dust + Aluminum Oxide (St/15-F/16-A/5.6 → St-F-A)

The chemical formulation of St-F-A mix is presented in TABLE 5.19.

TABLE 5.19 ST-F-A SAMPLE COMPOSITION

	BM	Steel fibre	Friction dust	Aluminum oxide	Sum
Content, in %vol	63.4	15	16	5.6	100
Content, in %wt	34.4	49.4	7.1	9.1	100

Tribology tests have been performed on St-F-A sample, containing steel fibres, friction dust and alumina. The results in matter of COF and wear data are presented in FIGURE 5.26 and FIGURE 5.27 respectively.

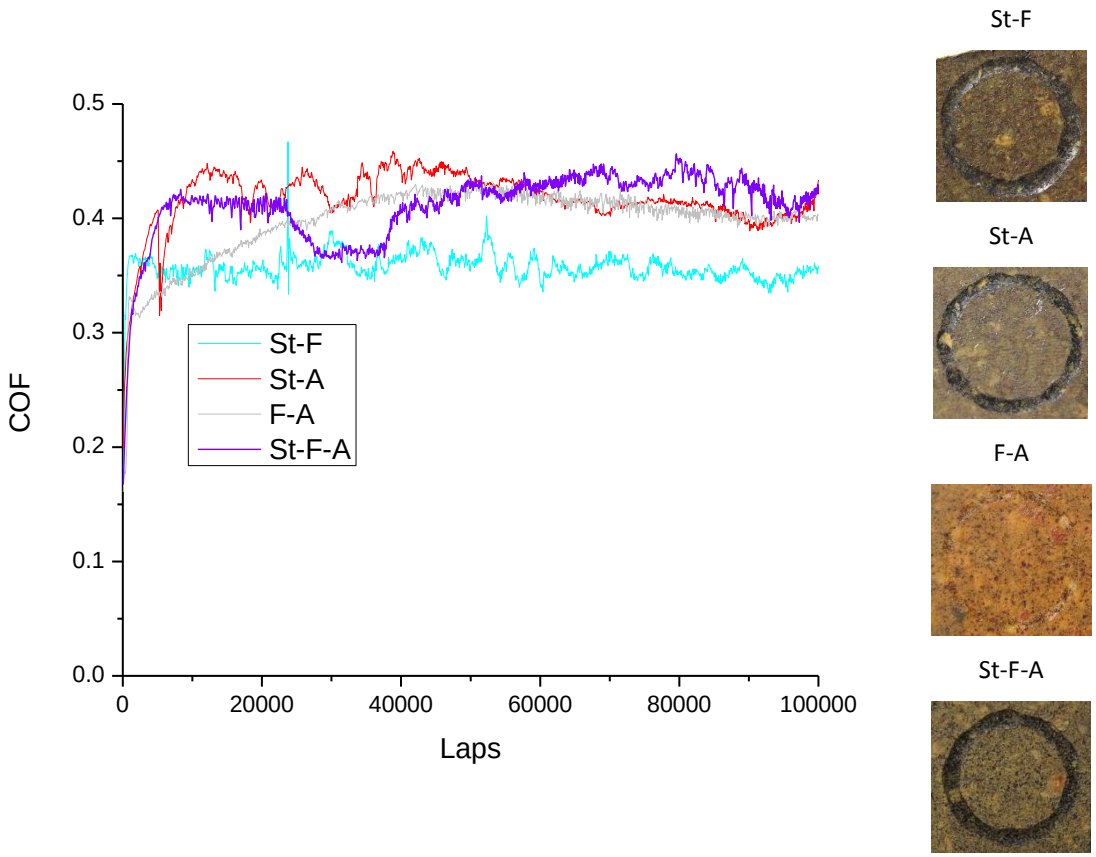

FIGURE 5.26 COEFFICIENT OF FRICTION IN FUNCTION OF THE NUMBER OF CYCLES, FOR ST-A (STEEL FIBRE-ALUMINUM OXIDE), ST-F (STEEL FIBRES-FRICTION DUST), F-A (FRICTION DUST-ALUMINUM OXIDE) AND ST-F-A (STEEL FIBRE-FRICTION DUST-ALUMINUM OXIDE) SAMPLES

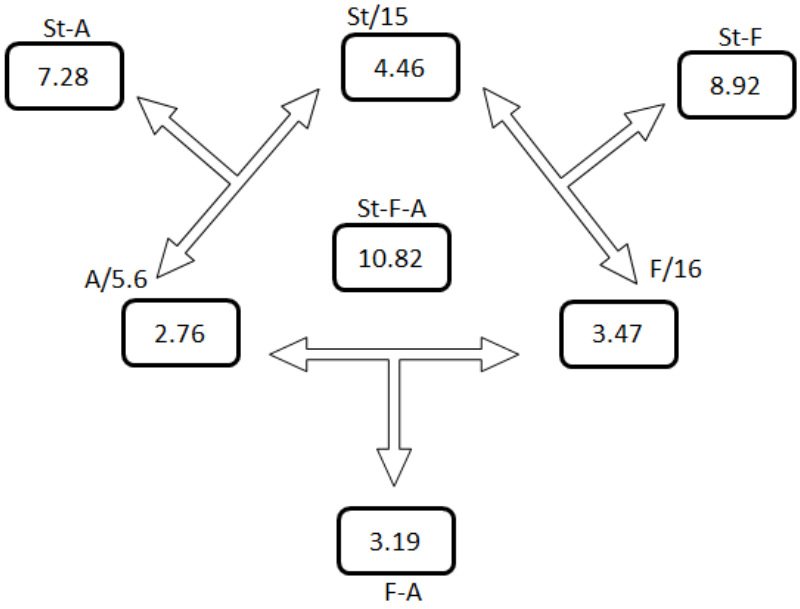

FIGURE 5.27 REPRESENTATION OF WEAR SPECIFIC RATE K FOR ST-A (STEEL FIBRE-ALUMINUM OXIDE), ST-F (STEEL FIBRES-FRICTION DUST), F-A (FRICTION DUST-ALUMINUM OXIDE), ST-F-A (STEEL FIBRE-FRICTION DUST-ALUMINUM OXIDE) SAMPLES AND THE CORRESPONDING MONOCOMPONENT SAMPLES, X10^4 $\mu M^3/Nm$

As presented in FIGURE 5.26, the medium COF value of St-F-A sample is 0.43, mainly due to the aluminum oxide presence, as the bicomponent sample St-F, the one without alumina, displays a medium COF as low as 0.36. The high vibration level of the COF curve is attributed to the steel fibres presence, as the sample exhibiting the most stable curve is the F-A one. As seen before, it is due to the fibres localizated on the surface, and their fundamental role in the third body formation.

St-F-A tricomponent sample presents a higher wear rate than all the corresponding bicomponent samples, even if it is still a contained value compared to others (see St-B sample for example, at 65.71 x10^4 $\mu M^3/Nm$ of wear rate). One reason for this behavior can be the lower resin content: 46.2%vol for St-F-A against 50.3%vol for St-F, 57.2%vol for F-A and 57.9%vol for St-A. Among the three components steel fibres, friction dust and aluminum oxide, it appears that the one having the strongest influence on wear increase is the steel fibres, as for F-A the wear factor K is equal to 3.19 x10^4 $\mu M^3/Nm$ and for St-F-A it is 10.82 x10^4 $\mu M^3/Nm$. It has been seen that at identical concentration in the steel fibre monocomponent the wear rate doesn't increase with respect to the basic mix (K =

4.46 x10^4 µM^3/Nm for the St/15 and K = 7.0 x10^4 µM^3/Nm for the basic mix), which is in agreement with the observed positive interaction (tan δ increased) for St/x samples. Then it can be concluded that steel fibres presence induce excessive wear due to a negative interaction with the other fillers as aluminum oxide, friction dust and barium sulfate as seen in the St-B-A sample study.

Some interaction between the components can be deduced from the previous bicomponents samples results. It has been seen that F-A, containing friction dust and aluminum oxide does not exhibit special interaction as the final material has intermediate properties between the monocomponents samples, but adding steel fibres, a decrease of the mechanical properties, as stiffness for instance (4.54 GPa for St-F-A against 6.43 GPa for F-A), can be observed. Such detriment of the mechanical properties leads to a high wear and a vibrated friction coefficient curve. St-F sample presents an excessive wear rate, mainly due to its porosity equal to 12%vol, which is still present in the St-F-A material at 11%vol so it contributes to the deterioration of the material. It is noteworthy that the tribological performances of both tricomponents St-B-A and St-F-A are very similar, as presented in TABLE 5.20, confirming the previous hypothesis: both barium sulphate and friction dust are relatively inert components, and can be considered more as space fillers than active components. On the opposite, steel fibres have a strong influence on the tribological performances, as the aluminum oxide abrasive.

TABLE 5.20 COF AND SPECIFIC WEAR RATE K VALUES FOR ST-F-A (STEEL FIBRE-FRICTION DUST-ALUMINUM OXIDE) AND ST-B-A (STEEL FIBRE-BARITE-ALUMINUM OXIDE) SAMPLES

Sample	St-F-A	St-B-A
COF mean	0.43	0.46
K, x10^4 µm^3/Nm	10.82	10.63

2. GRAPHITE BASED MATERIALS

2.1. Potassium hexatitanate fibres + Graphite + Aluminum Oxide (Ti/50-G/5-A/5.6 → Ti-G-A)

The chemical formulation of Ti-G-A mix is presented in TABLE 5.21.

TABLE 5.21 TI-G-A SAMPLE COMPOSITION

	BM	Potassium Hexatitanate fibre	Graphite	Aluminum oxide	Sum
Content, in %vol	69.4	20	5	5.6	100
Content, in %wt	46.3	36.9	5.6	11.2	100

In FIGURE 5.28 are presented the friction coefficient curves of bicomponents samples Ti-G and Ti-A and the resulting tricomponent Ti-G-A which contains the stronger abrasive (aluminum oxide) and the stronger lubricant (graphite) of the formula. All the samples contain potassium hexatitanate fibres, which give mechanical integrity to the materials. In FIGURE 5.29 are presented the wear data obtained for Ti-G-A and corresponding mono and bicomponent samples.

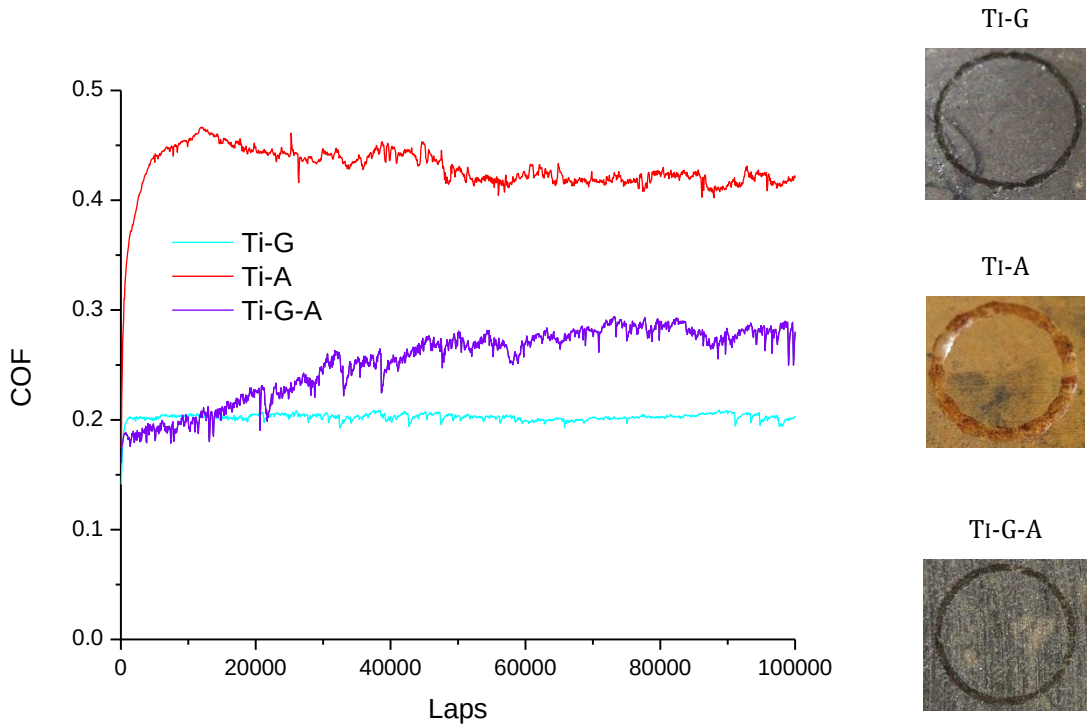

FIGURE 5.28 COEFFICIENT OF FRICTION IN FUNCTION OF THE NUMBER OF CYCLES, FOR TI-G (POTASSIUM HEXATITANATE FIBRE - GRAPHITE), TI-A (POTASSIUM HEXATITANATE FIBRE - ALUMINUM OXIDE), AND TI-G-A (POTASSIUM HEXATITANATE FIBRE - GRAPHITE - ALUMINUM OXIDE) SAMPLES

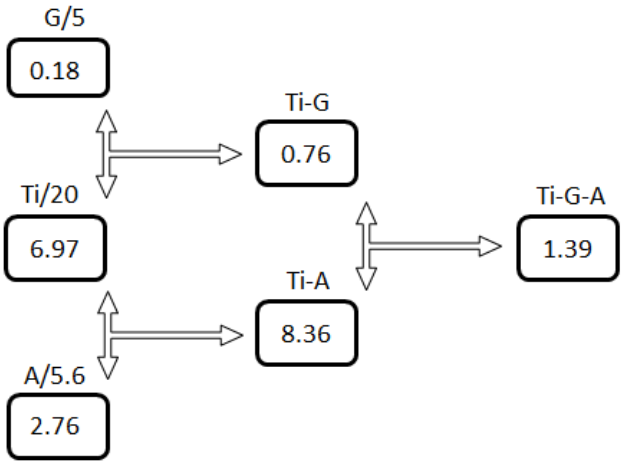

FIGURE 5.29 REPRESENTATION OF SPECIFIC WEAR RATE K FOR TI-G (POTASSIUM HEXATITANATE FIBRE - GRAPHITE), TI-A (POTASSIUM HEXATITANATE FIBRE - ALUMINUM OXIDE), AND TI-G-A (POTASSIUM HEXATITANATE FIBRE - GRAPHITE - ALUMINUM OXIDE) SAMPLES AND THE CORRESPONDING MONOCOMPONENT SAMPLES, X10^4 µM^3/NM

Friction coefficient of Ti-G-A sample starts at the graphite monocomponent sample level around 0.2 and then linearly increases to reach a medium value of 0.28. It can be hypothesized that the first component to get involved in the track formation is graphite, and then aluminum oxide particles previously covered step by step come in contact with the counterface and increase the COF, establishing a continuous cycle of transfer layer creation/destruction. The final plateau value is at a level between the two bicomponents samples, so no particular interaction is noticed here. For Ti-A sample, it appears that the wear increases a lot, presenting a value of 8.36x10^4 µm^3/Nm instead of 6.97x10^4 µm^3/Nm for Ti/20 and 2.76x10^4 µm^3/Nm for A/5.6 mainly due to the strength of the fibres network formed and the zones of aramid fibres accumulation on the track. For Ti-G-A the wear is much lower, demonstrating that the positive interaction found between potassium hexatitanate fibres and graphite is still present and protect the material from an excessive wear due to the aluminum oxide abrasive.

The high physical features values of Ti-A sample are not conserved for the Ti-G-A material, as the properties are intermediate or even lower between the corresponding bicomponents, as reported in FIGURE 5.30. The absence of supplementary interaction developed in Ti-G-A material is also visible on the tan δ curve, by DMTA measurements

presented in FIGURE 5.31, as the Tg temperature is the same for all the samples (Tg = 186°C for Ti-G, Tg = 186°C for Ti-A and Tg = 185°C for Ti-G-A).

There is no new interaction among the components in this sample, but the synergy found in Ti-G between potassium hexatitanate fibres and graphite is still present.

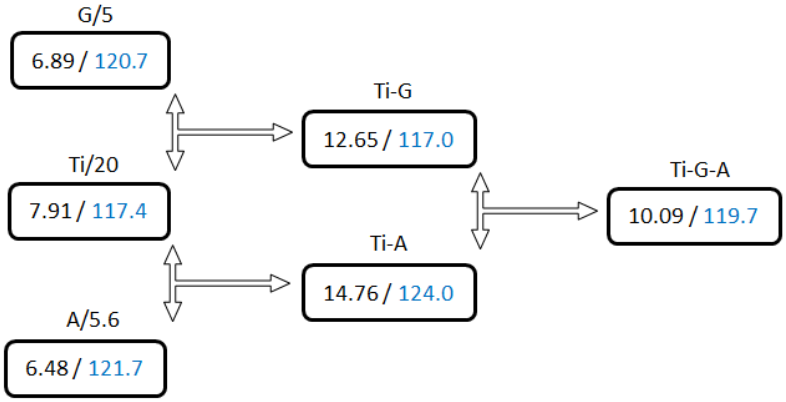

FIGURE 5.30 REPRESENTATION OF STIFFNESS (GPA, IN BLACK) AND HARDNESS (HRS, IN BLUE) VALUES FOR TI-G (POTASSIUM HEXATITANATE FIBRE - GRAPHITE), TI-A (POTASSIUM HEXATITANATE FIBRE - ALUMINUM OXIDE), AND TI-G-A (POTASSIUM HEXATITANATE FIBRE - GRAPHITE - ALUMINUM OXIDE) SAMPLES AND THE CORRESPONDING MONO AND BICOMPONENT SAMPLES

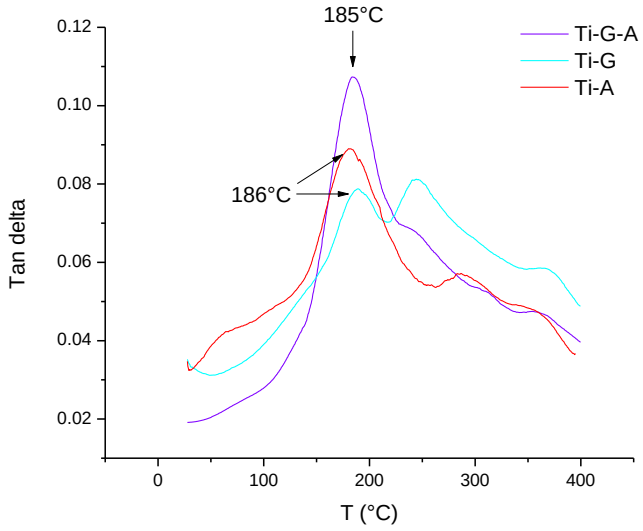

FIGURE 5.31 TAN DELTA CURVES OF TI-G (POTASSIUM HEXATITANATE - GRAPHITE), TI-A (POTASSIUM HEXATITANATE - ALUMINUM OXIDE) AND TI-G-A (POTASSIUM HEXATITANATE - GRAPHITE - ALUMINUM OXIDE) SAMPLES WITH TEMPERATURE

2.2. Friction Dust + Graphite + Aluminum Oxide (F/16-G/5-A/5.6 → F-G-A)

The chemical formulation of F-G-A mix is presented in TABLE 5.22.

TABLE 5.22 F-G-A SAMPLE COMPOSITION

	BM	Friction dust	Graphite	Aluminum oxide	Sum
Content, in %vol	73.4	16	5	5.6	100
Content, in %wt	65.7	11.7	7.6	15	100

Tribological tests are performed on F-G-A sample and the results together with the corresponding simpler samples are reported in FIGURE 5.32 and FIGURE 5.33.

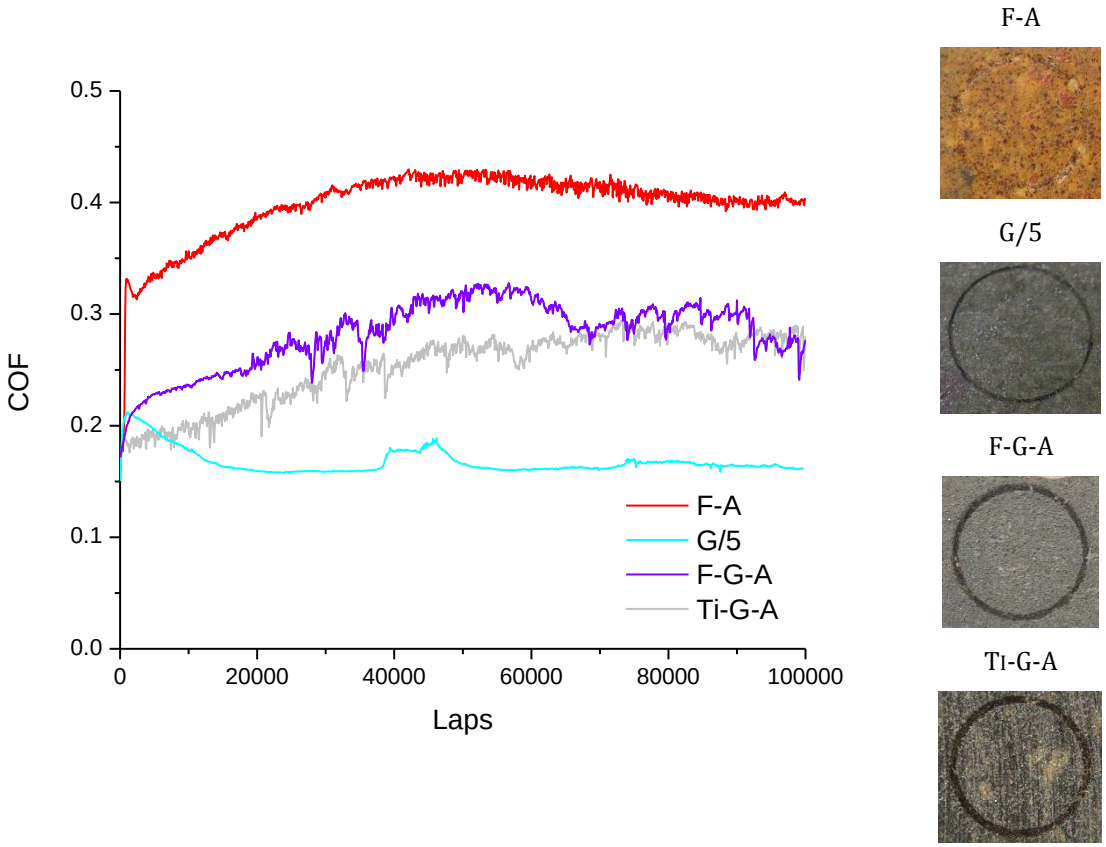

FIGURE 5.32 COEFFICIENT OF FRICTION IN FUNCTION OF THE NUMBER OF CYCLES, FOR F-A (FRICTION DUST – ALUMINUM OXIDE), G/5 (5%VOL GRAPHITE), F-G-A (FRICTION DUST - GRAPHITE - ALUMINUM OXIDE) AND TI-G-A (POTASSIUM HEXATITANATE - GRAPHITE - ALUMINUM OXIDE) SAMPLES

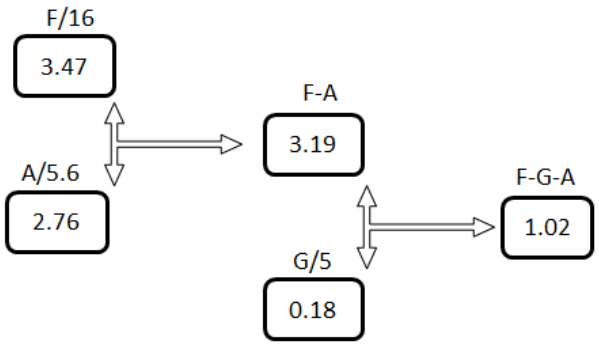

FIGURE 5.33 REPRESENTATION OF SPECIFIC WEAR RATE K FOR F-A (FRICTION DUST – ALUMINUM OXIDE) AND ITS CORRESPONDING MONOCOMPONENT SAMPLES, G/5 (5%VOL GRAPHITE) AND F-G-A (FRICTION DUST - GRAPHITE - ALUMINUM OXIDE) SAMPLES, $x10^4$ $\mu m^3/Nm$

Compared to the previous material Ti-G-A, the present sample does not contain any fibres except the aramid in the basic mix but the friction dust: it is expected to observe a weakening of the structure revealed by lower physico-mechanical properties as shown in TABLE 5.23. F-G-A friction coefficient curve presents the same trend as the F-A one, shifted at lower values due to graphite presence. This trend is also identical to the Ti-G-A one, demonstrating that friction dust and potassium hexatitanate don't have a particular influence on the friction contact. It has previously been seen that F-A does not exhibit special interaction between its components, so as F-G-A material: wear and COF values are slightly lower than the corresponding simpler samples due to the inert nature of friction dust, as demonstrated in the previous sample St-F-A. Once added to the matrix, friction dust dilutes the other components and leads to a decrease of the physical properties (see FIGURE 5.34). It permits to the material to be less fragile, get more adaptable and to reduce the wear, as it is shown by the comparison with Ti-G-A sample (TABLE 5.23).

TABLE 5.23 HARDNESS, STIFFNESS AND SPECIFIC WEAR RATE K VALUES FOR F-G-A (FRICTION DUST - GRAPHITE - ALUMINUM OXIDE) AND TI-G-A (POTASSIUM HEXATITANATE - GRAPHITE - ALUMINUM OXIDE) SAMPLES

Sample	F-G-A	Ti-G-A
Friction dust content, %vol	16	0
Aluminum oxide content, %vol	5.6	5.6
Graphite content, %vol	5	5
Potassium hexatitanate fibres content, %vol	0	20
Hardness, HRS	115.3±0.6	119.7±0.6
Stiffness, GPa	6.10±0.26	10.09±0.47
Wear Factor K, x10^4 µm^3/Nm	1.02	1.39

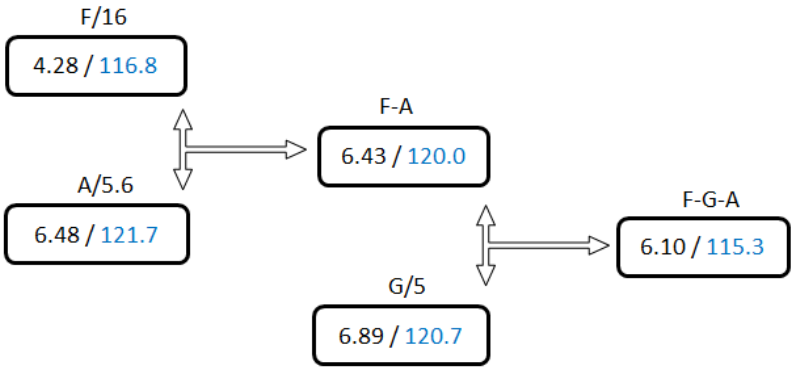

FIGURE 5.34 STIFFNESS (GPA, IN BLACK) AND HARDNESS (HRS, IN BLUE) VALUES OF F-G-A (FRICTION DUST - GRAPHITE - ALUMINUM OXIDE) SAMPLE AND OF ITS CORRESPONDING MONO AND BICOMPONENT SAMPLES

3. FROM MULTIPLE SYSTEMS TO COMPLETE FORMULA

3.1. Graphite + Silicon Carbide + Friction dust + Steel fibres (G/5-Si/3.4-F/16-St/15 → G-Si-F-St)

The chemical formulation of G-Si-F-St mix is presented in TABLE 5.24.

TABLE 5,24 G-SI-F-ST SAMPLE COMPOSITION

	BM	Silicon carbide	Graphite	Friction dust	Steel fibre	Sum
Content, in %vol	60.6	3.4	5	16	15	100
Content, in %wt	33.4	4.6	4.7	7.2	50.1	100

Tribological test results of G-Si-F-St and of the two bicomponents corresponding samples are presented in FIGURE 5.35 for COF variations and in FIGURE 5.36 for wear data.

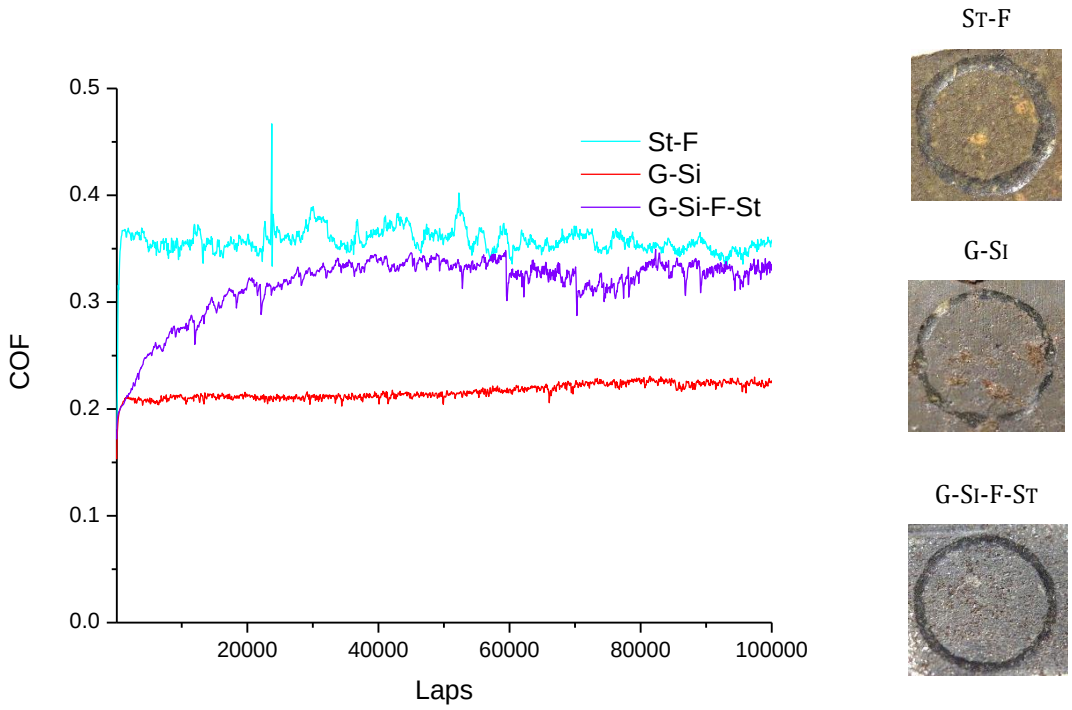

FIGURE 5.35 COF IN FUNCTION OF THE NUMBER OF CYCLES, FOR ST-F (STEEL FIBRES – FRICTION DUST), G-SI (GRAPHITE – SILICON CARBIDE) AND G-SI-F-ST (GRAPHITE – SILICON CARBIDE – FRICTION DUST – STEEL FIBRES) SAMPLES

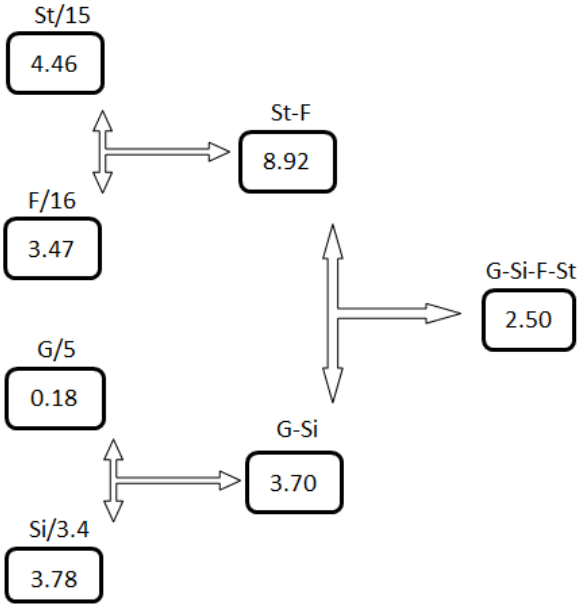

FIGURE 5.36 REPRESENTATION OF SPECIFIC WEAR RATE K FOR ST-F (STEEL FIBRES – FRICTION DUST), G-SI (GRAPHITE – SILICON CARBIDE) AND THEIR CORRESPONDING MONOCOMPONENT SAMPLES, AND G-SI-F-ST (GRAPHITE – SILICON CARBIDE – FRICTION DUST – STEEL FIBRES) SAMPLE, $X10^4$ $\mu M^3/NM$

Both St-F and G-Si samples COF curves are flat from the beginning of the test and the friction coefficient values appear immediately stabilized at 0.36 for St-F and 0.22 for G-Si. On the contrary, the quaternary mix G-Si-F-St presents a starting COF value at 0.20 and exponentially increase until a plateau at 0.33: there is competition between the lubricant graphite and the steel fibres starting from the lubricant COF level to finish with a plateau controlled by steel fibres. This sample contains steel fibres and graphite, the two elements individuated before as the main actors in the third body formation during friction. In that sense, it is not surprising to see that the resulting wear is much lower than both the bicomponents materials. Steel fibres constitute primary contact plateaus from which secondary and extended plateaus can build in order to form step by step an homogeneous third body, and graphite filler delaminates and contributes to the formation of a smooth protective layer. As a result there is a positive interaction as expected between graphite and steel fibres.

It is interesting to notice that even if no phenomenon of interaction filler-matrix has been observed for both bicomponents reported here, the glass transition temperature of the

quaternary mix G-Si-F-St is shifted toward higher temperatures (208°C instead of 181°C for St-F and 193°C for G-Si), as shown by the DMTA results in FIGURE 5.37. It means that the fillers network formed through the matrix is dense enough and well distributed to physically interfere with the oligomers dynamic, delaying the glass transition.

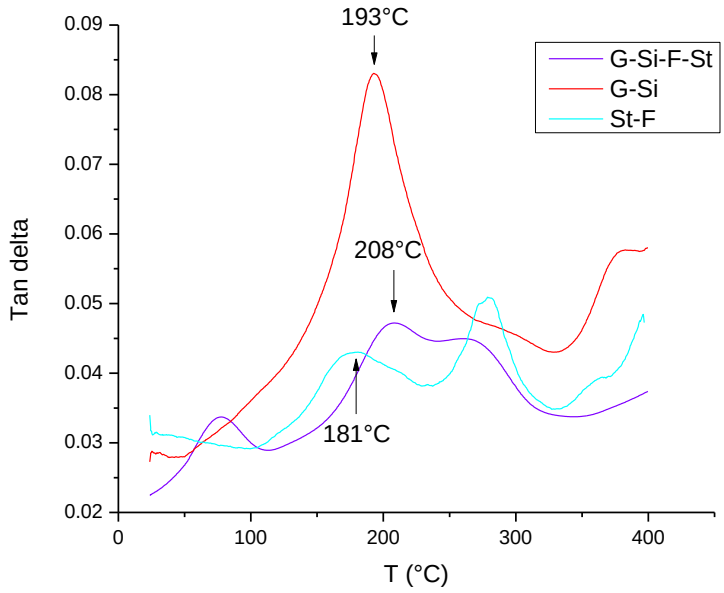

FIGURE 5.37 TAN DELTA VARIATIONS FOR G-SI (GRAPHITE – SILICON CARBIDE), ST-F (STEEL FIBRES – FRICTION DUST) AND G-SI-F-ST (GRAPHITE – SILICON CARBIDE – FRICTION DUST – STEEL FIBRES) SAMPLES IN FUNCTION OF TEMPERATURE

3.2. Barium Sulphate + Potassium hexatitanate + Petroleum Coke + Aluminum Oxide (B/50-Ti/20-C/10-A/5.6 → B-Ti-C-A)

The chemical formulation of B-Ti-C-A mix is presented in TABLE 5.25.

TABLE 5.25 B-TI-C-A SAMPLE COMPOSITION

	BM	Barium sulfate	Potassium hexatitanate	Coke	Aluminum oxide	Sum
Content, in %vol	33.1	39.1	15.7	7.7	4.4	100
Content, in %wt	14.3	55.9	18.8	5.3	5.7	100

The COF and wear values of B-Ti-C-A sample are reported with the Ti-A and B-C materials ones in FIGURE 5.38 and FIGURE 5.39 respectively.

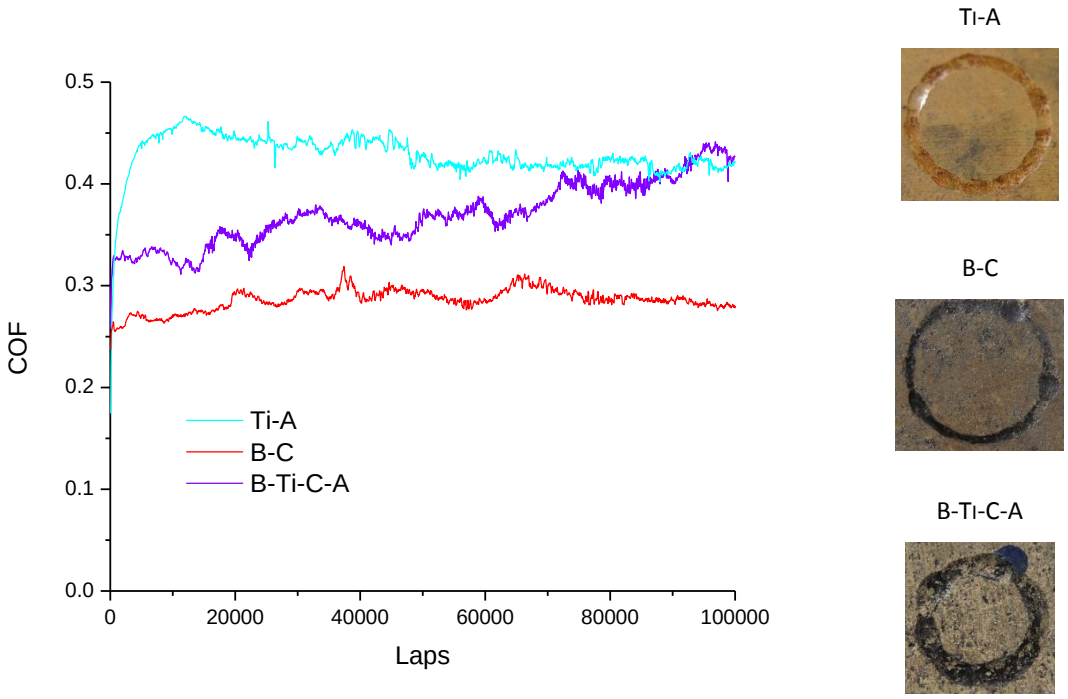

FIGURE 5.38 COF IN FUNCTION OF THE NUMBER OF CYCLES, FOR TI-A (POTASSIUM HEXATITANATE – ALUMINUM OXIDE), B-C (BARITE – COKE) AND B-TI-C-A (BARITE – POTASSIUM HEXATITANATE – COKE – ALUMINUM OXIDE) SAMPLES

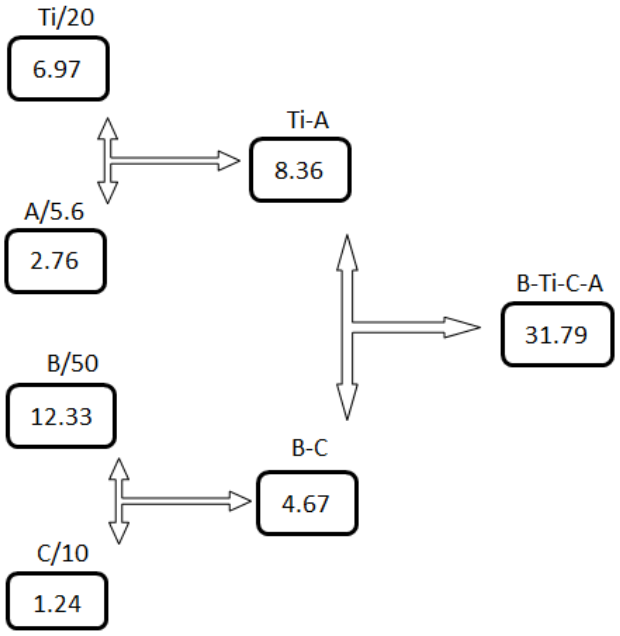

FIGURE 5.39 REPRESENTATION OF SPECIFIC WEAR RATE K FOR TI-A (POTASSIUM HEXATITANATE – ALUMINUM OXIDE), B-C (BARITE – COKE), THEIR CORRESPONDING MONOCOMPONENT SAMPLES AND B-TI-C-A (BARITE – POTASSIUM HEXATITANATE – COKE – ALUMINUM OXIDE) MIX, X10^4 $\mu m^3/Nm$

B-Ti-C-A sample friction coefficient curve presents higher vibrations than the two bicomponents ones, and a bigger tribological track. This observation together with the very high wear level reveals a global negative performance of the material. In details, the COF curve is composed of curve portions at low COF followed by curve portions at high COF, always holding a constantly increasing baseline. This is the signature of a continuous deterioration, which implies that the third body doesn't get formed efficiently, thus there is no protection of the surface. In fact, as seen before the main actors in the transfer layer construction are steel fibres and graphite, both absent in this material. Thus, the surface is not protected from abrasion and the wear rate is high, also due to the high porosity, as shown in TABLE 5.26.

TABLE 5.26 SPECIFIC WEAR RATE K, DENSITY AND POROSITY VALUES OF B-TI-C-A (BARITE – POTASSIUM HEXATITANATE – COKE – ALUMINUM OXIDE) SAMPLE

Sample	B-Ti-C-A
Specific wear rate K (x10^4 μm^3/Nm)	31.79
Density, g/cm^3	2.18± 0.04
Theoretical density, g/cm^3	3.01
Porosity, %vol	28

3.3. Complete formula (T)

The chemical formulation of T mix is presented in TABLE 5.27.

TABLE 5.27 T SAMPLE COMPOSITION

	BM	Barium sulfate	Potassium hexatitanate fibre	Coke	Aluminum oxide
Content, in %vol	30.8	18.6	11.9	7.7	4.1
Content, in %wt	14.3	28.5	15.3	5.6	5.7
	Graphite	Silicon carbide	Friction dust	Steel fibre	Sum
Content, in %vol	4.0	2.7	13.4	6.9	100
Content, in %wt	3.1	3.0	5.1	19.3	100

The complete formula has been used to prepare the T material. The tribological tests gave the results presented in FIGURE 5.40 (COF variations) and FIGURE 5.41 (wear data).

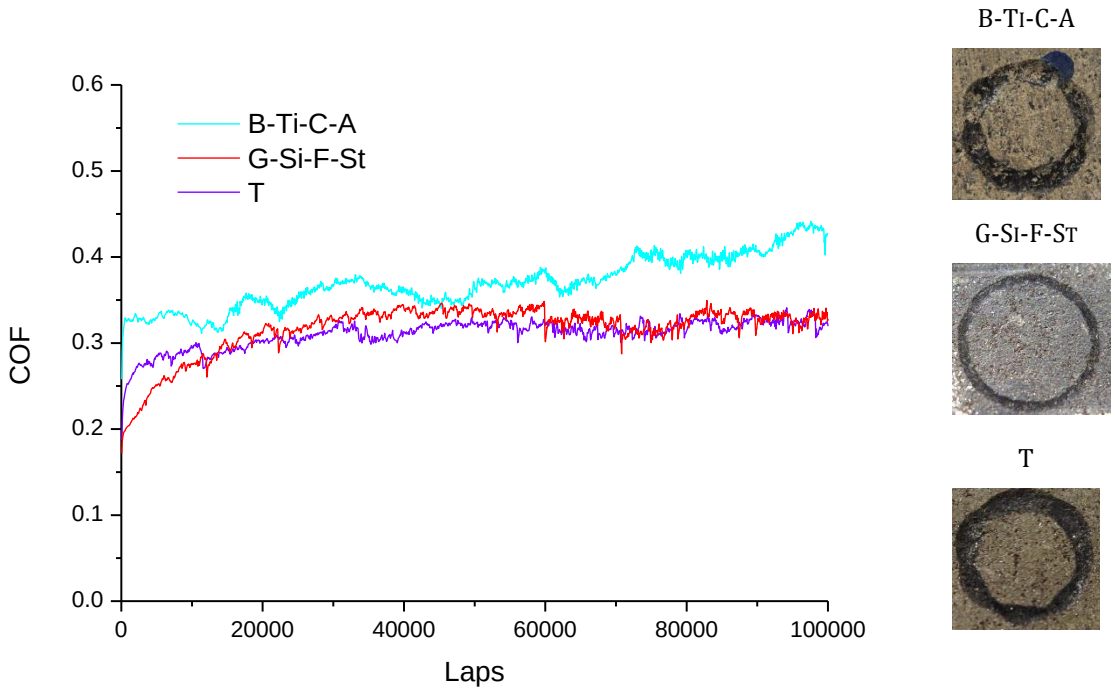

FIGURE 5.40 COF IN FUNCTION OF THE NUMBER OF CYCLES, FOR B-TI-C-A (BARITE – POTASSIUM HEXATITANATE – COKE – ALUMINUM OXIDE), G-SI-F-ST (GRAPHITE – SILICON CARBIDE – FRICTION DUST – STEEL FIBRES) AND T (ALL COMPONENTS) SAMPLES

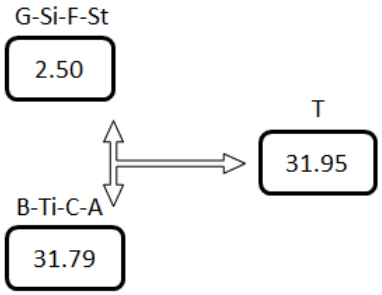

FIGURE 5.41 REPRESENTATION OF SPECIFIC WEAR RATE K FOR G-SI-F-ST (GRAPHITE – SILICON CARBIDE – FRICTION DUST – STEEL FIBRES), B-TI-C-A (BARITE – POTASSIUM HEXATITANATE – COKE – ALUMINUM OXIDE) AND T (ALL COMPONENTS) SAMPLES, $X10^4$ $\mu M^3/NM$

The tribological track design is very similar to the B-Ti-C-A material one and the specific wear rate are equal. The high wear rate here is probably due to the porosity value of 27%vol (see in TABLE 5.28), the higher measured in this study.

TABLE 5.28 COF, SPECIFIC WEAR FACTOR K AND POROSITY VALUES FOR T (ALL COMPONENTS) SAMPLE

Sample	T
COF mean	0.31
K, $x10^4$ $\mu m^3/Nm$	31.95
Porosity, %vol	27

CONCLUSION

The first category group together three bicomponent materials for which both fillers demonstrated an improvement on wear resistance property. Friction dust and aluminum oxide fillers don't present any kind of interaction and the resulting properties of F-A sample are intermediate between the corresponding monocomponents. Steel fibres and friction dust together lead to a negative effect on wear, due to porosity presence (inducing heat accumulation, and partial resin curing). Finally, St-A (steel fibres - aluminum oxide) sample also leads to a diminution of wear value, probably because of the strong interaction formed between fillers and matrix that causes a material embrittlement. Surprisingly, when fillers present good effect on wear, the resulting bicomponent exhibit negative tribology performances. B-C sample contains barium sulphate and petroleum coke, that both present a negative effect on wear, but it exhibits a resulting diminution in the wear value. A possible explanation is that there are high porosity and low density of the sample due to cavities on the sample surface that during friction contact get filled by fillers fragments. It is a good example of positive interaction.

The second category of bicomponent samples group together the ones composed by fillers with antagonist effect on the wear. The first sample is the one with steel fibres and barium sulphate (St-B). There is a clear negative interaction between these fillers: wear resistance worsen a lot. The friction coefficient level is controlled by barite but its vibrations are due to steel fibres presence at the surface. Excessive wear can be explained by the high density conjugated with porosity presence leading to heat accumulation. The further sample contains potassium hexatitanate fibres and graphite (Ti-G). Tribologic behaviour is close to the graphite monocomponent sample one, the thickened graphite film hinders the abrasive action of the fibres, but potassium hexatitanate fibres have a fundamental influence in the mechanical integrity of the material, as demonstrated by the

physical properties. As a result, this sample is a good example of positive interaction between fillers. For the graphite and silicon carbide containing material (G-Si), the friction coefficient curve is similar to the graphite sample one, while wear value is the one of the silicon carbide monocomponent. In fact, graphite protective layer is perpetually consumed due to the pressure applied on it and to the abrasive action of silicon carbide dispersed inside the matrix, and then regenerated. This material doesn't have additive fibres (except the aramid ones), so physical properties and wear resistance decline. The last bicomponent sample is made with potassium hexatitanate fibres and aluminum oxide (Ti-A). The resulting wear is much higher than the corresponding monocomponents; two reasons can be given to explain this behavior. First, hexatitanate fibres create a so strong network that the material becomes more brittle and second, it has been seen that there is accumulation and successive elimination of organic fibres pile on the tribological track.

Two tricomponent samples based on steel fibres as main transfer layer protagonist are studied, both containing aluminum oxide. As third component the first has barite. As observed in the bicomponent St-A, there is synergy between steel fibres and alumina but no new interaction is raised in St-B-A. This material presents a low wear rate, partly due to the positive interaction between alumina and resin. The neutral behavior of barite in the final properties are comparable to the friction dust one. The tribological results are identical for both tricomponent samples St-B-A and St-F-A: steel fibres and aluminum oxide are the active components of the formula. Two tricomponent samples based on graphite as protagonist of the transfer layer formation are studied, both with alumina. The first contains potassium hexatitanate fibres (Ti-G-A) and exhibits a low wear rate, demonstrating that the positive interaction found between potassium hexatitanate fibres and graphite is still present and protect the material, but there is no new interaction. The second sample has friction dust instead of fibres (F-G-A), and as concluded about St-F-A sample, friction dust in tribology shows a neutral behavior: once added to the matrix it dilutes the other components and leads to a decrease of the physical properties but COF and wear rate are not affected. For the first four-component sample G-Si-F-St there is a clear positive interaction; as expected, wear is low thanks to the presence of both steel fibres and graphite contributions to form the protective transfer layer. Positive

interaction is confirmed by the Tg temperature increase: it means that the fillers network formed through the matrix is dense enough and well distributed to physically interfere with the oligomers in a positive way and without embrittlement of the material. The other four-component sample B-Ti-C-A presents a very high wear, so a global negative tribological performance, which implies that the third body did not get formed efficiently.

LIST OF FIGURES

LIST OF TABLES

CONCLUSION

PRINCIPAL COMPONENT ANALYSIS

THEORY

Multivariate analysis often starts out with data involving numerous variables. Principal component analysis (PCA) is a dimension-reduction tool that can be used to reduce a large set of possible correlated variables to a smaller number of variables called *principal components* that still contain most of the information in the large set. It is useful to represent a multi variables analysis in many different directions, in a graphic in two dimensions that allows to loose very few information contained in the original dataset.

The PCA starts from an original dataset matrix made by variables and objects, in this study properties and samples respectively. The principal components are linear combinations of the original variables, weighted by their contributions to explain the variance in a particular orthogonal dimensions. PCA seeks a linear combination of variables so that the maximum variance is extracted from the variables. It then removes this variance and seeks a second linear combination which explains the maximum proportion of the remaining variance, and so on. The first principal components have a major variance, thus are more significative because contain more information. This analysis permits to use less principal components, more representative. So it is possible to represent in few dimensions the majority of all the original variables or the objects. It can be considered as a rotation of the axis of the original variable coordinate system to a new orthogonal axis, called *principal axis*, such as the new axes coincide with directions of maximum variation of the original variables. The principal component is a mathematical entity, so per definition it is only conceptual. The PCA rotation proceed to the transformation of physical variables into theoretical variables.

The mathematical method to determine the principal components consists in calculating *eigenvalues* and *eigenvectors* of the correlation matrix of the original data set matrix.

Eigenvectors and eigenvalues exist in pairs: every eigenvector has a corresponding eigenvalue. More precisely eigenvectors are the new space vectors while eigenvalues represent the correlation associated to each principal component. Afterwards the *matrix of the loadings* is formed by columns as eigenvalues and rows as variables, together with the *matrix of the scores* obtained from the product of matrix of the original data and the matrix of the loadings. Scores values determine the coordinates of the objects in the new space and are the sums of the products between old coordinates and the multiplicative coefficient, that are the corresponding loadings values.

Three types of plotting are possible:

- *The loading representation*, that permits to analyse the role of each variable in the principal components, their direct or inverse correlation and their importance. Once chosen the two principal components that constitute the coordinate axis (typically the first two), the coordinates of each variable are defined by the couple of loadings that each variable has in the two chosen components.
- *The scores plot* that permits to analyze the behavior of the objects in the different principal components, and their similarities. Once the two main components to constitute the coordinate axis are chosen, the coordinates of each object are defined by the couple of scores that each object has for the two considered components. The scores plot permits to visualize clusters of similar objects, presence of particular objects (outliers), and in general regularities and distributions.
- *The biplot*, the union of the first two. This graphic permits to contemporaneously represent objects and variables in order to evaluate the relations between them.

The variables have been selected from the whole study considering the pertinence they had in the general interaction case study. Nine variables have been retained: hardness, stiffness and storage modulus at 50°C for physico-mechanical characterization; glass transition temperature and thermal conductivity at 50°C for thermal characterization; COF average, COF standard deviation (evaluation of the COF curve vibrations), wear rate for the tribological characterization and porosity content for morphological characterization. Three different biplot graphics have been obtained. The first presents

only the monocomponent samples as objects, as they can be considered definitely different systems in respect of multiple containing fillers interactions ones. The second presents the construction and results of bicomponent samples from the monocomponent. The last presents as objects the entire set of 24 materials. The dataset is presented in TABLE 1.

RESULTS AND INTERPRETATION

TABLE 1 DATASET OF ORIGINAL VALUES

		Variables								
		Stiffness (GPa)	Thermal conductivity at 50°C (W/(m.K))	Hardness (HRS)	Porosity (%vol)	Tg (°C)	E' at 50°C (GPa)	COF average	COF dev. Stand.	Wear factor K (x10^4 μm^3/Nm)
Objects	**BM**	6.01	0.260	111.7	0	190	13.8	0.25	0.026	1.18
	St	3.76	0.955	98.3	12	207	11.53	0.42	0.023	5.75
	Ti	7.91	0.360	117.4	3	188	18.62	0.53	0.015	9.66
	F	4.28	0.189	116.8	9	193	5.23	0.41	0.021	3.96
	B	12.02	0.832	104.7	7	183	11.49	0.55	0.007	12.32
	G	6.89	0.317	120.7	3	185	11.77	0.19	0.016	0.09
	C	6.24	0.250	119.5	5	194	9.74	0.45	0.031	10.58
	A	6.48	0.269	121.7	7	191	8.54	0.57	0.014	4.88
	Si	6.35	0.249	119.7	6	167	9.84	0.48	0.046	15.83
	St-F	4.12	0.579	105.0	12	181	9.05	0.36	0.010	8.92
	Ti-G	12.65	0.842	117.0	0	186	20.12	0.20	0.003	0.76
	Ti-A	14.76	0.630	124.0	0	186	11.89	0.43	0.014	8.36
	B-C	10.11	1.074	96.0	22	190	9.73	0.29	0.008	4.67
	F-A	6.43	0.257	120.0	0	215	7.07	0.41	0.016	3.19
	G-Si	3.48	0.417	110.0	0	193	14.08	0.22	0.006	3.70
	St-B	9.48	1.334	104.0	13	213	19.61	0.48	0.027	65.71
	St-A	8.84	1.055	103.0	0	219	18.78	0.42	0.015	7.28
	Ti-G-A	10.09	0.698	119.7	3	185	21.57	0.27	0.010	1.39
	St-B-A	10.07	1.269	114.0	17	220	18.17	0.46	0.033	10.63
	St-F-A	4.54	0.739	118.0	11	231	12.65	0.43	0.011	10.82
	F-G-A	6.1	0.391	115.3	7	155	7.72	0.30	0.016	1.02
	G-Si-F-St	4.7	0.904	100.0	10	208	13.18	0.33	0.009	2.50
	B-Ti-C-A	6.29	0.889	92.3	28	211	6.87	0.39	0.025	31.79
	T	1.63	0.859	54.0	27	224	9.76	0.31	0.011	31.95

First, only monocomponent samples are considered as the objects of the biplot in order to recap the main observations done about the fillers main impact on the general material characteristics.

The calculation of the principal components compositions is presented in TABLE 2**.** The maximum of the variance is on the first three vectors F1, F2 and F3. For the corresponding biplot, the axis formed by F1 and F2 are chosen, as they represent 56% of the total variance, even if it implies that some information (mainly carried by F3 vector) gets partially lost. The biplot is presented in FIGURE 1.

TABLE 2 PRINCIPAL COMPONENTS COMPOSITIONS FOR MONOCOMPONENT SAMPLES

	F1	F2	F3	F4	F5	F6	F7	F8
Stiffness (GPa)	0.003	0.215	**0.637**	0.060	0.066	0.006	0.013	0.000
Thermal conductivity at 50°C (W/(m.K))	**0.772**	0.007	0.099	0.056	0.045	0.010	0.003	0.008
Hardness (HRS)	**0.745**	0.007	0.009	0.141	0.057	0.029	0.009	0.004
Porosity (%vol)	0.343	**0.575**	0.000	0.041	0.002	0.037	0.000	0.002
Tg (°C)	**0.543**	0.001	0.238	0.003	0.181	0.015	0.019	0.000
E' at 50°C (GPa)	0.003	**0.352**	0.155	0.350	0.122	0.016	0.003	0.000
COF average	0.015	0.221	**0.524**	0.085	0.128	0.016	0.009	0.002
COF dev. stand.	**0.356**	0.308	0.022	0.262	0.039	0.011	0.000	0.002
Wear factor K (x10^4 μm^3/Nm)	0.186	**0.400**	0.287	0.093	0.020	0.001	0.011	0.003

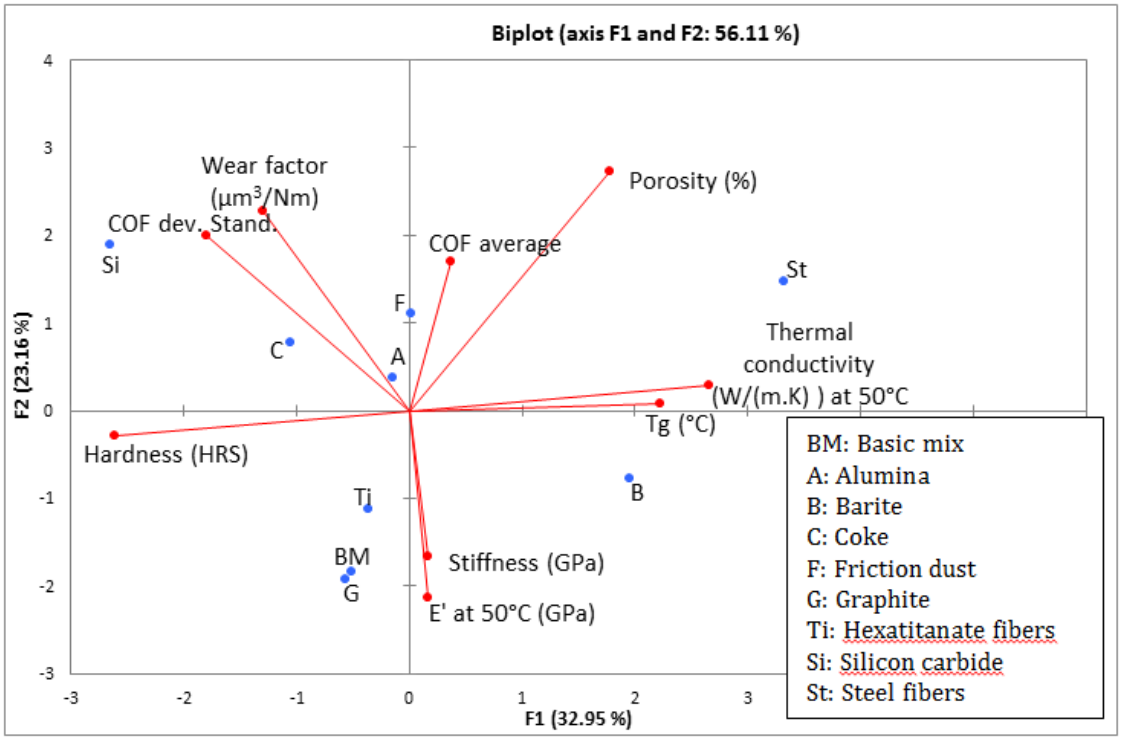

FIGURE 1 BIPLOT ON F1 AND F2 AXIS FOR MONOCOMPONENT SAMPLES

Stiffness vector is similar in direction and length to storage modulus one. This is in complete agreement with the theory: stiffness measured by ETEK instrument and storage modulus at 50°C both reveal information about the rigidity of the material. It is worthy to notice that the similarity on the monocomponent samples biplot between stiffness and storage modulus at 50°C is present in both other biplot graphics: the mono- and bicomponent samples one in FIGURE 2 and the all samples one in FIGURE 3. Anyway a correspondence is clearly visible between wear factor and COF standard deviation. In fact it can be hypothesized that more the friction coefficient vibrates more there are irregularities on the tribological track, which means that wear debris are generated during the friction. Two others variables are represented by vectors close to each other: thermal conductivity and glass transition temperature. There is no correlation between them, as the glass transition temperature is a measure of the affinity and interaction between the fillers dispersed in the matrix and the matrix itself (more precisely the resin), while the thermal conductivity reflects the capacity of the material to transmit heat, indirectly it measures the connection between the fillers. This observation in the biplot is due to the fact that for the samples in the vicinity ((St) and (B)) these two

properties vary in the same way, but the available data are insufficient to conclude about a relation between the two variables.

Besides, it is interesting to note that some variables are not correlated while the opposite could have been expected. For example wear factor is not linked with porosity. In fact the more porous sample is the one containing steel fibers (St) and the value is equal to 12%vol, which is far from the porosity values of some multicomponent samples (as 22%vol for (B-C) sample containing barite and coke, or 28%vol for (B-Ti-C-A) sample containing barite, potassium hexatitanate, coke and alumina). In the mono- and bicomponents samples biplot in FIGURE 2 and in the all samples biplot in FIGURE 3 these two variables are associated. Moreover, for all samples wear is not correlated with physico-mechanical parameters as hardness, stiffness and storage modulus. The opposite could have been explained by a too high strength and rigidity of the material leading to an embrittlement of the matrix, thus an excessive wear rate. The absence of correlation means that wear mechanisms are more complex and depends on many factors, including the interaction filler/matrix. In fact for the all samples biplot in FIGURE 3**,** wear factor is closely linked with the glass transition temperature: more the filler interacts with the resin higher is the glass transition, and higher the wear because the friction contact causes the estrangement not of fine particles of resin around the fillers but of bigger debris of matrix and filler due to the strong bonding between them. Due to the multiplicity of fillers inside the multicomponent samples, there are more interaction created and this correlation between wear and glass transition temperature is visible only on the monocomponent biplot graphic.

For the mono and bicomponent samples, there is correlation between COF average value and COF vibrations (quantified by the standard deviation value). This correspondence is explained by the filler nature: a lubricant as graphite generates a film on the material surface which leads to a low and stable friction coefficient value. On the other biplot this is not visible as these two variables are mainly expressed on the F3 vector.

Steel fibers monocomponent sample (St) is mainly characterized by its high thermal conductivity (it is the only metallic filler in this study) and its porosity (the highest among the monocomponent samples). Potassium hexatitanate fibers endows the material with strength and integrity, which is reflected by the most important variables to describe the (Ti) sample: hardness and stiffness/storage modulus. Silicon carbide is a

strong abrasion-resistant filler principally characterized by a high hardness value, and due to its abrasivity, a high wear factor and a COF vibrated curve. The petroleum coke monocomponent sample (C) at 10%vol presents similar characteristics to the SiC (Si) material: abrasive behavior with high wear and high hardness. As a consequence these two materials are close to each other on the biplot graphic. The graphite based sample (G) is very close to the blank material: according to the whole study performed, it is mainly characterized by its tribological features, but in this biplot the friction coefficient is not taken in account (as it is represented in the F3 vector). The graphite monocomponent sample is the only one for which the considered content is inferior to the literature reference one; its others properties are similar to the reference sample ones and that justify their proximity in the biplot. Barite sample (B) is characterized by its glass transition temperature and its stiffness/storage modulus values. This filler acts as a plasticizer, and its monocomponent sample is the most concentrated one (50%vol of filler), which leads to a drastic glass transition decrease. Stiffness and storage modulus are high due to the high filler concentration and the good cohesion of the entire material. Friction dust and alumina based materials (F) and (A) respectively are located in the center of the graphic. Their positions here are silent, as they correspond to projections on the F1-F2 biplot of other vectors.

After the study of the monocomponent samples, it is interesting to investigate the relative position of bicomponent samples in respect of their corresponding monocomponents. In TABLE 3 are presented the principal components compositions and then in FIGURE 2 the biplot.

TABLE 3 PRINCIPAL COMPONENTS COMPOSITIONS FOR THE MONO- AND BICOMPONENT SAMPLES

	F1	F2	F3	F4	F5	F6	F7	F8
Stiffness (GPa)	0.127	0.248	0.171	**0.353**	0.011	0.047	0.038	0.000
Thermal conductivity at 50°C (W/(m.K))	**0.939**	0.010	0.002	0.011	0.000	0.001	0.014	0.001
Hardness (HRS)	**0.587**	0.023	0.280	0.005	0.003	0.055	0.026	0.015
Porosity (%vol)	0.222	**0.346**	0.229	0.139	0.007	0.012	0.009	0.036
Tg (°C)	0.271	0.000	0.003	**0.455**	0.213	0.047	0.005	0.006
E' at 50°C (GPa)	**0.318**	0.248	0.188	0.037	0.090	0.093	0.005	0.020
COF average	0.009	**0.308**	0.225	0.073	0.292	0.093	0.001	0.000
COF dev. stand.	0.047	**0.488**	0.184	0.030	0.122	0.001	0.127	0.001
Wear factor K (x10^4 μm^3/Nm)	**0.371**	0.189	0.249	0.005	0.050	0.035	0.088	0.014

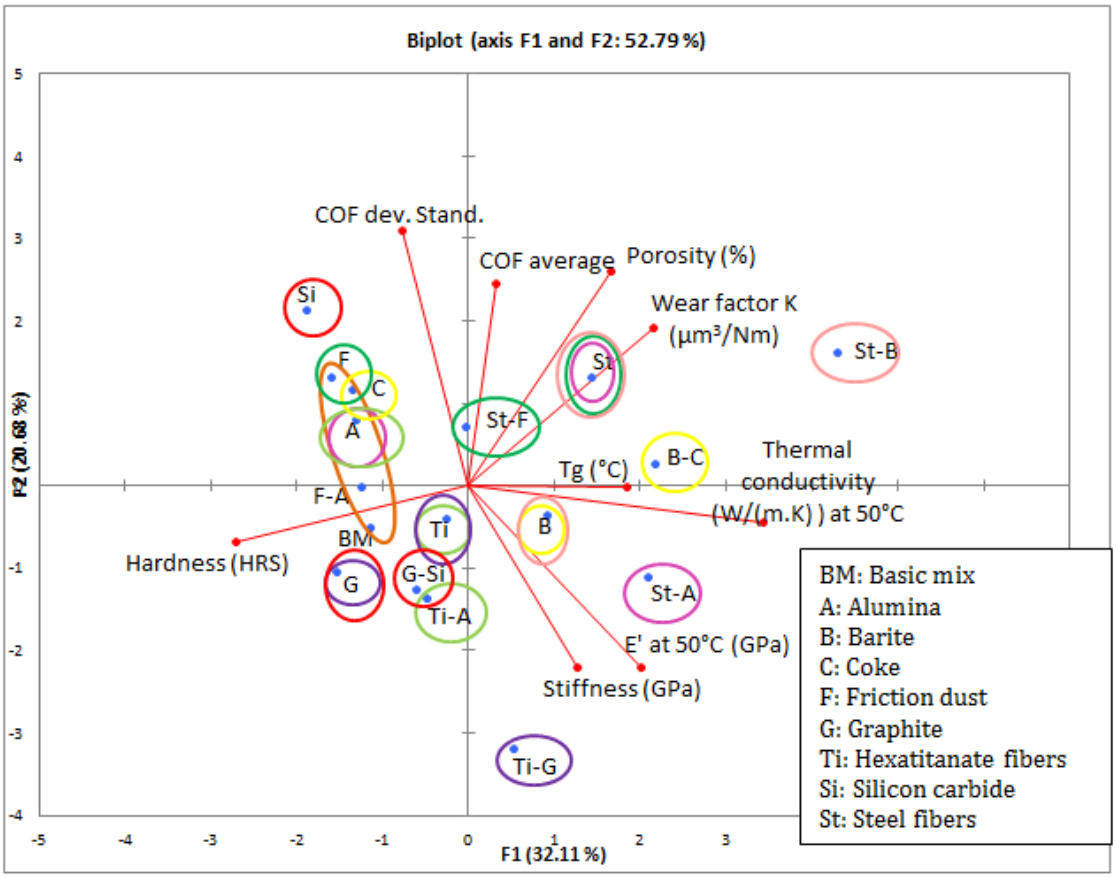

FIGURE 2 BIPLOT ON F1 AND F2 AXIS FOR MONO- AND BICOMPONENT SAMPLES

(F-A) (friction dust – alumina) sample is close to its monocomponent samples (F) and (A), shifted towards stiffness vector: in fact except a higher stiffness the other properties are intermediate between the (F) and (A) samples ones. The (St-A) (steel fibers – alumina) sample is clearly shifted toward stiffness and storage modulus vectors. In fact it has been demonstrated that due to the strong interaction developed in this material, stiffness is very high and leads to a global embrittlement which induces a high wear. A similar reasoning can be made about (Ti-A) (potassium hexatitanate fibers - alumina) sample aligned with (Ti) and (A) monocomponent materials where fibers presence leads to the formation of a strong network. (B-C) (barite – coke) sample points out the glass transition temperature vector. This sample is characterized by a strange behavior, as it is only partially cured during the process, presents a high porosity level but a low wear rate: there is liquefaction of the resin during friction that permits the crosslinking of the binder and the contemporaneous filling of the pores on surface. (Ti-G) (potassium titanate – graphite) sample material is drifted towards storage modulus and stiffness

vectors. In fact the hexatitanate fibers presence leads to an optimal dispersion and delamination of graphite and the combination of fibers (potassium hexatitanate) and flakes (graphite) creates a strong network, which significantly increase the mechanical strength of the material. (G-Si) (graphite – silicon carbide) bicomponent sample is much closer to the (G) one containing the lubricant instead of the Si one containing the abrasive, this observation corroborates the fact that graphite during the frictional contact forms a layer on the surface of the sample that hinders the rest of the material. The (St-F) (steel fibers – friction dust) bicomponent samples is placed in the in-between space of its corresponding monocomponent materials, revealing the absence of particular interaction between its ingredients. (St-B) (steel fibers – barite) sample compared to its monocomponents constitutents is shifted towards the wear vector. In fact it clearly appeared that this bicomponent material exhibits a very high wear rate. Lots of reasons can explain this phenomenon: difficulty to compact steel fibers, too low resin concentration to bind all the elements, high porosity content, high density leading to heat accumulation and then excessive degradation of the sample.

To complete this study a last PCA is performed with the entire set of data. The principal components compositions are presented in TABLE 4 and the corresponding biplot in FIGURE 3.

TABLE 4 PRINCIPAL COMPONENTS COMPOSITIONS FOR ALL SAMPLES

	F1	F2	F3	F4	F5	F6	F7	F8	F9
Stiffness (GPa)	0.057	**0.616**	0.049	0.191	0.011	0.012	0.030	0.028	0.007
Thermal conductivity at 50°C (W/(m.K))	**0.523**	0.355	0.006	0.019	0.000	0.037	0.006	0.006	0.047
Hardness (HRS)	**0.654**	0.039	0.152	0.017	0.002	0.016	0.041	0.078	0.000
Porosity (%vol)	**0.703**	0.081	0.002	0.115	0.000	0.034	0.000	0.037	0.027
Tg (°C)	**0.488**	0.021	0.002	0.329	0.078	0.033	0.040	0.006	0.003
E' at 50°C (GPa)	0.000	**0.761**	0.001	0.082	0.068	0.011	0.057	0.006	0.015
COF average	0.029	0.000	**0.623**	0.000	0.283	0.022	0.042	0.000	0.000
COF dev. stand.	0.009	0.069	**0.614**	0.010	0.196	0.086	0.005	0.011	0.000
Wear factor K (x10^4 μm^3/Nm)	**0.541**	0.007	0.157	0.002	0.073	0.158	0.060	0.001	0.001

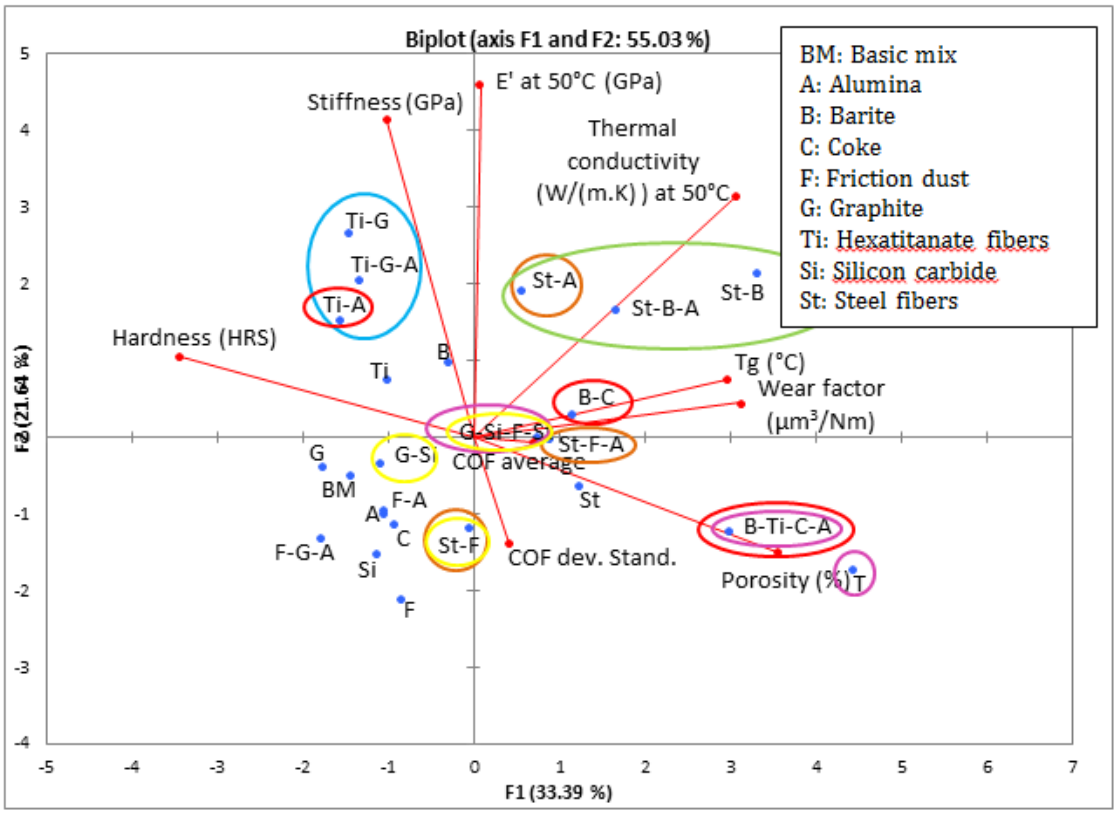

FIGURE 3 BIPLOT ON F1 AND F2 AXIS FOR ALL SAMPLES

From bi- to tricomponent samples, three materials on the biplot graphic are located between their corresponding bicomponent samples, demonstrating a general average of their properties and thus an absence of new interaction. These materials are (Ti-G-A) with potassium titatante fibers, graphite and alumina (from bicomponents (Ti-G) and (Ti-A)), (St-B-A) with steel fibers, barite and alumina (from bicomponents (St-B) and (St-A)) and (St-F-A) with steel fibers, friction dust and alumina (from bicomponents (St-F) and (St-A)). (G-Si-F-St) sample with graphite, silicon carbide, friction dust and steel fibers is not in the middle of (G-Si) and (St-F). Actually this observation is easily explained by the interaction developed in the material. Steel fibers promote the creation of plateaus on the sample surface while graphite filler contributes to the formation of a smooth protective layer. As a result there is a positive interaction between graphite and steel fibers revealed by the glass transition shift towards higher temperature. (B-Ti-C-A) sample with barite, hexatitanate fibres, coke and alumina is created from (B-C) and (Ti-A), which are both along the porosity vector; as for (B-Ti-C-A) it is not placed in the space between the two

bicomponents but clearly shifted in the direction of main porosity weight on the total material characteristics. It can be deduced that the other properties are in the average of the bicomponent ones. Total sample is created from (G-Si-F-St) and (B-Ti-C-A), but is not placed between them: its position on the biplot graphic is clearly shifted towards the porosity variable. In fact together with the (B-Ti-C-A) sample, they present the highest porosity contents with respect to all samples: this characteristic is the main explanation for their very high wear rate.

CONCLUSION

The work developed in this thesis proposes a method to study a complex system. This method consists in the formulation of an important number of samples which basis is a phenol formaldehyde resin mixed together with aramid fibres. These samples present an increasing complexity of formula, starting from the monocomponents containing only one filler to finish with the complete formula with a total of ten ingredients. A systematic and complete characterization of the entire bench of materials permits to understand first the single filler effect on the general properties and then the interaction created between fillers themselves when dispersed in the matrix. Good physical properties are essential to insure a sufficient mechanical strength to the material, as a high thermal resistance is primordial considering the braking temperatures. Among all the performed measurements, some seem more relevant to discriminate the influence of the fillers on the material features as glass transition temperature revealed by DMTA, porosity value, COF and wear rate, ecc, while others turned out to be less pertinent, for instance DSC for rigid materials, FT-IR, ecc.

Among the eight fillers dispersed in the matrix, graphite and steel fibres demonstrated a particular behavior, more precisely due to their role in the third body formation as it is largely reported in literature. Their functions are especially highlighted in the four-component sample containing both of them together with silicon carbide and friction dust, as this material exhibit one of the lowest wear rate measured in this study. In the case of graphite when dispersed together with another ingredient it controls the friction coefficient trend but wear rate is relatively high due to the perpetual consummation and reconstruction of the lubricant protective layer. In many of the materials, porosity grows with the growing formula complexity and it appeared that in the majority of the cases its

presence explains the high wear rate. In fact porosity leads to heat accumulation, partial resin curing and extra wear. In other cases interaction between fillers is strong enough to cause an embrittlement of the material and to cause excessive wear debris production. The complete material presents a high wear rate due to an excessive porosity level; in fact the formula has been elaborated from monocomponent content in order to evaluate the filler interaction effect, not to obtain a high performant friction material. This last observation highlights the fact that formulation is more an art than a science, and even if lots of individual conclusions have been deduced from the present work about filler interaction, considering the complexity of the system experimental tests are always indispensable.

In this last part a chemometrics analysis has been performed, showing how it is possible to connect a large set of data and analyse it in order to evaluate the goodness of numerous materials. The three drawn biplots highlighted some of the phenomena found out during the samples characterization, given them a graphical representation. This method of analysis permits to formulate hypothesis in basis of tests non performed, by analogy with other samples.

This PhD thesis work opened a vast field of analogous studies which are for the moment absent from literature. It could be interesting to investigate deeper on one method performing more samples or adding variables to this bunch of materials. The latter idea already opened a parallel PhD work about tribological characterization of raw materials in powder form.

BIBLIOGRAPHY

1. **M.G. Jacko, S.K. Rhee.** Kirk-Othmer Encyclopedia of Chemical Technology. *Wiley.* 4th. New York : s.n., 1992, Vol. 4.

2. **M.G. Jacko, P.H.S. Tsang, S.K. Rhee.** 1984, Wear, Vol. 100, pp. 503–515.

3. **Anderson, A.E.** *ASM Handbook, Friction, Lubrication and Wear Technology ASM International.* 1992, Vol. 18, pp. 569–577.

4. **Friedrich, K.** Advances in Composite Tribology.

5. **Moore, D.F.** Principles and Applications of Tribology. s.l. : Elsevier, 2013.

6. **Spa, Metelli.** *Technical manual .*

7. **M. Duchene, M. Charloteaux.** *Le Freinage .* Antwerp : Plantyn, 1975.

8. **Baker, A.K.** *Vehicle Braking.* London : Pentech Press, 1987.

9. **TP. Newcomb, R.T. Spurr.** *Commercial Vehicle Braking.* London : Newnes-Butterworths, 1981.

10. **Goodsell, D.** *Dictionary of Automotive Engineering.* London : Butterworths, 1989.

11. **Crouse, W.H.** *Automotive Mechanics .* New York : McGraw-Hill, 1970.

12. **W. Alley, W.E. Billiet.** *Disc and Drum Brake Service .* Chicago : American Technical Society, 1976.

13. **Anonymous.** *Bosch Automotive Handbook .* Stuttgart : Robert Bosch GmbH, 1976.

14. *Thermal and fade aspects of a non asbestos semi metallic disc brakepad formulation with two different resins.* **M.A. Sai Balaji, K. Kalaichelvan.** 2013, AdvancedMaterials Research, Vols. 622-623, pp. 1559–1563.

15. **Nicholson, G.** *Facts about Friction.* Winchester, Virginia : Gedoran.

16. *Composites as friction materials: recent developments in non-asbestos fiber reinforced friction materials—a review.* **Bijwe, J.** 3, 1997, Polymer Composites, Vol. 18, pp. 378–396.

17. *Compositions, Functions, and Testing of Friction Brake Materials and Their Additives.* **Blau, P.J.** 2000. ORTN/TM-2001/64.

18. **G. Crosa, I.M.R. Baumvol.** Tribology of Polymer Composites Used as Frictional Materials. *Advances in Composite Tribology.* s.l. : Elsevier Science Publishers B.V., 1993, 16.

19. *Technical Paper 800667.* **Loken, H.Y.** 1980. SAE.

20. *Combinatorial Screening of Ingredients for Steel Wool Based Semimetallic and Aramid Pulp Based Nonasbestos Organic Brake Materials.* **C.-F. Tang, Y. Lu.** 1, 2004, Journal of Reinforced Plastics and Composites, Vol. 23.

21. *Development of a Friction Material Formulation Without Metals by Taguchi Design of Experiments.* **D.M. Elzey, R. Vancheeswaran.** 2000. Proceedings of the 18th Annual Brake Colloquium and Engineering Display (Society of Automotive Engineers). pp. 17-34.

22. *The wear of aramid fiber reinforced brake pads: the role of aramid fibers.* **T. Kato, A. Magario.** 1994, Tribol. Trans., Vol. 37, pp. 559-565.

23. *Friction Material Design for Brake Pads Using Database.* **T. Kato, H. Soutome.** 2001, Trib. Trans., Vol. 44.

24. *Application of Chemometrics to the Production of Friction Materials: Analysis of Previous Data and Search of New Formulations.* **G. Drava, R. Leardi, A. Portesani, E. Sales.** 1996, Chemom. Intelligent Lab., Vol. 32, pp. 245–255.

25. *Optimizing Friction Formulation Technique with Emphasis on Relational Grade Analysis.* **Y. Lu, M.A. Wright.** 2000. International SAMPE Symposium and Exhibition. Vol. 45, pp. 1972–1978.

26. *Design of Experiments to Identify Material Properties.* **T. Tryland, O.S. Hopperstad, M. Langseth.** 2000, Mater. and Design, Vol. 21, pp. 477–492.

27. *A combinatorial approach for automotive friction materials: Effects of ingredients on friction performance.* **Lu, Y.** 2006, Composites Science and Technology , Vol. 66, pp. Composites Science and Technology 66 (2006) 591–598.

28. *A combinatorial approach for automotive friction materials: combined effects of ingredients on friction performance.* **Y., Lu.** 5, 2002, Polym Compos , Vol. 23, pp. 814–823.

29. **Chawla, K.K.** *Composite Materials: Science and Engineering, 2nd Edition.* New York : Springer, 1998.

30. **Salamone, J.C.** *Polymeric Materials Encyclopedia.* Boca Raton : CRC Press, 1996, Vol. 7.

31. **H.S. Okubo, C.E. Albertson, R.K. Nibert.** *Asbestos free friction materials. US Pat. 4446203* 1984. United States Patent and Trademark Office.

32. **W.N. Smith, P. Boyd.** *Carbonaceous friction materials. US Pat. 5965658* 1999. United States Patent and Trademark Office.

33. **R.A. Carlson, J.L. Headley.** *Fiber mixtures for brake pads. US Pat. 5871159* 1999. United States Patent and Trademark Office.

34. **Brinzey, A.E.** *Friction materials with universal core of non-asbestos fibres. US Pat. 5041471* 1991. United States Patent and Trademark Office.

35. **D. Chan, G.W. Stachowiak.** Review of automotive brake friction materials. *Proc. Instn Mech. Engrs Part D: J. Automobile Engineering.* 2004, Vol. 218.

36. *Friction and wear of friction materials containing two different phenolic resins reinforced with aramid pulp.* **S.J. Kim, H. Jang.** 2000, Tribology International, Vol. 33, pp. 477–484.

37. **P. Gopal, L.R. Dharani, Frank D. Blum.** Hybrid phenolic friction composites containing Kevlar pulp. Part I. Enhancement of friction and wear performance. *Wear .* 1996, Vol. 193, pp. 199-206.

38. *Synergistic effects of aramid pulp and potassium titanate whiskers in the automotive friction material.* **S.J. Kim, M.H. Cho, D.-S. Lim, H. Jang.** 2001, Wear, Vol. 251 , pp. 1484–1491.

39. **S.K. Sinha, S.K. Biswas.** Effect of sliding speed on friction and wear of unidirectional aramid fibre-phenolic resin composite. *J. Mater. Sci.* 1995, Vol. 30, pp. 2430-2437.

40. *Fibres in friction materials symposium.* **Anderson, A.E.** Atlantic City, New Jersey : s.n., 1987. Society Automotive Engineers.

41. **H. Jang, K. Ko, S.J. Kim, R.H. Basch, J.W. Fash.** The effect of metal fibers on the friction performance of automotive brake friction materials. *Wear.* 2004, Vol. 256, pp. 406–414.

42. **Gulledge, H.C.** *Ind. Eng. Chem.* 1960, Vol. 52, pp. 117–118.

43. **J.V. Milewski, H.S. Katz.** *Handbook of Reinforcements for Plastics.* New York : Van Nostrand Reinhold, 1987.

44. **N. Masaki, S. Uchida, H. Yamane, T. Sato.** Characterization of a New Potassium Titanate, KTiO2(OH) Synthesized via Hydrothermal Method. 2002, Vol. 14, 1, pp. 419–424.

45. **A. Hikichi, M. Haruta, K. Horiguchi.** *Friction material. U.S. Patent 6,670,408* 2003.

46. **I. Kobayashi, Y. Aramaki.** *U.S. Patent 5,383,963* 1995.

47. *Tribological properties of potassium titanate in the brake friction material; Morphological effects.* **K.H. Cho, M.H. Cho, S.J. Kim, H. Jang.** 2008, Tribol Lett, Vol. 32, pp. 59–66.

48. **M. Kumar, B.K. Satapathy, A. Patnaik, D.K. Kolluri, B.S.Tomar.** Hybrid composite friction materials reinforced with combiation of potassium titanate whiskers and aramid fibre: Assessment of fade and recovery performance. *Tribology International.* 2011, Vol. 44, pp. 359–367.

49. *Characterization of substituted phenol-formaldehyde Resins using solid-state carbon-13 NMR.* **B.R. Sinha, D. O'Connor, F.D. Blum.** 1989, Journal of Applied Polymer Science, Vol. 38, pp. 163-171.

50. **J.H.P. Tyman, N. Jacobs.** *J. Chromatogr.* 1971, Vol. 54, 83.

51. **P.H. Gedham, P.S. Sampathkumaran.** Cashew nut shell liquid: extraction, chemistry and application. *Prog. Org. Coatings.* 1986, Vols. 115-157, 14.

52. *Effect of Cashew Nut Shell Liquid (CNSL) on Properties of Phenolic Resins.* **P.A. Mahanwar, D.D. Kale.** 1996, Journal of Applied Polymer Science, Vol. 61, pp. 2107-2111.

53. **Harvey, M.T.** *Composition of matter and methods and steps of making and using the same. US Pat. 2157126 A* [ed.] Harvel Corp. 1935.

54. *Cure characteristics of alkali catalyzed cashew nut shell liquid-formaldehyde resin.* **L.Y. Mwaikambo, M.P. Ansell.** 2001, J Mater Sci. , Vol. 36, pp. 3693–3698 .

55. *Cashew Nut Shell Liquid–Based Tailor-Made Novolac Resins: Polymer Morphology Quantitation by 1-D and 2-D NMR Techniques and Performance Evaluation.* **D. Roy, P.K. Basu, P. Raghunathan, S.V. Eswaran.** 2003, Journal of Applied Polymer Science, Vol. 89, pp. 1959 –1965 .

56. **Y.T. Vu, J.E. Mark.** Blends of Natural Rubber with Cardanol-Formaldehyde Resins. *Polym-Plast Technol Eng. .* 1999, Vol. 38, p. 189.

57. *A new crosslinkable polyphenol from a renewable resource.* **R. Ikeda, H. Tanaka, H. Uyama, S. Kobayashi.** 2000, Macromol. Rapid Commun., Vol. 21, pp. 496–499.

58. **A.K. Misra, G.N. Pandey.** Kinetics of Alkaline-Catalyzed Cardanol–Formaldehyde Reaction. *J. Appl. Polym. Sci.* 1984, Vol. 29, pp. 361–372.

59. *The effect of phenolic resin, potassium titanate, and CNSL on the tribological properties of brake friction materials.* **Y.C. Kim, M.H. Cho, S.J. Kim, H. Jang.** 2008, Wear, Vol. 264, pp. 204–210.

60. **T. Komori, S. Miyake, Y. Senoo.** *Brake friction material . US Pat. 4954536* 1990. United States Patent and Trademark Office.

61. **Guo, X.** Radiopaque, Barium Sulfate-Filled Biomedical Compounds of a Poly(Ether-Block-Amide) Copolymer. *Journal of Applied Polymer Science.* 2008, Vol. 109, pp. 4015–4024.

62. *Tribological properties of polymer composites containing barite (BaSO4) or potassium titanate (K2O . 6(TiO2)).* **S.J. Kim, M.H. Cho, R.H. Basch, J.W. Fash, H. Jang.** 3, 2004, Tribology Letters, Vol. 17, pp. 655-661.

63. **P.J. Bryant, P.L. Gutshall, L.H. Taylor.** Study of mechanisms of graphite friction and wear. *Wear.* 1964, Vol. 7, pp. 118-126.

64. **Bragg, W.L.** Introduction to Crystal Analysis. London : G Bell and Son, 1928, p. 64.

65. **Savage, R.H.** Graphite lubrication. *J. Appl. Phys. .* 1948, Vol. 19, 1.

66. **Y.N. Vasilev, I.A. Kolyaev, V.A. Fugol.** On the Friction Mechanism of Solid Lubricants. *Journal of Friction and Wear.* 2011, Vol. 32, 5, pp. 324–332.

67. **Bragg, W.** The Investigation of Properties of Thin Films by Means of X-rays. *Nature.* 1925, 115, pp. 266–269.

68. **U.G. Bregg, U.L. Bregg.** X-rays and Crystal Structure. 1915.

69. **Sathma, D.** Properties Of Graphite and Diamond and Other Carbon Structures. [Online] 2012. chemistrycarbons.blogspot.it.

70. **A.J. Taylor, S.K. Taylor, D.A. Hubbard, M. Lotfipour.** *Friction pads for use in disc brakes. US Pat. 5725077* 1998. United States Patent and Trademark Office.

71. **K. Takahasi, M. Yoshida, Y. Hagiwara, K. Kondoh, Y. Takano, Y. Yamashita.** *Titanium and/or titanium alloy sintered friction material. US Pat. 5922452* 1999. United States Patent and Trademark Office.

72. **Booher, B.V.** *Pultrusion method of making brake linings. US Pat. 5156787* 1992. United States Patent and Trademark Office.

73. *Tribological properties of solid lubricants (graphite, Sb2S3, MoS2) for automotive brake friction materials.* **M.H. Cho, J. Ju, S.J. Kim, H. Jang.** 2006, Wear , Vol. 260, pp. 855–860.

74. **G. Yi, F. Yan.** Mechanical and tribological properties of phenolic resin-based friction composites filled with several inorganic fillers. *Wear.* 2007, Vol. 262, pp. 121–129.

75. The Different Types of Commercially Available Grades. *The A to Z of Materials.* 2007.

76. **H. Etemadi, A. Shojaei.** Characterization of Reinforcing Effect of Alumina Nanoparticles on Novolac Phenolic Resin. *Polym. Composites.* 2014, Vol. 35, 7.

77. *Effects of alumina in nonmetallic brake friction materials on friction performance.* **V. Tomasek, G. Kratosova, R. Yun, Y. Fan, Y.i Lu.** 2009, J Mater Sci, Vol. 44, pp. 266–273.

78. **H.S. Kong, B.L. Jiang, J.T. Glass, G.A. Rozgonyi, K.L. More.** An examination of double positioning boundaries and interface misfit in beta-SiC films on alpha-SiC substrates. *J Appl Phys.* 1988, Vol. 63, pp. 2645–2650.

79. *Effects of silicon carbide particle sizes on friction-wear properties of friction composites designed for car brake lining applications.* **V. Matejka, Y. Lu, L. Jiao, L. Huang, G.S. Martynkova, V. Tomasek.** 2010, Tribology International , Vol. 43, pp. 155-151.

80. **Shanks, R.A.** Chapter 13 . [book auth.] G.E. Zaikov, S.V. Valsaraj, A.P. Meera S. Thomas. *Recent advances in polymer nanocomposites: synthesis and characterization.*

81. **A. Bergeret, A. Agbossou, N. Alberole, P. Cassagnau, T. Sarraf.** Micromechanical properties of random copolymers of styrene with methacrylic acid experimental and theoretical approaches. *Eur. Polym. J.* 1992, Vol. 28, pp. 1201-18.

82. **A. Bergeret, N. Alberola.** A study of the interphase in styrene-methacrylic acid polymer/glass bead composites. *Polymer.* 1996, Vol. 37, pp. 2759-2765.

83. **Cavaille, S., et al., et al.** A comparison of the micromechanical properties of various poly(2,6-dimethyl-1,4-phenylene oxide)-polystyrene (PPO-PS) polymer blends. *Polymer.* 1986, Vol. 27, 549.

84. **Harris, O.G., et al., et al.** Study of carbon fibre surface treatments by dynamic mechanical analysis. *J. Mat. Sci.* 1993, Vol. 28, pp. 3353-66.

85. **Ibarra, L., Macias, A. and Palma, E.** Viscoelastic properties of short carbon-fiber thermoplastic (sbs) elastomer composites. *J. Appl. Polym. Sci.* 1995, Vol. 57, pp. 831-842.

86. **Oréfice, R.L., Hench, L.L. and Brennan, A.B.** Effect of Particle Morphology on the Mechanical and Thermo-Mechanical Behavior of Polymer Composites. *J. Braz. Soc. Mech. Sci. .* 2001, Vol. 23, 1.

87. **S. Manoharan, B. Suresha, G. Ramadoss, B. Bharath.** Effect of Short Fiber Reinforcement on Mechanical Properties of Hybrid Phenolic Composites. *Journal of Materials.* Vol. 2014, Article ID 478549.

88. **Bowden, F.P.** A review of the friction of solids. *Wear.* 1957, Vol. 1, pp. 333-346.

89. **Crosa, I. B. G.** Tribology of Polymer Composites Used as Frictional Materials. *Advances in Composite Tribology.* s.l. : Elsevier Science Publishers B.V., 1993.

90. *Effect of aspect ratios of aramid fiber on mechanical and tribological behaviors of friction materials.* **P. Cai, Z. Li, T. Wang, Q. Wang.** 2015, Tribology International, Vol. 92, pp. 109-116.

91. *Friction and wear of friction materials containing two different phenolic resins reinforced with aramid pulp.* **S. J. Kim, H. Jang.** 2000, Tribology International , Vol. 33, pp. 477–484.

92. **S. Thomas, K. Joseph, S.K. Malhotra, K. Goda, M.S. Sreekala.** Kevlar fiber-reinforced polymer composites. *Polymer Composites, Macro- and Microcomposites.* 7.

93. *Polymer nanofibers with outstanding thermal conductivity and thermal stability: fundamental linkage between molecular characteristics and macroscopic thermal properties. .* **T. Zhang, X. Wu, T. Luo.** 36, 2014, J. Phys. Chem. C, Vol. 118 , pp. 21148–21159.

94. *Tribological performance of brake friction materials containing carbon nanotubes.* **H.J. Hwang, S.L. Jung, K.H. Cho, Y.J. Kim, H. Jang.** 2010, Wear, Vol. 268, pp. 519–525.

95. *Mechanical and tribological properties of phenolic resin-based friction composites filled with several inorganic fillers.* **G. Yi, F. Yan.** 2007, Wear , Vol. 262 , pp. 121–129.

96. *Comparative performance assessment of cenosphere and barium sulphate based friction composites.* **A. Tiwari, H.S.Jaggi, R.K. Kachhap, B. K. Satapathy, S.N. Maiti, B.S.Tomar.** 2014, Wear, Vol. 309, pp. 259–268.

97. *Epoxy Composite Reinforced with Nano and Micro SiC Particles: Curing Kinetics and Mechanical Properties.* **J. Abenojar, M.A. Martínez, M. Pantoja, F. Velasco, J.C. Del Real.** 2012, The Journal of Adhesion, Vol. 88, pp. 418-434.

98. *Mechanical and thermal properties of phthalonitrile resin reinforced with silicon carbide particles.* **M. Derradji, N. Ramdani, T. Zhang, J. Wang, T.-T. Feng, H. Wang, W.-B. Liu.** 2015, Materials and Design , Vol. 71, pp. 48–55.

99. *Microhardness studies of functionally graded polymer composites.* **M. Krumova, C. Klingshirn, F. Haupert, K. Friedrich.** 2001, Composites Science and Technology , Vol. 61, pp. 557-563.

100. *Characterization of Reinforcing Effect of Alumina Nanoparticles on Novolac Phenolic Resin.* **H. Etemadi, A. Shojaei.** 2014, Polym. Compos., Vol. 35, pp. 1285–1293.

101. **M. Kristkova, P. Filip, Z. Weiss, R. Peter.** Influence of metals on the phenol–formaldehyde resin degradation. *Polymer Degradation and Stability .* 2004, Vol. 84, pp. 49–60.

102. **Nriagu, J.O.** Stability of vivianite and ion-pair formation in the system Fe3(PO4)2-H3PO4H3PO4-H2O. *Geochimica et Cosmochimica Acta.* 1972, Vol. 36, 4, pp. 459-470.

103. **Harvey, M.T.** *2157126* [ed.] Harvel Corp. 1939.

104. **S.N. Aggarwal, M.A. Sivasamban, J.J. Aggarwal.** 1966, Paint Mfr, Vol. 36, pp. 29-36.

105. **Vernekar, S.P.** 1980, Indian J. Technol., Vol. 18, p. 170.

106. *Synthesis of Phenolic Bio-resins For Advanced Composites in Civil Engineering Structures.* **F. Cardona, T. Aravinthan, J. Fedrigo, C. Moscou.** Toowoomba, Australia : s.n., 11-12 November 2010. Southern Region Engineering Conference . SREC2010-T3-3.

107. *Mechanical and tribological properties of phenolic resin-based friction composites filled with several inorganic fillers.* **G. Yi, F. Yan.** 2007, Wear , Vol. 262, pp. 121–129.

108. **Bijwe, J.** Composites as friction materials: Recent developments in non-asbestos fiber reinforced friction materials—a review. *Polym. Compos.* 1997, Vol. 3, 18, pp. 378–396.

109. **P. Gopal, L.R. Dharani, F.D. Blum.** Fade and wear characteristics of a glass-fiber-reinforced phenolic friction material. *Wear.* 1994, Vol. 174, 1-2, pp. 119-127.

110. **K.J. Lee, J.H.C. Lin, C.P. Ju.** Surface effect on braking behavior of PAN-pitch carbon-carbon composite. *Wear.* 1996, Vol. 199, 2, pp. 228-236.

111. **A. Jullien, M.H. Meurisse, Y. Berthier.** Determination of tribological history and wear through visualisation in lubricated contacts using a carbon-based composite. *Wear.* 1996, Vol. 194, 1-2, pp. 116-125.

112. **B.K. Satapathy, J. Bijwe.** Performance of friction materials based on variation in nature of organic fibres: Part I. Fade and recovery behaviour. *Wear.* 2004, Vol. 257, 5, pp. 573-584.

113. **Satapathy, B.K.** *Performance Evaluation of Non-Asbestos Fibre Reinforced Organic Friction Materials.* Delhi : Indian Institute of Technology, 2002. Ph.D. Thesis.

114. **S.C. Bera, C.K.S. Pillai, P.N. Rangan, A.R. Arankale, J.H. Chirmade.** Frictional and wear properties of asbestos short fibre filled phosphorylated CNSL (cashew nut shell liquid) polymers for automobile brake lining. *Ind. J. Technol.* 1989, Vol. 27, pp. 393-397.

115. *Physicochemical Properties of Kevlar 49 Fiber.* **L. Penn, F. Larsen.** 1979, Journal of Applied Polymer Science, Vol. 23, pp. 59-73.

116. *Structure and property development in poly(p-phenylene terephthalamide) during heat treatment under tension.* **K.G. Lee, R. Barton, J.M. Schultz.** 1, 1995, Journal of Polymer Science: Part B: Polymer Physics, Vol. 33, pp. 1-14.

117. *Comparison and Analysis of Thermal Degradation Process of Aramid Fibers (Kevlar 49 and Nomex).* **Zhang, H.-T.** 3, 2010, Journal of Fiber Bioengineering and Informatics, Vol. 3, pp. 163-167.

118. *High pressure DSC of phenolformaldehyde moulding compounds.* **R. C. Korosec, L.Z. Meznar, P. Bukovec.** 1, 2009, Journal of Thermal Analysis and Calorimetry, Vol. 95, pp. 235–240.

119. *Phenolic Resins: Chemistry, Applications, Standardization, Safety and Ecology.* **A. Gardziella, L.A. Pilato, A. Knop.** Berlin : s.n., 2000.

120. **T.A. Osswald, G. Menges.** *Materials Science of Polymers for Engineers, 2nd Ed.* Munich : s.n., 2003.

121. *13C and 15N NMR studies of curing with hexamethylenetetramine.* **X. Zhang, M.G. Looney, D.H. Solomon, A.K. Whittaker.** 1997, Polymer, Vol. 38, pp. 5835-5848.

122. *Microstructure Evolution of Ammonia-Catalyzed Phenolic Resin During Thermooxidative Aging.* **D.-D. Guo, M.-S. Zhan, K. Wang.** 2012, Journal of Applied Polymer Science, Vol. 126, pp. 2010-2016.

123. *Comparative study of carbon dioxide and nitrogen atmospheric effects on the chemical structure changes during pyrolysis of phenol-formaldehyde spheres.* **Y.J. Kim, M.I. Kim,**

C.H. Yun,J.Y. Chang, C.R. Park, M. Inagaki. 2004, J Colloid Interface Sci, Vol. 274, pp. 555-562.

124. *Control of Gaseous Emission During the Curing of Novolac Phenolic Resin in Friction Materials Production: Production Cycle, Physical properties and Tribological Properties Improvements.* **D.A. Santamaria Razo, D. Pellerej.** Jacksonville, Florida : s.n., 2013. 2013-01-2058.

125. *Dynamic mechanical properties of epoxy-phenolic mixtures.* **J.M. Laza, J.L. Vilas, M.T. Garay, M. Rodríguez, L.M. León.** 2005, Journal of Polymer Science Part B: Polymer Physics, Vol. 43, pp. 1548-1555.

126. *Polymer nanofibers with outstanding thermal conductivity and thermal stability: fundamental linkage between molecular characteristics and macroscopic thermal properties.* **T. Zhang, X. Wu, T. Luo.** 2014, J. Phys. Chem. C, Vol. 118, pp. 21148–21159.

127. [Online] www.engineeringtoolbox.com.

128. **A.M. James, M.P. Lord.** Macmillan's Chemical and Physical Data. London, UK : s.n., 1992.

129. **Iacoviello, F.** Comportamento a temperatura elevata. Università di Cassino-Di.M.S.A.T. : s.n.

130. *Optimization of Tribological Properties of Nonasbestos Brake Pad Material by Using Steel Wool.* **R. Vijay, M. Jees Janesh, M.A. Saibalaji, V. Thiyagarajan.** 2013, Advances in Tribology, Vol. 2013.

131. *Effect of Short Fiber Reinforcement on Mechanical Properties of Hybrid Phenolic Composites.* **S. Manoharan, B. Suresha, G. Ramadoss, B. Bharath.** 2014, Journal of Materials, Vol. 2014, p. 9.

132. *Dynamic analysis studies of the interphase.* **Chua, P.S.** 5, 1987, Poly Comp, Vol. 8, pp. 308-313.

133. **Young, D. Hugh.** Vol. 7th. Ed, Table 15-5.

134. *Percolation and conduction.* **Kirkpatrick, S.** 4, 1973, Rev. Mod. Phys., Vol. 45, pp. 574-588.

135. **Zallen, R.** *The Physics of Amorphous Solids.* 1985, 4.

136. *Agglomeration and electrical percolation behavior of carbon black dispersed in epoxy resin.* **R. Schüeler, J. Petermann, K. Schulte, H.-S. Wentzel.** 1997, J. Appl. Polymer Sci, Vol. 63, pp. 1741-1746.

137. *Thermal characterization of Al2O3 and ZnO reinforced silicone rubber as thermal pads for heat dissipation purposes .* **L.C. Sim, S.R. Ramanan, H. Ismail, K.N. Seetharamu, T.J. Goh.**

138. *Thermal characterization of Al2O3 and ZnO reinforced silicone rubber as thermal pads for heat dissipation purposes.* **L.C. Sim, S.R. Ramanan, H. Ismail, K.N. Seetharamu, T.J. Goh.** 2005, Thermochimica Acta, Vol. 430, pp. 155–165.

139. *Thermal conductivities of powder filled epoxy resins.* **F. Lin, G.S. Bahtia, J.D. Ford.** 1993, J. Appl. Polym. Sci. , Vol. 49, pp. 1901–1908.

140. *Thermal conductivity of polystyrene aluminum nitride composite.* **S. Yu, P. Hing, X. Hu.** 2002, Compos. Part A, Vol. 33, pp. 289–292.

141. *Thermal conductive polymer composites for electronic packaging.* **X. Lu, G. Xu.** 1997, J. Appl. Polym. Sci. , Vol. 65, pp. 2733–2738.

142. *Thermal conductivities of composites in several types of dispersion systems.* **Y. Agari, A. Ueda, S. Nagai.** 1997, J. Appl. Polym. Sci., Vol. 65, pp. 2733–2738.

143. *Estimation on thermal conductivities of filled polymers.* **Y. Agari, T. Uno.** 1986, J. Appl. Polym. Sci. , Vol. 32, pp. 5705–5712.

144. *Effect of hexagonal boron nitride and calcined petroleum coke on friction and wear behavior of phenolic resin-based friction composites.* **G. Yi, F. Yan.** 2006, Materials Science and Engineering A, Vol. 425, pp. 330–338.

145. **E.G. Morris, J.M. Faircloth.** Thermal and Electrical Properties of Petroleum Cokes.

146. *Epoxy- phenol-cardanol-formaldehyde system: Thermogravimetry analysis and their carbon fiber composites.* **N.H. Nieu, T.T.M. Tan, N.L. Huong.** 1996, Journal of Applied Polymer Science, Vol. 61, pp. 2259-2264.

147. [Online] www.engineeringtoolbox.com.

148. **Guo, M.** Dynamic mechanical thermal analysis of polymer composites. *Beijing: Chemical Industry.* 2002.

149. *Preparation, damping and thermal properties of potassium titanate whiskers filled castor oil-based polyurethane/epoxy interpenetrating polymer network composites.* **S. Chen, Q. Wang, T. Wanga, X. Pei.** 2011, Materials and Design, Vol. 32, pp. 803-807.

150. *Thermal and Mechanical Properties of Aluminum Alloy Composite Reinforced with Potassium Hexatitanate Short Fiber.* **K. Asano, H. Yoneda, Y. Agari, M. Matsumuro, K. Higashi.** 2015, Materials Transactions, Vol. 56, pp. 160-166.

151. *Comparative performance assessment of cenosphere and barium sulphate based friction composites.* **A.Tiwari, H.S.Jaggi, R.K. Kachhap, B.K. Satapathy, S.N. Maiti, B.S.Tomar.** 2014, Wear, Vol. 309, pp. 259–268.

152. *Dynamic mechanical properties of particulate filled composites.* **T.B. Lewis, L.E. Nielsen.** 1970, J. Appl. Polym. Sci. , Vol. 14, pp. 1449–1471.

153. *Dynamic mechanical properties of polymer filled with agglomerated particles.* **Nielsen, L.E.** 1979, J. Appl. Polym. Sci. , Vol. 17, pp. 1897–1901.

154. *Dynamic mechanical analysis of banana fiber reinforced polyester composites.* **L.A. Pothan, Z. Oommen, S. Thomas.** 2003, Composites Science and Technology, Vol. 63, pp. 283–293.

155. *Barium Sulfate-Filled Biomedical Compounds of a Poly(Ether-Block-Amide) Copolymer.* **Guo, X.** 2008, Journal of Applied Polymer Science, Vol. 109, pp. 4015–4024.

156. **W.H. Diment, H.R. Pratt.** *Thermal conductivity of some rockforming minerals: a Tabulation.* U. S. Geol. Survey. Denver Co : s.n., 1988. p. 15, U.S.G.S. Open file report 88-690.

157. **T. Komori, S. Miyake, Y. Senoo.** *Brake friction material containing BT resin dust. 4954536* 1995.

158. **U. Grigull, H. Sandner.** *Heat Conduction (Wtirmeleitung).* s.l. : Springer, 1990, p. 163.

159. *Material properties of a sintered α-SiC.* **Munro, R.G.** 5, 1997, J. Phys. Chem., Vol. 26, pp. 1195-1203.

160. *Preparation and Properties of SiC/Phenolic Resin for the Heat of LED.* **C. Wu, K. Zhao, Y. Tang, J. Mad.** 2016, Materials Science Forum, Vol. 848, pp. 454-459.

161. **Kato, K.** Classification of wear mechanism/models. *Wear-materials, mechanism and practice.* UK : Wiley, 2005, pp. 5-20.

162. **M. Atarian, H. Reza Salehi, M. Atarian, A. Shokuhfar.** Effect of oxide and carbide nanoparticles on tribological properties of phenolic-based nanocomposites. *Iran Polym J.* 2012, Vol. 21, pp. 297–305.

163. **B. Naga Raju, K. Ramji, V.R.S.K. Prasad.** Studies on tribological properties of ZnO filled polymer nanocomposites. *ARPN J Eng Appl Sci.* 2011, Vol. 6, pp. 75-82.

164. **H. Fu, B. Liao, Y.H. Wang, F.R. Xiao, B.C. Sun.** Thermal stability of poly (ether ether ketone) composites under dry-sliding friction and wear conditions. *Iran Polym J.* 2008, Vol. 17, pp. 493-501.

165. **Bijwe, J.** Composites as friction materials: recent developments in non-asbestos reinforced friction materials. *Polym Compos.* 1997, Vol. 18, pp. 378–395.

166. **H.R. Salehi, S.M.R. Khalili.** Thermal, mechanical and carbonization behavior of high temperature phenolic polymer. *Adv Mater Eng.* 2011, Vol. 30, 2, pp. 69-81.

167. *Effect of aspect ratios of aramid fiber on mechanical and tribological behaviors of friction materials.* **P.Cai, Z. Li, T. Wang, Q. Wang.** 2015, Tribology International, Vol. 92, pp. 109-116.

168. *The effect of phenolic resin, potassium titanate, and CNSL on the tribological properties of brake friction materials.* **Y.C. Kima, M.H. Choa, S.J. Kimb, H. Jang.** 2008, Wear, Vol. 264 , pp. 204–210.

169. *Influence of modified phenolic resins on the fade and recovery behavior of friction materials.* **J. Bijwe, Nidhi, N. Majumdar, B.K. Satapathy.** 2005, Wear, Vol. 259, pp. 1068–1078.

170. *On the Friction Mechanism of Solid Lubricants.* **Y.N. Vasil'eva, I.A. Kolyaeva, V.A. Fugol.** 5, 2011, Journal of Friction and Wear, Vol. 32, pp. 324–332.

171. *Solid lubricant additives-effect of concentration and other additives on anti-wear performance.* **Bartz, W.J.** 1971, Wear, Vol. 17 , pp. 421-432.

172. **Jerzy, G.A.** *Graphite lubricant. US Pat. 3383311* [ed.] The British Petroleum Company Limited. London, England., 1968.

173. **A.J. Taylor, S.K. Taylor, D.A. Hubbard, M. Lotfipour.** *Friction pads for use in disc brakes. 5725077* 1998.

174. *Tribological screening tests for the selection of raw materials for automotive brake pad formulations.* **W. Österle, C. Deutsch, T. Gradt, G. Orts-Gil, T. Schneider, A.I. Dmitriev.** 2014, Tribology International, Vol. 73, pp. 148-155.

175. *Analysis of tribological behaviour of nanocomposite coating for die casting application.* **Faga, M.G.** Portoroz (Slovenia) : s.n., 2015. 23rd International Conference on Materials and Technology .

176. *Friction and wear behavior of copper matrix composites reinforced with SiC and graphite particles.* **Y. Zhan, G. Zhang.** 1, 2004, Tribology Letters, Vol. 17.

177. *Tribological surfaces of organic brake pads.* **M. Eriksson, S. Jacobson.** 2000, Tribology International , Vol. 33, pp. 817–827.

178. **M. Eriksson, S. Jacobson.** Tribological surfaces of organic brake pads. *Tribol Int.* 2000, Vol. 33, pp. 817–827.

179. *The third-body approach: a mechanical view of wear.* **Godet, M.** 1984, Wear, Vol. 100, pp. 437-452.

180. *Tribological characteristics of binder resins for brake friction materials at elevated temperatures.* **M.W. Shin, K.H. Cho, W.K. Lee,H. Jang.** 2, 2010, Tribology Letters, Vol. 38, pp. 161-168.

181. *Dynamic analysis studies of the interphase.* **Chua, P.S.** 5, 1987, Poly Comp, Vol. 8, pp. 308-313.

182. *Fibres in friction materials symposium.* **Anderson, A.E.** Atlantic City, New Jersey : s.n., 1987. Society Automotive Engineers.

183. *A combinatorial approach for automotive friction materials: combined effects of ingredients on friction performance.* **Lu, Y.** 5, 2002, Polym Compos , Vol. 23, pp. 814–823.

184. **Z. Zhang, W. Zhong, D. Zhang, W. Shi, J. Sejjm.** China : s.n., 1999. p. 25.

185. *Preparation of smooth potassium hexatitanate nanofilms by sol–gel method.* **Q.H. Qian, X.F. Zhou, Y.Y. Hu, C. Liu, X. Feng, X.H. Lu.** 2007, J Mater Sci , Vol. 42, pp. 8222–8229.

APPENDICES

MATERIALS AND METHODS

ARAMID FIBERS: DATA FROM LITERATURE

Article Relevance (/5)				
3	**Title**	Friction and wear of friction materials containing two different phenolic resins reinforced with aramid pulp		
	Authors	S. J. Kim, H. Jang		
	Reference	Tribology International 33 (2000) 477–484		
	Studied property		**Measurement instrument/ Protocol/ Comment**	**Optimal [filler] / Tendency**
	μ stability		pad-on-disk type friction tester (gray cast iron)	Increase (10%vol.)
	Hardness (HRS)		Rockwell hardness tester in S scale	Decrease
	Porosity (%)		Mercury porosimeter	Increase
	Specific wear (mm^3/Nm)		pad-on-disk type friction tester (gray cast iron)	Increase

Article Relevance (/5)				
4	**Title**	Hybrid phenolic friction composites containing Kevlar pulp. Part I. Enhancement of friction and wear performance		
	Authors	P. Gopal, L.R. Dharani, Frank D. Blum		
	Reference	Wear 193 (1996) 199-206		
	Studied property		**Measurement instrument/ Protocol/ Comment**	**Optimal [filler] 0 o 12%vol. / Tendency**
	Coefficient of Friction		Chase friction material testing machine	Decrease ; Enhance friction stability
	Wear		Chase friction material testing machine	Decrease
	Noise (squeal)		Record due to motor connected to drum	Eliminated high frequency noise (>5 kHz)

Article Relevance (/5)			
3	**Title**	Synergistic effects of aramid pulp and potassium titanate whiskers in the automotive friction material	
	Authors	S.J. Kim, M.H. Cho, D.-S. Lim, H. Jang	
	Reference	Wear 251 (2001) 1484–1491	
	Studied property	**Measurement instrument/ Protocol/ Comment**	**Optimal [filler] (total of 30%vol. of fibrous ingredients) / Tendency**
	Friction	pad-on-disk type friction tester	More stable for 22.5%vol.
	Wear	pad-on-disk type friction tester	Less important for composite at ≥15 vol.%

Article Relevance (/5)			
4	**Title**	The wear of aramid fiber reinforced brake pads: the role of aramid fibers	
	Authors	T. Kato, A. Magario	
	Reference	Tribol. Trans., 37. 559-565 (1994)	
	Studied property	**Measurement instrument/ Protocol/ Comment**	**Optimal [filler] (0-40 wt%) / Tendency**
	μ	Slider on disk-type wear tester	Decrease until 15%wt, then plateau
	Hardness (HRR)		Decrease linearly
	Thermal conductivity		Decrease linearly
	Wear rate	Slider on disk-type wear tester	Decrease (optimum for 25-35%wt)
	Observation counterpart	SEM	More firmly attached transfer film

Article Relevance (/5)			
4	**Title**	Friction and wear behaviour of continuous fibre as cast Kevlar-phenolic resin composite; Effect of sliding speed on friction and wear of unidirectional aramid fibre-phenolic resin composite	
	Authors	S. K. Sinha, S. K. Biswas	
	Reference	J. Mater. Sci., 27, 3085 (1990) ; J. Mater. Sci., 30, 2430 (1995)	
	Studied property	**Measurement instrument/ Protocol/ Comment**	**Optimal [filler] (0/30 wt% fiber) / Tendency**
	μ	Pin-on-disk machine	Reducing μ (without : 1.5-1.2; with : 0.8-0.31)
	Wear resistance	Pin-on-disk machine	Enhancing (30-40 times)

STEEL FIBERS: DATA FROM LITERATURE

Article Relevance (/5)			
3	**Title**	The effect of metal fibers on the friction performance of automotive brake friction materials	
	Authors	H. Jang, K. Ko, S.J. Kim, R.H. Basch, J.W. Fash	
	Reference	Wear 256 (2004) 406–414	
	Studied property	**Measurement instrument**	**[Filler] in the tested formulation**
	Friction	Small-scale friction tester	Maintain the COF at elevated temperatures with steel than Al or Cu fibres (at 15%vol.)
	Wear	Small-scale friction tester	Better with steel than Al or Cu fibres (at 15%vol.)
	Fade	Small-scale friction tester	Improved with steel fibers at high T (at 15%vol.)

POTASSIUM HEXATITANATE FIBERS: DATA FROM LITERATURE

Article Relevance (/5)			
2	**Title**	Tribological Properties of Potassium Titanate in the Brake Friction Material; Morphological Effects	
	Authors	Keun Hyung Cho, Min Hyung Cho, Seong Jin Kim, Ho Jang	
	Reference	Tribol Lett (2008) 32:59–66	
	Studied property	**Measurement instrument/ Protocol / Effect**	**[Filler] in the tested formulation**
	Friction stability	Krauss type friction tester	20%vol of splinter filler shape
	Wear	Krauss type friction tester	20%vol of splinter filler shape

Article Relevance (/5)			
4	**Title**	Hybrid composite friction materials reinforced with combination of potassium titanate whiskers and aramid fibre: Assessment of fade and recovery performance	
	Authors	M. Kumar, B. K. Satapathy, A. Patnaik, D. K.Kolluri, B.S.Tomar	
	Reference	Tribology International 44 (2011) 359–367	
	Studied property	**Measurement instrument/ Protocol / Effect**	**[Filler] in the tested formulation**
	Fade/recovery	Krauss type Rubber Wheel Direct Current	potassium titanate:aramid pulp = 5:1

FRICTION DUST: DATA FROM LITERATURE

Article Relevance (/5)				
2	**Title**	Effect of cashew nut shell liquid (CNSL) on properties of phenolic resins		
	Authors	P. A. Mahanwar and d. D. Kale		
	Reference	Journal of applied polymer science, vol. 61, 2107-2111 (1996)		
	Studied property		**Measurement instrument**	**Optimal [filler] / Tendency**
	Breakdown voltage (V/mm)			Increase and then decrease Phenol:CNSL = 75:25 for novolac ; 55:45 for resole
	Hardness (shore D)			Increase
	Charpy impact (J/mm^2)			Increase for resole.
	Tensile strength (kg/cm^2)			Decrease

Article Relevance (/5)				
3	**Title**	The effect of phenolic resin, potassium titanate, and CNSL on the tribological properties of brake friction materials		
	Authors	Y.C. Kim, M.H. Cho, S.J. Kim, H. Jang		
	Reference	Wear 264 (2008) 204–210		
	Studied property		**Measurement instrument/ Protocol / Effect**	**Optimal [filler] between 8, 16 or 24%vol / Tendency**
	Compressibility (µm/kN)		Jurid compression tester	Increase
	Hardness (HRS)		Rockwell hardness tester in S scale	Decrease
	Porosity (%)		Mercury porosimeter	Increase
	Friction coefficient		Rotating gray iron disk	Increase
	Wear rate (mm3/Nm)		Rotating gray iron disk	Increase

BARIUM SULFATE: DATA FROM LITERATURE

Article Relevance (/5)			
3	**Title**	Tribological properties of polymer composites containing barite ($BaSO_4$) or potassium titanate (K_2O . 6(TiO_2))	
	Authors	S.J. Kim, M.H. Cho, R.H. Basch, J.W. Fash, and H. Jang	
	Reference	Tribology Letters, Vol. 17, No. 3, October 2004 (2004)	
	Studied property	**Measurement instrument/ Protocol / Effect**	**Optimal [filler] between 70%vol BaSO4 or potassium titanate / Tendency**
	Worn surface morphology	SEM	hair cracks, patches of compacted fine particles → poor wear resistance
	COF	block-on-disk type tribometer	Increase at low sliding velocity COF instability for BaSO4

GRAPHITE: DATA FROM LITERATURE

Article Relevance (/5)			
3	**Title**	Tribological properties of solid lubricants (graphite, Sb2S3, MoS2) for automotive brake friction materials	
	Authors	Min Hyung Cho, Jeong Ju, Seong Jin Kim, Ho Jang	
	Reference	Wear 260 (2006) 855–860	
	Studied property	**Measurement instrument/ Protocol / Effect**	**[Filler] in the tested formulation**
	Friction stability and fade resistance	Brake dynamometer - Early fading	Increases with content of graphite
	Lubricating capability	Brake dynamometer - At high T decomposition and loses	With increase of graphite content
	Wear resistance	Brake dynamometer	Increases with graphite content

PETROLEUM COKE: DATA FROM LITERATURE

Article Relevance (/5)				
4	**Title**	Mechanical and tribological properties of phenolic resin-based friction composites filled with several inorganic fillers		
	Authors	G. Yi, F. Yan		
	Reference	Wear 262 (2007) 121–129		
	Studied property		**Measurement instrument/ Protocol / Effect**	**[Filler] in the tested formulation**
	Hardness and bending strength		Optical hardness tester	Increase when content increase
	Friction		Pin-on-disc tribometer	Decrease when content increase
	Wear		Pin-on-disc tribometer	Decrease when content increase

ALUMINUM OXIDE: DATA FROM LITERATURE

Article Relevance (/5)				
3	**Title**	Characterization of reinforcing effect of alumina nanoparticles on novolac phenolic resin		
	Authors	H. Etemadi, A. Shojaei		
	Reference	Polym. Compos.		
	Studied property		**Measurement instrument/ Protocol / Effect**	**Optimal [Filler] in the tested formulation**
	Tensile strength		Universal testing machine according to ASTM D 3039 - Increase	2.5 %wt.
	Crosslinking density - tanδ - Tg		DMA	5%wt.

Article Relevance (/5)				
5	**Title**	Effects of alumina in nonmetallic brake friction materials on friction performance		
	Authors	V. Tomasek, G. Kratosova, R. Yun, Y. Fan, Y. Lu		
	Reference	J Mater Sci (2009) 44:266–273		
	Studied property		**Measurement instrument/ Protocol / Effect**	**Optimal [Filler] in the tested formulation**
	μ stability		JF151 friction tester	0-14.6%vol. Best: 5.6%vol.
	Wear rate		JF151 friction tester	0-14.6%vol. Best >3%vol.

SILICONE CARBIDE: DATA FROM LITERATURE

Article Relevance (/5)			
5	**Title**	Effects of silicon carbide particle sizes on friction-wear properties of friction composites designed for car brake lining applications	
	Authors	V. Matejka, Y. Lu, L. Jiao, L. Huang, G.S. Martynkova, V. Tomasek	
	Reference	Tribology International 43 (2010) 144–151	
	Studied property	**Measurement instrument/ Protocol / Effect**	**Optimal [Filler] in the tested formulation**
	Specific Wear	Friction tester	0-14.6 %vol. with 3.4%vol. best
	Friction coefficient	Friction tester	0-14.6 %vol. with 3.4%vol. best